IMPROVING THE PHOTOELECTROCHEMICAL ACTIVITY OF PHOTOELECTRODES THROUGH SURFACE ENGINEERING: SYSTEMATIC ELECTROCATALYSIS AND CO-CATALYSIS STUDIES

Javier Quiñonero Aliaga

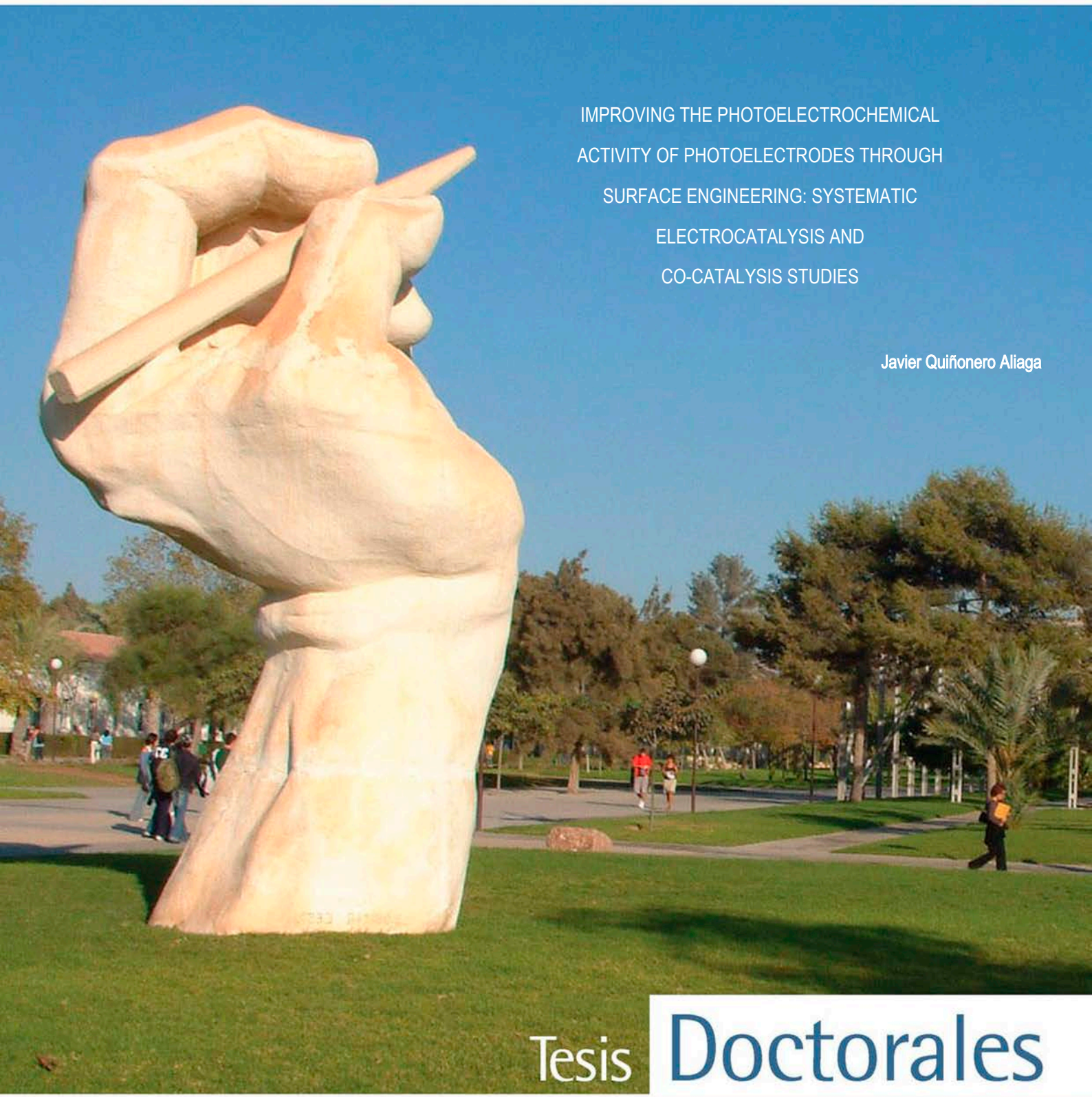

Universitat d'Alacant
Universidad de Alicante

FACULTAD DE CIENCIAS
DEPARTAMENTO DE QUÍMICA FÍSICA

IMPROVING THE PHOTOELECTROCHEMICAL ACTIVITY OF PHOTOELECTRODES THROUGH SURFACE ENGINEERING: SYSTEMATIC ELECTROCATALYSIS AND CO-CATALYSIS STUDIES

Memoria presentada para optar al grado de Doctor con Mención Internacional por la Universidad de Alicante por:

JAVIER QUIÑONERO ALIAGA

Programa de doctorado en Ciencia de Materiales

Dirigida por

Dr. D. Roberto Gómez Torregrosa

Catedrático del Departamento de Química Física
de la Universidad de Alicante

La realización de la presente tesis doctoral ha sido financiada por el Ministerio español de Educación, Cultura y Deporte mediante una ayuda para la Formación de Profesorado Universitario (FPU15/02005).

Universitat d'Alacant
Universidad de Alicante

Dr. D. ROBERTO GÓMEZ TORREGROSA, catedrático del Departamento de Química Física de la Universidad de Alicante

CERTIFICA

Que el trabajo con título 'Improving the photoelectrochemical activity of photoelectrodes through surface engineering: Systematic electrocatalytic and co-catalyst studies', presentado por Javier Quiñonero Aliaga para aspirar al grado de Doctor con Mención Internacional dentro del programa de doctorado en Ciencia de Materiales, ha sido realizado en los laboratorios del Departamento de Química Física de la Universidad de Alicante (Alicante, España) bajo mi supervisión y que, a mi juicio, reúne los requisitos necesarios y exigidos para un trabajo de estas características.

Y para que así conste a los efectos oportunos, se firma el presente certificado.

Alicante, septiembre de 2020

Dr. D. Roberto Gómez Torregrosa

Universitat d'Alacant
Universidad de Alicante

Dra. Dña. TERESA LANA VILLARREAL, secretaria del Departamento de Química Física de la Universidad de Alicante

CERTIFICA

Que el trabajo con título 'Improving the photoelectrochemical activity of photoelectrodes through surface engineering: Systematic electrocatalytic and co-catalyst studies', presentado por Javier Quiñonero Aliaga para aspirar al grado de Doctor con Mención Internacional dentro del programa de doctorado en Ciencia de Materiales, ha sido realizado en el Departamento de Química Física de la Universidad de Alicante (Alicante, España) bajo la dirección del Dr. D. Roberto Gómez Torregrosa.

Y para que así conste a los efectos oportunos, se firma el presente certificado.

Alicante, septiembre de 2020

Dra. Dña. Teresa Lana Villarreal

AGRADECIMIENTOS

Al director de esta tesis, el profesor Roberto Gómez, por haberme ofrecido participar en su grupo de investigación y darme la oportunidad de realizar este trabajo.

Al Ministerio español de Educación, Cultura y Deporte por la concesión de una Ayuda para la Formación de Profesorado Universitario (FPU15/02005), que ha facilitado la realización de esta tesis, y de una Ayuda a la movilidad para estancias breves (EST17/00429) que me permitió disfrutar de una estancia de investigación en la École Polytechnique Fédérale de Lausanne (Lausana, Suiza).

A la profesora Teresa Lana, por haber sido quien me acompañó en mis inicios en el laboratorio, y por su amabilidad y continua predisposición a ayudar. También le agradezco su colaboración en muchas de las tareas experimentales necesarias para completar esta tesis (especialmente, las incluidas en el Capítulo III y en lo referido a la realización y discusión de las medidas de espectroscopía Raman). De igual manera, al profesor Pedro L. Bonete por su ayuda y apoyo, y por haber sido el vínculo a través del que llegué al Departamento de Química Física.

A todos los compañeros y compañeras con los que he coincidido en el grupo de investigación a lo largo de estos años: Milena Jankulovska, Dejan Cibrev, Irene Barceló, Marisa Díez, Débora Ruiz, Victoria Manzi, Fran Navarro, Néstor Mendieta, Maxime Contreras y, muy especialmente, a Ainhoa Cots, Carmen Miralles, Fran Pastor y Ana Korina Díaz. A ellos les agradezco el buen ambiente de trabajo y todos los momentos compartidos, de los que me llevo muy buenos recuerdos y, que, sin duda, han enriquecido mucho todos

estos años de doctorado. También quiero agradecer a Damián Monllor por estar siempre dispuesto a escuchar.

Mi estancia en la École Polytechnique Fédérale de Lausanne se convirtió en una experiencia a todos los niveles. Por ello, agradezco al profesor Kevin Sivula el haberme permitido realizar esta estancia en su grupo de investigación, y a Néstor Guijarro por su ayuda y compromiso durante los meses que pasé en Lausana.

A Verónica Sáez por su profesionalidad en el laboratorio, y a Violeta Molina, Margarita Parres, Marina Marco y Mª José Lucas por facilitarme las tareas administrativas.

A mis padres, Isabel y Paco, por ser el mejor de los ejemplos, y a mi hermano, Jorge, por su apoyo incondicional. Pienso que formamos un buen equipo.

A mis amigos y amigas que, desde fuera de la universidad, me han acompañado y animado durante esta etapa (y durante muchas otras más).

LIST OF CONTENTS

LIST OF ACRONYMS, ABBREVIATURES AND PHYSICAL CONSTANTS

A	Absorbance
A	Acceptor impurity
A	Electrode area (cm^2)
A	Pre-exponential factor
ABPE	Applied bias photon-to-current efficiency (%)
AM 0	Air mass 0 (referred to solar spectrum)
AM 1.5 G	Air mass 1.5 Global (referred to solar spectrum)
ASTM	American Society for Testing and Materials
α	Absorption coefficient (cm^{-1})
α	Anodic transfer coefficient
BE	Binding energy
BEP	Band edge pinning
β	Cathodic transfer coefficient
C	Capacitance per geometric unit area ($F \cdot cm^{-2}$)
CB	Conduction band
CBD	Chemical bath deposition
CE	Counter electrode
COD	Crystallography Open Database
CV	Cyclic voltammetry
C_H	Capacitance of the Helmholtz layer ($F \cdot cm^{-2}$)
C_{SCR}	Capacitance of the space charge region ($F \cdot cm^{-2}$)
c_{red}^{s}	Surface concentration of the reduced species
c_{ox}^{s}	Surface concentration of the oxidized species
d	Interplanar space of the crystal (nm)
d	Thickness of the nanocrystalline film

dn	Equilibrium concentration of electrons
D	Donor impurity
DFT	Density functional theory
DOS	Density of states
D_{CB}	Density of states in the conduction band
$D_{n,p}$	Diffusion coefficient of electrons (n) or holes (p) ($cm^2 \cdot s^{-1}$)
D_{VB}	Density of states in the valence band
e	Elementary charge ($e = 1.6 \cdot 10^{-19}\ C$)
e^-	Electron
E	Cell potential (V)
E	Electrode potential (V)
E_0	Potential perturbation amplitude (V)
$E_{applied}$	Applied potential (V)
EE	Electrolyte-electrode illumination mode
E_b	Binding energy (eV)
E_{eq}	Equilibrium potential (V)
E_{fb}	Flat band potential (V)
EIS	Electrochemical impedance spectroscopy
E_{kin}	Kinetic electron of the emitted electron (eV)
$E_{photo-onset}$	Potential of the photocurrent onset (V)
E_{ref}	Potential measured *versus* a reference electrode (V)
E_{red}	Potential of the reduction semi-reaction (V)
E_{ox}	Potential of the oxidation semi-reaction (V)
E^0_{red}	Standard potential of the reduction semi-reaction (V)
E^0_{ox}	Standard potential of the oxidation semi-reaction (V)
$E^0_{H^+/H_2}$	Standard potential of the redox couple H^+/H_2 (V)
$E^0_{O_2/H_2O}$	Standard potential of the redox couple O_2/H_2O (V)
$E_{1,2,...}$	Potential limits (V)
$E_{1,2,...}$	Energy levels

$\Delta E(t)$	Sinusoidal potential perturbation as a function of time (V)
ε	Dielectric constant
ε_0	Vacuum permittivity ($\varepsilon_0 = 8.85 \cdot 10^{-12}\ F \cdot m^{-1}$).
ε_{CB}	Energy associated with the bottom edge of the conduction band (eV)
ε_{CB}^{b}	Energy of the conduction band edge in the semiconductor bulk (eV)
ε_{CB}^{s}	Energy of the conduction band edge at the semiconductor surface (eV)
ε_F	Fermi level energy (eV)
$\varepsilon_{F,CC}$	Fermi level of the co-catalyst (eV)
$\varepsilon_{F,n}^{*}$	*Quasi*-Fermi level for electrons in a photoexcited semiconductor (eV)
$\varepsilon_{F,p}^{*}$	*Quasi*-Fermi level for holes in a photoexcited semiconductor (eV)
$\varepsilon_{F,redox}$	Energy level of the redox couple in solution (eV)
ε_g	Band gap energy of the semiconductor (eV)
ε_{ph}	Energy variation corresponding to photopotential (eV)
ε_{SS}	Energy level of the surface states (eV)
ε_{VB}	Energy associated with the top of the valence band (eV)
ε_{VB}^{b}	Energy of the valence band edge in the semiconductor bulk (eV)
ε_{VB}^{s}	Energy of the valence band edge in the semiconductor surface (eV)
f	Frequency (s^{-1})
$f(\varepsilon)$	Probability that a state with energy ε is occupied by an electron
F	Faraday constant ($F = 96485.3365\ C \cdot mol^{-1}$)
$\mathrm{FE-SEM}$	Field emission scanning electron microscopy
FLP	Fermi level pinning
FTO	Fluorine tin oxide
ϕ	Potential at the semiconductor surface (V)
ϕ	Shift in phase
ϕ	Work function (eV)
ϕ_M	Potential of a metal electrode (V)
ϕ_{ref}	Potential corresponding to a reference electrode (V)
ϕ_{SC}	Potential of a semiconductor electrode (V)
$\Delta\phi_{GC}$	Potential drop across the Gouy-Chapman layer (V)

$\Delta\phi_H$	Potential drop across the Helmholtz layer (V)
$\Delta\phi_{SCR}$	Inner potential difference between the semiconductor bulk and surface (V)
$\Delta\phi_{SCR}(x)$	Inner potential difference between a location in the semiconductor space charge region at a distance x from the bulk and surface (V)
G_{red}	Gibbs energy of the reduced state
G_{ox}	Gibbs energy of the oxidized state
ΔG	Gibbs energy change (J)
ΔG_{red}	Gibbs energy of activation of the cathodic process (J)
ΔG_{ox}	Gibbs energy of activation of the anodic process (J)
h	Planck constant ($h = 6.63 \cdot 10^{-34}\ J \cdot s$).
h^+	Hole
HER	Hydrogen evolution reaction
HFI	High-frequency intercept
HPLC	High-performance liquid chromatography
i	Imaginary unit ($i = \sqrt{-1}$).
i_p	Peak current (A)
I_A	Intensity of light absorbed ($W \cdot cm^{-2}$)
I_T	Intensity of light transmitted ($W \cdot cm^{-2}$)
I_0	Current perturbation amplitude (A)
I_0	Incident photon flux ($cm^{-2} \cdot s^{-1}$)
I_{DC}	Current base intensity (A)
ICDD	International Center of Diffraction Data
ICP − MS	Inductively coupled plasma mass spectrometry
IHP	Inner Helmholtz plane
IMPS	Intensity-modulated photocurrent spectroscopy
IMVS	Intensity-modulated photovoltage spectroscopy
IPCE	Incident photon-to-current efficiency (%)
IPCC	International Panel on Climate Change
ITO	Indium tin oxide
$\Delta I(t)$	Sinusoidal current response as a function of time (A)

j	Current density (mA·cm^{-2})
j_0	Exchange current density (mA·cm^{-2})
j_c	Capacitive current density (mA·cm^{-2})
j_{dark}	Current density recorded in the dark (mA·cm^{-2})
j_F	Faradaic current density (mA·cm^{-2})
j_{H_2O}	Photocurrent density for water oxidation (mA·cm^{-2})
$j_{H_2O_2}$	Photocurrent density for H_2O_2 oxidation (mA·cm^{-2})
j_{OER}	Current density for O_2 evolution (mA·cm^{-2})
j_{ph}	Photocurrent density (mA·cm^{-2})
j_{ph_0}	Amplitude of the modulated photocurrent density (A)
j_{light}	Current density recorded under illumination (mA·cm^{-2})
J_{abs}	Theorical maximum photocurrent density delivered by a photoelectrode on the basis of its absorption spectra (mA·cm^{-2})
JCPDS	Joint Committee on Powder Diffraction Standards
k	Boltzmann constant ($k = 1.3806\, J \cdot mol^{-1} \cdot K^{-1}$).
k_{ox}	Rate constant for the anodic reaction
k_{rec}	Rate constant for charge recombination at the photoelectrode/electrolyte interface
k_{red}	Rate constant for the cathodic reaction
k_{tran}	Rate constant for charge transfer at the photoelectrode/electrolyte interface
K_{ps}	Solubility product constant
L_D	Debye length (cm)
$L_{n,p}$	Diffusion length of electrons (n) or holes (p) (cm)
L_{SCR}	Space charge region width (cm)
LDH	Layered double hydroxide
LFI	Low-frequency intercept
LFO	$LaFeO_3$
LSV	Linear sweep voltammetry
λ	Wavelength (nm)

$\mu_{n,p}$	Mobility of electrons (n) or holes (p) ($cm^2 \cdot V^{-1} \cdot s^{-1}$)
n	Density of free electrons in the dark (cm^{-3})
n	Number of moles reacted
n	Order of reflection
n_b	Electron density in the bulk (cm^{-3})
n_e	Number of electrons transferred in a redox process
$n_{(x)}$	Electron density for an *n*-type semiconductor within the space charge region as a function of the distance to the electrode surface, x (cm^{-3})
n^*	Electron density under illumination (cm^{-3})
Δn^*	Additional electrons produced by photoexcitation
N_A	Density of acceptor species in the semiconductor (cm^{-3})
N_{CB}	Effective density of states of the bottom of the conduction band (cm^{-3})
N_D	Density of donor species in the semiconductor (cm^{-3})
$N_{\mathrm{Ni/Co/Fe}}$	Number of electroactive Ni/Co/Fe atoms
N_{SS}	Density of surface states (cm^{-3})
N_{VB}	Effective density of states of the top of the valence band (cm^{-3})
NFO	$NiFeO_x$
NPs	Nanoparticles
m_e	Electron mass
m_e^*	Electron effective mass
m_h^*	Hole effective mass
ML	Monolayer
MOD	Metal-organic decomposition
MOF	Metal-organic framework
MS	Mott-Schottky
η	Overpotential (V)
η_{bulk}	Charge separation efficiency in the bulk
η_F	Faradaic efficiency
$\eta_{surface}$	Charge transfer efficiency at the electrode/electrolyte interface
O_{vac}	Oxygen vacancies

O_{latt}	Lattice oxygen
OCP	Open cell potential (V)
OEC	Oxygen evolution catalyst
OER	Oxygen evolution reaction
OHP	Outer Helmholtz plane
Ox	Oxidized form of a redox couple
p	Density of free holes in the dark (cm^{-3})
p_b	Hole density in the bulk (cm^{-3})
$p_{(x)}$	Hole density for a *p*-type semiconductor within the space charge region as a function of the distance to the electrode surface, *x* (cm^{-3})
p^*	Hole density under illumination (cm^{-3})
Δp^*	Additional holes produced by photoexcitation
PDF	Powder diffraction file
PEC	Photoelectrochemical
PEEK	Polyether ether ketone
PEIS	Photoelectrochemical impedance spectroscopy
PTFE	Polytetrafluoroethylene
P_{solar}	Irradiance, power density ($mW \cdot cm^{-2}$)
PV	Photovoltaics
q_{Co}^{rev}	Reversible voltammetric charge density for the oxidation of CoOOH to CoO_2 ($mC \cdot cm^{-2}$)
q_{Co}^{total}	Total voltammetric charge density for the oxidation of CoOOH to CoO_2 ($mC \cdot cm^{-2}$)
q_{Fe}	Voltammetric charge density for the oxidation of $Fe(OH)_2$ to FeOOH ($mC \cdot cm^{-2}$)
q_{Ni}	Voltammetric charge density for the reduction of NiOOH to $Ni(OH)_2$ ($mC \cdot cm^{-2}$)
rpm	Revolutions per minute
R	Ideal gas constant ($R = 8.31\ J \cdot mol^{-1} \cdot K^{-1}$).
R_{ct}	Charge transfer resistance (Ohm)
R_d	Intensity of diffuse reflected light ($W \cdot cm^{-2}$)

R_s	Electrolytic solution resistance (Ohm)
RE	Reference electrode
Red	Reduced form of a redox couple
REN21	Renewable Energy Policy Network for the 21st Century
RHE	Reversible hydrogen electrode
R_S	Electrolytic solution resistance (Ohm)
R_{sp}	Intensity of light specularly reflected ($W \cdot cm^{-2}$)
S	Intensity of light refracted ($W \cdot cm^{-2}$)
SCE	Saturated calomel electrode
SCR	Space charge region
SE	Substrate-electrode illumination mode
SE	Secondary electrons
SEM	Scanning electron microscopy
SHE	Standard hydrogen electrode
STH	Solar to hydrogen efficiency (%)
SS	Surface states
$\rho(x)$	Net charge density
σ	Electrical conductivity ($\Omega^{-1} \cdot cm^{-1}$)
t	Time (s)
t_d	Deposition time (min)
T	Temperature (K)
T	Transmittance
TEM	Transmission electron microscopy
TOF	Turnover frequency for O_2 evolution (s^{-1})
TRPL	Time-resolved photoluminescence
$\tau_{n,p}$	Carrier life-time for electrons (n) or holes (p) (s)
θ	Angle of incidence of the X-ray beam
UV	Ultraviolet
$UV-vis$	Ultraviolet visible
v	Overall rate of an electrochemical reaction

v_{sr}	Scan rate ($mV \cdot s^{-1}$)
VB	Valence band
V_{fb}	Flat-band potential (V)
V_0	Amplitude of the modulated voltage (V)
ν	Wavenumber (cm^{-1})
ν	Frequency (s^{-1})
υ_0	Wavenumber (cm^{-1})
$\nu_{scattered}$	Wavenumber of the scattered radiation (cm^{-1})
$\Delta\nu$	Raman shift (cm^{-1})
W	Mass transfer control (Warburg element)
WE	Working electrode
ω	Angular frequency ($rad \cdot s^{-1}$)
XPS	X-ray photoelectron spectroscopy
XRD	X-ray diffraction
Z	Impedance (Ohm)
Z'	Real part of the impedance (Ohm)
Z''	Imaginary part of the impedance (Ohm)
Z_0	Impedance amplitude (Ohm)

ABSTRACT AND OBJECTIVES

This doctoral thesis has been developed in the Department of Physical Chemistry of the University of Alicante and focuses on the synthesis of semiconductor materials and co-catalysts, and on the study of their applications in photoelectrochemical procedures leading to devices that perform photosynthesis artificial. Specifically, the aim is to design photoelectrodes that allow the photodissociation of water, paying particular attention to the use of certain co-catalysts that work on the surface of these photoelectrodes increasing the kinetics of the redox processes for the generation of hydrogen and oxygen.

Solar radiation provides about 120000 TW of energy each year, an amount that is four orders of magnitude greater than the technological consumption made by humanity. Therefore, and due to the growing demand for energy worldwide, the idea of trying to tackle the current energy problem from the point of view of the photochemical conversion and accumulation of solar energy is interesting. This strategy would also allow solving the serious environmental problems caused by the consumption of fossil fuels, which remain as the majority source of energy today.

In this context, hydrogen represents one of the most promising and sustainable alternatives to fossil fuels. In fact, as a fuel, hydrogen stands out for its high energy density and because its combustion does not release carbon compounds. In a scenario where traditional methods for obtaining pure hydrogen face great challenges, water presents itself as an ideal source of hydrogen, abundant and free from the harmful greenhouse gases that otherwise arise as by-products. The photoelectrolysis of water on semiconductor electrodes,

which consists of splitting that molecule into its components, oxygen and hydrogen, requires applying electricity from an external source with the use of suitable electrocatalysts to break chemical bonds. The first study on this topic was published by Fujishima and Honda in 1972, who described a photoelectrochemical cell for the dissociation of water into oxygen and hydrogen, consisting of a titanium dioxide photoanode and a platinum counter electrode:

$$H_2O_{(l)} \rightarrow H_{2(g)} + \tfrac{1}{2}\, O_{2(g)} \qquad \Delta G^0_{298\,K} = 237\ kJ \cdot mol^{-1}$$

However, it has not yet been possible to develop a photoelectrochemical system of these characteristics that offers truly competitive efficiencies and stability. The choice and development of photoactive electrode materials (photoanode and photocathode) is one of the variables that determine both factors decisively. Among the main characteristics that semiconductor materials must fulfill to act as photoanodes or photocathodes, the following stand out: (i) efficient transport of electrical charge, (ii) favorable position of the valence and conduction bands to induce the reduction and oxidation reactions of the water, (iii) good absorption of visible light (which implies a bandgap value between 1.9 and 3.1 eV), (iv) high chemical stability both in aqueous media and under illumination conditions, in order to ensure a long useful life of the devices, and (v) low economic cost.

Although semiconductor oxides are the most promising materials in this area, no semiconductor material that meets all these requirements has yet been identified with which photodissociation of water can be carried out efficiently: many have a bandgap value too large or too small or are unstable in aqueous media. Among the different strategies aimed at increasing the efficiency of the oxygen and hydrogen generation processes on semiconductor electrodes, its superficial modification with electrocatalyst particles (known as co-catalysts) are among the most extensively studied. They serve to improve the transfer of photogenerated

charge carriers and limit their recombination, and to decrease the overpotentials for oxygen and hydrogen evolution reactions.

In fact, in order to facilitate an efficient reaction, that co-catalysts must exhibit a high durability, a high catalytic activity and a large surface area. Platinum is very efficient for electrocatalysis, but its extremely high price, greater than $30000 per kilogram, and its low abundance makes its commercial use on a large scale unfeasible. For all these reasons, it is of great importance to explore new, more feasible routes that allow the electrocatalysis of both redox processes. Based on the latest research, certain metal hydroxides, nitrides, phosphides, sulfides, and carbides of certain transition elements could act as co-catalysts on semiconductor photoelectrodes.

In this context, the main objectives of this doctoral thesis are the following:

- Synthesize different compact nanocrystalline or polycrystalline semiconductor electrodes from ternary oxides of the ABO_4 family and the perovskite family (ABO_3) using sol-gel synthesis techniques, for their later use as photoanodes or photocathodes in photoelectrochemical water splitting processes.

- Characterize from an electrochemical and photoelectrochemical point of view the different synthesized photoelectrodes to evaluate their activity as photoanodes or photocathodes in photoelectrochemical water splitting processes. For these purposes, techniques such as cyclic voltammetry, linear sweep voltammetry, chronoamperometry and (photo)electrochemical impedance measurements were conducted.

- Synthesize different metal hydroxides from the iron group (Fe, Co and Ni) using a chemical bath synthesis technique, for their later use as electrocatalysts for the oxygen evolution reaction in alkaline media, and as co-catalysts for the photoelectrochemical reaction of oxygen evolution on the obtained photoanodes.

- Characterize from an electrochemical and photoelectrochemical point of view the different metal hydroxides prepared to evaluate their activity as electrocatalysts for the reaction of oxygen generation in alkaline media and as co-catalysts of the photoelectrochemical reaction of oxygen generation on the obtained photoanodes, in order to improve their photoelectrochemical properties and thus enhance their applicability in photoelectrochemical water splitting processes. For these purposes, techniques such as cyclic voltammetry, linear sweep voltammetry and chronoamperometry were conducted.

- Synthesize metallic particles (mainly Ni), by means of an electrodeposition synthesis technique, that can be used as co-catalysts of the photoelectrochemical hydrogen evolution reaction on the obtained photocathodes to improve their photoelectrochemical properties. and thus, enhance its applicability in artificial photosynthesis cells. The possibility of generating a TiO_2 passivating/extracting layer between the photocathode surface and the co-catalyst deposit that favors its activity is also contemplated. For these purposes, techniques such as cyclic voltammetry, linear sweep voltammetry, chronoamperometry and (photo)electrochemical impedance measurements were conducted.

- Characterize structurally, compositionally, and morphologically the prepared photoelectrodes and electrocatalysts using X-ray diffraction techniques, spectroscopic techniques (ultraviolet-visible absorption spectroscopy, X-ray photoelectron spectroscopy and Raman spectroscopy), and microscopy techniques (scanning and transmission electron microscopies).

The development of these objectives, the corresponding results, and the derived conclusions are exposed in detail in eleven related chapters. Chapter I consists in an introduction where the basic physical and electrochemical principles of semiconductors and the state-of-the-art of the materials used throughout this thesis are presented. In Chapter II,

the different synthesis and characterization techniques employed in these studies are reviewed. Chapters III to X are specifically dedicated to the development of the aforementioned objectives related to the preparation and characterization of photoelectrodes, electrocatalysts and co-catalysts. Chapters III to VI have been published in indexed journals, whereas the results provided from Chapter VII to X have already been submitted or will be submitted for publication in the near future. Finally, Chapter XI shows the general and specific conclusions of this thesis.

Chapter I. Introduction.

In Chapter I, the general context regarding the current energy and environmental challenge where this doctoral thesis can be located is firstly reviewed. The continuously growing energy demand together with the severe environmental problems induced by the excessive emission of polluting gases from the combustion of fossil fuels have motivated the search for sustainable and green energy sources.

Since hydrogen was identified as one of the most promising energy vectors, new methodologies based on artificial photosynthesis on semiconductor electrodes to generate solar hydrogen have received a great deal of attention. In them, the search and optimization of semiconductor materials acting as light absorbers is a key element in the development of efficient photoelectrochemical devices. So, a review of the main physics and electrochemical properties of semiconductors is presented.

In this sense, the main characteristics, properties, and recent advances made in the field of the ternary semiconductor oxides used in this thesis as photoanodes ($BiVO_4$, $FeVO_4$, and $LaFeO_3$) and as photocathodes ($NdFeO_3$) are described. Finally, and regarding the use of co-catalysts on photoelectrodes as a strategy to improve their performance, the main points of

the use of iron-group metal hydroxides and metal particles on photoelectrodes as co-catalysts are exposed.

Chapter II. Experimental methods.

In this Chapter II, the main experimental procedures and the structural, morphological, compositional and (photo)electrochemical characterization techniques employed in the context of this thesis are presented in detail.

First, the synthesis methods for the preparation of the semiconductor photoelectrodes and the electrocatalysts and co-catalysts studied in the following chapters are briefly described. As already stated, the photoelectrode materials have been prepared through a sol-gel synthesis procedure, while chemical bath deposition and electrodeposition have been used for the synthesis of electrocatalysts and co-catalysts.

After that, the experimental setups (mainly, (photo)electrochemical cells and illumination sources) used for the (photo)electrochemical characterization of the prepared materials are presented, including the three-electrode cells used for this characterization. Finally, brief descriptions of the fundamentals and characteristics of the (photo)electrochemical (cyclic voltammetry, linear sweep voltammetry, chronoamperometry, and electrochemical impedance spectroscopy), spectroscopic (UV-vis, XPS, and Raman), diffraction (XRD) and microscopic techniques (SEM and TEM), and computational methods employed in these studies are provided.

Chapter III. Improving the photoactivity of bismuth vanadate thin film photoanodes through doping and surface modification strategies.

The preparation of pristine and doped bismuth vanadate photoanodes and their photoelectrochemical behavior for water photooxidation are reported in this Chapter III. In fact, among the ternary oxides based on earth-abundant metals, bismuth vanadate has recently emerged as a promising photoanode. Herein, $BiVO_4$ thin film photoanodes have been successfully synthesized by a modified metal-organic precursor decomposition method, followed by an annealing treatment. In an attempt to improve the photocatalytic properties of this semiconductor material for photoelectrochemical water oxidation, the as-prepared electrodes have been modified (i) by doping with La and Ce by modifying the composition of the $BiVO_4$ precursor solution with the desired concentration of the doping element, and (ii) by surface modification with Au nanoparticles potentiostatically electrodeposited. La and Ce doping at concentrations of 1 and 2 at% in the $BiVO_4$ precursor solution, respectively, enhance significantly the electrocatalytic performance of $BiVO_4$ without introducing important changes in either the material structure or the electrode morphology, according to XRD and SEM characterization. In addition, surface modification of the electrodes with Au nanoparticles further enhances the photocurrent as such metallic nanoparticles act as co-catalysts, promoting charge transfer at the semiconductor/solution interface. These two complementary ways of modifying the electrodes have resulted in a significant increase in the photoresponse, facilitating its potential application in artificial photosynthesis devices.

Chapter IV. Controlling the amount of co-catalyst as a critical factor in determining the efficiency of photoelectrodes: the case of nickel (II) hydroxide on vanadate photoanodes.

Chapter IV is dedicated to the surface modification of vanadate photoanodes ($BiVO_4$ and $FeVO_4$) with controlled amounts of $Ni(OH)_2$ acting as co-catalyst. In fact, a commonly followed strategy to enhance the performance of photoelectrodes for achieving viable water splitting devices consists in the use of co-catalysts. However, fine control of the amount of co-catalyst deposited on the electrode surface usually does not receive much attention, although it is an essential factor that crucially determines the efficiency of photoelectrodes.

In this context, this Chapter illustrates how the dark electrochemical characterization of co-catalyst-modified photoanodes may provide valuable information on the precise amount of electroactive co-catalyst present on the surface, facilitating our understanding of the manner in which co-catalysts work and paving the way for their optimization. For this purpose, ultrathin $Ni(OH)_2$ layers were deposited on either doped or pristine $BiVO_4$ and $FeVO_4$ photoanodes by a cost-effective and versatile chemical bath deposition method in which the deposition time allows to control the $Ni(OH)_2$ loading. The deposited $Ni(OH)_2$ is demonstrated to successfully catalyze the photoelectrochemical water oxidation process on both $BiVO_4$ and $FeVO_4$ electrodes, by improving the effective transfer of photogenerated holes from the semiconductor to solution. In fact, the electrocatalytic activity of the $Ni(OH)_2$-modified photoanodes rapidly increases with the amount of deposited $Ni(OH)_2$ until an optimum value is reached equivalent to only 0.46 and 1.68 $Ni(OH)_2$ monolayers for $BiVO_4$ and $FeVO_4$ electrodes, respectively.

Under these conditions, $Ni(OH)_2$ enhances the photocurrent generation by a factor of 2 for $BiVO_4$ and of 1.2 for $FeVO_4$ photoanodes in contact with slightly alkaline solutions.

The small loadings of $Ni(OH)_2$ leading to an optimum photoanode behavior indicate that hole transfer is favored on vanadate active surface sites, which would also be the preferential sites for $Ni(OH)_2$ deposition. Additional amounts of co-catalyst deposited for longer times induce a drastic decrease in the $Ni(OH)_2$ photoelectrocatalytic activity due to charge recombination at the semiconductor/$Ni(OH)_2$ interface, probably enhanced by the low carrier mobility in $Ni(OH)_2$. On the other hand, this study demonstrates that the preparation of efficient photoanodes for oxygen evolution with an extremely small amount of co-catalyst through a facile and scalable method is possible.

Chapter V. Iron and cobalt hydroxides: describing the oxygen evolution reaction activity trend with the amount of electrocatalyst.

In Chapter V, a detailed characterization of iron and cobalt hydroxide deposits as electrocatalysts for the oxygen evolution reaction in alkaline media is presented as a first step before their use co-catalysts on the surface of vanadate photoanodes. This type of preliminary studies is essential since, although the amount of oxygen evolution electrocatalyst is a factor determining its efficiency, its fundamental correlation with activity remains unclear.

To address this issue, we take advantage of a urea-based chemical bath deposition method (CBD) that enables to control the amount of electrocatalyst ($Fe(OH)_2$ and α-$Co(OH)_2$) deposited on conducting glass. The thickness of the resulting films, whose use in electrocatalysis is unprecedented, is tuned by controlling the deposition time. The turnover frequency (TOF) for O_2 generation decreases drastically as the electrocatalyst amount increases, beginning at equivalent coverages of 3.5 monolayers (ML) for $Fe(OH)_2$ and of 0.05 ML for α-$Co(OH)_2$ electrodes. The contrasting behavior of both hydroxides comes from the different structure of the incipient deposits, formed by small acicular nanoparticles in the

case of $Fe(OH)_2$ and larger flat microparticles in the case of α-$Co(OH)_2$. The former structure allows a large fraction of the Fe sites to be in direct contact with solution, while such a fraction rapidly diminishes with loading for α-$Co(OH)_2$. In addition, the resulting $Co(OH)_2$ electrodes show TOFs similar or higher than those of electrodes prepared by more complex routes. The optimum ultrathin films are remarkably stable in alkaline media, showing that the preparation of efficient electrocatalysts for oxygen evolution with an extremely small amount of metal through a novel, facile and scalable CBD is possible.

Chapter VI. Tuning the oxygen evolution reaction activity of Ni- and Co-modified $Fe(OH)_2$ electrodes through structure and composition control.

Chapter VI takes a step forward with respect Chapter V and presents NiFe- and CoFe-based (oxy)hydroxides as promising and highly active earth-abundant electrocatalysts for the oxygen evolution reaction (OER) in alkaline media. In a similar strategy to that followed in the previous chapter, $Fe(OH)_2$-$Ni(OH)_2$ and $Fe(OH)_2$-$Co(OH)_2$ electrodes have been prepared through a urea-based chemical bath deposition (CBD) method that enables to control and optimize structure and loading. The effect of the spatial arrangement of the metals in the hydroxide deposits on the electrocatalytic activity in alkaline media has been evaluated. Ultrathin films formed by bilayers resulting from the deposition of submonolayer amounts of Ni or Co hydroxides on previously deposited $Fe(OH)_2$ layers were found to exhibit the best electrocatalytic behavior. The turnover frequency for O_2 generation increases drastically as the amount of either Ni or Co decreases, reaching maximum values 2.6 and 1.6 times higher than those for FTO/$Ni(OH)_2$ and FTO/$Co(OH)_2$ electrodes, respectively. This shows that the presence of underlying $Fe(OH)_2$ nanoparticles plays a crucial role in enhancing the electrocatalytic properties of Ni or Co sites. The fact that these ultrathin electrodes, formed

by extremely small amounts of electrocatalysts, show good stability in alkaline media paves the way for their use as transparent electrodes or co-catalysts for water splitting photoanodes.

Chapter VII. Sequentially deposited $Fe(OH)_2/Ni(OH)_2$ oxygen evolution co-catalyst: boosting the performance of bismuth vanadate photoanodes.

It is known that the highest-performing water splitting devices to drive the oxygen evolution reaction use semiconducting oxide photoanodes coated with water-oxidation co-catalysts. In this sense, Chapter VII constitutes the last step in the development of optimized photoanodes superficially-modified with hydroxide-based hydroxides. Given that the quantity of co-catalyst has been identified as a factor crucially determining the photoelectrochemical performance of photoanodes (as shown in Chapter II), this Chapter shows a simple strategy to carry out the necessary optimization of the deposited amount of electrocatalyst. To do so, the previously developed $Fe(OH)_2/Ni(OH)_2$ co-catalyst has been deposited on $BiVO_4$ photoanodes by means of a urea-based chemical bath deposition method that allows for a sequential, precise, and fine control of the deposited mass loading of the two different hydroxides by only controlling the deposition time. The optimum photoactivity (according to the photocurrent value at 1.23 V vs. RHE) for BiVO4/Fe(OH)2/Ni(OH)2 photoanodes is obtained for equivalent coverage values of 2.4 and 0.8 monolayers for $Fe(OH)_2$ and $Ni(OH)_2$, respectively, which underlines the relatively small amounts of co-catalyst needed for an optimum photoelectrochemical performance.

Chapter VIII. Defect engineering nanostructured $LaFeO_3$ photoanodes improves the activity for solar water oxidation.

The search for low-cost yet highly active materials for solar water oxidation to enable a competitive photoelectrochemical (PEC) technology for solar-driven water splitting has positioned $LaFeO_3$ (LFO) as an emerging candidate for solar water oxidation. Unfortunately, reports on LFO photoanodes still depict a PEC response that lay far behind its ferrite counterparts. With the aim of identifying the key performance bottlenecks in this material and propelling the implementation of LFO as photoanode, Chapter VIII reports on a new manufacturing route, which produces a nanorod array-type electrode of LFO, with defect and surface engineering protocols, to deliver a benchmarking performance of 0.4 mA cm^{-2} at 1.23 V *vs* RHE and onset potentials below 0.55 V *vs* RHE. Firstly, it is found that oxygen defects activate the interface towards oxygen evolution reaction (OER), as confirmed by the drop of the Tafel slope from 160 to 110 mV dec^{-1}, while coating with $NiFeO_x$ drastically suppressed the surface recombination. However, a gradual deterioration of the response resulting from the refilling of oxygen within the structure outcompeting OER reaction is observed. Secondly, a rapid bulk recombination of photogenerated carriers at nanosecond timescales as well as identified weak space-charge field and an ultrashort hole diffusion length (< 5 nm) which ultimately limit the performance is identified. Overall, in this Chapter, guidelines to accelerate the progress on LFO photoanodes as well as new insights into the operational behavior of the emerging family of oxide perovskites for solar fuel production are provided.

The research leading to the results shown in this Chapter was carried out in the facilities of the Laboratory for Molecular Engineering of Optoelectronic Nanomaterials (LIMNO) in

the École Polytechnique Fédérale de Lausanne (EPFL), in Lausanne (Switzerland), during a research stay supervised by Dr. Kevin Sivula and Dr. Néstor Guijarro.

Chapter IX. Photoelectrochemical behavior and computational insights of $NdFeO_3$ thin film photocathodes.

Chapter IX constitutes a first study on the employment of neodymium ferrite ($NdFeO_3$) as a photocathode. In fact, among the ternary oxides and similar to the more studied $LaFeO_3$, $NdFeO_3$ may be considered as a suitable candidate to this end. In this way, transparent $NdFeO_3$ thin film photocathodes have been successfully prepared by a citric-based sol-gel procedure, followed by a thermal treatment. These photocathodes show photocurrents for both the hydrogen evolution and oxygen reduction reactions. DFT calculations have allowed gaining insights into the nature of the p-type semiconducting behavior of this material, also pointing to the importance of nanostructuring and passivating Fe surface states to boost the performance of these photocathodes. To improve their photoactivity, Mg^{2+} and Zn^{2+} doping at a concentration of 5 at% has been observed to significantly enhance the photoelectrocatalytic performance of $NdFeO_3$ toward oxygen reduction. Such an improvement, which is primarily attributed to an increase in density and mobility of the majority charge carriers, reveals that $NdFeO_3$ has the potential to be used as photocathode in photoelectrochemical applications.

Chapter X. Effective interface engineering of $NdFeO_3$ photocathodes for improving photoelectrochemical hydrogen evolution.

Chapter X focuses on the development of a strategy to improve the photoactivity of previously developed $NdFeO_3$ photocathodes based on the use of an extraction layer and

metal particles acting as co-catalysts. In fact, the coupling of an extraction layer with a metal co-catalyst on the surface of a photocathode is among the most common procedures today to enhance the photoelectrochemical activity for the hydrogen evolution reaction.

In this context, Chapter X presents the deposition of a TiO_2 extracting layer on pristine and doped $NdFeO_3$ photocathodes by means of simple drop-casting procedure, followed by the electrodeposition of controlled amounts of Ni nanoparticles as co-catalysts for the hydrogen evolution reaction. The highest photoactivity (according to the photocurrent value at 0.1 V *vs*. Ag/AgCl) is achieved for optimum coverages of Ni deposit of around 4.7, 4.9 and 3.7 monolayers for $NdFeO_3/TiO_2$/Ni, Mg (5 at%)-$NdFeO_3/TiO_2$/Ni and Zn (5 at%)-$NdFeO_3/TiO_2$/Ni photocathodes, respectively. This implies significant photocurrent enhancements by factors of 5.8, 4.8 and 5.2, respectively, compared to the corresponding pristine or doped $NdFeO_3/TiO_2$ photoelectrode. This study points to the possibility of approaching surface engineering strategies on photocathodes from simple synthesis techniques and without resorting to co-catalysts based on noble metal particles.

Chapter XI. Conclusions.

Chapter XI shows the main general and specific conclusions obtained from the development of this thesis.

CHAPTER I

Introduction

1.1. GENERAL CONTEXT: ENERGY AND ENVIRONMENTAL CHALLENGE

Among the challenges faced by the world community in these first decades of the twenty-first century, one has grown clearer than any other in both urgency and importance: the supply of enough energy to meet current living standards. Present global power consumption is estimated to be around 15 TW but, according to the constant growth rate of the global population, it is expected to more than double that value by 2050 [1]. Around 85% of the total power supply is provided by traditional fossil fuels, but they will be unable to keep up with this increase in demand due to a limited availability of the reserves. Based on the current consumption rate, estimated reserves range from 150 to 400 years for coal, 40-80 for oil, and 60-160 years for natural gas [2]. However, the effect of these diminishing reserves will be felt on a much shorter scale since those still available are becoming increasingly hard to recover and the peak in their exploitation will occur long before the supplies run out.

Another important concern regarding the use of fossil fuels is their undeniable impact on the natural environment, as it is the case of the emission of huge amounts of polluting and greenhouse gases (in particular, carbon dioxide) and their contribution to the global warming phenomenon. Since the beginning of the First Industrial Revolution (around 1760), the atmospheric CO_2 levels have risen from 280 to 414.38 ppm (in July 2020) [3], and it is currently rising by about 2.5 ppm per year. According to the International Panel on Climate Change (IPCC), a CO_2 concentration higher than 450 ppm entails a high risk of causing global warming by more than 2ºC by 2100 [4]. This probable increase in temperature is likely to have a severe adverse impact on ecosystems dynamics and human society which will last for years [5].

To reduce this dependence on fossil fuels and curb the emissions of CO_2, the need for a large-scale transition toward new and sustainable sources of energy is pressing, and

it is assumed to be unavoidable by most scientist and politicians. Based on the Renewable Energy Policy Network for the 21st Century's (REN21) 2019 report, renewable energies contributed 18.1% to humans' global energy consumption and 26.2% to their generation of electricity in 2017 and 2018, respectively. This energy consumption is divided as 7.5% coming from traditional biomass, 4.2% as heat energy (modern biomass, geothermal and solar heat), 3.6% from hydroelectricity, 1.0% from biofuels for transport and the remaining 2.0% is electricity from wind, solar, geothermal, and other forms of biomass [6]. However, there is much uncertainty about the route to follow and the speed at which this can and should be done since, as expected, the viability of a certain route is determined by economic considerations, rather than by technological impediments.

Table 1.1. Overview of global power generation capacities for sustainable energy sources (adapted from [2]).

Energy source	Power / TW	Comments
Wind	4	Represents 10-15% of global technological potential for on- and off-shore installations.
Hydroelectric	1-2	Remaining untapped potential is 0.5 TW.
Geothermal	<2	Only a small fraction of this can be exploited.
Biomass	10	Requires 10% of Earth's land surface to be covered with switchgrass.
Solar	>20	Requires 0.16% of the Earth's surface to be covered with efficient solar cells. Total solar power reaching the Earth's surface is 120000 TW.

Table 1.1 shows an overview of global power generation capacities for different sustainable energy sources. The first consideration regarding sustainable energy sources is that any future energy infrastructure will almost certainly be composed by a mixture of these (and other) technologies. The optimal mix for a particular region will be determined by local circumstances, such as geography, climate, and population density characteristics. In addition, it is also important to note that many of these sustainable technologies are still in the early stages of their development and large-scale

implementation [7,8]. That is why fossil fuels will continue to play an important role for the next few decades as attempts to achieve Terawatt scale energy productions with any of these technologies will take time [9].

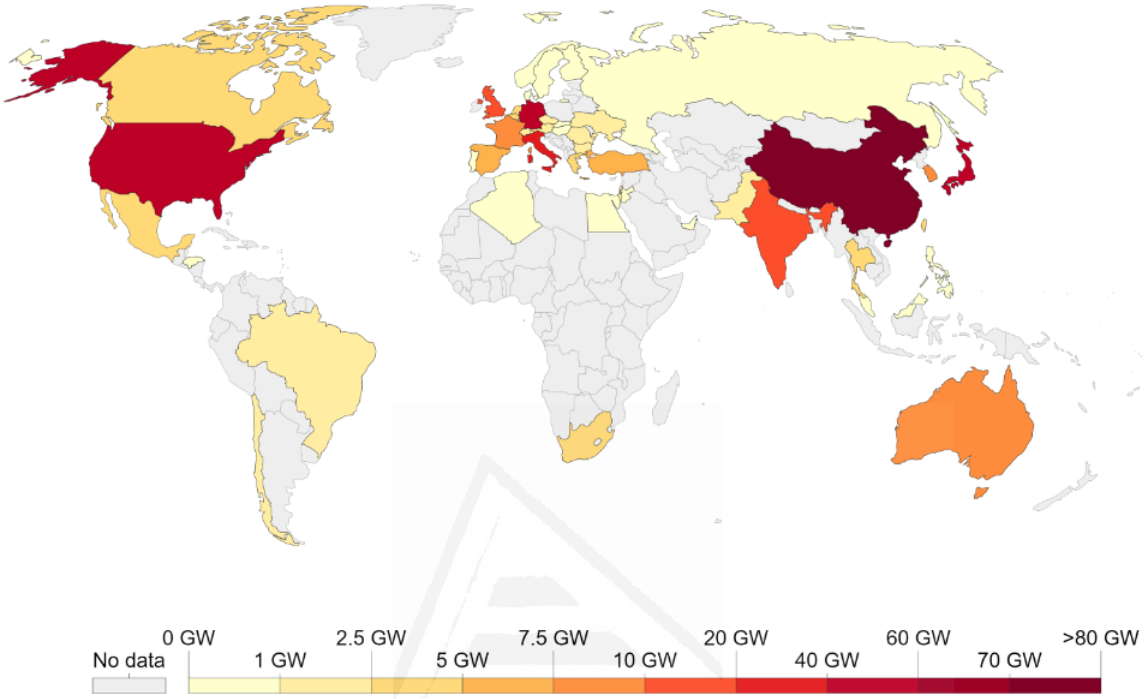

Figure 1.1. Installed solar capacity (2018), measured in gigawatts (GW) [10].

Of the sources presented in Table 1.1, solar energy is by far the only source that has the required potential to meet all current energy needs, and its development is promising: the solar cell market is one of today's fastest growing markets, growing by 35-40% per year. In 2018, with a total installed capacity of near 490 GW (Figure 1.1), the global production was 485 TWh [10]. Although it is difficult to predict the development of this market over the next years, and irrespective of future uncertainties, solar energy will undoubtedly become an essential component of the energy mix in the decades to come.

1.2. HYDROGEN AS ENERGY VECTOR

As the contribution of solar energy to the total energy mix increases, it is important to bear in mind the intermittent nature of solar power (day and night cycle, clouds, daily weather…), which stands out as one of its most important limitations today. Given that grid-based storage capacities will be exceed and large-scale energy storage solutions need to be developed, one of the more attractive possibilities is to store energy in the form of a chemical fuel [11]. The energy of a visible-light photon ranges between 1 and 3 eV, or 100-300 $kJ \cdot mol^{-1}$, which is more than sufficient for many chemical synthesis routes. Resulting chemical fuels (including hydrogen, methane, methanol, gasoline, diesel…) combine the advantages of high energy storage densities and ease of transportation when compared to batteries and mechanical or gravity-based storage systems (such as flywheels and pumped water reservoirs) [12].

All mentioned chemical fuels (except hydrogen) require a source of carbon, which significantly difficult their widespread. While atmospheric CO_2 could be an obvious candidate in view of its negative impact on environment, capturing it from the atmosphere involves a huge entropic cost (which translates into an energy penalty) due to its diluted nature (it currently constitutes approximately 0.04% of the atmosphere composition). Fossil fuel-based power plants may seem attractive point-sources of highly concentrated CO_2, but the use of fossil fuels must be avoided. Finally, direct photo(electro)chemical conversion of CO_2 to a fuel seems to be even more challenging since the electrochemical half-reactions for the conversion of this molecules to, for example, methanol or methane involve six- and eight-electron transfer steps, respectively.

In this context, the conversion of solar energy into hydrogen appears to be a much more attractive and viable option. Water is a convenient and abundant source of hydrogen considering that the 75% of the surface of the Earth is covered by this compound. Proper

estimations underline that around $3.5 \cdot 10^{13}$ L of water (equivalent to the $2 \cdot 10^{-6}$% of the amount of water in the world's oceans) is needed to store the energy the world consumes in one year [2]. The water splitting reaction can be written as follows (Eq. 1.1):

$$2\,H_2O + \text{sunlight} \leftrightarrows 2\,H_2 + O_2;\ \Delta G = 237\ \text{kJ} \cdot \text{mol}^{-1} \qquad \text{Eq. } \mathbf{1.1}$$

The reduction half-reaction is an easy two-electron transfer reaction, while four electrons are involved in the oxidation counterpart to obtain oxygen from water. As demonstrated, it is considerably easier to photo-reduce water than it is to photo-reduce CO_2 due to the high stability of this compound and the variety of products formed in the process [13].

Table 1.2. Gravimetric and volumetric energy densities of several fuels (at 1 bar) [2].

	Energy density	
Fuel	**Gravimetric / MJ·kg^{-1}**	**Volumetric / MJ·L^{-1}**
Coal	24	-
Wood	16	-
Gasoline / petrol	44	35
Diesel	46	37
Methanol	20	18
Natural gas	54	0.036
Hydrogen	143	0.011

One of the main concerns associated with hydrogen is the difficulty in storing it. While hydrogen has a very high gravimetric energy density, the volumetric energy density is rather low, compared to other fuels (Table 1.2). Possible solutions consider high pressure storage containers (up to 700 bar), liquid cryo-storage, or physisorption at high-surface area metal organic frameworks (MOFs) or in clathrate hydrate cages. Another possible solution is to store hydrogen by forming chemical bonds [14]. This can be in the form of metal hydrides, such as MgH_2, $LaNi_5H_6$, and $LiBH_4$, or by using hydrogen and CO_2 to produce chemical fuels. This last route is much easier than the direct photochemical or electrochemical activation of CO_2 since CO_2 and hydrogen can be

converted into CO *via* the so-called water-gas shift reaction (Eq. 1.2), although it is important to remark that CO is not the best option to accumulate large quantities of energy:

$$CO_2 + H_2 \leftrightarrows H_2O + CO;\ \Delta G = 42\ kJ \cdot mol^{-1}$$ Eq. **1.2**

1.3. PHOTOELECTROCHEMICAL WATER SPLITTING ON SEMICONDUCTOR ELECTRODES

Many different pathways for the conversion of water and sunlight into hydrogen exist: (i) photoelectrochemical water splitting, (ii) photocatalytic water splitting, (iii) coupled photovoltaic-electrolysis system, (iv) thermochemical conversion, (v) photobiological methods, (vi) molecular artificial photosynthesis, (vii) plasma-chemical conversion, and (viii) mechano-catalytic, magnetolysis, radiolysis, among others [14,15].

Among these methods, photoelectrochemical (PEC) water splitting using semiconductor photoelectrodes is an appealing approach. One of its main advantages is that hydrogen and oxygen are produced at separated electrodes, which avoids serious safety concerns (related to explosion and flammability properties of H_2) and allows an easy separation. Another positive aspect is that it can be carried out at room temperature and does not need large-scale solar concentrators that would limit its application [2]. Finally, the device required for photoelectrochemical water splitting can be prepared using inorganic materials, which offers a chemical robustness and durability hardly achievable with organic or biological systems [16].

At this point, it is important to highlight that these advantages are equally applicable to widely extended coupled photovoltaic-electrolysis systems. In fact, all the necessary components of such a system (solar cell, electrolyzer, DC-DC converter) are commercially available, and solar-to-hydrogen efficiencies around 8% have already been

achieved. The PEC approach offers in principle three important advantages compared to the PV + electrolysis systems. The first one lies in the fact that commercial electrolyzers require cell voltages of around 1.9 V in order to reach their optimal operating current densities (near 1 $A \cdot cm^{-2}$). Since the thermodynamically required potential for water splitting is 1.23 V, this places an upper limit of 65% on the overall energy conversion efficiency. In contrast, the current density at a semiconductor photoelectrode immersed in water is much smaller (usually lower than 10-20 $mA \cdot cm^{-2}$), and, therefore, the required overpotential is substantially lower [17,18]. The second advantage is that a PEC system can be constructed as a single, monolithic device, which requires fewer packaging components (frame, glass, connections…) and may lead to significantly lower costs [19]. Finally, PEC water splitting may offer a route toward hydrogen production costs of 3-5€/kg, which is competitive with existing energy sources. Estimated costs for hydrogen produced with PV + electrolysis exceeds 8 €/kg, well above the target set by the US Departament of Energy (equivalent to 2-4 €/kg) for future hydrogen production pathways [2,20].

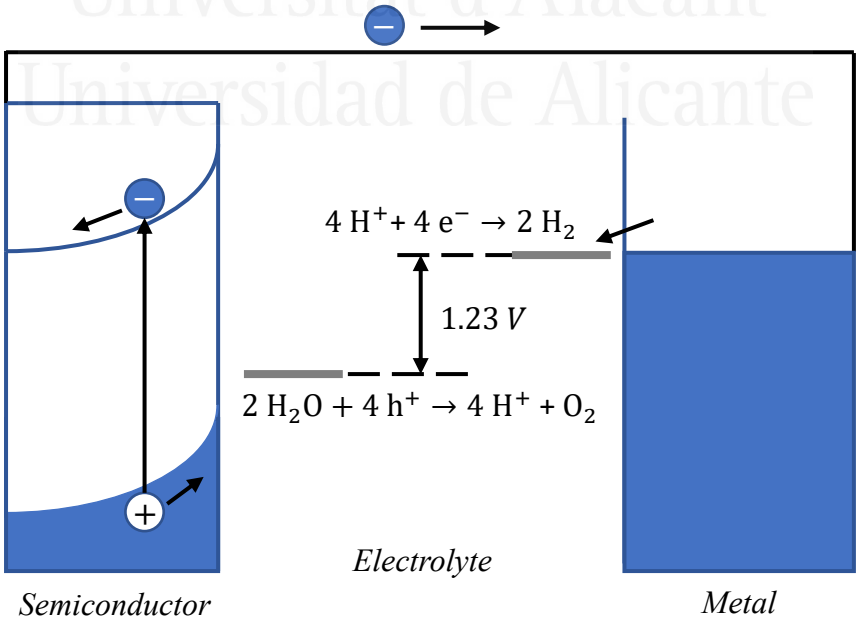

Figure 1.2. Simplified energy diagram of a PEC cell consisting of a semiconductor photoanode and a metal cathode.

Figure 1.2 shows a simplified energy diagram of a PEC cell based on a single photoanode and a metal counter electrode (more complicated configurations that involve photocathodes and/or more than one photoelectrode are discussed in the following sections). The main component of a PEC cell is the semiconductor, which converts incident photons to electron-hole pairs. These electrons and holes are spatially separated from each other due to the presence of an electric field inside the semiconductor (see following sections). The photogenerated electrons are swept toward the conducting back-contact, and are transported to the metal counter-electrode *via* an external wire, where they reduce water to form hydrogen gas. On the other hand, the photogenerated holes are swept toward the semiconductor-electrolyte interface, where the oxidation of water to form oxygen gas takes place [2,15,16].

From an alkaline electrolyte, the reduction and oxidation reactions can be written as Eq. 1.3 and 1.4, respectively:

$$4\,H_2O + 4\,e^- \leftrightarrows 2\,H_2 + 4\,OH^-;\ E^0_{red} = -0.828\ V\ (vs.\ SHE) \qquad \text{Eq. } \mathbf{1.3}$$

$$4\,OH^- + 4\,h^+ \leftrightarrows 2\,H_2O + O_2\ ;\ E^0_{ox} = -0.401\ V\ (vs.\ SHE) \qquad \text{Eq. } \mathbf{1.4}$$

For an acidic environment, the appropriate reactions are the following (Eq. 1.5 and 1.6):

$$4\,H^+ + 4\,e^- \leftrightarrows 2\,H_2;\ E^0_{red} = 0.0\ V\ (vs.\ SHE) \qquad \text{Eq. } \mathbf{1.5}$$

$$2\,H_2O + 4\,h^+ \leftrightarrows 4\,H^+ + O_2\ ;\ E^0_{ox} = -1.229\ V\ (vs.\ SHE) \qquad \text{Eq. } \mathbf{1.6}$$

The Gibbs energy change for the overall water splitting reaction is given by the expression (Eq. 1.7):

$$\Delta G = -n \cdot F \cdot E \qquad \text{Eq. } \mathbf{1.7}$$

where E is the cell potential ($E_{ox} - E_{red}$).

At 298 K and standard condition (1 bar, ideal gas behavior), the electrochemical cell voltage of -1.229 V corresponds to a Gibbs energy change of 273 kJ·mol^{-1} H_2. This

is markedly different from the photocatalysis reactions (for example, photo-assisted degradation of organic pollutants), for which the Gibbs energy change is negative [2,15,16].

1.4. FUNDAMENTALS OF SEMICONDUCTOR PHYSICS

1.4.1. Density of states and charge carrier density

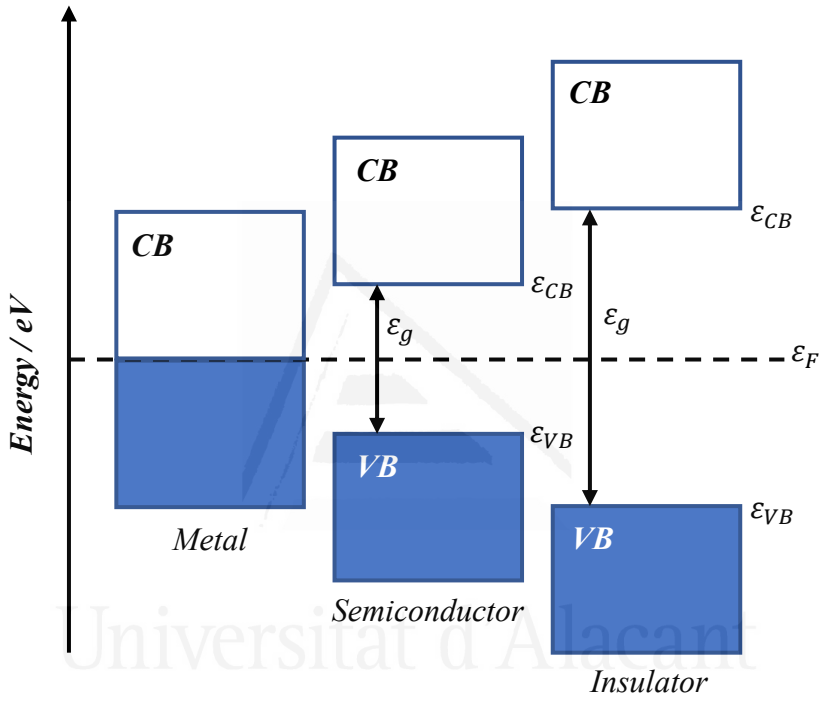

Figure 1.3. Band diagram for metals, semiconductors, and insulators. ε_F is the Fermi energy level.

A common way to classify materials is based on their electrical conductivity (σ) value. In this way, three different groups can be defined: insulating materials ($\sigma < 10^{-10}$ $\Omega^{-1}\cdot cm^{-1}$), semiconductor materials ($10^{-10} < \sigma < 10^{4}$ $\Omega^{-1}\cdot cm^{-1}$), and metal ($\sigma > 10^{4}$ $\Omega^{-1}\cdot cm^{-1}$) [21]. In a solid consisting of N equal atoms, the molecular orbitals can be considered as a linear combination of atomic orbitals. Due to the low energy difference between neighboring energy levels in a solid, it can be assumed that the molecular orbitals form a continuous band of energies (instead discrete energy levels). These molecular orbitals

may or may not contain electrons. According to these considerations, a scheme of the band structure for metals, semiconductors and insulators (such as the one presented in Figure 1.3) can be presented. The highest in energy filled band is called valence band (VB) and the lowest in energy empty band is known as conduction band (CB). ε_{VB} and ε_{CB} denote the energy value corresponding to the top edge of the VC and the bottom edge of the CB, respectively, and ε_g refers to the difference between both band edges (the so-called band gap energy).

To continue with the analysis, it is important to know that the electric conductivity of a material relies on where the electrons are located. In the case of metals, the conduction band overlaps with the valence band, with is filled with electrons. This situation allows the electrons to freely move along the solid. The great electric conductivity of metals generally arises from this band overlap. In contrast, for a situation in which the valence band and the conduction band are separated by a band gap greater than 3 eV, electrons cannot move from the VB to the CB even in the presence of an intense electric field. This gives place to a low electrical conductivity, characteristic of insulating materials. However, when the energy difference between band edges is not extremely large (below 3 eV), some electrons in the VB can promote to the CB as a result of thermal excitation or light absorption. This happens for a semiconductor material, and that is why the band gap value is one of its most important features since it directly affects and controls the solid electronic properties.

Because of this electron excitation in a semiconductor material, it is generated a hole in the VB per each electron promoted to the CB. Similarly to electrons, holes (understood as positive charges generated by the lack of an electron) can also act as charge carriers. That is the reason why the general term of charge carrier in semiconductors can refer to either electrons or holes.

One usual strategy to enhance the electrical conductivity of pristine semiconductor materials (also called intrinsic semiconductors) when the band gap is relatively large consists on doping them with impurity atoms that can behave as either electron donors or acceptors. In this context, they are called doped (or extrinsic) semiconductors (Figure 1.4). When the impurity atoms present a larger number of valence electrons that the atoms of the host material, the resulting material is called *n*-type semiconductor. They are characterized by the existence of an electron enrichment in the lattice and the impurities act as electron-donor centers. On the contrary, if the impurity atoms have a lower number of valence electrons than the host atom, it results in a hole-enriched material (or *p*-type semiconductor). According to this, electrons are the majority charge carriers in *n*-type semiconductors, while for *p*-type semiconductors there are the holes.

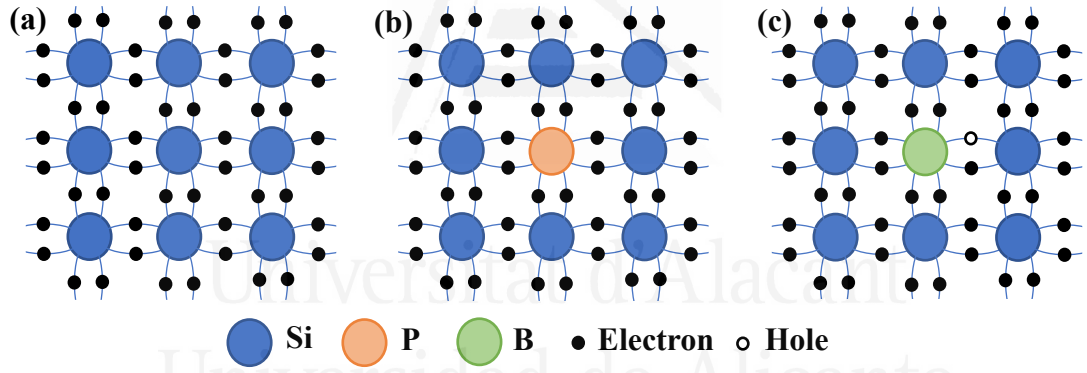

Figure 1.4. Bond representation for (a) intrinsic silicon, (b) *n*-type silicon (doped with phosphorus), and (c) *p*-type silicon (doped with boron).

When a semiconductor is in equilibrium (absence of illumination and of an electric field), only thermal excitation generates charge carrier density. The density of state function in a semiconductor is then defined as the number of quantum states per unit volume and per unit energy [21–23]. The free electron model links the kinetic energy of a free electron and the k wave vector. The energy versus momentum plot shows a parabolic shape, given by Eq. 1.8:

$$\varepsilon = \frac{h^2 k^2}{8\pi^2 m_e} \qquad \text{Eq. } \mathbf{1.8}$$

where m is the electron mass [21,22]. The resolution of the Schördinger equation for a semiconductor also defines a parabolic shape of the CV edge, especially near the minimum energy, but with an important deviation with respect to the above equation. In this context, electron mass in the free electron model equation is substituted by an 'effective mass' in order to correct such a deviation (Eq. 1.9) [22]:

$$\varepsilon = \frac{h^2 k^2}{8\pi^2 m_e^*} \qquad \text{Eq. } \mathbf{1.9}$$

The density of states in the conduction and valence band (D_{CB} and D_{VB}, respectively) derived from Eq. 1.9 corresponds to the following expressions (Eq. 1.10 and 1.11, respectively) [21]:

$$D_{CB}(\varepsilon) = \frac{1}{2\pi^2 \hbar^3}(2m_e^*)^{3/2}(\varepsilon - \varepsilon_C)^{1/2} \qquad \text{Eq. } \mathbf{1.10}$$

$$D_{VB}(\varepsilon) = \frac{1}{2\pi^2 \hbar^3}(2m_h^*)^{3/2}(\varepsilon_V - \varepsilon)^{1/2} \qquad \text{Eq. } \mathbf{1.11}$$

Thus, the density of states (DOS) of the conduction and valence bands depends on the effective mass of the electron and hole (m_e^* and m_h^*, respectively) and the corresponding energy of the edge of the conduction and valence band. Figure 1.5 illustrates the density of states given by Eq. 1.10 and 1.11.

Eq. 1.10 and 1.11 are deduced for idealized conditions and they are usually not accurate for most metal oxides, particularly far from the CB minimum and VB maximum. The real DOS are more commonly obtained from spectroscopic measurements or quantum calculations based on DFT calculations. Nevertheless, they offer a very good approximation to the semiconductor behavior.

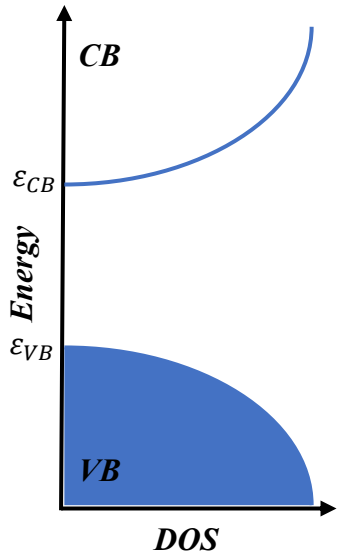

Figure 1.5. Schematic plot of the DOS ($D_{CB}(\varepsilon)$ and $D_{VB}(\varepsilon)$) in a semiconductor given by Eq. 1.10 and 1.11.

It is also important to consider the probability of occupation of a particular state. In the case of fermions, which are particles with a half-integral spin (following the Pauli exclusion principle), this probability is described by the Fermi-Dirac distribution (Eq. 1.12):

$$f(\varepsilon) = \frac{1}{1 + exp\left(\frac{\varepsilon - \varepsilon_F}{kT}\right)} \qquad \text{Eq. } \mathbf{1.12}$$

where $f(\varepsilon)$ indicates the probability that a state with energy ε is occupied by an electron and ε_F is the so-called Fermi level, which corresponds to the electrochemical potential of the electrons in the solid, and formally defined as the energy of the quantum state for which the probability of finding and electron is 0.5 [21–23]. This equation is applicable to electrons since they are fermions.

The equilibrium concentration of electrons (dn) in an interval of energy ($d\varepsilon$) in the CB can be determined as the product of the occupancy probability and the density of the states in this region: $dn = f(\varepsilon) \cdot D(\varepsilon) \cdot d\varepsilon$. The total density of free electrons (n) in the conduction band can be obtained by integration this expression from the edge of the

conduction band to infinity (Eq. 1.13). For the free hole density in the valence band (p), a similar treatment can be applied (Eq. 1.14):

$$n = \int_{E_c}^{\infty} D_{CB}(\varepsilon) \cdot f(\varepsilon) \cdot d\varepsilon \qquad \text{Eq } \mathbf{1.13}$$

$$p = \int_{-\infty}^{E_c} D_{VB}(\varepsilon) \cdot (1 - f(\varepsilon)) \cdot d\varepsilon \qquad \text{Eq } \mathbf{1.14}$$

These integrals cannot be solved analytically. As the concentration of thermally excited electrons and holes is usually small, it can be assumed that $\varepsilon - \varepsilon_F/kT >> 1$, and the Fermi-Dirac function approximates the Boltzmann distribution. Figure 1.6 shows Boltzmann and Fermi-Dirac distributions (which overlaps at low values of $f(\varepsilon)$) at a given temperature.

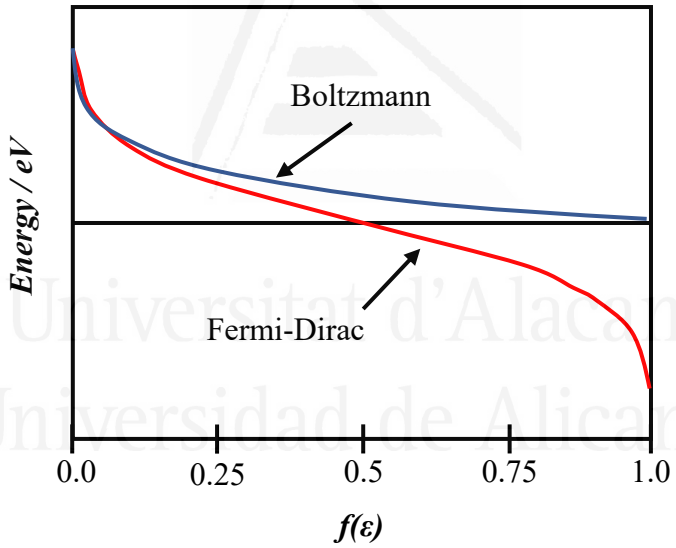

Figure 1.6. Comparison between Fermi-Dirac and Boltzmann distributions at a given temperature.

For intrinsic semiconductors [24], the density of electrons and holes can be defined considering this Boltzmann distribution (Eq. 1.15 and 1.16, respectively):

$$n = N_{CB} \cdot exp\left(-\frac{\varepsilon_{CB} - \varepsilon_F}{kT}\right) \qquad \text{Eq. } \mathbf{1.15}$$

$$p = N_{VB} \cdot exp\left(\frac{\varepsilon_{VB} - \varepsilon_F}{kT}\right) \qquad \text{Eq. } \mathbf{1.16}$$

where N_{CB} and N_{VB} are the effective densities of states (bottom of the CB and top of the VB, respectively), ε_F is the Fermi level, k is the Boltzmann constant, and T is the absolute temperature.

In intrinsic semiconductor, and in order to preserve charge neutrality, electron and hole densities must be equal (*i.e.*, the $n = p$ condition must be fulfilled, Eq. 1.17):

$$n \cdot p = n_i^2 = N_{CB} \cdot N_{VB} \cdot exp\left(\frac{\varepsilon_{VB} - \varepsilon_{CB}}{kT}\right) = N_{CB} \cdot N_{VB} \cdot exp\left(-\frac{\varepsilon_g}{kT}\right) \qquad \text{Eq. } \mathbf{1.17}$$

where n_i is known as the intrinsic density of charge carriers (electrons or holes). The Fermi level position (Eq. 1.18) can be obtained by combining Eq. 1.15 and 1.16:

$$\varepsilon_F = \frac{\varepsilon_{VB} + \varepsilon_{CB}}{2} + \frac{kT}{2} \cdot ln\frac{N_{VB}}{N_{CB}} \qquad \text{Eq. } \mathbf{1.18}$$

For extrinsic semiconductors [21,24], the density of charge carriers would depend on the amount of introduced impurities. The introduction of donor (D) or acceptor (A) species alter the electronic structure and, subsequently, also the Fermi level position. It can be assumed that, for an *n*-type semiconductor, $n \approx N_D$ and $p \approx n_i$, whilen for a *p*-type semiconductor, $p \approx N_A$ and $n \approx n_i$. In this regard, the Eq. 1.18 can be rewritten for and *n*-type and *p*-type semiconductor as Eq. 1.19 and 1.20, respectively:

$$\varepsilon_F = \varepsilon_{CB} - kT \cdot ln\frac{N_{CB}}{N_D} \qquad \text{Eq. } \mathbf{1.19}$$

$$\varepsilon_F = \varepsilon_{VB} + kT \cdot ln\frac{N_{VB}}{N_A} \qquad \text{Eq. } \mathbf{1.20}$$

Figure 1.7 illustrates the band structure of different semiconductor materials. As shown, and according to Eq. 1.19 and 1.20, the Fermi level is located either in the proximity of the conduction band edge in *n*-type materials or close to the valence band edge in *p*-type materials, and in both cases within the band gap.

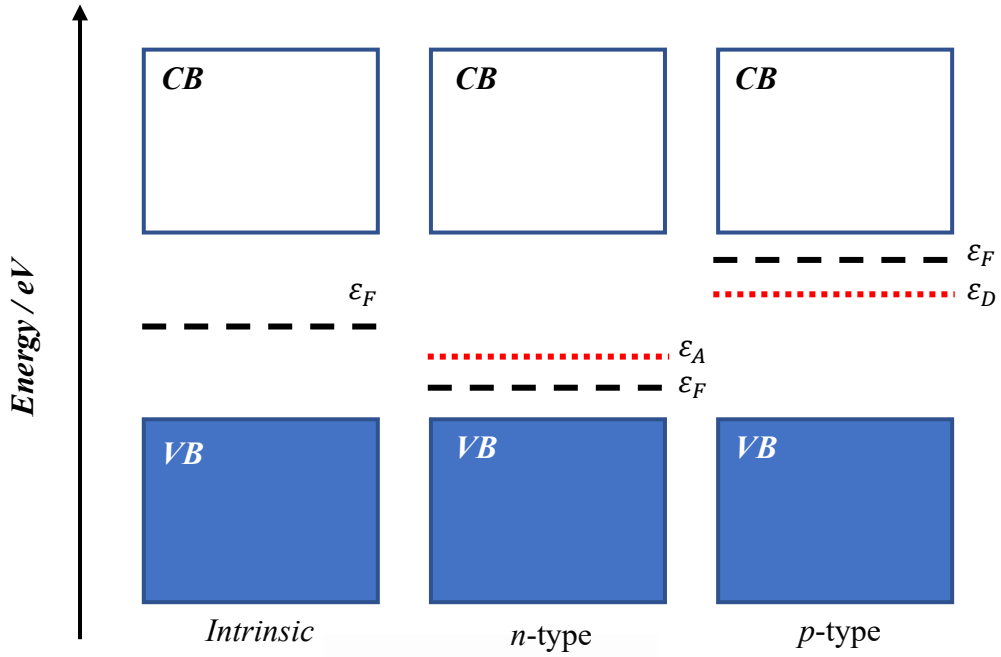

Figure 1.7. Band structure for an intrinsic semiconductor, *n*-type and *p*-type extrinsic semiconductor. ε_A and ε_D denote the energy levels of donor or acceptor impurities, respectively.

1.4.2. Double layer at the semiconductor-electrolyte interface

When analyzing an electrochemical system, the effect of the electric field on the permittivity of the solvent, its structure and the electrolyte ion concentration in the vicinity of the interface must be considered in order to describe the nature and characteristics of the double layer at the semiconductor-electrolyte interface. In fact, the double layer formation has significant consequences on the charge and potential distribution across the semiconductor-electrolyte interface. Due to the great difficulty in treating this problem, it must be treated using models s simplified as possible. One of them is to consider that the double layer is divided in three different regions: the electrode itself, the compact layer, and the diffuse layer, which interact only electrostatically with each other [25].

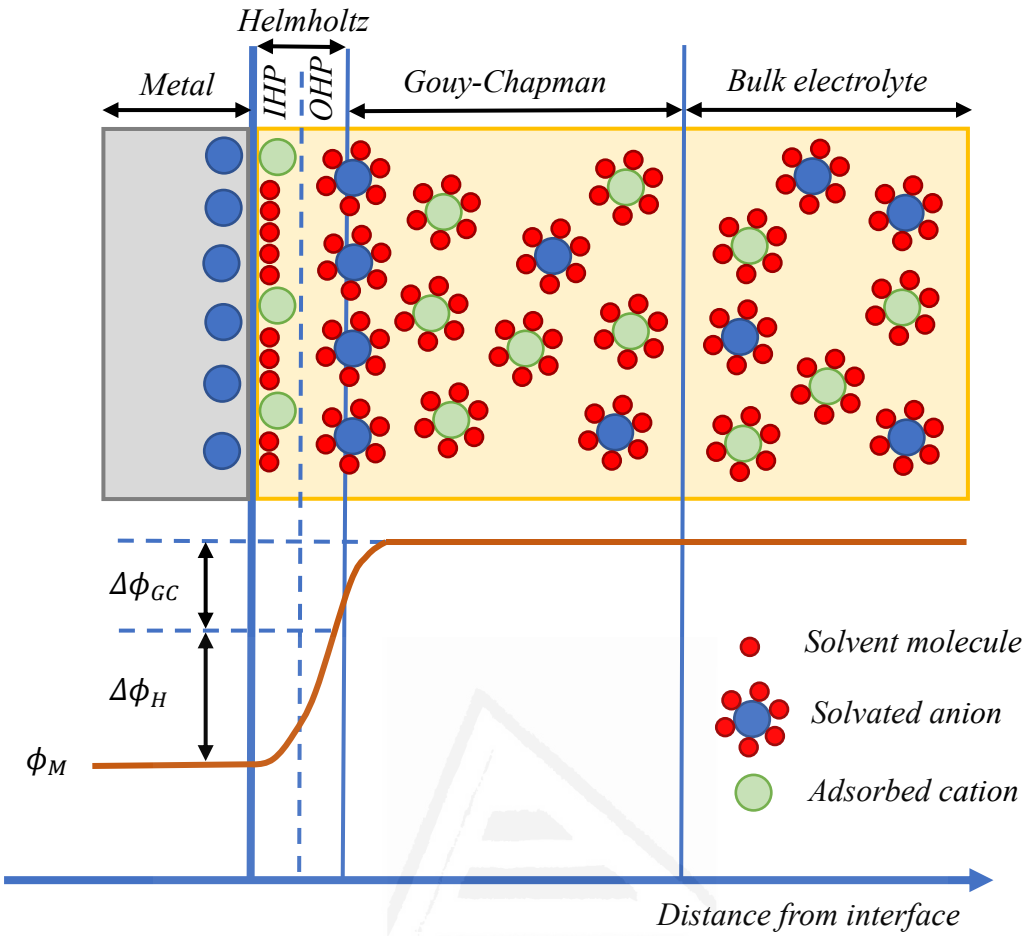

Figure 1.8. Scheme for the double layer region at a metal-electrolyte interface.

Considering the double layer formation in the case of an electrochemical system formed by a metal electrode in direct contact with an electrolyte with high ion concentration (Figure 1.8), it can be assessed that the compact layer (usually known as Helmholtz layer) involves the space between the electrode surface and the so-called outer Helmholtz plane (OHP). In the absence of specific ion adsorption phenomena, the surface of the metal electrode is covered by a monolayer of solvent molecules. However, and since cations are specifically adsorbed at the electrode surface, an equivalent negative charge appears on the metal surface. This charge separation induces a corresponding potential drop ($\Delta\phi_H$) across the Helmholtz layer. This potential drop is mainly determined by the specifically adsorbed ions and, in a minor extend, by the solvated ones. As

consequence, two different regions can be defined within the Helmholtz layer: the one between the electrode surface and the inner Helmholtz plane (IHP), comprising the surface electrode atoms, the ionic adsorbed species on it, and solvent molecules, and the other that goes from the IHP to the OHP, formed by electrostatic forces established when solvated ions of opposite charge to those located at the electrode surface are present [22]. The thickness of the Helmholtz layer is almost constant and independent of the nature of the metal electrode: it is approximately between 1.5 and 2.0 times the thickness of a monomolecular water layer (of around 0.3-0.5 nm) [23].

The diffuse layer (also known as Gouy-Chapman layer) appears beyond the OHP and it extends into the bulk electrolyte until the existence of a net electrical charge is no longer observed. In this region, charges near the interface are distributed over a diffuse layer due to low ion concentrations. It is important to consider that the contribution of the overall potential drop across the diffuse layer ($\Delta\phi_{GC}$) cannot be neglected for electrolyte concentrations below 10^{-3} M [22].

The situation corresponding to a semiconductor electrode is more complex (Figure 1.9). First, it must be considered that the carrier density for a semiconductor material is much smaller than for a metal. As consequence, the charge in the solid electrode is distributed over a certain range from the surface to the semiconductor bulk, giving place to another electric region: the space charge region (SCR). The resulting charge distribution within the SCR is quantitatively by the Poisson equation, which relates the potential in this layer (ϕ_{SCR}) with the net charge density ($\rho(x)$) as follows (Eq. 1.21):

$$\frac{d^2\phi_{SCR}}{dx^2} = -\frac{\rho(x)}{\varepsilon \cdot \varepsilon_0} \qquad \text{Eq. } \mathbf{1.21}$$

where the charge density as an implicit function of the distance from the surface (x) can be expressed as (Eq. 1.22):

$$\rho(x) = e \cdot [N_D - N_A - n(x) + p(x)] \qquad \text{Eq. } \mathbf{1.22}$$

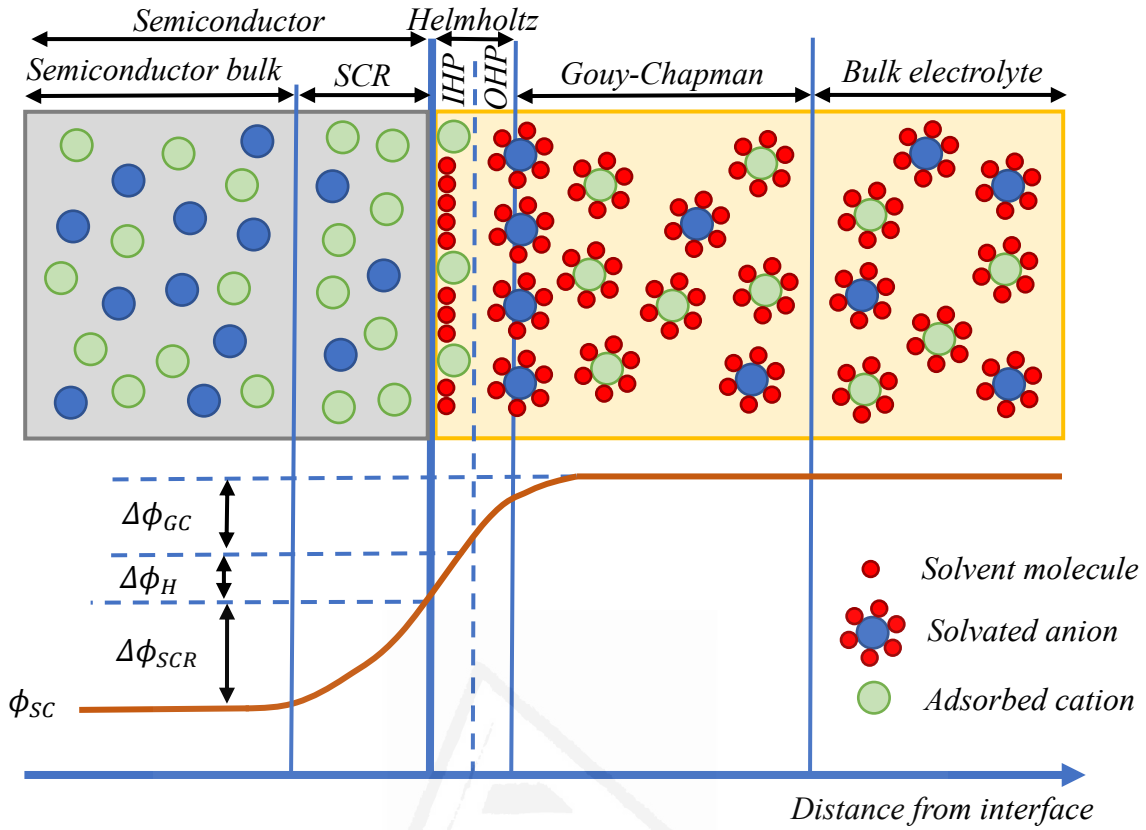

Figure 1.9. Scheme for the double layer region at a semiconductor-electrolyte interface.

being e the elementary charge. Since the Fermi level location is expected to remain constant within the space charge region at equilibrium, the level of the energy of the conduction and valence bands (ε_{CB} and ε_{VB}, respectively) vary with the distance. From Eq. 1.15 and 1.16, electron and hole densities ($n(x)$ and $p(x)$, respectively) are given by Eq. 1.23 and 1.24:

$$n(x) = n_b \cdot exp\left(-\frac{\varepsilon_{CB}(x) - \varepsilon_{CB}^b}{kT}\right) = n_b \cdot exp\left(-\frac{e \cdot \Delta\phi_{SCR}(x)}{kT}\right) \qquad \text{Eq. } \mathbf{1.23}$$

$$p(x) = p_b \cdot exp\left(\frac{\varepsilon_{VB}(x) - \varepsilon_{VB}^b}{kT}\right) = p_b \cdot exp\left(\frac{e \cdot \Delta\phi_{SCR}(x)}{kT}\right) \qquad \text{Eq. } \mathbf{1.24}$$

where b refers to the bulk. The potential drop in the SCR ($\Delta\phi_{SCR}$), which appears in the previous equations, is defined by Eq. 1.25, and it is a measure of the band-bending:

$$\Delta\phi_{SCR} = \phi_{SC} - \phi_S \qquad \text{Eq. } \mathbf{1.25}$$

where s refers to the semiconductor surface. In the same manner, the electron and hole densities at the surface are defined by Eq. 1.26 and 1.27, respectively:

$$n_s = n_b \cdot exp\left(-\frac{\varepsilon_{CB}^s - \varepsilon_{CB}^b}{kT}\right) = n_b \cdot exp\left(-\frac{e \cdot \Delta\phi_{SCR}(x)}{kT}\right) \quad \text{Eq. } \mathbf{1.26}$$

$$p_s = p_b \cdot exp\left(\frac{\varepsilon_{VB}^s - \varepsilon_{VB}^b}{kT}\right) = p_b \cdot exp\left(\frac{e \cdot \Delta\phi_{SCR}(x)}{kT}\right) \quad \text{Eq. } \mathbf{1.27}$$

For an *n*-type semiconductor, for which the hole density is negligible compared to that of electrons ($n(x) \gg p(x)$), the potential within the SCR can be expressed as (Eq. 1.28) [26]:

$$\frac{d^2\phi_{SCR}}{dx^2} = -\frac{e}{\varepsilon \cdot \varepsilon_0}\left(N_D - n(x)\right) = -\frac{e}{\varepsilon \cdot \varepsilon_0}\left[N_D - n \cdot exp\left(-\frac{e \cdot \Delta\phi_{SCR}(x)}{kT}\right)\right] \quad \text{Eq. } \mathbf{1.28}$$

From the considerations made in section 1.2, which imply that for an *n*-type material, *n* can be assimilated to N_D ($n \approx N_D$), the latter expression can be simplified to (Eq. 1.29):

$$\frac{d^2\phi_{SCR}}{dx^2} = -\frac{e \cdot N_D}{\varepsilon \cdot \varepsilon_0}\left[1 - exp\left(-\frac{e \cdot \Delta\phi_{SCR}(x)}{kT}\right)\right] \quad \text{Eq. } \mathbf{1.29}$$

The analytical solution to Eq. 1.29 leads to the Mott-Shottky equation (Eq. 1.30), which links the differential capacitance to the potential drop across the SCR:

$$\frac{1}{C_{SCR}^2} = \frac{2}{\varepsilon\varepsilon_0 N_d e}\left(\Delta\phi_{SCR} - \frac{k_B T}{e}\right) \quad \text{Eq. } \mathbf{1.30}$$

Analogously, for a *p*-type semiconductor, the Mott-Schottky equation has the following form (Eq. 1.31):

$$\frac{1}{C_{SCR}^2} = -\frac{2}{\varepsilon\varepsilon_0 N_d e}\left(\Delta\phi_{SCR} - \frac{k_B T}{e}\right) \quad \text{Eq. } \mathbf{1.31}$$

Assuming the SCR as an ideal parallel plate capacitor, its thickness can be calculated according to $L_{SCR} = {\varepsilon\varepsilon_0}/{C_{SCR}}$. From the Mott-Schottky equations for the

capacitance for both *n*- and *p*-type semiconductor materials, it can be obtained the Eq. 1.32, which can be applied for both types of semiconductors:

$$L_{SCR} = \sqrt{\left(\frac{2\varepsilon\varepsilon_0}{e \cdot N_{A,D}} \cdot \left|\Delta\phi_{SCR} - \frac{k_B T}{e}\right|\right)} \qquad \text{Eq. } \mathbf{1.32}$$

1.4.3. Semiconductor band-bending

In a situation where a semiconductor material (with a certain Fermi level, ε_F) is immersed into a electrolyte containing a redox couple (with a Fermi energy, $\varepsilon_{F,redox}$), the electrochemical potential for electrons from side to side of the interface is initially different. The equilibration of the Fermi levels of the two phases in contact requires a charge transfer between them. Thus, a band-bending within the semiconductor at the interfacial region takes place [27], enabling that the electrochemical potential is the same throughout the considered system (Figure 1.10).

An *n*-type semiconductor material presents a Fermi level which is typically higher than that corresponding to the redox couple in the electrolyte. After establishing contact between both media, free carriers from the semiconductor (for an *n*-type semiconductor, electrons) are transferred to the electrolyte until ε_F and $\varepsilon_{F,redox}$ balance. Because of this electron transfer, an electron depletion in the semiconductor space charge layer occurs, resulting in an upward band-bending. On the contrary, *p*-type semiconductors show a Fermi level usually located at lower energy values than $\varepsilon_{F,redox}$. In this case, holes (free carriers in this type of semiconductors) travel from the electrode to the electrolyte, inducing now a downward bending of the bands along the space charge region.

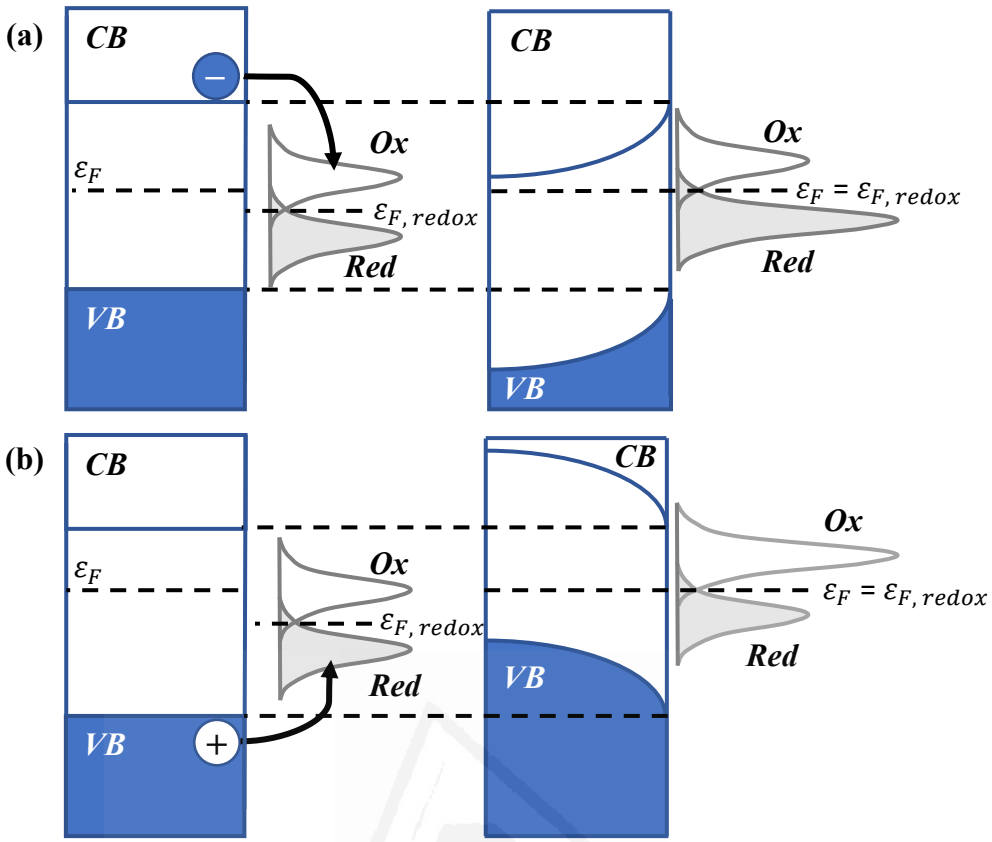

Figure 1.10. Band diagrams immediately upon contact (left) and in equilibrium (right) for (a) an *n*-type and a (b) *p*-type semiconductor, under dark conditions and with a redox pair contained in the electrolyte.

1.4.4. Surface states

In an intrinsic (*i.e.*, non-doped) semiconductor, the so-called surface states may appear as consequence of the abrupt termination of the lattice periodicity at the solid surface. In this type of semiconductor material, and since the valence band is filled with electrons while the conduction band is completely empty, the Fermi level (ε_F) would be located in the middle of the band gap. For a semiconductor under vacuum conditions, if it is considered that the energy level of the surface states (ε_{SS}) is also located in this same position (ε_F and ε_{SS} have the same value), there would not be any net charge transfer between the bulk and the surface. Then, the semiconductor bands would be flat, without any bending phenomena (Figure 1.11a) [12].

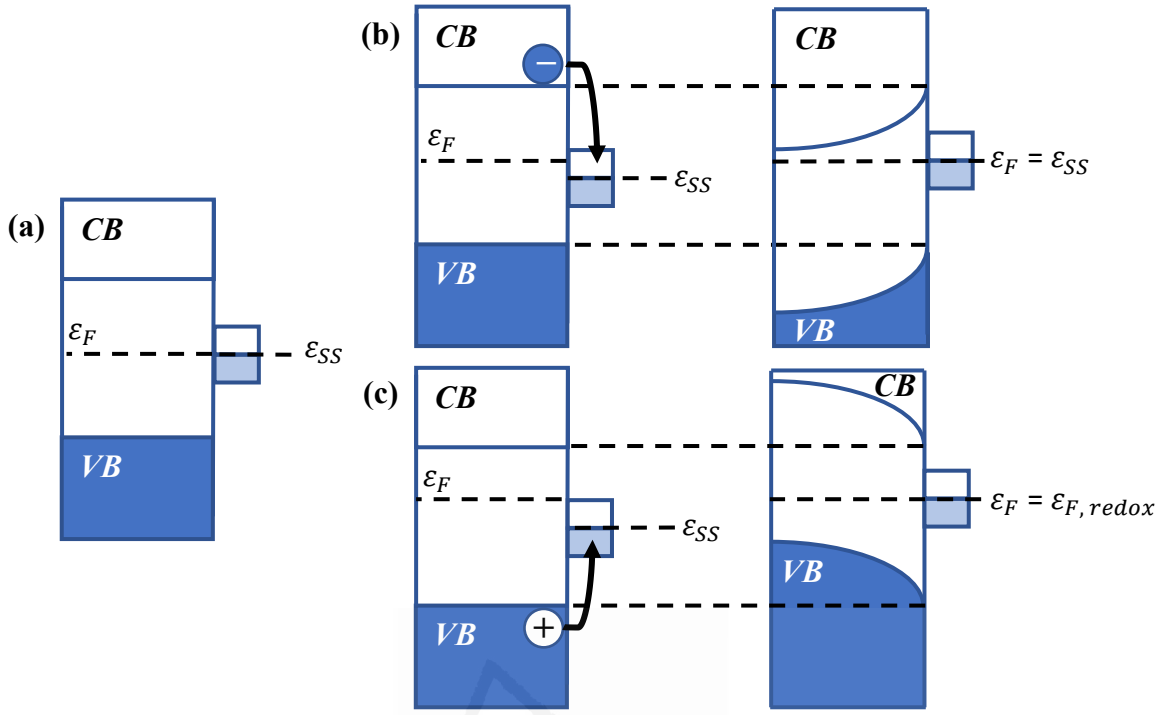

Figure 1.11. Surface-state band-bending for an (a) intrinsic semiconductor, and for non-equilibrium (left) and equilibrium (right) conditions for an (b) *n*-type and a (c) *p*-type semiconductor.

However, for doped semiconductors, the Fermi level at the surface is usually shifted from the middle of the band gap, being closer to the edge of the conduction or valence band (considering an *n*-type or *p*-type doping, respectively). Due to the resulting energy difference between ε_F and ε_{SS}, there is a majority charge carrier net flow from the bulk to surface states until both energy levels equilibrate. This results in an upward or downward band-bending (for an *n*-type or *p*-type semiconductor, respectively) with the subsequent appearance of a depletion region in the space charge region of the semiconductor (Figure 1.11b and c). It is important to consider that, since surface states are mostly determined by the atomic structure of the semiconductor surface, the surface-state-induced band-bending would be different for the same semiconductor depending on its different surface structure.

Surface states usually present great importance in the semiconductor characterization. In fact, they can act as surface trapping centers for electrons and holes, motivating the appearance of a surface charge density that subsequently produces a charge density of opposite sign in the semiconductor bulk and thus altering the properties of the semiconductor. In addition, the existence of these surface states within the bandgap can also result in significant changes in the kinetics of the charge transfer processes due to the fact that they act as recombination centers, mediators in charge transfer phenomena and determining factors of surface change and band-bending. All this together can importantly affect the (photo)electrochemical response of the semiconductor material.

1.4.5. Application of a potential

In a system formed by a semiconductor immersed in an electrolyte in equilibrium (*i.e*, ε_F and $\varepsilon_{F,redox}$ have the same value), any net charge carrier transfer across the interface occurs (Figure 1.12a). Considering a limit situation where $C_{SCR} \ll C_H$, and since the potential drop across the Helmholtz layer (and, by extension, across the diffuse layer) remains unaltered, the edged of the semiconductor bands would be pinned at the surface [21]. Under these conditions, a band edge pinning (BEP) context can be defined.

The application of an external bias can significantly alter this situation since it will change the potential drop across the space charge region, modifying the extent of the band-bending [2,21,28]. If the applied potential is higher than the equilibrium potential ($E_{applied} > E_{eq}$), the band-bending would increase and the electron density at the surface would decrease in comparison to the equilibrium state (Figure 1.12b). For the opposite situation, in which the applied potential is lower than that of the equilibrium situation ($E_{applied} < E_{eq}$), the effects are the contrary: the electron density would increase due to a decrease in the band-bending until a context in which the bands become completely flat

are achieved (Figure 1.12c). The potential that induces a flattening of the semiconductor bands is called flat band potential (E_{fb}), and it indicates the position of the Fermi level in the semiconductor.

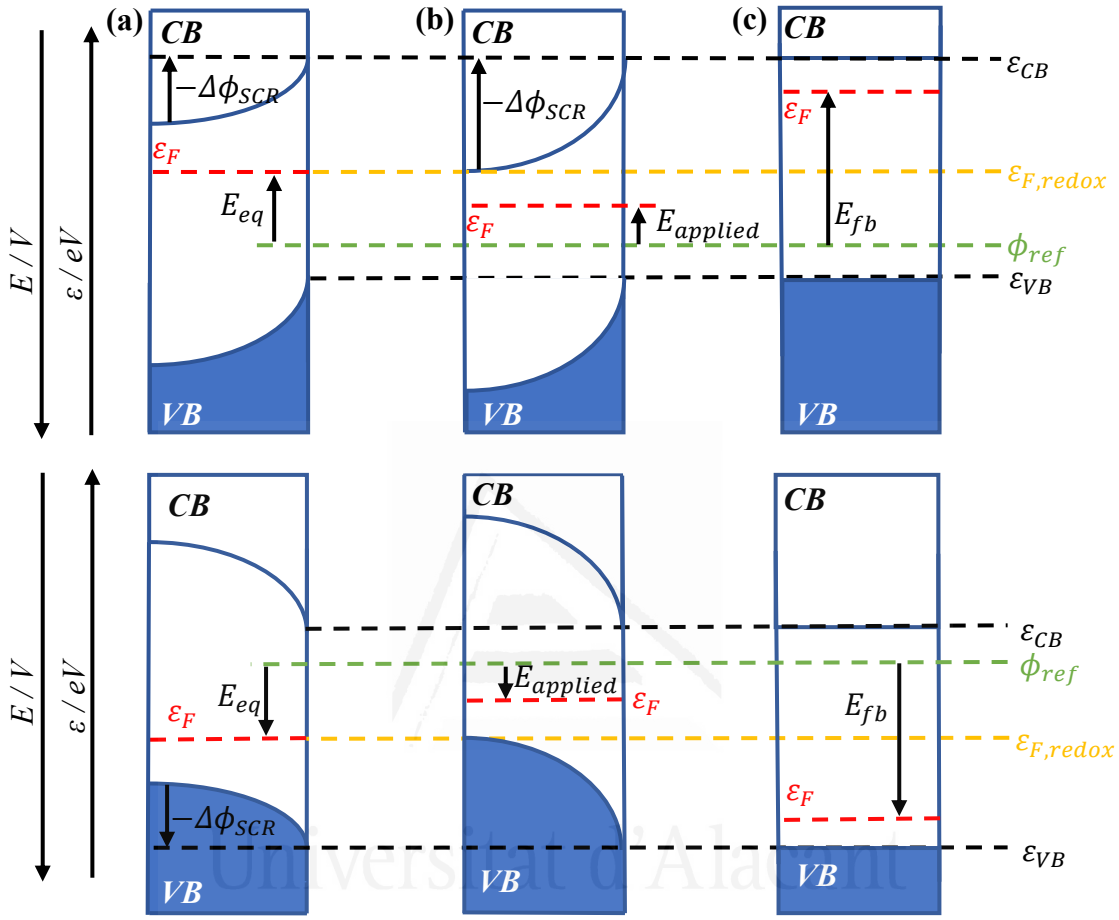

Figure 1.12. Band energy diagram for an *n*-type (top) and *p*-type (bottom) semiconductor electrodes under different conditions: (a) equilibrium, (b) BEP with $E_{applied} > E_{eq}$, and (c) BEP with $E_{applied} < E_{eq}$. The value of the reference potential (ϕ_{ref}) is arbitrary located.

In the other limiting case, in which $C_{SCR} \gg C_H$, the application of an external bias will produce a variation of the potential drop across the Helmholtz layer. Under these conditions, the energy levels at the surface are shifted with respect to those energy levels in equilibrium. Consequently, the band edges in the semiconductor maintain the same relative positions since $\Delta\phi_{SCR}$ remains virtually unaltered. To highlight the difference

between this situation and the previous one (*i.e.*, band edge pinning), it is said that now the bands are unpinned due to a Fermi level pinning (FLP) situation (Figure 1.13) [21,29].

Since both situations are defined for limit cases, real systems are not expected to present exclusively any of them. In fact, the semiconductor-electrolyte interface is governed by an intermediate situation between BEP and FLP, which means that the application of an external bias induces a simultaneous potential drop across the space charge region and the Helmholtz layer.

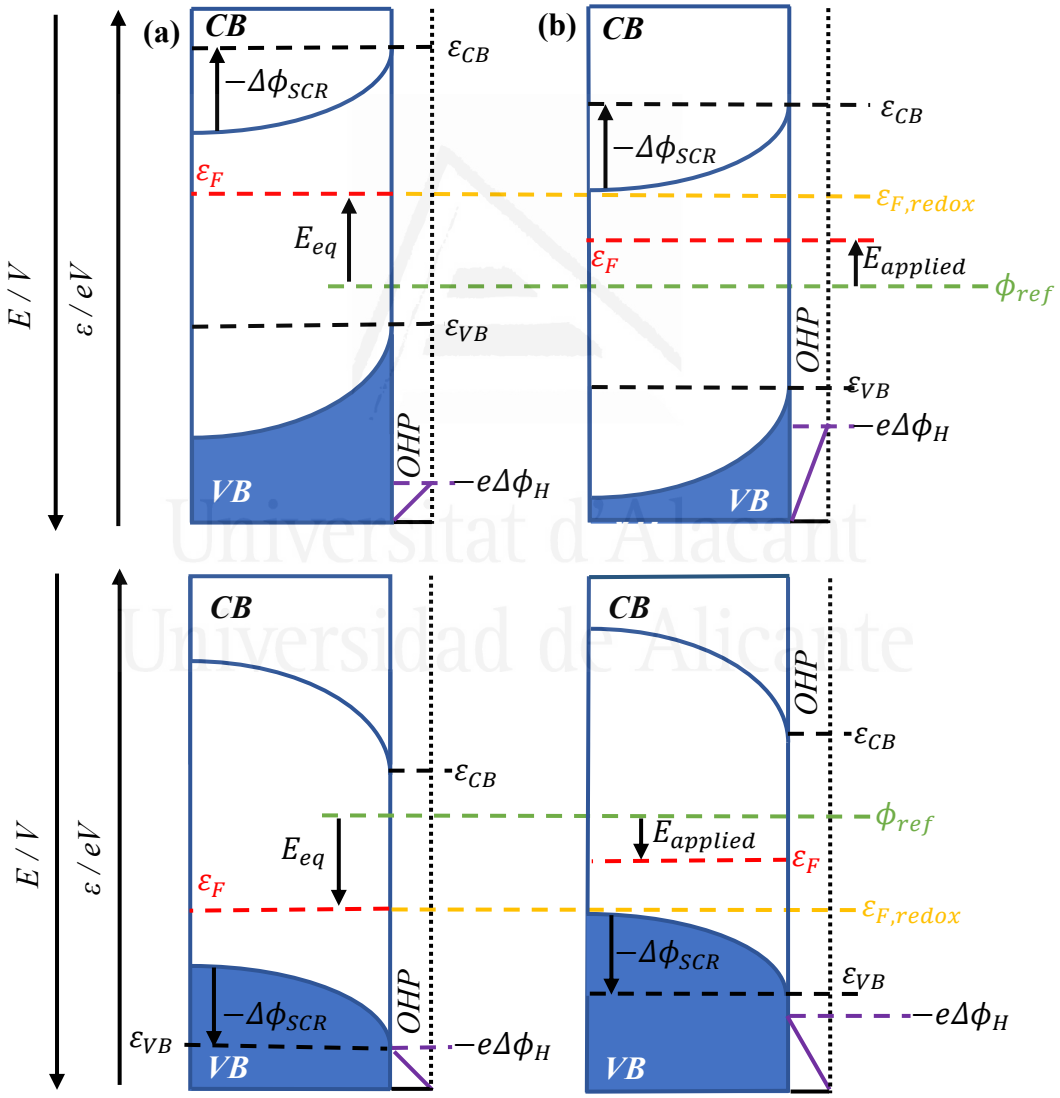

Figure 1.13. Band energy diagram for an *n*-type (top) and *p*-type (bottom) semiconductor electrodes under different conditions: (a) equilibrium, and (b) FLP with $E_{applied} > E_{eq}$. The value of the reference potential (ϕ_{ref}) is arbitrary located.

1.4.6. Kinetics of charge transfer reactions at the semiconductor-electrolyte interface

Electron-transfer reactions are the simplest class of electrochemical reactions, and they play a special role in every electrochemical reaction that involves, at least, one electron-transfer step. This is even true if the current across the electrochemical interface is carried by ions since, depending on the direction of the current, the ions must either be generated or discharged by an exchange of electrons with the surroundings.

In general electron-transfer reactions can be quite complicated since they involve the breaking or formation of chemical bonds, adsorption of at least one of the redox partners, or the presence of certain catalysts. In this regard, it is it is common to distinguish between outer-sphere and inner-sphere electron electron-transfer reactions. The so-called outer-sphere electron-transfer reactions constitute the simplest possible case since, in the course of such a reaction, no bonds are broken or formed, the reactants are not specifically adsorbed, and catalysts play no role. So, from a chemist's point of view, nothing happens but the exchange of one electron (in fact, the simultaneous transfer of two or more electrons is highly unlikely). If one of these conditions is not fulfilled, the reaction is said to proceed via an inner-sphere pathway, which is the most common electrode reaction mechanism [26,30].

From a macroscopic point of view of electron-transfer reactions, the overall rate of an electrochemical reaction (v) is the difference between the rates of oxidation (the anodic reaction) and reduction (the cathodic reaction); it is customary to denote the anodic reaction, and the current associated with it, as positive (Eq. 1.33):

$$v = k_{ox} c_{red}^{s} - k_{red} c_{ox}^{s} \qquad \text{Eq. } \mathbf{1.33}$$

where c_{red}^{s} and c_{ox}^{s} denote the surface concentrations of the reduced and oxidized species, respectively, and k_{ox} and k_{red} are the corresponding rate constants. Using absolute rate theory, the latter can be written in the following form (Eq. 1.34 and 1.35):

$$k_{ox} = A \cdot exp\left(-\frac{\Delta G_{ox}(E)}{RT}\right) \quad \text{Eq. } \mathbf{1.34}$$

$$k_{red} = A \cdot exp\left(-\frac{\Delta G_{red}(E)}{RT}\right) \quad \text{Eq. } \mathbf{1.35}$$

The phenomenological treatment assumes that the Gibbs energies of activation (G_{ox} and G_{red}) depend on the electrode potential (E), but the pre-exponential factor (A) does not. Expanding the energy of activation about the standard equilibrium potential (E_{eq}) of the redox reaction and keeping terms up to first order, for the anodic reaction it is obtained (Eq. 1.36):

$$\Delta G_{ox}(E) = \Delta G_{ox}(E_{eq}) - \alpha F(E - E_{eq}), \text{ where } \alpha = -\frac{1}{F} \cdot \frac{\partial \Delta G_{ox}}{\partial E}\Big|_{E_{eq}} \quad \text{Eq. } \mathbf{1.36}$$

The quantity α (dimensionless) is the anodic transfer coefficient. The factor $1/F$ is introduced since the $F \cdot E$ is the electrostatic contribution to the molar Gibbs energy, and the sign is chosen such that α is positive since an increase in the electrode potential makes the anodic reaction go faster, and decreases the corresponding energy of activation.

Similarly, for the cathodic reaction (Eq. 1.37):

$$\Delta G_{red}(E) = \Delta G_{red}(E_{eq}) + \beta F(E - E_{eq}), \text{ where } \beta = \frac{1}{F} \cdot \frac{\partial \Delta G_{red}}{\partial E}\Big|_{E_{eq}} \quad \text{Eq. } \mathbf{1.37}$$

where β, the cathodic transfer coefficient, is also positive and dimensionless.

The Gibbs energies of activation are related by (Eq. 1.38):

$$\Delta G_{ox}(E) - \Delta G_{red}(E) = G_{ox} - G_{red} \quad \text{Eq. } \mathbf{1.38}$$

to the molar Gibbs energies of the oxidized and reduced state (G_{ox} and G_{red}, respectively). In particular (Eq. 1.39):

$$\Delta G_{ox}(E_{eq}) = \Delta G_{red}(E_{eq}) = \Delta G(E_{eq}) \quad \text{Eq. } \mathbf{1.39}$$

When the electrode potential is changed from E_{eq} to a value E, the Gibbs energy of the electrons on the electrode is lowered by an amount $-F(E - E_{eq})$, and so is the energy of the oxidized state. If the reactants are so far from the electrode surface that their electrostatic potentials are unchanged when the electrode potential is varied, then the Gibbs energy of the reaction is also changed by $-F(E - E_{eq})$. This condition is generally fulfilled for outer-sphere reactions in the presence of a high concentration of an inert electrolyte which screens the electrode potential; it is not fulfilled when the reactants are adsorbed as in inner-sphere reactions. When it is fulfilled, Eq. 1.40 is accomplished:

$$\Delta G_{ox}(E) - \Delta G_{red}(E) = -F(E - E_{eq}) \qquad \text{Eq. } \mathbf{1.40}$$

By differentiation, the sume of the two transfer coefficients obeys the relation (Eq. 1.41):

$$\alpha + \beta = 1 \qquad \text{Eq. } \mathbf{1.41}$$

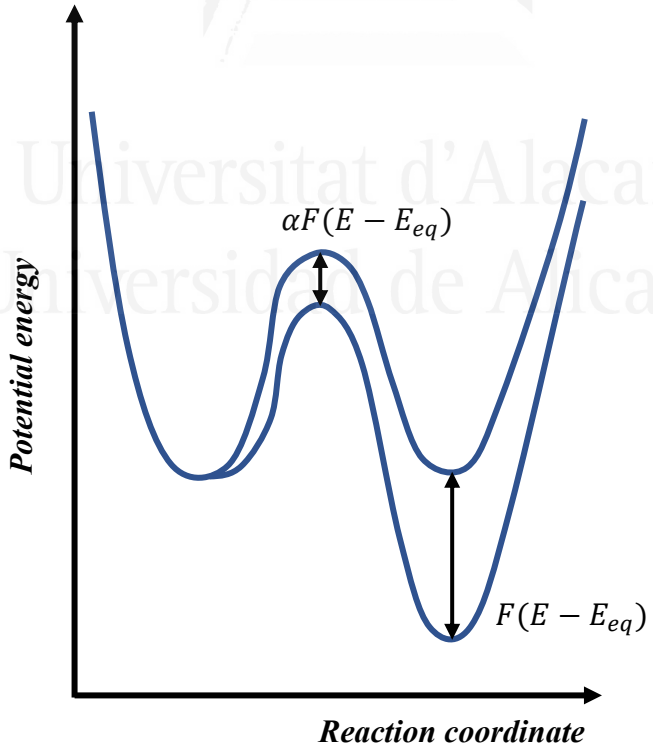

Figure 1.14. Potential energy curves for an outer-sphere reaction; the upper curve is for the standard equilibrium potential E_{eq}; the lower curve for $E > E_{eq}$.

Since both coefficients are positive, they lie between zero and one; we can generally expect a value near 1/2 unless the reaction is strongly unsymmetrical. The transfer coefficients have a simple geometrical interpretation. In a one-dimensional picture, the potential energy of the system as a function of a generalized reaction coordinate can be plotted (Figure 1.14). The reduced and the oxidized states are separated by an energy barrier. Changing the electrode potential by an amount $(E - E_{eq})$ changes the molar Gibbs energy of the oxidized state by $-F(E - E_{eq})$; the Gibbs energy of the transition state located at the maximum will generally change by a fraction $-\alpha F(E - E_{eq})$, where $0 < \alpha < 1$.

The current density j associated with the reaction is simply $j = Fv$. Combining Eq. 1.33 to 1.37 and 1.41 gives the Butler-Volmer equation [31,32] in the form (Eq. 1.42):

$$j = Fk_0 c_{red}^s \cdot exp\frac{\alpha F(E - E_{eq})}{RT} - Fk_0 c_{ox}^s \cdot exp\frac{(1-\alpha)F(E - E_{eq})}{RT} \qquad \text{Eq. } \mathbf{1.42}$$

where $k_{red} = A \cdot exp\left(-\frac{\Delta G(E_{eq})}{RT}\right)$.

Using the Nernst equation for the equilibrium potential (E_{eq}) and introducing the overpotential $\eta = E - E_{eq}$, which is the deviation from the equilibrium potential, the Butler-Volmer equation can be rewritten in the form (Eq. 1.43):

$$j = j_0\left[exp\frac{\alpha F\eta}{RT} - exp\left(-\frac{(1-\alpha)F\eta}{RT}\right)\right] \qquad \text{Eq. } \mathbf{1.43}$$

where $j_0 = Fk_0(c_{red}^s)^{(1-\alpha)}(c_{ox}^s)^{\alpha}$ is the exchange current density. At the equilibrium potential the anodic and cathodic current both have the magnitude j_0 but opposite sign, thus cancelling each other.

According to the Butler-Volmer law, the rates of simple electron-transfer reactions follow a particularly simple law. Both the anodic and the cathodic current densities depend exponentially on the overpotential η (Figure 1.15). For large absolute values of

η, one of the two partial currents dominates, and a plot of $ln\,|j|$ (or of $log|j|$) versus η, a so-called Tafel plot (Figure 1.16) [33], yields a straight line in this region. From its slope and intercept the transfer coefficient and the exchange current density can be obtained. These two quantities completely determine the current-potential curve.

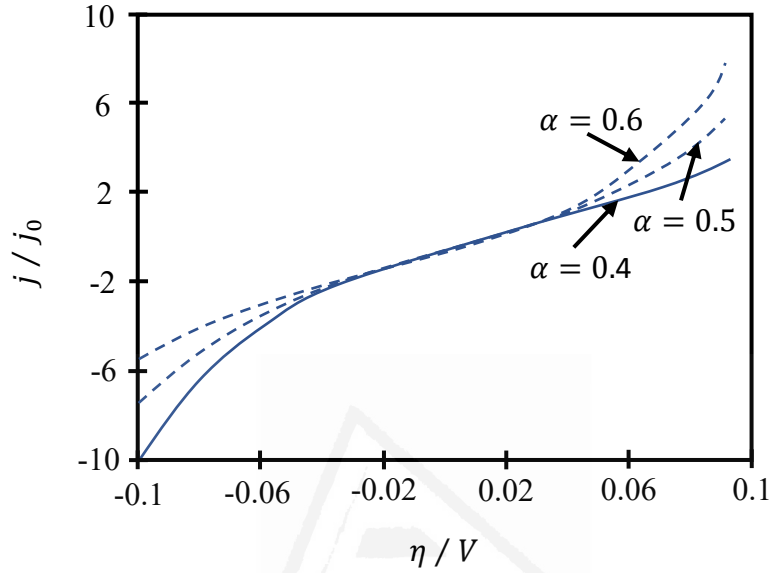

Figure 1.15. Current-potential curves according to the Butler-Volmer equation.

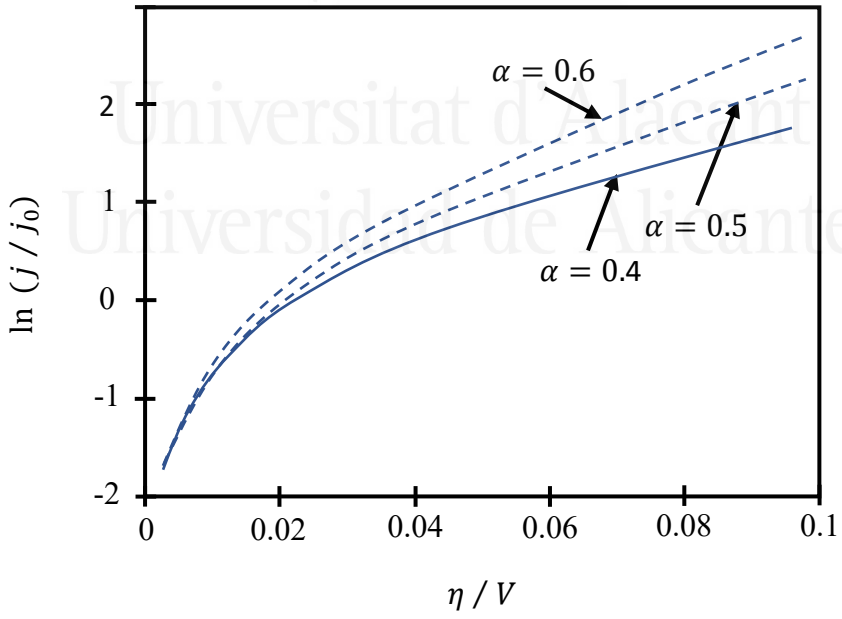

Figure 1.16. Tafel plot for the anodic current density of an outer-sphere reaction.

For small overpotentials, in the range $|F\eta| << RT$, the Butler-Volmer equation can be linearized by expanding the exponentials (Eq. 1.44):

$$j = j_0 \frac{F\eta}{RT} \qquad \text{Eq. } \mathbf{1.44}$$

The quantity η/j is called the charge-transfer resistance. It is important to note that the transfer coefficient does not appear in the current-voltage relation for small overpotentials, and hence cannot be determined from measurements at small deviations from equilibrium, they give the exchange current density only. However, α can be obtained by varying the surface concentrations, measuring the exchange current density, and using the expression for the exchange current density.

1.4.7. Light absorption by semiconductors

Between the most remarkable properties of semiconductors, there is their capability to absorb light in the ultraviolet and visible range. The absorption of photons by a semiconductor induces an optical excitation that can result in different types of electronic transitions (Figure 1.17) [21,22]. The transition labelled as (a) refers to the so-called intraband transitions, originated by the absorption of light by free carriers within the bands. Transitions denoted as (b) and (c) involve either acceptor or donor impurity levels, respectively. In these cases, the absorption of light occurs by charge carriers localized in impurity atoms or structural imperfections in the lattice. Finally, the interband transition (d) is that implying that the absorbed radiation generates a delocalized electron in the conduction band, leaving behind a delocalized hole in the valence band (which is called an electron-hole pair). To obtain an interband transition, the semiconductor must absorb photons with an energy ($h\nu$) equal or higher than that corresponding to its band gap value (E_g). That is the reason why this parameter is widely used to define the light absorption ability of a semiconductor.

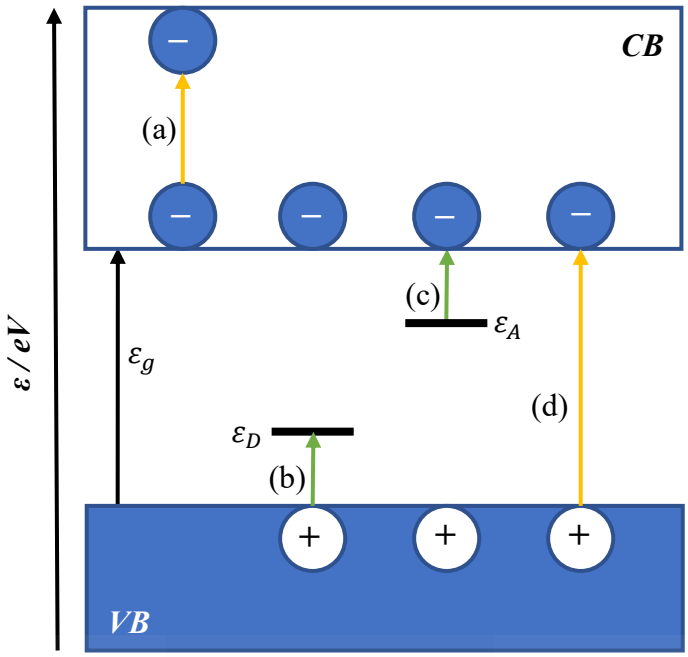

Figure 1.17. Different light-induced electronic transitions in a semiconductor: (a) intraband transition, transitions involving (b) donor and (c) acceptor impurity levels, and (d) interband transition. The yellow arrows indicate those transitions which are light-induced, while the green ones denote transitions motivated by thermal excitation.

An interband transition can present two variants: the direct and the indirect one (Figure 1.18) [2,21,22]. In the former, the momentum is conserved, which means that the top edge of the valence band and the bottom edge of the conduction band are both located at the same *k*-vector [28]. On the contrary, the indirect intraband transition occurs when the absorption of a photon is accompanied by a change in the crystal momentum. Additionally, and since photons barely carry momentum, an indirect transition requires the simultaneous absorption or emission of a photon [34,35]. It is important to consider that indirect transitions rarely occur and materials having such behavior commonly present lower optical absorption coefficients in comparison to materials with direct transitions.

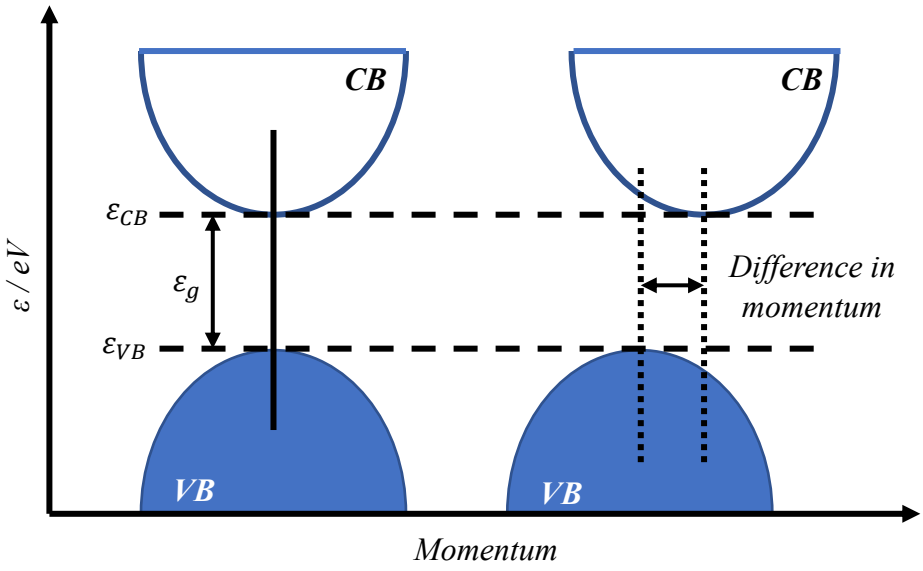

Figure 1.18. Electron energy as a function of the crystal momentum for (a) direct and (b) indirect interband transitions.

In this regard, and assuming that the bottom of the conduction band and the top of the valence band present parabolic shapes, the optical absorption coefficient (α) for an interband transition can be defined as (Eq. 1.45) [21,22]:

$$\alpha = \frac{A}{h\nu}\left(h\nu - E_g\right)^m \qquad \text{Eq. } \mathbf{1.45}$$

where A is a constant and the value of the exponent m depends on the nature of the optical transition. For direct transitions, m has a value of 0.5, while for indirect ones its value is 2. This equation is widely used to determine the optical band gap value of semiconductor materials by plotting $(\alpha h\nu)^{1/2}$ or $(\alpha h\nu)^2$ with respect to $h\nu$ for an indirect or direct optical transition, respectively. This representation is known as Tauc plot, and it will be discussed in detail in the next chapter.

In this context, a key factor is that the absorptions depths (given by $1/\alpha$) are significantly different for direct and indirect transitions: while, for the former, absorption lengths of between 100 and 1000 nm can be obtained, they can be as large as 10^4 nm for the latter [28,36].

It is important to remark that the optical band gap is intimately related to the electronic band gap of a semiconductor material, which is an essential parameter defining its light absorption ability. In the context of photoelectrochemical cells and regarding light absorption, narrow band gap semiconductors are desirable (as explained below, in section 1.5.1) in order to absorb most of the solar spectrum (Figure 1.19). As shown, the maximum values of irradiance are within the visible and near infrared regions.

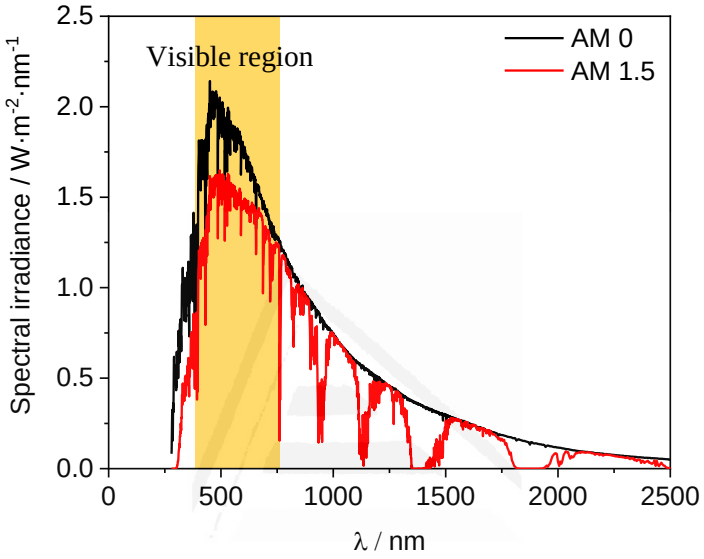

Figure 1.19. Solar spectrum with and without atmospheric absorption (AM 0 and AM 1.5, respectively).

Since the solar spectrum does not exactly present the same spectral distribution and irradiance intensity across the Earth's surface, the photovoltaic industry, in conjunction with the American Society for Testing and Materials (ASTM), defined a terrestrial spectral irradiance (AM 1.5G) for standardization purposes [2]. AM 1.5G (*i.e.*, air mass 1.5 global) refers to the spectral distribution and intensity of sunlight on a 37º south-facing tilted surface after it has traveled through 1.5 times the thickness of the Earth's atmosphere, with a solar zenith angle of 48.19º. This spectrum, with a total integrated intensity of 1000 $W \cdot m^{-2}$, includes the contribution of the incident sunlight.

1.5. PHOTOELECTROCHEMISTRY OF SEMICONDUCTORS

1.5.1. Illuminated semiconductor-electrolyte interface

As previously commented in section 1.3.6, semiconductors can absorb photons of energy higher than that corresponding to their band gap when they are illuminated with light in the UV-vis range. This absorbed energy induces the generation of electron-hole pair, thus disturbing the thermal equilibrium existing in the dark. The light-induced excitation allows to increase both the free electron and hole densities in the conduction and valence bands, respectively [2,21]. In this situation, the charge carriers are no longer in equilibrium, but in a steady-state once the electron-hole generation and recombination processes are finally balanced. The total electron and hole concentration upon illumination (n^* and p^*, respectively) can be described as the sum of the carrier concentration generated by thermal excitation (*i.e.*, the carrier concentration in dark conditions, previously denoted as n and p) and the additional electrons and holes produced by photoexcitation (Δn^* and Δp^*, respectively). It is important to note that $\Delta n^* = \Delta p^*$.

Additionally, under illumination, electrons and holes may have different (but defined) electrochemical potentials, which leads to the definition of the so-called *quasi*-Fermi levels for both carriers (denoted as $\varepsilon_{F,n}^*$ and $\varepsilon_{F,p}^*$ for electrons and holes, respectively). Considering Eq. 1.12 and total electron and hole concentration upon photoexcitation (n^* and p^*, respectively), those *quasi*-Fermi levels can be defined as (Eq. 1.46 and 1.47):

$$\varepsilon_{F,n}^* = \varepsilon_{CB} - kT \cdot ln\frac{N_{CB}}{n^*} = \varepsilon_{CB} - kT \cdot ln\frac{N_{CB}}{n + \Delta n^*} \quad \text{Eq. } \mathbf{1.46}$$

$$\varepsilon_{F,p}^* = \varepsilon_{VB} + kT \cdot ln\frac{N_{VB}}{p^*} = \varepsilon_{VB} + kT \cdot ln\frac{N_{VB}}{p + \Delta p^*} \quad \text{Eq. } \mathbf{1.47}$$

The combination of Eq. 1.19, 1.20, 1.46 and 1.47 leads to the following expressions for $\varepsilon_{F,n}^{*}$ and $\varepsilon_{F,p}^{*}$ (Eq. 1.48 and 1.49, respectively):

$$\varepsilon_{F,n}^{*} = \varepsilon_F - kT \cdot ln\frac{n}{n + \Delta n^{*}} \qquad \text{Eq. } \mathbf{1.48}$$

$$\varepsilon_{F,p}^{*} = \varepsilon_F + kT \cdot ln\frac{p}{p + \Delta p^{*}} \qquad \text{Eq. } \mathbf{1.49}$$

Since the density of electrons in an *n*-type semiconductor is high, assuming that $n \gg \Delta n^{*}$, which implies that $n^{*} \approx n$, is then justified. For this reason and for this type of semiconductor, the *quasi*-Fermi level of electrons matches the Fermi level in the dark. Following a similar reasoning, it can be concluded that the *quasi*-Fermi level of holes in a *p*-type semiconductor material ($p \gg \Delta p^{*}$ and $p^{*} \approx p$) coincides with the Fermi level in the dark ($\varepsilon_{F,p}^{*} = \varepsilon_F$). Both cases are shown in Figure 1.20.

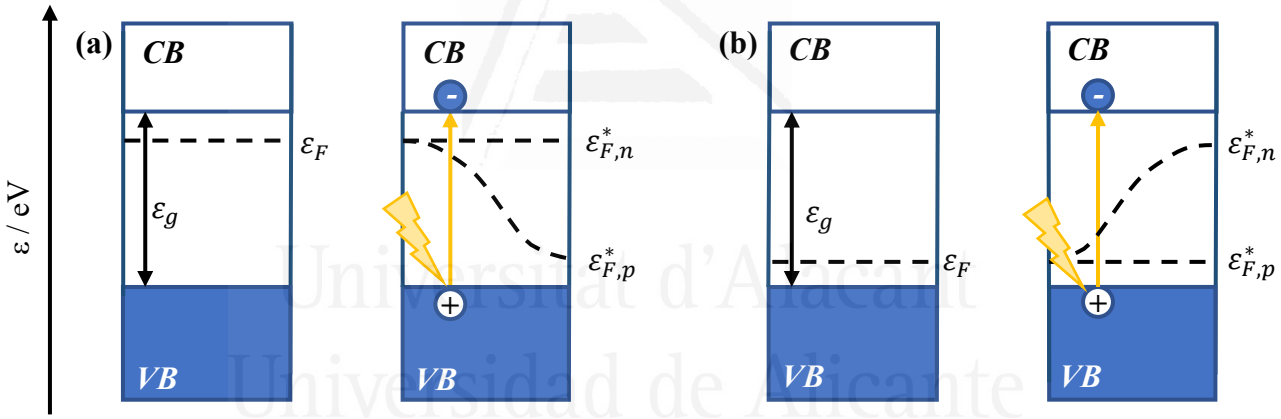

Figure 1.20. Band diagrams showing the light-induced Fermi level splitting into the *quasi*-Fermi level for electrons and holes, for an (a) *n*-type and (b) *p*-type semiconductor material.

1.5.2. Carrier collection under illumination

As expected, the space charge region of a semiconductor in equilibrium with a redox couple in solution is also affected upon illumination. In this region, the generated electric field separates photoexcited electrons and holes displacing them in opposite directions. If this photogenerated carriers do not recombine (they can do so, dissipating

the energy in the form of photon or heat emission), their movement induces the appearance of an inverse potential within the electrode, reducing the potential drop across the space charge region. As consequence, the initial band-bending decreases and the *quasi*-Fermi level of the majority charge carriers varies. The difference existing between the *quasi*-Fermi level of these carriers under illumination and in dark conditions (Figure 1.21) is known as photopotential $\left({}^{\varepsilon_{ph}}/_{e}\right)$ [21,23]. In this regard, and according to Figure 1.21, the photopotential for an *n*-type semiconductor is negative, while for a *p*-type semiconductor is positive. It must be noted that the *quasi*-Fermi level of the minority charge carriers under illumination is shifted only within a limited depth in the semiconductor, coinciding with the distance that photons can penetrate.

This splitting of the Fermi level of the semiconductor electrode upon illumination has serious implications since it allows for promoting chemical reactions that are not spontaneous under dark conditions. In fact, the location of the *quasi*-Fermi levels is of great importance because it determines the thermodynamic driving force of the (photo)electrochemical reactions that can take place on the electrode surface.

Under illumination and in a semiconductor electrode, the direction of the electric field at the interface is such that the minority carriers are swept to its surface, where they induce a photoelectrochemical reaction with the redox pair present in the electrolyte. On the other hand, the majority charge carriers are driven to the bulk part of the material until they reach the external circuit through the electric contact. The characteristic diffusion length of the minority charge carriers (L_n or L_p, for an *n*-type or *p*-type semiconductor, respectively), can be defined as (Eq. 1.50):

$$L_{n/p} = \left(D_{n/p} \cdot \tau_{n/p}\right)^{1/2} = \left(\frac{kT\mu_{n/p} \cdot \tau_{n/p}}{e}\right)^{1/2} \qquad \text{Eq. } \mathbf{1.50}$$

where D is the diffusion coefficient, τ is the carrier lifetime, and μ is the mobility of the minority carrier. The characteristic length defines the region fully effective for the photogenerated electron-hole pairs. In fact, pairs generated at depths longer than the so-called Debye length ($L_D = L_{SCR} + L_{n/p}$) will simply recombine.

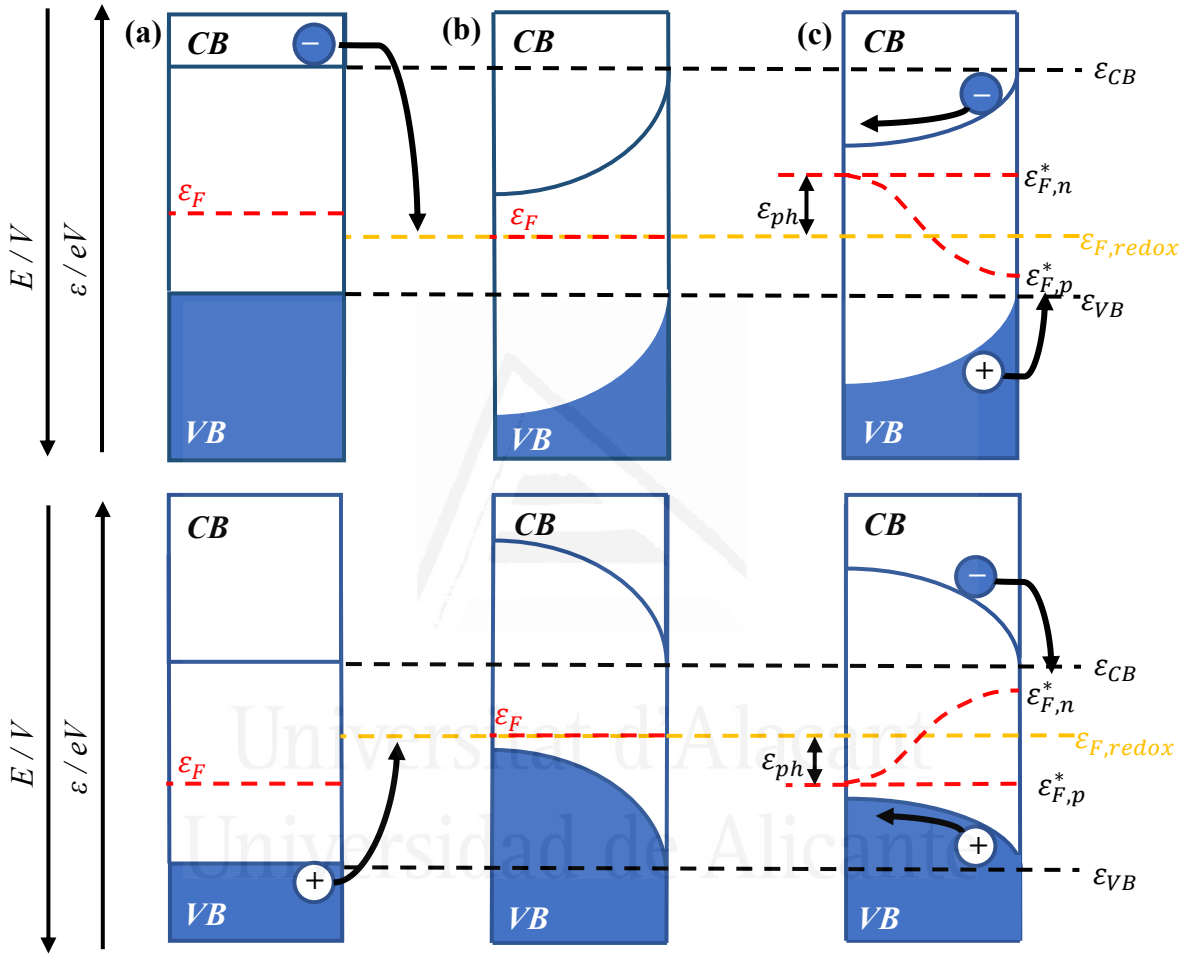

Figure 1.21. Band diagrams for an *n*-type (top) and *p*-type (bottom) semiconductors (a) before equilibrium with a redox pair in the electrolyte, (b) after equilibrium, and (c) under illumination (BEP is supposed).

In this context, the flux of charge carriers is measured as photocurrent density (j_{ph}). The photocurrent flowing across the interface can be anodic or cathodic (*i.e.*, with positive or negative sign, respectively) depending on whether it is an *n*-type or a *p*-type semiconductor material, respectively [21,28,37,38]. The maximum photocurrent value is

that corresponding to the rate of photon absorption. However, important photocurrent losses due to electron-hole recombination phenomena in the bulk, space charge region and semiconductor surface must be considered.

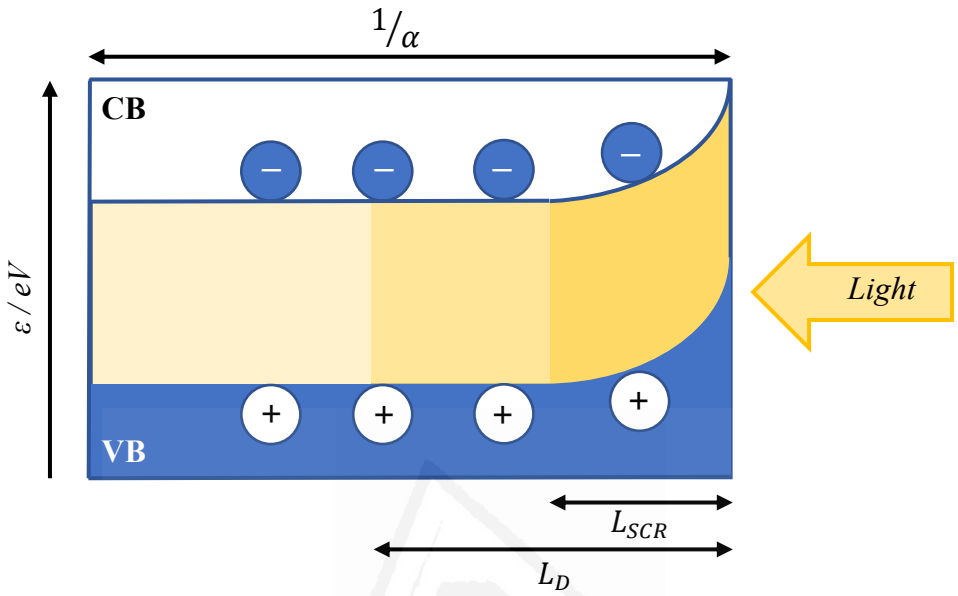

Figure 1.22. Photogeneration of electron-hole pairs in an *n*-type semiconductor, showing the penetration depth of incoming light $(1/\alpha)$, the space charge region width (L_{SCR}), and the Debye length of holes (L_D).

In order to simplify the analysis, the photocurrent is assumed to be equal to the sum of the current associated to minority carriers photogenerated in the space charge region layer and in the bulk, as long as they can reach the surface by diffusion. According to this, supposedly all the photogenerated minority carriers in the space charge region would be able to reach the electrode surface, thus contributing to the generation of photocurrent [28]. The so-called Gärtner model expresses the photocurrent density as a function of the incident photon flux (I_0), the absorption coefficient (α), the width of the space charge region (L_{SCR}) and the diffusion length of the minority carriers (Eq. 1.51) [21,39,40]:

$$\left|j_{ph}\right| = eI_0\left[1 - \frac{exp(-\alpha L_{SCR})}{1 + \alpha L_{n/p}}\right] \qquad \text{Eq. } \mathbf{1.51}$$

This model is satisfactory for large values of band bending (*i.e.*, large values of $\Delta\phi_{SCR}$), but its limitations are that it significantly deviates from the experimental behavior for situations close to the flat band conditions and because it ignores surface recombination phenomena [28,40].

In Figure 1.22, the different characteristic lengths considered in the Gärtner model are shown for an *n*-type semiconductor material under illumination.

1.5.3. Photoelectrochemistry of nanocrystalline semiconductor electrodes

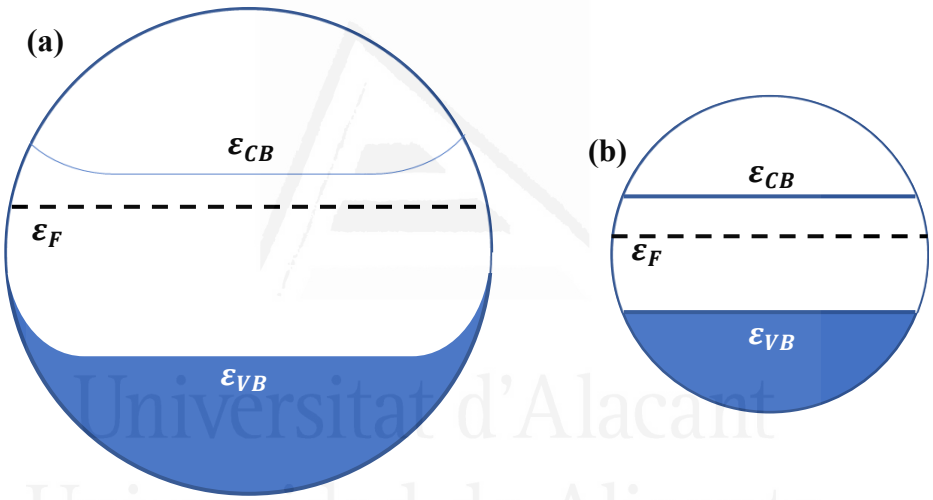

Figure 1.23. Comparison between the width of the space charge region (L_{SCR}) an the diameter (d) of a nanocrystal with a particle size (a) $d > L_{SCR}$, and (b) $d < L_{SCR}$.

From a materials point of view, the (photo)electrochemical field has historically evolved from the use of single crystal semiconductors to polycrystalline films and more recently, to nanocrystalline thin films. The main advantage of using nanocrystalline semiconductor electrodes is their large surface area (motivated by their usually large roughness factor), which enables a large contact area between the electrode surface and the electrolyte [41–44]. In addition, their usually particular geometries (especially in

ordered nanocrystalline electrodes) can favor an efficient charge separation since minority carriers need to travel shorter distances [28].

In the context of nanocrystalline semiconductor electrodes, understanding the electrostatics across the electrode-electrolyte interface involves important challenges. In fact, the concepts of space charge region, band-bending and flat band potential cannot be always applied in this case due to the fact that crystalline dimensions of this type of semiconductor electrodes are in the same order of magnitude (or even smaller) to the width of the space charge region (L_{SCR}) (Figure 1.23). This is especially true for barely doped materials, since smaller N_A or N_D values cause larger L_{SCR} values (according to Eq. 1.24) [28]. The complete interpretation implies that the Helmholtz double layer extends throughout the interior surface of the nanoporous network, much as in a supercapacitor case [45,46].

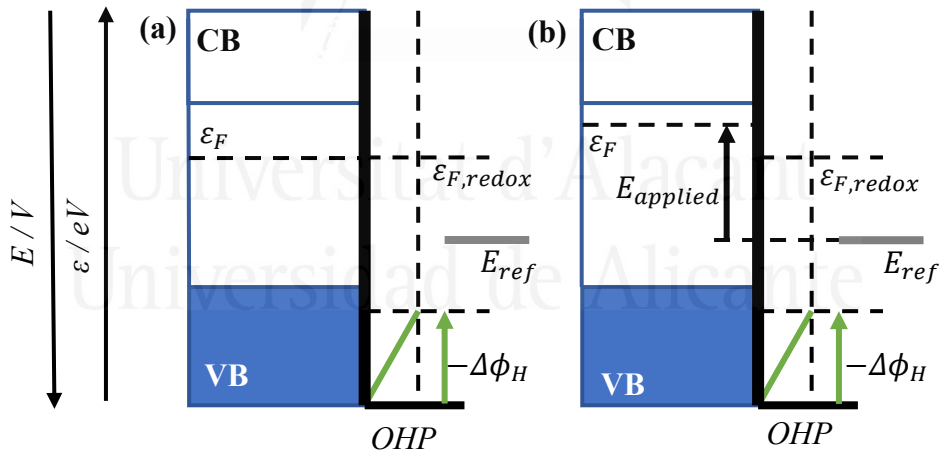

Figure 1.24. Band diagram for a nanostructured *n*-type semiconductor in (a) equilibrium, and (b) under the application of a potential ($E_{applied}$), under band edge pinning conditions.

Focusing on an *n*-type semiconductor, when the Fermi level is located considerably below the bottom edge of the conduction band and, in addition, the band gap is wide enough, the electrode material behaves as an insulator. Only upon negative polarization,

the nanocrystalline electrode can acquire conductivity. In this situation, in which the band edges are pinned, the electrode would be homogeneously charged, and the Fermi level would approach the conduction band. Figure 1.24 shows the change in the Fermi level as a result of a forward bias potential, achieving a *quasi*-metallic state with a sufficiently negative polarization (under band edge pinning conditions). This accumulation of negative charge must be compensated by cations from the electrolyte, which can be absorbed on the electrode surface or intercalated into its structure [28].

When the electrode is illuminated, the mechanism for charge separation is not promoted by the existence of an electric field inside the particles, but by the different reactivity of electrons and holes toward species present in the electrolyte. The inexistence of a well-defined space charge region motivates a diffusion-based charge carrier transport within the electrode, which is thus purely governed by the difference in concentrations along the nanoparticle network [47,48].

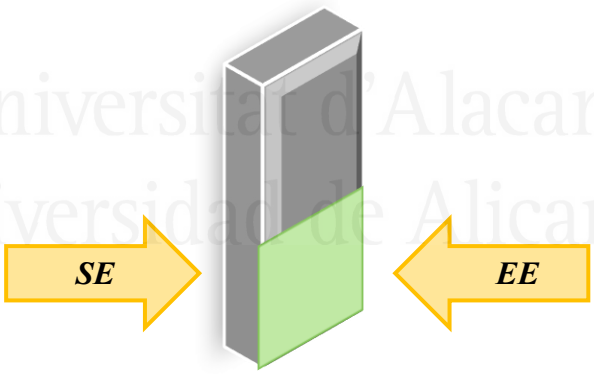

Figure 1.25. Scheme of the two different illumination modes for electrodes supported on optically transparent substrates: substrate-electrode (SE) and electrolyte-electrode (EE).

Considering the three basic processes involving charge carriers (generation, transportation and recombination), the density of charged species in a nanocrystalline electrode would be given by the continuity equation. In fact, the electron concentration profile across the films is dependent on the potential applied to the electrode. For

example, if the applied potential is equivalent to a Fermi level below $\varepsilon_{F,redox}$, the concentration of electrons in the back contact would be lower than in the bulk. So, the application of a proper potential can result in an electron concentration gradient which can effectively extract electrons at the back contact. The photocurrent density will be proportional to the charge carrier flux at the back contact of the nanocrystalline film. For solving the continuity equation, steady state and boundary conditions (which depend on illumination direction) must be considered. It must be noted that two different illumination directions can be distinguished (Figure 1.25): electrolyte-electrode (EE) illumination, which means that the electrode is illuminated from the electrolyte side, and substrate-electrode (SE) illumination, in which the electrode is illuminated from the substrate side. This last illumination mode can only be performed using transparent substrates.

To obtain expressions for maximum photocurrents under both EE and SE illumination conditions, some assumptions must be applied [49]. Among them, the most important ones are the following: (i) significant migration contributions are neglected, (ii) the diffusion coefficient is considered as constant, (iii) only one type of carrier is considered for charge transport, (iv) the generation of carriers is governed by the Lambert-Beer law, and (v) recombination phenomena follows a first-order kinetics. Assuming this, the following equations corresponding to the *n*-type semiconductor photocurrent density under EE (Eq. 1.52) and SE (Eq. 1.53) illumination, respectively, can be derived:

$$j_{ph}^{EE} = e \cdot I_0 \cdot \left(\frac{L_n \cdot \alpha \cdot \mathrm{e}^{-d\alpha}}{1 - L_n^2 \alpha^2}\right)\left[L_n \cdot \alpha + tanh\left(\frac{d}{L_n}\right) - \frac{L_n \cdot \alpha \cdot \mathrm{e}^{-d\alpha}}{cosh\left(\frac{d}{L_n}\right)}\right] \qquad \text{Eq. } \mathbf{1.52}$$

$$j_{ph}^{SE} = e \cdot I_0 \cdot \left(\frac{L_n \cdot \alpha}{1 - L_n^2 \alpha^2}\right)\left[-L_n \cdot \alpha + tanh\left(\frac{d}{L_n}\right) + \frac{L_n \cdot \alpha \cdot e^{-d\alpha}}{cosh\left(\frac{d}{L_n}\right)}\right] \qquad \text{Eq. } \mathbf{1.53}$$

where I_0 is the incident light intensity, α is the absorption coefficient, L_n is the minority carrier diffusion length, and d is the thickness of the nanocrystalline film. An analogous treatment can be applied to nanocrystalline *p*-type semiconductor electrodes.

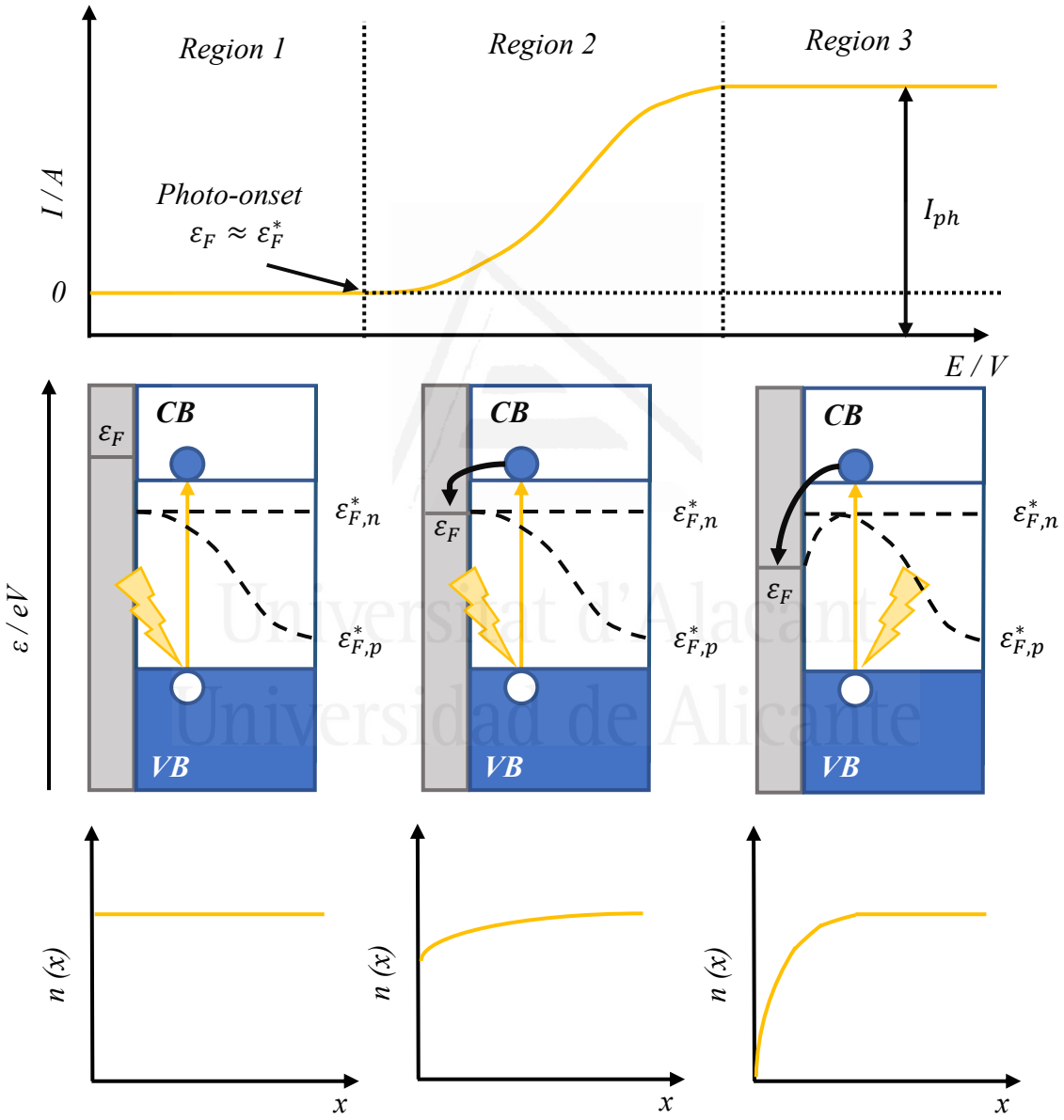

Figure 1.26. Photocurrent-potential plot for an *n*-type semiconductor, showing anodic photocurrent. ε_F is the Fermi level of the conductive substrate (FTO), and $\varepsilon_{F,n}^*$ and $\varepsilon_{F,p}^*$ are the electron and hole quasi-Fermi level under illumination, respectively.

Following with *n*-type nanocrystalline semiconductors, Figure 1.26 offers a brief description on how the photocurrent is affected by potential. The bottom panels summarize how the electron concentration varies with the distance in the film for the different regions in the photocurrent-potential curve. In region 1, the electrons cannot reach the conductive substrate due to the absence of a driving force. However, in region 2, a transfer of electrons from the semiconductor to the substrate occurs, producing an electron density gradient as electron concentration starts to decrease in the contact. In this case, the higher the applied potential, the lower the electron concentration at the contact, and, thus, higher the concentration gradient is. Finally, in region 3, the photogenerated electron concentration in the contact is almost null, so the photocurrent will not depend on the applied potential and will only be limited by diffusion.

1.6. PHOTOELECTROCHEMICAL TANDEM CELLS

A scheme of a tandem photoelectrochemical cell is shown in Figure 1.27. In this case, the device is constituted of two-sided light absorber electrodes: a *p*-type photocathode and an *n*-type photoanode, where hydrogen and oxygen evolution reactions take place, respectively. This configuration has an improved overall efficiency due to the different band gap values of the two semiconductors used, which can be smaller since each one only supports a half-reaction. In addition, these smaller band gaps can increase the absorption of light from the visible region, which represents most of the photon flux from the Sun. With this cell configuration, the achievement of enough photovoltage values to drive the hydrogen evolution reaction is easier. However, to this end, one of the essential requirements that must be met is that the conduction band of the photoanode must lie at a lower (or very similar) potential than the valence band of the photocathode [2,37,50,51].

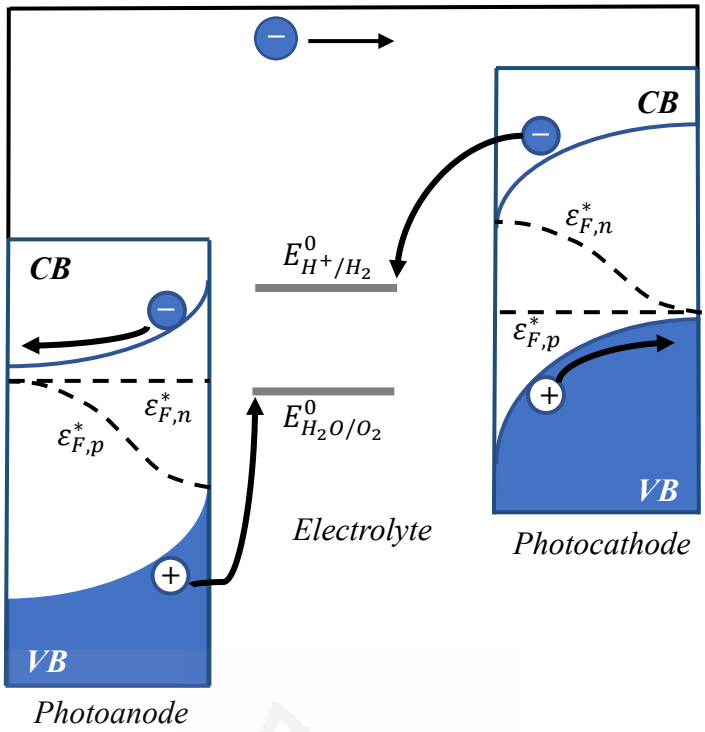

Figure 1.27. Tandem cell device in a wired configuration.

It is important to note that the following discussion starts from the working principle of a photoelectrochemical tandem cell, which states that the band gap energy of the photoanode ($\varepsilon_{g,1}$) must be higher than that of the photocathode ($\varepsilon_{g,2}$). The absorption of solar radiation by the photoanode and the photocathode induces the promotion of an electron from the conduction band to the valence band, leaving behind the corresponding hole (and thus generating an electron-hole pair). In both cases, the electric field in the space charge region physically separates these photogenerated charges. In the case of the photoanode, the holes in the valence band drift to the semiconductor-electrolyte interface, inducing the oxidation of water to oxygen, while in the photocathode, the electrons in the conduction band reach also reach the semiconductor-electrolyte interface promoting the reduction of water to hydrogen [52]. The majority charge carriers in the semiconductor electrodes (*i.e.*, electrons in the photoanode and holes in the photocathode) are collected in the back contact and recombine in the external circuit. To avoid the reaction between

the obtained products (oxygen and hydrogen), a separating membrane located between both electrodes must be employed.

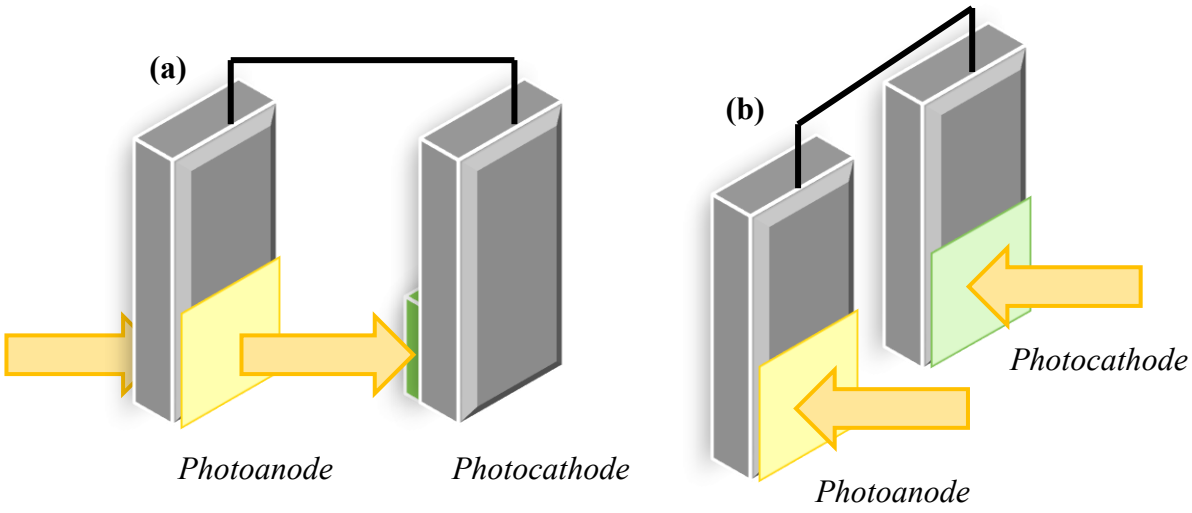

Figure 1.28. Different illumination modes in photoelectrochemical cells: (a) tandem illumination mode (mode T), and (b) parallel illumination mode (mode P).

For a photoelectrochemical tandem cell, two different configurations are available: (i) in serie, named tandem illumination mode (mode T), and (ii) side-by-side, known as parallel illumination mode (mode P) or, for many authors, as tandem cell [53]. They are depicted in Figure 1.28, respectively. While in mode P each photoelectrode is exposed to the full solar spectrum, mode T is characterized by a more efficient used of the solar energy: here, the incident light beam arrives to the photoanode (which absorbs its corresponding energy portion of the incoming solar irradiation) and transmits the remainder to the photocathode. To this end, transparent substrates (that allow the trespassing of radiation) for the photoelectrodes are required. In fact, in this context, the word 'tandem' usually refers to a photoelectrochemical cell formed by two photoelectrodes illuminated in serie. A photoelectrochemical cell configuration in mode T can be identified as the most promising for commercial applications since it can enhance the amount of light harvested by the device and offer improved photovoltage values. It is important to note that, in this mode T, the wired option (as seen in Figure

1.28) is usually preferred to the wireless one, in which the photoelectrodes are directly joined back-to-back) as it minimized the distance that ions in the electrolyte have to travel across it.

The efficiency of a photoelectrochemical device is a very important factor and it is usually quantified through the so-called solar-to-hydrogen (STH) parameter. It can be expressed as (Eq. 1.54):

$$STH\ /\ \% = \frac{1.23 \cdot \eta_F \cdot j_{ph}}{P_{solar}} \cdot 100 \qquad \text{Eq. } \mathbf{1.54}$$

where j_{ph} is the operating photocurrent density (measured in mA·cm^{-2}), η_F is the Faradic efficiency, and $P_{solar}$is the irradiance power density (expressed in mW·cm^{-2}). In the same way, and in the case of applied bias (V_{bias}), the conversion efficiency is defined through the applied bias photon-to-current efficiency (ABPE) (Eq. 1.55):

$$ABPE\ /\ \% = \frac{(1.23 - |V_{bias}|) \cdot j_{ph}}{P_{solar}} \cdot 100 \qquad \text{Eq. } \mathbf{1.55}$$

1.6.1. Requirements of photoelectrode materials

As expected, among the most critical aspects involved in the design of a photoelectrochemical device for water splitting is the choice of suitable photoanode and photocathode materials. The requirements that they should ideally meet are the following: (i) good visible light absorption, (ii) high chemical stability, both in dark and illumination conditions, in order to endure continuous and long-term photoelectrochemical operation, (iii) band edge positions straddling the water reduction and oxidation potentials, (iv) efficient charge transport across the semiconductor, (v) low overpotentials for the reduction or oxidation of water, (vi) be constituted by earth-abundant elements, and (vii) low cost [50,51,54].

The requirement of presenting a good visible light absorption is closely related to the band gap value of the semiconductor. Theoretically, the minimum bad gap should be of 1.9 eV in order to overcome the thermodynamic (1.23 V) [54] and kinetic (between 0.4 and 0.6 V) [55–58] barriers for photoelectrochemical water splitting. On the other extreme, it is important to consider that below 400 nm, the intensity of sunlight decreases rapidly, thus imposing an upper limit of 3.1 eV for the band gap. According to this, the optimum band gap for a semiconductor supposed to be used as photoelectrode in a photoelectrochemical cell should present a value between 1.9 and 3.1 eV, which comprises the visible range of the solar spectrum.

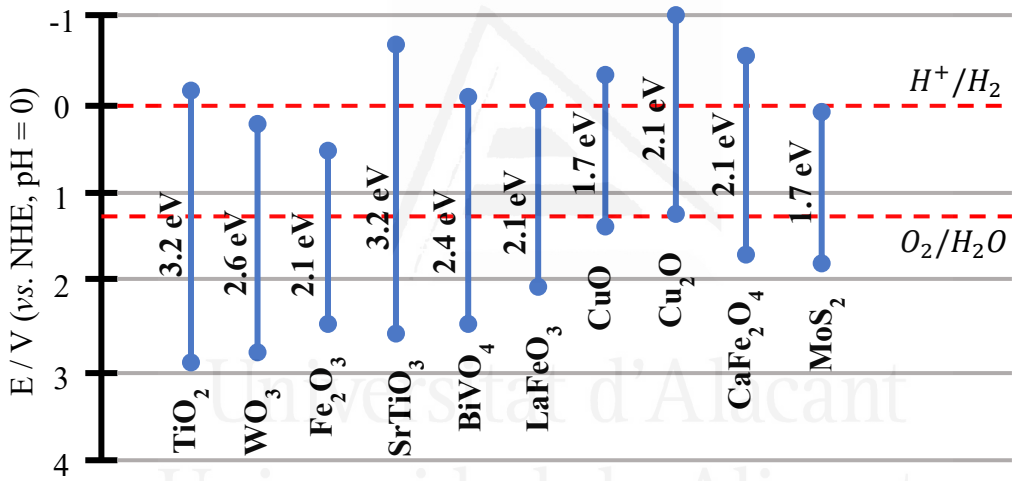

Figure 1.29. Band gap values and band edge positions for common *n*-type and *p*-type semiconductors used in photoelectrochemistry.

As already introduced, stability plays an essential role since it limits the usefulness and shelf life of many photoactive materials. Most non-oxide semiconductors either progressively dissolve or form a surface thin oxide layer that hinders proper charge transfer across the semiconductor-electrolyte interface. However, oxide semiconductors tend to be more stable. Generally, the stability under working conditions tends to increase with increasing band gap values.

The band edge positions requirement is unfortunately only fulfilled by only a few semiconductor materials. As shown in Figure 1.29, those that meet this requirement present extremely large band gap values (as it is the case of TiO_2 and $SrTiO_3$, for example [59–61]) or are unstable in aqueous environments (such as Cu_2O or MoS_2 [62–64]).

Compliance with the requirement related to need for an efficient charge transport is also not homogeneous: while it is easily fulfilled by common semiconductor materials (as TiO_2 and WO_3), in others it is the main cause for poor overall conversion efficiencies, which affects particularly to α-Fe_2O_3. Charge transport across the semiconductor material and the semiconductor-electrolyte interface should be fast enough to avoid undesirable charge carrier accumulation which lead to a decrease in the electric field and to an increase of electron-hole recombination phenomena. To improve the kinetics of charge transfer, catalytic active species (co-catalysts) may be added [65–67].

As expected, a single semiconductor material meeting all these requirements has not been found yet.

1.7. TERNARY OXIDES AS PHOTOANODES

Any semiconductor material supposed to be used as a photoanode in a photoelectrochemical cell for water splitting should present, as already stated, a narrow bandgap, high quantum efficiency in the range of visible light, good photochemical stability and photocatalytic activity, and it should be made from earth–abundant elements [58,68,69]. This is reason why some binary semiconductor metal oxides have been the primary choice of photoelectrodes for photoelectrochemical water oxidation during the past few decades. Attention has been traditionally focused on TiO_2 (E_g = 3.2 eV, for anatase phase [70,71]), α-Fe_2O_3 (E_g = 2.2 eV [72–74]) and WO_3 (E_g = 2.7 eV [75,76]) as to utilize at least part of the solar spectrum. However, it seems that none of these binary

oxides (or other tested candidates) fulfill all the requirements needed for achieving efficient devices for artificial photosynthesis. Therefore, in the last years, efforts have been redirected toward several ternary semiconductor materials capable of oxidizing water under illumination, generating molecular oxygen. At this respect, and in contrast to what happens in the case of binary oxides, the photoelectrochemical properties of ternary oxides are basically unexplored. A difficulty that should not be avoided stems from the fact that there is significant large number of ternary oxides (according to Turner, there were more than 50000 [77], a number that Parkinson's increases to 200000 [78]).

In the specific case of ternary semiconductor materials with application as photoanodes, the first selection includes some titanates ($SrTiO_3$ [79,80], $PbTiO_3$ [81], and $BaTiO_3$ [82]), tantalates ($KTaO_3$ [83,84], $LiTaO_3$ [83,84] and $NaTaO_3$ [83,85]) and ferrites ($LaFeO_3$ [86–88]) from the perovskite (ABO_3) family, and certain vanadates ($InVO_4$ [89,90], $BiVO_4$ [91–93] and $FeVO_4$ [94,95]) and tungstates (mainly $CuWO_4$ [96]), with general formula ABO_4. Most of them are characterized by their visible light activity, stability in aqueous electrolytes and low cost. However, the actual conversion efficiencies for major part of these ternary semiconductor metal oxides have been shown to be much lower than their theoretical limits, most likely due to fast charge recombination resulting from poor carrier mobility or slow interfacial charge transfer [97].

1.7.1. ABO_4 family: bismuth vanadate ($BiVO_4$) and iron vanadate ($FeVO_4$)

Among semiconductor candidate materials from the ABO_4 family, bismuth vanadate ($BiVO_4$) has received a great deal of attention. In fact, this *n*–type semiconductor has been identified as one of the most promising photoanode materials since the publication of the first report on its use as a photocatalyst in 1998 [91]. $BiVO_4$ is a low–toxicity material with a good chemical and photochemical stability composed of

relatively inexpensive elements, which occurs naturally as the mineral pucherite with an orthorhombic crystal structure [98]. However, $BiVO_4$ prepared in the laboratory crystallizes either in a scheelite structure (with a tetragonal or a monoclinic crystal system) or a zircon-type structure, with a tetragonal crystal system (Figure. 1.30) [99].

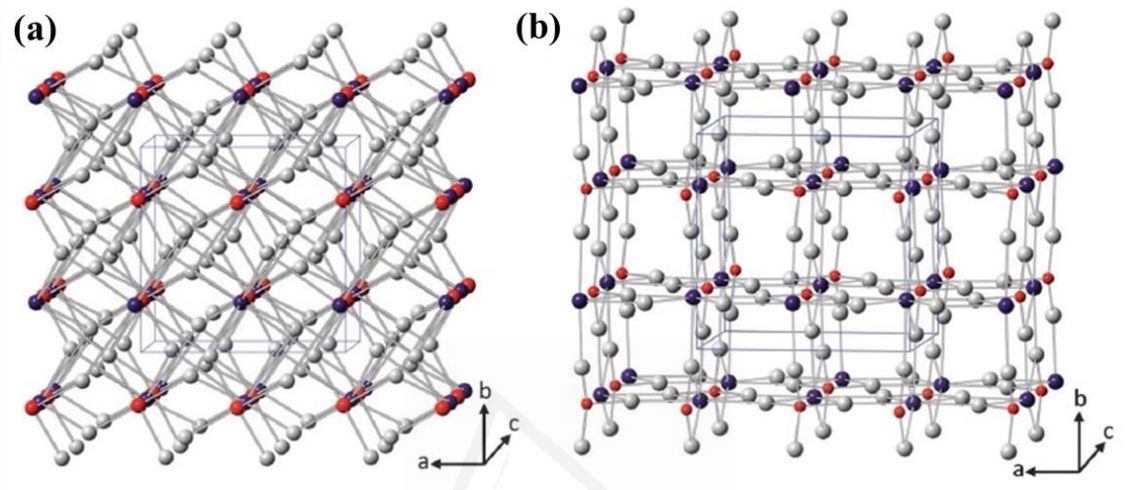

Figure 1.30. Crystal structures of (a) tetragonal scheelite and (b) zircon-type $BiVO_4$ (red: V, purple: Bi, and gray: O). The crystal structure of monoclinic scheelite is very similar to what is shown in (a) with the exception being the subtle changes in atomic positions of Bi, V, and O [93].

In the scheelite structure, each V^{5+} ion is coordinated by four O^{2-} anions in a tetrahedral site and each Bi^{3+} is coordinated by eight O^{2-} from eight different VO_4 tetrahedral units [100]. The only difference between the tetragonal and monoclinic scheelite structure is that the local environments of V and Bi ions are more significantly distorted in the monoclinic structure, which removes the four-fold symmetry necessary for a tetragonal system. In the zircon-type structure, V is still stabilized by four O atoms and Bi is coordinated by eight O atoms. However, each Bi is surrounded by only six VO_4 units because two VO_4 units provide two O atoms to Bi. It has been reported that low temperature synthesis results in a zircon-type structure [101,102]. A phase transition from tetragonal zircon to monoclinic scheelite occurs irreversibly at 670-770 K [101,103].

Among scheelite structures, the tetragonal phase is a high temperature phase and the phase transition between monoclinic scheelite $BiVO_4$ and tetragonal scheelite $BiVO_4$ was observed to occur reversibly at 528 K [101].

This structure discussion is essential since the photocatalytic properties of $BiVO_4$ are strongly related to its crystal structures. It has been observed that $BiVO_4$ with a monoclinic scheelite structure shows the highest photocatalytic activity for water oxidation [101,104]. The enhanced photoactivity of scheelite $BiVO_4$ over zircon-type $BiVO_4$ appears to be mainly due to the enhanced photon absorption of the scheelite $BiVO_4$ because the bandgap energies for scheelite and zircon-type $BiVO_4$ are 2.4 eV and 2.9 eV, respectively [101]. The schematic band structures of tetragonal zircon-type $BiVO_4$ and monoclinic scheelite $BiVO_4$ are shown in Figure 1.31. In the zircon-type structure, the band gap transition is due to the charge transfer transition from O 2*p* orbitals to empty V 3*d*. In the scheelite structure, the band gap is reduced because the 6*s* state of Bi^{3+} appears above the O 2*p* and the transition from Bi $6s^2$ (or hybrid Bi $6s^2$-O 2*p* orbitals) to the V 3*d* becomes possible.

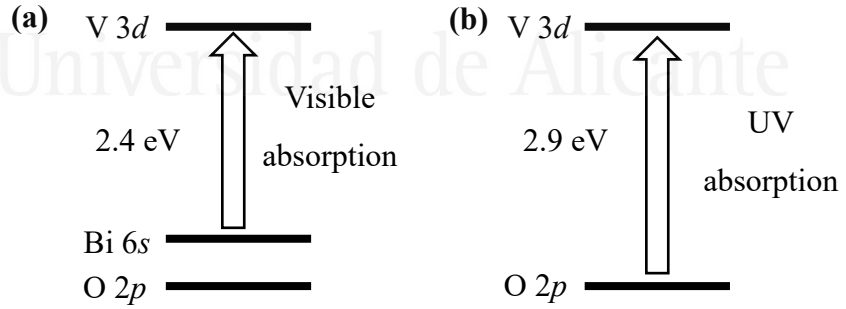

Figure 1.31. Schematic band structures for the (a) tetragonal monoclinic scheelite $BiVO_4$ and (b) zircon-type $BiVO_4$.

Another advantageous feature of $BiVO_4$ for its use as photoanode is that its valence band edge is located at approximately 2.4 V (*vs*. RHE), providing enough overpotential for photogenerated holes to oxidize water, while the conduction band edge is located just

close to the level of the H_2O/H_2 redox pair (0.05 V *vs*. RHE) [105]. Although its band gap is slightly wider than desired for a photoelectrode, the very negative conduction band edge potential compensates for this disadvantage, as not many *n*-type semiconductors absorbing visible light have a conduction band edge potential that is as negative as that of $BiVO_4$ [27,106]. In addition, DFT calculations reveal that the effective masses of electrons and holes in $BiVO_4$ should be much smaller than those of other oxide materials such as TiO_2 [107,108] and In_2O_3 [109–111]. In this regard, predicted effective masses of photogenerated electrons and holes are on the order of $0.9m_0$ and $0.7m_0$, respectively, where m_0 stands for the electron rest mass [112]. This would facilitate the separation and transport processes of photoexcited charge carriers, which would finally translate into relatively long diffusion lengths for electrons and holes. All these facts allow this compound to have a theoretical solar-to-hydrogen (STH) conversion efficiency close to 9.2% [113].

On the other hand, the much less studied iron vanadate ($FeVO_4$) presents even a lower bandgap (for the triclinic structure, the band gap value is close to 2.06 eV), which facilitates the absorption of around 45% of the incident solar energy [95]. Despite $FeVO_4$ is supposed to show a very similar photocatalytic and photoelectrocatalytic activity to that of $BiVO_4$ due to the similarity of structure and electronic properties, $FeVO_4$ presents the added advantage that Fe is much more abundant and environmental- and health-friendly than Bi.

Nevertheless, the typical STH conversion efficiencies of unmodified $BiVO_4$ and $FeVO_4$ photoanodes are disappointingly low (lower than 1%) as they suffer from excessive electron–hole recombination and poor photogenerated carrier transport properties [114]. The poor water oxidation kinetics, due to the high kinetic barrier for water oxidation reaction together with the extremely poor catalytic properties of both

materials, is another important limitation for the use and applicability of these vanadates in photoelectrochemical devices [93].

1.7.2. Perovskite (ABO_3) family: lanthanum iron oxide ($LaFeO_3$)

Lanthanum iron oxide ($LaFeO_3$) has become the most studied perovskite for photoelectrochemical applications in very recent years since it has several attractive features for its use as photoelectrode. This material shows an orthorombic perovskite-type structure (Figure. 1.32) [88], in which it is important to highlight the important difference in ionic radii between La^{3+} (117.2 pm) and Fe^{3+} (78.5 pm).

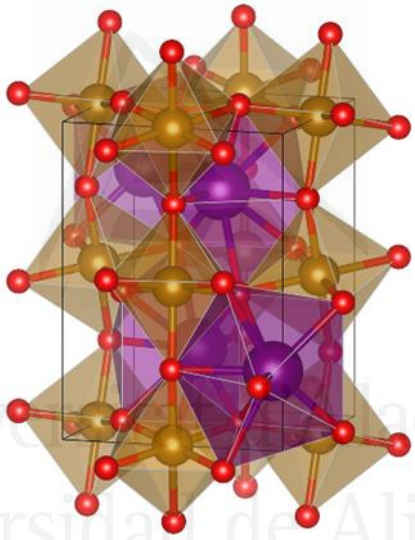

Figure 1.32. Crystal structure of an orthorhombic $LaFeO_3$ (red: O, purple: La, and gray: Fe).

$LaFeO_3$ band gap energy is reported to be around 2.1 eV, which allows for the utilization of a large portion of the visible solar spectrum [115–117]. At the same time, its conduction band and valence band positions seem to be suitable for both water reduction and oxidation, respectively [86,88]. This, together with the fact that the electrical properties of this material seem to critically depend on the synthesis procedure

(including the electrode architecture and the presence of impurities [86,118]), is the reason why this material has been characterized both as photocathode (more frequently) and as photoanode. As a photoanode, *n*-type $LaFeO_3$ prepared by a sol-gel method delivers photocurrent densities up to 8.2 $mA \cdot cm^{-2}$ at 1.7 V (*vs*. Ag/AgCl) [119]. Doping with different transition metals (such as Cu, Co and Mn) has been employed as an effective approach to alter the electrical and optical properties of $LaFeO_3$, resulting in a substantially improved photoelectrochemical water oxidation performance under visible light ($\lambda > 420$ nm) [120]. Finally, surface modification with Co-P_i down-shifts the onset potential of anodic photocurrents by around 560 mV for anodic photocurrent due to the suppression of photogenerated electron–hole recombination after the Co-P_i coating and also increases the photocurrent magnitude by four times [121,122].

1.8. TERNARY OXIDES AS PHOTOCATHODES

Regarding ternary semiconductor oxides acting as photocathodes, it is worth noting that the number of reports on this topic is much scarcer than that dealing with photoanodes mainly because, generally, *p*-type semiconductor metal oxides present limited corrosion resistance and low carrier mobility. In fact, the limited number of useful metal oxides in (photo)electrochemistry makes difficult finding a semiconductor material with adequate properties as a photocathode [123,124]. In the last years, some works devoted to ternary oxides based on earth-abundant components have shed more light on this field, and some of them have been identified as good candidates as photocathodes in water splitting applications. These include some spinels (with the general formula AB_2O_4, such as $CaFe_2O_4$ [125–128], $CuBi_2O_4$ [129–132] and $ZnRh_2O_4$ [133]), delafossites (with an ABO_2 stoichiometry, as it is the case of $CuFeO_2$ [134–136], $CuCrO_2$ [137] and $CuRhO_2$ [138]), perovskites (ABO_3, mainly $LuRhO_3$ [139,140], $CuNbO_3$ [141], $LaFeO_3$ [86,88,118,142]

and $YFeO_3$ [143]) and other more complex compounds, such as $Sr_7Fe_{10}O_{22}$ [128]. These candidates are able to absorb visible light and have suitable conduction band edge locations to induce water reduction.

1.8.1. Perovskite (ABO_3) family: neodymium iron oxide ($NdFeO_3$)

Although the first works on perovskite oxides as photocathodes were released in 1980, to the best of our knowledge, Chapters IX and X constitute the first studies in which the neodymium iron oxide ($NdFeO_3$) is characterized as photocathode. So, there is a lack of studies dealing with the characterization of this material at a photoelectrochemical level. In any case, it is expected to show a very similar behavior as $LaFeO_3$ due to the expected similarities in composition and structure. For the latter material acting as photocathode, the low mobility of the holes and the competition of oxygen evolution reaction with hole collection have been found to be limiting factors for obtaining a high efficiency for hydrogen evolution [86,88,118]. This results in very limited negative photocurrent densities toward the hydrogen evolution reaction appearing at 1.1 V *vs*. RHE [86]. To intensify its *p*-type character, doping with metals with an accessible +2 oxidation state and radii similar to that of Fe^{3+} (such as Mg^{2+} and Zn^{2+} [86]) has been revealed as an effective strategy with applications in photoelectrochemistry [81,139] and photocatalysis [145].

1.9. IMPROVEMENT OF PHOTOELECTRODE PERFORMANCE

Among the most usual strategies aimed to improve the charge transport efficiency in the bulk and the transfer along the semiconductor-electrolyte interface, impurity doping procedures and the surface modification with co-catalysts (for the oxygen or hydrogen

evolution reaction) stand out due to their importance. In the following, a brief discuss about these two strategies is given.

1.9.1. Doping procedures

Impurity doping can be presented as the most common method for the modification of the properties of a semiconductor. By introducing dopant atoms into a semiconductor (which offers a so-called host lattice, see Figure 1.4), certain properties such as charge carrier density and electrical conductivity can be significantly improved. In fact, the main objective of doping (either *n* or *p*) is to increase the concentration of one of the charge carriers (electrons or holes, respectively). Considering that the electrical conductivity of an intrinsic semiconductor is defined as the sum of the conductivities of electron and holes, a proper doping procedure results in a better electrical conductivity since the mobility of electrons and holes is improved [146–152].

In this case of $BiVO_4$, doping strategies have been employed in an attempt to overcome its relatively slow electron transport. In fact, the incorporation into $BiVO_4$ of donor-type dopants such as Ag [92], Cr [114], W [153,154], Mo [155,156], Si [157], Ti [158], Nb [158], Zn [158], Sn [158] or Pd [159], and certain lanthanide such as Eu [160] and Dy [161] has been found to enhance the photoelectrochemical performance of the semiconductor, strengthening its *n*-type characteristics by supplying additional conduction band free electrons and thus enhancing electric conductivity. Doping also has been found to improve carrier separation by creating a space charge region in the solid part of the semiconductor-electrolyte interface. Nevertheless, the slow charge transfer to solution likely remains the performance bottleneck, mainly for driving complex reactions such as water oxidation [93]. The doping of $FeVO_4$ photoanodes in order to improve its photoelectrochemical properties is not as explored as in the case of $BiVO_4$, In fact, only

successful results for this type of application are reported after doping with W [95]. Nevertheless, the incorporation of Er [162], Ag [163], Al [164], Cs, Rb or K [165] as dopants in the $FeVO_4$ structure contributed to significantly improve the photocatalytic activity of this material in dye degradation processes.

Finally, doping has also been revealed as an effective strategy to improve the photoelectrochemical properties of $LaFeO_3$.On the one hand, and already introduced in section 1.6.2, the introduction of different transition metals (such as Cu, Co and Mn [120]) in a suitable concentration has been employed as an effective approach to modify the electrical and optical properties of $LaFeO_3$. This resulted in a substantially improved photoelectrochemical water oxidation performance under visible light, delivering photocurrent values around three-times higher than those obtained with intrinsic $LaFeO_3$ photoanodes. On the other hand, the $LaFeO_3$ efficiency as photocathode for oxygen reduction has been improved drastically by doping with relatively large amounts of Mg^{2+} and Zn^{2+} (5% with respect to Fe atoms [86]). This effect was primarily attributed to an increase in the majority carrier concentration resulting from a dopant-induced increase of the Fe^{4+} density caused by charge compensation upon the substitution of Fe^{3+} by Mg^{2+} and Zn^{2+}. Despite this, it is also important to consider the distortions induced by the introduction of the dopants, likely increase hole mobility, and a possible contribution from Zn- or Mg-induced photocathode surface passivation [86].

1.9.2. Co-catalysis on the photoelectrode surface

Incorporating a co-catalyst on the semiconductor absorber surface is an almost indispensable step at the time of achieving highly efficient photoelectrodes. Even if the photogenerated electrons or holes present appropriate potentials for driving the water splitting reactions, they may recombine if a reduced number of reaction sites exists on the

surface of the semiconductor. Thus, a surface-loaded co-catalyst is usually needed to facilitate the transfer of either electrons or holes across the semiconductor-electrolyte interface since it reduces the energy barrier for the reaction. Figure 1.33 schematically displays the contact between a co-catalyst loaded at the interface between a semiconductor photoelectrode and the electrolyte. In equilibrium, the Fermi levels of the semiconductor (ε_F), the co-catalyst ($\varepsilon_{F,CC}$) and the redox pair in the electrolyte ($\varepsilon_{F,redox}$) have the same value. Under illumination, the photogenerated holes or electrons (considering an *n*-type or a *p*-type semiconductor, respectively) are transferred to the co-catalyst and, after that, to the electrolyte. In this situation, it is assumed that the *pseudo*-Fermi level of photogenerated charges in the semiconductor is equilibrated with the co-catalyst Fermi level.

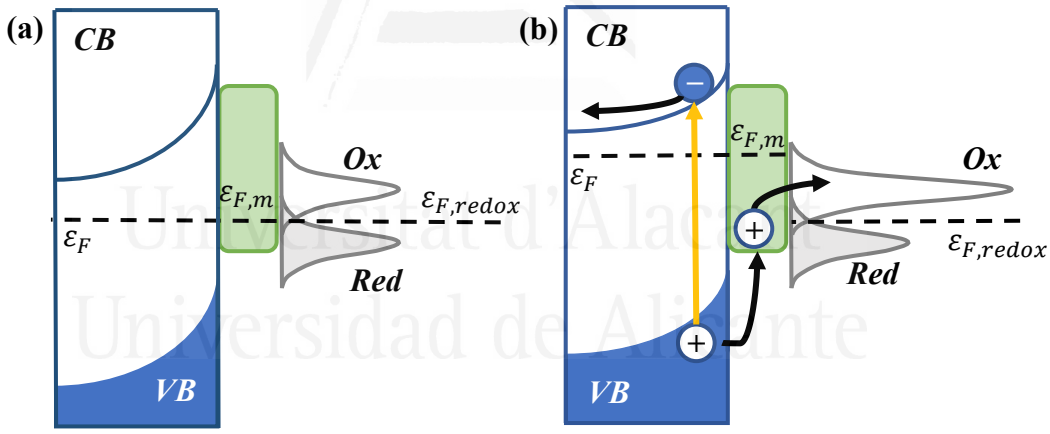

Figure 1.33. Band energy diagram in an *n*-type semiconductor material surface modified with a co-catalyst at (a) equilibrium and (b) under illumination.

From a practical point of view, the introduction of a co-catalyst on the surface of a photoelectrode implies a decrease in the reaction kinetic barrier and a promotion of charge injection to the reactants [166–169], which is finally manifested through an increase in the photocurrent and/or photopotential associated to the co-catalyzed reaction [170–172]. In this context, it is important to remark that a functional coupling of electrocatalysts with

photoelectrodes must fulfill certain requirements, as that the co-catalyst does not block sunlight from reaching the light absorber, interfere in the transfer of photogenerated charge carriers or diminish the photoelectrode surface catalytic efficiency.

1.9.2.1. Iron-group (oxy)hydroxides

Among all the electrocatalysts used as oxygen evolution co-catalysts (OECs) on the surface of photoanodes, the interest in the iron-group (oxy)hydroxides ($Fe(OH)_2$, $Co(OH)_2$, and $Ni(OH)_2$) has grown very significantly in recent years. This is due to the fact that they are especially active at the time of favoring the separation of photogenerated electrons and holes and reducing the kinetic barrier for photoelectrochemical water oxidation reaction on photoanodes surface under alkaline conditions [173].

In fact, the oxygen evolution reaction (OER), which is characterized by its slow kinetics (*i.e.*, large anodic overpotential) remains as a critical step in this process and represents a significant efficiency loss in both electricity-driven and photodriven water splitting [69,174–177]. This fact prevents the straightforward development of certain clean energy technologies, including rechargeable metal-air batteries, water electrolysis systems, and solar-fuel devices.

Since the earliest works on OER electrocatalysis were reviewed by Trasatti [178,179] and Matsumoto [180] over thirty years ago, considerable research effort has been devoted to the design, synthesis, and characterization of efficient oxygen evolution catalysts. Currently, the optimal OECs in acidic media are noble metal-based catalysts, such as IrO_2 and RuO_2, since these oxides exhibit the lowest overpotentials for the OER at practical current densities [181–184]. However, the scarcity of the corresponding metals, high cost, and poor long-term stability in alkaline media have hindered large-scale

applications and highlighted the need for OECs with prospects of being employed at a practical level.

In this context, several studies reveal that first-row transition metal oxides and (oxy)hydroxides (Mn [185–187], Fe [188–190], Co [191–193], and Ni[194–196]), along with certain spinel [197–199] and perovskite oxides [200–202], could offer a compromise solution: although they possess inferior electrocatalytic activity for OER, their environmental friendliness, low cost, and abundance in nature convert them into practical candidates for electrocatalytic OER [203–205]. In addition, they are stable in neutral to alkaline solutions and display moderate to good electrical conductivities. Nevertheless, due to the existence of polymorphs, incidental impurity incorporation, and complicating effects of electronic conductivity and electrochemically active surface area, the fundamental correlations of activity to structure, composition, and amount of electrocatalyst are not quantitatively described.

In any case, iron-group metal hydroxides ($Fe(OH)_2$, $Co(OH)_2$ and $Ni(OH)_2$) with a layered structure have been suggested to be active, stable, and inexpensive electrocatalysts for OER. The catalytic properties of the $NiOOH/Ni(OH)_2$ system have been rationalized on the basis of the four phases described in the Bode diagram [206,207], and primarily ascribed to the low degree of occupancy of the *d* orbitals in the oxidized forms [195,208]. In fact, the OER-active phase of nickel catalysts contains a mixture of Ni^{3+} and Ni^{4+} in a NiOOH-type structure [209–211]. At potentials well below the onset for the OER, the catalyst is present as $Ni(OH)_2$, while, prior to the onset of oxygen evolution, this phase is oxidized to NiOOH according to $Ni(OH)_2 + OH^- \rightarrow NiOOH + H_2O + e^-$ [209,212]. Analogously, cobalt hydroxide ($Co(OH)_2$) crystallize in two polymorphs (α- and β-$Co(OH)_2$), which can be oxidized to γ- and β-CoOOH, respectively [213]. Although both hydroxides have been found able to catalyze OER effectively

[191,214], recent studies indicate that α-$Co(OH)_2$ shows better activity towards OER than β-$Co(OH)_2$, regardless of the particle size or surface area [215]. This has motivated the search for synthesis methods able to stabilize the alpha form of the material for its application as OEC. On the other hand, due to the Fe high abundance and non-toxicity, $Fe(OH)_2$-based OECs are also appealing [216], although they have been considered to have poor OER activity due to the intrinsic low electronic conductivity and relative instability of its oxidized form (γ-FeOOH) [217]. Despite this, the interest in its study as an OEC lies in the fact that the incorporation of Fe impurities into $Ni(OH)_2$-[218,219] and $Co(OH)_2$-based [220] OECs has been found to be responsible for an enhancement of their electrocatalytic performance. These observations have promoted the development of double hydroxide systems (such as Ni-Fe [207,221,222], Ni-Co [223,224], and Co-Fe [220]), facilitated by the capacity of iron-group transition metals of presenting different oxidation states and coordination environments. Interestingly, they have indeed exhibited enhanced OER activity compared to monometallic hydroxide systems. When these mixed hydroxides have a layer morphology, they are commonly called layered double hydroxides (LDH).

In this context, studies on different ways to increase the OER activity of the $NiOOH/Ni(OH)_2$ system have clearly revealed that Fe incorporation into the $Ni(OH)_2$ structure enhances its performance [225–229]. Corrigan and co-workers [230–232] first investigated the catalytic activity of these systems in the late 1980s and hypothesized that one of the factors inducing this improvement was an increase of the electrical conductivity of NiOOH caused by Fe impurities. The electrochemical characterization of these electrodes showed a positive shift of the Ni redox waves as the iron content increases, which suggests changes in the NiOOH electronic structure [221,230,233,234]. More recently, Trotochaud and co-workers have also concluded that intentional or incidental

incorporation of iron impurities from alkaline electrolytes into NiOOH/$Ni(OH)_2$ thin films promotes a significant decrease in the oxygen overpotential [218]. This effect was ascribed to a significant increase in conductivity and, more importantly, to an activation of the nickel catalytic centers through partial electron transfer to the incorporated iron [218,235].

Recent studies on the addition of Fe to Co (oxy)hydroxides have also revealed a beneficial effect on the OER activity [220,236,237], although it is not so well documented. All these observations have stimulated attempts to optimize the electrocatalytic response of electrodes based on Ni-Fe and Co-Fe hydroxides. To date, for Ni-Fe (oxy)hydroxide films, the optimum OER activity has been achieved with iron contents between 17 and 25% [235], while for Co-Fe (oxy)hydroxides, the incorporation of Fe at levels between 40 and 60% increases the intrinsic activity of the CoOOH phase by two orders of magnitude [220].

As already stated, the surface modification of photoanodes with iron-group (oxy)hydroxides has significantly promoted their activity toward the oxygen evolution reaction under illumination. In this regard, the deposition of controlled amounts of $Ni(OH)_2$ on $BiVO_4$ and $FeVO_4$ photoanodes was demonstrated to be successfully catalyze the photoelectrochemical water oxidation process by improving the effective transfer of photogenerated holes from both semiconductors to solution. For optimum $Ni(OH)_2$ loadings, photocurrent enhancements by factors of 2 and 1.2 for $BiVO_4$ and $FeVO_4$ photoanodes, respectively, are observed [238]. On the other hand, the modification of $BiVO_4$ photoanodes with layered-double NiFe- and CoFe-(oxy)hydroxides on $BiVO_4$ photoanodes triggers an about 4-fold photocurrent enhancement at 1.23 V (*vs.* RHE) and remarkable negative shift (320 mV) of the onset potential for the oxygen evolution reaction [239]. In this regard, more systematic studies revealed that, as expected, the

stability and the photocurrent response of $BiVO_4$/NiFe-LDHs photoanodes at 1.23 V *vs* RHE is higher than those of $BiVO_4/Ni(OH)_2$, $BiVO_4/Fe(OH)_2$ and unmodified $BiVO_4$ photoanodes under visible-light illumination [240]. This has been ascribed to a reduced interface recombination at the $BiVO_4$/OEC junction and to a creation of a more favorable Helmholtz layer potential drop at this junction [241].

1.9.2.2. Metal particles

Transition metals, especially noble metals, are traditionally used as effective co-catalysts for hydrogen evolution since they act not only as electron sinks, but also provide effective proton reduction sites. So, they are mainly used as co-catalysts for the hydrogen evolution reaction on photocathodes surface.

Among transition metals, platinum still stands out as the classical choice due to its unbeatable electrocatalytic activity toward the hydrogen evolution reaction. In fact, and to the best of our knowledge, this metal is the only co-catalyst employed for ternary oxide semiconductors to date. It has been demonstrated to act as an effective co-catalyst with the most often studied *p*-type materials, such as Cu_2O [242–244] and Si [245,246]. In the context of ternary oxides, it has been electrochemically deposited on the surface of $CaFe_2O_4$ and $Sr_7Fe_{10}O_{22}$. On both semiconductors, it was able to significantly improve photocurrent values through a decrease of the kinetical requirements for the hydrogen evolution and an inhibition of surface recombination [128]. Pt was also tested as co-catalyst on the surface of $CuBi_2O_4$ photocathodes [132,247,248], increasing IPCE values from around 3% (for the bare material) to 20%, and on $CuFeO_2$ previously covered with an Al-doped ZnO (AZO) overlayer [135].

The fact that Pt has been the only co-catalyst employed for ternary oxides can be explained considering that these studies are eminently fundamental in nature, and they

are still relatively far from practical applications. The low Pt abundance on the Earth's crust and its high price (around 18000 €/Kg) clearly restricts its use for scaling up practical devices for water splitting.

Nickel (both in metal and NiO form) has been identified as an effective low-cost co-catalyst at photocathodes for hydrogen generation. Although there are no clear precedents in the case of ternary oxide photoelectrodes, its effectiveness has been tested in the case of *p*-Cu_2O electrodes. A simple photodeposition method of Ni nanoparticles on Cu_2O resulted in increased photocurrents in a photoelectrochemical system working without the application of a bias, but in the presence of a sacrificial hole acceptor [249]. In the same line, a nanocomposite based on Cu_2O/NiO_x showed an improved catalysis and photostability compared to bare Cu_2O [250], while ABPE factors of around 2.7% have been reached with a Ni-decorated Cu_2O/CuO photocathode [251]. In the context of Ni-based co-catalysts, Ni-Mo deposits have also been identified as a competitive and inexpensive alternative to noble metals, with an energy conversion efficiency quite similar to Ni co-catalysts [246,252]. Photocurrents as large as -6.3 $mA \cdot cm^{-2}$ at 0 V (*vs.* RHE) have been achieved using a Cu_2O photocathode surface modified with a Ni-Mo co-catalyst [253].

It is important to highlight that, when it comes to performing surface modification of photocathodes with a co-catalyst, it is generally necessary to introduce an extracting or passivating layer at the interface. This implies the coating of the photocathode with relatively thin additional layers (frequently, between 1 and 2 nm) that increase its photoelectrochemical performance by favoring the charge transfer across the semiconductor-electrolyte interface (extracting layer) or simply by suppressing other competitive processes consuming photogenerated carriers (passivating layer) in surface states [254]. These processes can be the (photo)corrosion of the material or deleterious

recombination phenomena of photogenerated electrons and holes at the surface. In many occasions, it is difficult to differentiate between a purely extracting effect and a purely passivating layer, so the outcome can be usually described as a combination of both.

Although to the best of our knowledge this approach has not yet been described for ternary oxides, it has been extensively tested with binary semiconductor oxides acting as photoanodes, especially hematite. Regarding *p*-type materials, only a few studies have been published related to passivation effects motivated by very thin coating layers. The main materials used for this goal have been Al_2O_3 [255,256] and TiO_2 [257,258] on semiconductor electrodes such as Si and InP. In most cases, the observed effect was a decrease in the overpotential for the photoelectrochemical hydrogen evolution reaction, which is evinced by a shift of the photocurrent onset toward more positive potentials compared to the bare semiconductor material. This is usually ascribed to the passivation of surface trapping centers, but addition effects derived from the junction between the absorber semiconductor and the coating (especially depending on the coated film thickness) cannot be discarded [259].

1.10. REFERENCES

[1] N.S. Lewis, D.G. Nocera, Proc. Natl. Acad. Sci. 2. 103 (2006) 15729.
[2] R. van de Krol, M. Grätzel, Photoelectrochemical Hydrogen Production, Springer, New York, 2012.
[3] Trends in Atmospheric Carbon Dioxide. Earh System Research Laboratory-U.S. Departament of Comerce and National Oceanic & Atmospheric Administration. Found under https://www.esrl.noaa.gov/gmd/ccgg/trends/.
[4] J. Oppenheim, E.D. Beinhocker, Climate change and the economy-myths versus reality, McKinsey & Company, Inc., Davos, Switzerland, 2009.
[5] J. Barber, Chem. Soc. Rev. 38 (2009) 185.
[6] R.E.N.21 Members, Renewables 2019. Global Status Report (2019), can be found under https://www.ren21.net/reports/global-status-report/.
[7] S. Pacala, R. Socolow, Science. 305 (2007) 968.
[8] M.I. Hoffert, Science. 329 (2010) 1292.
[9] D.G. Nocera, M.P. Nash, Proc. Natl. Acad. Sci. 103 (2006) 15729.
[10] H. Ritchie, M. Roser, Renewable Energy-Global energy renewable energy consumption, OurWorldInData.Org (2020), can be found under

https://ourworldindata.org/renewable-energy.
[11] V. Smil, Energy Transitions: Global and National Perspectives, Colorado P, Santa Bárbara (California), 2016.
[12] C. Jiang, S.J.A. Moniz, A. Wang, T. Zhang, J. Tang, Chem. Soc. 2Rev. 46 (2017) 4645.
[13] P.P. Edwards, V.L. Kuznestsov, W.I.F. David, N.P. Brandon, Energy Policy. 36 (2008) 4645.
[14] K. Rajeshwar, R. McConnell, S. Licht, Solar Hydrogen Generation - Toward a Renewable Energy Future, Springer, New York, 2008.
[15] C.A. Grimes, O.K. Varghese, S. Ranjan, Light, Water, Hydrogen - The Solar Generation of Hydrogen by Water Photoelectrolysis, Springer, New York, 2008.
[16] D. Stolten, Hydrogen and Fuel Cells: Fundamentals, Technologies and Applications, Wiley, Weinheim, 2010.
[17] A. de Vos, J. Phys. D Appl. Phys. 13 (1980) 839.
[18] J. Jia, L.C. Seitz, J.D. Benck, Y. Huo, Y. Chen, J.W.D. Ng, T. Bilir, J.S. Harris, T.F. Jaramillo, Nat. Commun. 7 (2016) 13237.
[19] O. Khaselev, J.A. Turner, Science. 280 (1998) 425.
[20] K. Zhang, M. Ma, P. Li, D.H. Wang, J.H. Park, Adv. Energy Mater. 6 (2018) 160002.
[21] Y.V. Pleskov, Y.Y. Gurevich, Semiconductor Photoelectrochemistry, Consultants Bureau, New York, 1986.
[22] R. Memming, Semiconductor Electrochemistry, Wiley–VCH, Weinheim, 2001.
[23] N. Sato, Electrochemistry at Metal and Semiconductor Electrodes, Elsevier B.V, Amsterdam, 1998.
[24] J.-P. Colinge, Physics of Semiconductor Devices, New York, 2006.
[25] J. Koryta, W. Dvorak, J. Wiley, Principles of Electrochemistry, Chichester, 1993.
[26] W. Schmickler, Interfacial Electrochemistry, Oxford University Press, New York, 1996.
[27] M.G. Walter, E.L. Warren, J.R. McKone, S.W. Boettcher, Q. Mi, E.A. Santoni, N.S. Lewis, Chem. Rev. 110 (2010) 6446.
[28] K. Rajeshwar, Fundamentals of Semiconductor Electrochemistry and Photoelectrochemistry, in: S. Licht (Ed.), Encycl. Electrochem. Vol. 6, Wiley–VCH, Weinheim, 2002: pp. 1–551.
[29] A.J. Bard, A.B. Bocarsly, F.R.F. Fan, E.G. Walton, M.S. Wrighton, J. Am. Chem. Soc. 102 (1980) 3671.
[30] J.G. Velasco, Fotoelectroquímica de semiconductores. Su aplicación a la conversión y almacenamiento de energía solar, Reverté, Madrid, 2010.
[31] J.A. Butler, Trans. Faraday Soc. 19 (1924) 729.
[32] T. Erdey-Gruz, M. Volmer, Z. Phys. Chem. 150 (1930) 203.
[33] J. Tafel, Z. Phys. Chem.1. 50 (1905) 641.
[34] N.W. Ashcroft, N.D. Mermin, Solid State Physics, Hartcourt College, Orlando, 1976.
[35] T. Faunce, S. Styring, R.M. Wasielewski, G.W. Brudvig, A.W. Rutherford, J. Messinger, A.F. Lee, C.L. Hill, H. Degroot, M. Fontecave, D.R. MacFarlane, B. Hankamer, D.G. Nocera, D.M. Tiede, H. Dau, W. Hillier, L. Wang, R. Amal, Energy Environ. Sci. 6 (2013) 1074.
[36] R.C. Alkire, D.M. Kolb, Advances in Electrochemical Science and Engineering, Wiley–VCH, Weinheim, 1999.
[37] S. Giménez, J. Bisquert, Photoelectrochemical Solar Fuel Production: from Basic Principles to Advanced Devices, Springer, New York, 2016.

[38] L.M. Peter, Photoelectrochemistry: from Basic Principles to Photocatalysis, in: Photocatal. Fundam. Perspect., Royal Society of Chemistry, Cambridge, 2016: pp. 3–28.
[39] W. Gärtner, Phys. Rev. 116 (1959) 84.
[40] L.M. Peter, Chem. Rev. 90 (1990) 753.
[41] A. Hagfeldt, G. Boschloo, L. Sun, L. Kloo, H. Petterson, Chem. Rev. 110 (2010) 6595.
[42] M. Grätzel, J. Photochem. Photobiol. C Photochem. Rev. 4 (2003) 145.
[43] P.V. Kamat, J. Phys. Chem. C. 112 (2008) 18737.
[44] A.J. Nozik, Phys. E Low-Dimensional Syst. Nanostructures. 14 (2002) 115.
[45] J.J. Kelly, D. Vanmaekelbergh, Electrochim. Acta. 43 (1998) 2773.
[46] D. Vanmaekelbergh, P.E. de Jongh, J. Phys. Chem. B1. 103 (1999) 747.
[47] A. Hagfeldt, M. Grätzel, Chem. Rev. 95 (1995) 49.
[48] A. Hagfeldt, H. Lindström, S. Södergren, S.-E. Lindquist, J. Electroanal. Chem. 381 (1995) 39.
[49] S. Södergren, A. Hagfeldt, J. Olsson, S.-E. Lindquist, J. Phys. Chem. 98 (1994) 5552.
[50] H.J. Lewerenz, L. Peter, Photoelectrochemical Water Splitting. Materials, Processes and Architectures, The Royal Society of Chemistry, Cambridge, 2013.
[51] Z. Chen, H. Dinh, E. Miller, Photoelectrochemical Water Splitting. Standards, Experimental Methods, and Protocols, Springer, New York, 2013.
[52] K. Sivula, R. Van De Krol, Nat. Rev. Mater. 1 (2016) 15010.
[53] C. Ding, W. Qin, N. Wang, G. Liu, Z. Wang, P. Yan, J. Shi, C. Li, Phys. Chem. Chem. Phys. 16 (2014) 15608.
[54] R. van de Krol, Y. Liang, J. Schoonman, J. Mater. Chem. 18 (2008) 2311.
[55] J.R. Bolton, S.J. Stickler, J.S. Connolly, Nature. 316 (1985) 495.
[56] M.F. Weber, M.J. Dignam, Int. J. Hydrog. Energy. 11 (1986) 225.
[57] M.F. Weber, M.J. Dignam, J. Electrochem. Soc. 131 (1984) 1258.
[58] A.B. Murphy, P.R.F. Barnes, L.K. Randeniya, I.C. Plumb, I.E. Grey, M.D. Horne, J.A. Glasscock, Int. J. Hydrogen Energy. 31 (2006) 1999.
[59] M. Sing, G. Berner, K. Goss, A. Müller, A. Ruff, A. Wetscherek, S: Thiel, J. Mannhart, S.A. Pauli, C.W. Schneider, P.R. Willmott, M. Gorgoi, F. Schäfers, R. Claessen, Phys. Rev. Lett. 102 (2009) 176805.
[60] T.H. Jeon, G.H. Moon, H. Park, W. Choi, Nano Energy. 39 (2017) 211.
[61] R. Marschall, Adv. Funct. Mater. 24 (2014) 2421.
[62] J. Jamali, A. Moshaii, Appl. Surf. Sci. 419 (2017) 269.
[63] J. Luo, L. Steier, M.K. Son, M. Schreier, M.T. Mayer, M. Grätzel, Nano Lett. 16 (2016) 1848.
[64] U. Gupta, C.N.R. Rao, Nano Energy. 41 (2017) 49.
[65] J. Qiu, H. Hajibabaei, M.R. Nellist, F.A.L. Laskowski, S.Z. Oener, T.W. Hamann, S.W. Boettcher, ACS Energy Lett. 3 (2018) 961.
[66] M.R. Nellist, F.A.L. Laskowski, F. Lin, T.J. Mills, S.W. Boettcher, Acc. Chem. Res. 49 (2016) 733.
[67] X. Xu, L. Pan, X. Zhang, L. Wang, J.-J. Zou, Adv. Sci. 6 (2018) 1801505.
[68] T. Bak, J. Nowotny, M. Rekas, C.C. Sorrell, Int. J. Hydrogen Energy. 27 (2002) 991.
[69] M.G. Walter, E.L. Warren, J.R. McKone, S.W. Boettcher, Q. Mi, E.A. Santoni, N.S. Lewis, Chem. Rev. 110 (2010) 6446.
[70] F. Han, V.S.R. Kambala, M. Srinivasan, D. Rajarathnam, R. Naidu, Appl. Catal. A. 359 (2009) 25.

[71] T. Berger, D. Monllor-Satoca, M. Jankulovska, T. Lana-Villarreal, R. Gómez, ChemPhysChem. 13 (2012) 2824.
[72] K. Sivula, F.L. Formal, M. Grätzel, ChemSusChem. 4 (2011) 432.
[73] I. Cesar, K. Sivula, A. Kay, R. Zboril, M. Grätzel, J. Phys. Chem. C. 113 (2009) 772.
[74] I. Cesar, A. Kay, J.A.G. Martinez, M. Grätzel, J. Am. Chem. Soc. 128 (2006) 4582.
[75] C. Santato, M. Odziemkowski, M. Ulmann, J. Augustynski, J. Am. Chem. Soc. 123 (2001) 10639.
[76] J.A. Seabold, K.-S. Choi, Chem. Mater. 23 (2011) 1105.
[77] M.N. Huda, Y.F. Yan, A. Walsh, S.-H. Wei, J.A. Turner, M.M. Al-Jassim, Proceedings Volume 7770, Solar Hydrogen and Nanotechnology V; 77700F (2010).
[78] B. Parkinson, Y. Liang, C. Jiang, J. He, Combinatorial methods for the Improvement of Semiconductor Metal Oxide Photoelectrodes, in: Annu. Merit Rev. Meet., 2011.
[79] T. Watanabe, A. Fujishima, K. Honda, Bull. Chem. Soc. Jpn. 98 (1976) 2774.
[80] M.S. Wrighton, A.B. Ellis, P.T. Wolczanski, D.L. Morse, H.B. Abrahamson, D.S. Ginley, J. Am. Chem. Soc. 98 (1976) 2774.
[81] H.G. Kim, O.S. Becker, J.S. Jang, S.M. Ji, P.H. Borse, J.S. Lee, J. Solid State Chem. 179 (2006) 1214.
[82] J.H. Kennedy, J. K. W. Frese, J. Electrochem. Soc. 123 (1976) 1683.
[83] H. Kato, A. Kudo, J. Phys. Chem. B. 105 (2001) 4285.
[84] H. Kato, A. Kudo, Chem. Phys. Lett. 295 (1998) 487.
[85] H. Kato, A. Kudo, Catal. Letters. 58 (1999) 153.
[86] M.I. Díez-García, R. Gómez, ChemSusChem. 10 (2017) 2457.
[87] Q. Zhang, Y. Huang, S. Peng, Y. Zhang, Z. Shen, J.-J. Cao, W. Ho, S.C. Lee, D.Y.H. Pui, Appl. Catal. B Environ. 204 (2017) 346.
[88] G.P. Wheeler, K.S. Choi, ACS Energy Lett. 2 (2017) 2378.
[89] J. Ye, Z. Zou, M. Oshikiri, A. Matsushita, Chem. Phys. Lett. 356 (2002) 221.
[90] C.S. Enache, D. Lloyd, M.R. Damen, J. Schoonman, R. Van De Krol, J. Phys. Chem. C. 113 (2009) 19351.
[91] A. Kudo, K. Ueda, H. Kato, I. Mikami, Catal. Letters. 53 (1998) 229.
[92] K. Sayama, A. Nomura, T. Arai, T. Sugita, R. Abe, T. Oi, Y. Iwasaki, Y. Abe, H. Sugihara, J. Phys. Chem. B. 3 (2006) 11352.
[93] Y. Park, K.J. McDonald, K.-S. Choi, Chem. Soc. Rev. (2013) 2321.
[94] C.D. Morton, I.J. Slipper, M.J.K. Thomas, B.D. Alexander, J. Photochem. Photobiol. A Chem. 216 (2010) 209.
[95] S.K. Biswas, J.O. Baeg, Int. J. Hydrogen Energy. 38 (2013) 14451.
[96] J. Yourey, K. Pyper, B.M. Bartlett, J. Phys. Chem. C 117 (2013) 24726.
[97] F.E. Osterloh, Chem. Mater. 20 (2008) 35.
[98] J.D. Bierlein, A.W. Sleightv, Solid State Commun. 16 (1975) 69.
[99] R.S. Roth, J.L. Waring, Am. Miner. 48 (1963) 1348.
[100] A.W. Sleight, H.-Y. Chen, A. Ferretti, D.E. Cox, Mater. Res. Bull. 14 (1979) 1571.
[101] A. Kudo, K. Omori, H. Kato, J. Am. Chem. Soc. 121 (1999) 11459.
[102] A.K. Bhattacharya, K.K. Mallick, A. Hartridge, Mater. Lett. 30 (1997) 7.
[103] R.S. Roth, J.L. Waring, Am. Miner. 48 (1963) 1348.
[104] S. Tokunaga, H. Kato, A. Kudo, Chem. Mater. 13 (2001) 4624.
[105] B. Xie, H. Zhang, P. Cai, R. Qiu, Y. Xiong, Chemosphere. 63 (2006) 956.
[106] T. Bak, J. Nowotny, M. Rekas, C. Sorrell, Int. J. Hydrog. Energy. 27 (2002) 991.
[107] H.P.R. Frederikse, J. Appl. Phys. 32 (1961) 2211.

[108] J. Pascual, J. Camassel, H. Mathieu, Phys. Rev. Lett. 39 (1977) 1490.
[109] A. Walsh, J.L.F.D. Silva, S.-H. Wei, Phys. Rev. B Condens. Matter. 78 (2008) 075211.
[110] A. Walsh, Y. Yan, M.N. Huda, M.M.A.-J. And, S.-H. Wei, Chem. Mater. 21 (2009) 547.
[111] Z. Zhao, Z. Li, Z. Zou, Phys. Chem. Chem. Phys. 13 (2011) 4746.
[112] S.M. Sze, K.K. Ng, Physics of semiconductor device, Wiley, New York, 2007.
[113] J. Quiñonero, T. Lana–Villarreal, R. Gómez, Appl. Catal. B Environ. 194 (2016) 141.
[114] H.W. Jeong, T.H. Jeon, J.S. Jang, W. Choi, H. Park, J. Phys. Chem. C. 117 (2013) 9104.
[115] K.M. Parida, K.H. Reddy, S. Martha, D.P. Das, N. Biswal, Int. J. Hydrogen Energy. 35 (2010) 12161.
[116] J. Ding, X. Lü, H. Shu, J. Xie, H. Zhang, Mater. Sci. Eng. B Solid-State Mater. Adv. Technol. 171 (2010) 31.
[117] S.N. Tijare, M. V. Joshi, P.S. Padole, P.A. Mangrulkar, S.S. Rayalu, N.K. Labhsetwar, Int. J. Hydrogen Energy. 37 (2012) 10451.
[118] V. Celorrio, K. Bradley, O.J. Weber, S.R. Hall, D.J. Fermín, ChemElectroChem. (2014) 1667.
[119] I.M. Nassar, S. Wu, L. Li, X. Li, Chem. Select. 3 (2018) 968.
[120] Q. Peng, B. Shan, Y. Wen, R. Chen, Int. J. Hydrogen Energy. 40 (2015) 15423.
[121] Q. Peng, J. Wang, Y.W. Wen, B. Shan, R. Chen, RSC Adv. 6 (2016) 26192
[122] R.C. Qi Peng, Yanwei Wen, Bin Shan, EECS Tr. 64 (2015) 27.
[123] I. Sullivan, B. Zoellner, P.A. Maggard, Chem. Mater. 28 (2016) 5999–6016.
[124] N.K. Awad, E.A. Ashour, N.K. Allam, J. Renew. Sustain. Energy. 6 (2014) 022702.
[125] J. Cao, T. Kako, P. Li, S. Ouyang, J. Ye, Electrochem. Commun. 13 (2011) 275.
[126] S. Ida, K. Yamada, T. Matsunaga, H. Hagiwara, Y. Matsumoto, T. Ishihara, J. Am. Chem. Soc. 132 (2010) 17343.
[127] Y. Matsumoto, K. Sugiyama, E. Sato, J. Electrochem. Soc. 135 (1988) 98.
[128] Y. Matsumoto, M. Omae, K. Sugiyama, E. Sato, J. Phys. Chem. 91 (1987) 577.
[129] T. Arai, Y. Konishi, Y. Iwasaki, H. Sugihara, K. Sayama, J. Comb. Chem. 9 (2007) 574.
[130] N.T. Hahn, V.C. Holmberg, B.A. Korgel, C.B. Mullins, J. Phys. Chem. C. 116 (2012) 6459.
[131] Y. Nakabayashi, M. Nishikawa, Y. Nosaka, Electrochim. Acta. 125 (2014) 191.
[132] S.P. Berglund, F.F. Abdi, P. Bogdanoff, A. Chemseddine, D. Friedrich, R. van de Krol, Chem. Mater. 28 (2016) 4231.
[133] S. Kamimura, M. Higashi, R. Abe, T. Ohno, J. Mater. Chem. A. 4 (2016) 6116.
[134] M.S. Prévot, X.A. Jeanbourquin, W.S. Bourée, F. Abdi, D. Friedrich, R. van de Krol, N. Guijarro,F. Le Formal, K.. Sivula, Chem. Mater. 29 (2017) 4952.
[135] M.S. Prévot, N. Guijarro, K. Sivula, ChemSusChem. 8 (2015) 1359.
[136] C.G. Read, Y. Park, K.-S. Choi, J. Phys. Chem. Lett. 3 (2012) 1872.
[137] A.K. Díaz-García, T. Lana-Villarreal, R. Gómez, J. Mater. Chem. A. 3 (2015) 19683.
[138] J. Gu, Y. Yan, J.W. Krizan, Q.D. Gibson, Z.M. Detweiler, R.J. Cava, A.B. Bocarsly, J. Am. Chem. Soc. 136 (2014) 830.
[139] H.S. Jarrett, A.W. Sleight, H.H. Kung, J.L. Gillson, J. Appl. Phys. 51 (1980) 3919.
[140] P. Company, Surf. Sci. 101 (1980) 205.
[141] U.A. Joshi, A.M. Palasyuk, P.A. Maggard, J. Phys. Chem. C. 115 (2011) 13534.

[142] Q. Yu, X. Meng, T. Wang, P. Li, L. Liu, K. Chang, G. Liu, J. Ye, Chem. Commun. 51 (2015) 3630.
[143] M.I. Díez-García, V. Celorrio, L. Calvillo, D. Tiwari, R. Gómez, D.J. Fermín, Electrochim. Acta. 246 (2017) 365.
[144] M.I. Díez-García, R. Gómez, ChemSusChem. 10 (2017) 1457.
[145] S. Dong, K. Xu, G. Tian, J. Mater. Sci. 44 (2009) 2548.
[146] B. Zoellner, S.Stuart, C.-C. Chung, D.B. Dougherty, J.L. Jones, P.A. Maggard, J. Mater. Chem. A. 4 (2016) 3115.
[147] X. Chen, C. Burda, J. Am. Chem. Soc. 130 (2008) 5018.
[148] M.S. Prévot, K. Sivula, J. Phys. Chem. C. 117 (2013) 17879.
[149] H. Liu, A. Imanishi, Y. Nakato, J. Phys. Chem. C. 111 (2007) 8603.
[150] K. Iwashina, A. Kudo, J. Am. Chem. Soc. 133 (2011) 13272.
[151] S. Kawasaki, K. Nakatsuji, J. Yoshinobu, F. Komori, R. Takahashi, M. Lippmaa, K. Mase, K. Kudo, Appl. Phys. Lett. 101 (2012) 033910.
[152] K. Sekizawa, T. Nonaka, T. Arai, T. Morikawa, ACS Appl. Mater. Interfaces. 6 (2014) 10696.
[153] M. Li, L. Zhao, L. Guo, Int. J. Hydrogen Energy. 35 (2010) 7127.
[154] R. Saito, Y. Miseki, K. Sayama, Chem. Commun. 48 (2012) 3833.
[155] W. Yao, H. Iwai, J. Ye, Dalton Trans. (2008) 1426.
[156] W. Luo, Z. Yang, Z. Li, J. Zhang, J. Liu, Z. Zhao, Z. Wang, S. Yan, T. Yu, Z. Zou, Energy Environ. Sci. 4 (2011) 4046.
[157] X. Zhang, X. Quan, S. Chen, Y. Zhang, J. Hazard. Mater. 177 (2010) 914.
[158] H. Ye, J. Lee, J.S. Jang, A.J. Bard, J. Phys. Chem. C. 114 (2010) 13322.
[159] G. Lei, , Mater. Lett. 62 (2008) 926.
[160] A. Zhang, J. Zhang, J. Hazard. Mater. 173 (2010) 265.
[161] Q. Wang, H. Liu, J. Li, J. Yuan, W. Shangguan, Catal. Lett. 131 (2009) 160.
[162] M. Casanova, J. Llorca, A. Sagar, K. Schermanz, A. Trovarelli, Catal. Today. 241 (2014) 159.
[163] M. Wang, Q. Liu, Adv. Mater. Res. 197–198 (2011) 919.
[164] R. Häggblad, J.B. Wagner, S. Hansen, A. Andersson, J. Catal. 258 (2008) 345.
[165] A.P.E. York, A. Bruckner, P.M. Wilde, H. Mehner, M. Kraum, M. Baerns, Catal. Lett. 43 (1997) 107.
[166] C. Ding, J. Shi, Z. Wang, C. Li, ACS Catal. 7 (2017) 675.
[167] C. Jiang, S.J.A. Moniz, A. Wang, T. Zhang, J. Tang, Chem. Soc. Rev. 46 (2017) 4645.
[168] Y. Kuang, T. Yamada, K. Domen, Joule. 1 (2017) 290.
[169] R.L. House, N.Y.M. Iha, R.L. Coppo, L. Alibabaei, B.D. Sherman, P. Kang, M.K. Brennaman, P.G. Hoertz, T.J. Meyer, J. Photochem. Photobiol. C Photochem. Rev. 25 (2015) 32.
[170] C. Du, X.G. Yang, M.T. Mayer, H. Hoyt, J. Xie, G. McMahon, G. Bischoping, D. Wang, Angew. Chemie-Int. Ed. 52 (2013) 12692.
[171] S.D. Tilley, M. Cornuz, K. Sivula, M. Gratzel, Angew. Chemie-Int. Ed. 49 (2010) 6405.
[172] D.K. Zhong, D.R. Gamelin, J. Am. Chem. Soc. 132 (2010) 4202.
[173] F.A.L. Laskowski, M.R. Nellist, J. Qiu, S.W. Boettcher, J. Am. Chem. Soc. 141 (2019) 1394.
[174] J.R. Mckone, N.S. Lewis, H.B. Gray, Chem. Mater. Mater. 26 (2014) 407.
[175] T.R. Cook, D.K. Dogutan, S.Y. Reece, Y. Surendranath, T.S. Teets, D.G. Nocera, Chem. Rev. 110 (2010) 6474.
[176] H. Zhou, T. Fan, D. Zhang, ChemCatChem. 3 (2011) 513.

[177] N.S. Lewis, D.G. Nocera, Proc. Natl. Acad. Sci. 103 (2006) 15729.
[178] S. Trasatti, G. Lodi, Oxygen and Chlorine Evolution at Conductive Metallic Oxide Anodes, in: Electrodes Conduct. Met. Oxides, Elsevier, Amsterdam, The Netherlands, 1981.
[179] S. Trasatti, J. Electroanal. Chem Chem. 111 (1980) 125.
[180] Y. Matsumoto, E. Sato, Mater. Chem. Phys. 14 (1986) 397.
[181] A. Di Blasi, C. D'Urso, V. Baglio, V. Antonucci, A.S. Arico', R. Ornelas, F. Matteucci, G. Orozco, D. Beltran, Y. Meas, L.G. Arriaga, J. Appl. Electrochem. 39 (2009) 191.
[182] Y. Lee, J. Suntivich, K.J. May, E.E. Perry, Y. Shao-Horn, J. Phys. Chem. Lett. 3 (2012) 399.
[183] T. Reier, M. Oezaslan, P. Strasser, ACS Catal. 2 (2012) 1765.
[184] E. Tsuji, A. Imanishi, K.I. Fukui, Y. Nakato, Electrochim. Acta. 56 (2011) 2009.
[185] Y. Gorlin, B. Lassalle-Kaiser, J.D. Benck, S. Gul, S.M. Webb, V.K. Yachandra, J. Yano, T.F. Jaramillo, J. Am. Chem. Soc. 135 (2013) 8525.
[186] D.M. Robinson, Y.B. Go, M. Mui, G. Gardner, Z. Zhang, D. Mastrogiovanni, E. Garfunkel, J. Li, M. Greenblatt, G.C. Dismukes, J. Am. Chem. Soc. 135 (2013) 3494.
[187] K. Mette, A. Bergmann, J.-P. Tessonnier, M. Hävecker, L. Yao, T. Ressler, R. Schlölg, P. Strasser, M. Behrens, ChemCatChem. 4 (2012) 851.
[188] R.L. Doyle, M.E.G. Lyons, ECS Trans. 45 (2013) 3.
[189] M.E.G. Lyons, R.L. Doyle, M.P. Brandon, Phys. Chem. Chem. Phys. 13 (2011) 21530.
[190] Y. Wu, M. Chen, Y. Han, H. Luo, X. Su, M.T. Zhang, X. Lin, J. Sun, L.Wang, L. Deng, W. Zhang, Angew. Chemie-Int. Ed. 54 (2015) 4870.
[191] Y.-C. Liu, J.A. Koza, J.A. Switzer, Electrochim. Acta. 140 (2014) 359.
[192] B.S. Yeo, A.T. Bell, J. Am. Chem. Soc. 133 (2011) 5587.
[193] Y.Q. Gao, H.B. Li, G.W. Yang, J. Appl. Phys. 119 (2016) 034902.
[194] J. Liang, Y.-Z. Wang, C.-C. Wang, S.-Y. Lu, IJ. Mater. Chem. A. 4 (2016) 9797.
[195] D. Cibrev, M. Jankulovska, T. Lana-Villarreal, R. Gómez, Int. J. Hydrogen Energy. 38 (2013) 2746.
[196] X. Du, Y. Ding, C. Li, ChemCatChem. 7 (2015) 2370.
[197] C. Iwakura, A. Honji, H. Tamura, Electrochim. Acta. 26 (1981) 1319.
[198] R.-N. Singh, M. Hamdani, J.-F. Koenig, G. Poillerat, J.L. Gautier, P. Chartier, J. Appl. Electrochem. 20 (1990) 442.
[199] I. Nikolov, R. Darkaoui, E. Zhecheva, R. Stoyanova, N. Dimitrov, T. Vitanov, J. Electroanal. Chem. 429 (1997) 157.
[200] J. Suntivich, K.J. May, H.A. Gasteiger, J.B. Goodenough, Y. Shao-Horn, Science 334 (2011) 1383.
[201] J.O. Bockris, T. Otagawa, J. Electrochem. Soc. 131 (1984) 290.
[202] J.O. Bockris, T. Otagawat, J. Phys. Chem. 87 (1983) 2960.
[203] A. Singh, L. Spiccia, Coord. Chem. Rev. 257 (2013) 2607.
[204] L. Trotochaud, S.W. Boettcher, Scr. Mater. 74 (2014) 25.
[205] J.R. Galán-Mascarós, ChemElectroChem. 2 (2015) 37.
[206] H. Bode, K. Dehmelt, J. Witte, Electrochim. Acta. 11 (1966) 1079.
[207] F. Dionigi, P. Strasser, Adv. Energy Mater. 6 (2016) 1600621.
[208] D. Pletcher, J. Appl. Electrochem. 14 (1984) 403.
[209] R. Kostecki, F. McLarnon, J. Electrochem. Soc. 144 (1997) 485.
[210] J. Desilvestro, J. Electrochem. Soc. 135 (1988) 885.
[211] B.C. Cornilsen, P.J. Karjala, P.L. Loyselle, J. Power Sources. 22 (1988) 351.

[212] M.E.G. Lyons, M.P. Brandon, Int. J. Electrochem. Sci. 3 (2008) 1386.
[213] J.R.S. Brownson, C. Lévy-Clément, Electrochim. Acta. 54 (2009) 6637.
[214] M. Dinamani, P.V. Kamath, J. Appl. Electrochem. 30 (2000) 1157.
[215] X. Leng, K.-H. Wu, Q. Zeng, I.R. Gentle, D.-W. Wang, Asia-Pacific J. Chem. Eng. 11 (2016) 415.
[216] S. Zou, M.S. Burke, M.G. Kast, J. Fan, N. Danilovic, S.W. Boettcher, Chem. Mater. 27 (2015) 8011.
[217] R. Subbaraman, D. Tripkovic, K.-C. Chang, D. Strmcnik, A.P. Paulikas, P. Hirunsit, M. Chan, J. Greeley, V. Stamenkovic, N.M. Markovic, Nat. Mater. 11 (2012) 550.
[218] L. Trotochaud, S.L. Young, J.K. Ranney, S.W. Boettcher, J. Am. Chem. Soc. 136 (2014) 6744.
[219] A.M. Smith, L. Trotochaud, M.S. Burke, S.W. Boettcher, Chem. Commun. 51 (2015) 5261.
[220] M.S. Burke, M.G. Kast, L. Trotochaud, A.M. Smith, S.W. Boettcher, J. Am. Chem. Soc. 137 (2015) 3638.
[221] S.L. Candelaria, N.M. Bedford, T.J. Woehl, N.S. Rentz, A.R. Showalter, S. Pylypenko, B.A. Bunker, S. Lee, B. Reinhart, Y. Ren, S.P. Ertem, E.B. Coughlin, N.A. Sather, J.L. Horan, A.M. Herring, L.F. Greenlee, ACS Catal. 7 (2017) 365.
[222] M. Gong, Y. Li, H. Wang, Y. Liang, J.Z. Wu, J. Zhou, J. Wang, T. Reiger, F. Wei, H. Dai, J. Am. Chem. Soc. 135 (2013) 8452.
[223] H. Lin, Y. Zhang, G. Wang, J.B. Li, Front. Mater. Sci. 6 (2012) 142.
[224] S. Chen, J. Duan, M. Jaroniec, S.Z. Qiao, Angew. Chemie-Int. Ed. 52 (2013) 13567.
[225] A. Kleiman-Shwarsctein, Y.S. Hu, G.D. Stucky, E.W. McFarland, Electrochem. Commun. 11 (2009) 115.
[226] J. Landon, E. Demeter, I. Nilay, C. Keturakis, I.E. Wachs, R. Vasic, A.I. Frenkel, J.R. Kitchin., ACS Catal. 2 (2012) 1793.
[227] C.C.L. McCrory, S. Jung, J.C. Peters, T.F. Jaramillo, J. Am. Chem. Soc. 135 (2013) 16977.
[228] L. Trotochaud, J.K. Ranney, K.N. Williams, S.W. Boettcher, J. Am. Chem. Soc. 134 (2012) 17253.
[229] T.W. Kim, K.-S. Choi, Science. 343 (2014) 990.
[230] D.A. Corrigan, J. Electrochem. Soc. 134 (1987) 377.
[231] D.A. Corrigan, R.S. Conell, C.A. Fierro, D.A. Scherson, J. Phys. Chem. 91 (1987) 5009.
[232] D.A. Corrigan, R.M. Bendert, J. Electrochem. Soc. 136 (1989) 723.
[233] M.W. Louie, A.T. Bell, J. Am. Chem. Soc. 135 (2013) 12329.
[234] R.D.L. Smith, M.S. Prevot, R.D. Fagan, S. Trudel, C.P. Berlinguette, J. Am. Chem. Soc. 135 (2013) 11580.
[235] S. Klaus, Y. Cai, M.W. Louie, L. Trotochaud, A.T. Bell, J. Phys. Chem. C. 119 (2015) 7243.
[236] W. Liu, H. Liu, L. Dang, H. Zhang, X. Wu, B. Yang, Z. Li, X. Zhang, L. Lei, S. Jin, Adv. Funct. Mater. 27 (2017) 3904.
[237] L. Feng, A. Li, Y. Li, J. Liu, L. Wang, L. Huang, Y. Wang, X. Ge, ChemPlusChem. 82 (2017) 483.
[238] J. Quiñonero, R. Gómez, Appl. Catal. B Environ. 217 (2017) 437.
[239] Y. Zhu, J. Ren, X. Yang, G. Chang, Y. Bu, G. Wei, W. Han, D. Yang, J. Mater. Chem. A. 5 (2017) 9952.
[240] Q. Wang, T. Niu, L. Wang, J. Huang, H. She, Chinese J. Catal. 39 (2018) 613.

[241] T.W. Kim, K.S. Choi, Science. 343 (2014) 126.
[242] Z. Jin, Z. Hu, J.C. Yu, J. Wang, J. Mater. Chem. A. 4 (2016) 73736.
[243] P. Chatchai, A.Y. Nosaka, Y. Nosaka, Electrochemistry. 79 (2011) 821.
[244] A. Paracchino, N. Mathews, T. Hisatomi, M. Stefik, S.D. Tilley, M. Grätzel, Energy Environ. Sci. 5 (2012) 8673.
[245] N.P. Dasgupta, C. Liu, S. Andrews, F.B. Prinz, P. Yang, J. Am. Chem. Soc. 135 (2013) 12932.
[246] Y. Lin, C. Battaglia, M. Boccard, M. Hettick, Z. Yu, C. Ballif, J. W. Ager, A. Javey, Nano Lett. 13 (2013) 5615.
[247] H.S. Park, C.-Y. Lee, E. Reisner, Phys. Chem. Chem. Phys. 16 (2014) 22462.
[248] D. Kang, J.C. Hill, Y. Park, K.-S. Choi, Chem. Mater. 28 (2016) 4331.
[249] S. Somasundaram, C.R.N. Chenthamarakshan, N.R. de Tacconi, K. Rajeshwar, Int. J. Hydrog. Energy. 32 (2007) 4661.
[250] C.-Y. Lin, Y.-H. Lai, D. Mersch, E. Reisner, Chem. Sci. 3 (2012) 3482.
[251] A.A. Dubale, C.-J. Pan, A.G. Tamirat, H.-M. Chen, W.-N. Su, C.-H. Chen, J. Rick, D.W. Ayele, B.A. Aragaw, J.-F. Lee, Y.W. Yang, B.-J. Hwang, J. Mater. Chem. A. 3 (2015) 12482.
[252] J.R. McKone, E.L. Warren, M.J. Bierman, S.W. Boettcher, B.S. Brunschwig, N.S. Lewis, H.B. Gray, Energy Environ. Sci. 4 (2011) 3573.
[253] C.G. Morales-Guio, L. Liardet, M.T. Mayer, S.D. Tilley, M. Grätzel, X. Hu, Angew. Chemie-Int. Ed. 54 (2015) 664.
[254] R. Liu, Z. Zheng, J. Spurgeon, X. Yang, Energy Environ. Sci. 7 (2014) 2504.
[255] M.-J. Park, J.-Y. Jung, Y.-H. Nam, J.-W. Song, C. Jeong, J.-H. Lee, Thin Solid Films. 616 (2016) 550.
[256] M.J. Choi, J.-Y. Park, J.-W. Song, J.-H. Lee, J.-H. Bang, J. Mater. Chem. A. (2014) 2928.
[257] B. Seger, T. Pedersen, A.B. Laursen, P.C.K. Vesborg, O. Hansen, I. Chorkendorff, J. Am. Chem. Soc. 135 (2013) 1057.
[258] M.H. Lee, K. Takei, J. Zhang, R. Kapadia, M. Zheng, Y.-Z. Chen, J. Nah, T.S. Matthews, Y.-L. Chueh, J.W. Ager, A. Javey, Angew. Chemie-Int. Ed. 51 (2012) 10760.
[259] M. Tallarida, C. Das, D. Cibrev, K. Kulki, A. Tamm, M. Ritala, T. Lana-Villarreal, R. Gómez, M. Leskelä, D. Schmeisser, J. Phys. Chem. Lett. 5 (2014) 3582.

CHAPTER II

Experimental methods

In this Chapter, the main experimental procedures and the structural, morphological, compositional and (photo)electrochemical characterization techniques employed in the context of this thesis are presented. First, the synthesis methods for the preparation of the semiconductor photoelectrodes and the electrocatalysts and co-catalysts studied in the following chapters are briefly described (section 2.1). Then, the experimental setups (mainly, (photo)electrochemical cells and illumination sources) used for the (photo)electrochemical characterization of the prepared materials are presented (section 2.2). Finally, brief descriptions of the fundamentals and characteristics of the (photo)electrochemical, spectroscopic, diffraction and microscopic techniques employed in these studies are provided, including a brief reference to computational methods (sections 2.3 to 2.7).

2.1. SYNTHESIS METHODS

In this section, the synthesis methodologies used for the preparation of electrocatalysts and semiconductor photoelectrodes (and their subsequent surface modification with co-catalysts) are briefly described. For full and detailed experimental details, the reader is referred to the following chapters (Chapters III to X).

As a general comment regarding the preparation of photoelectrodes, it is important to highlight that the use of transparent substrates is highly desirable. The ones used throughout these studies consist of a glass plate covered with a thin film of SnO_2 strongly doped with F (F:SnO_2, FTO). They are suitable substrates for (photo)electrochemical applications since they present high transparency, high conductivity (the high degree of doping with F causes the SnO_2 to have a *quasi*-metallic electrical conductivity) and weak light absorption in the visible range. In addition, and compared to other common transparent substrates (such as, In_2O_3-doped SnO_2, ITO), FTO presents higher stability, a wider working potential window

and higher glass transition temperature. These FTO glass plates were also used as substrates for the dark electrocatalysts (Chapters V and VI). In all cases, and prior to their utilization, FTO-coated glass substrates were thoroughly cleaned by sonication in acetone and ethanol for 15 min in each, and air dried.

2.1.1. Photoelectrode preparation: sol-gel-based methods

In the present thesis, $BiVO_4$ (Chapters III, IV and VII), $FeVO_4$ (Chapter IV) and $LaFeO_3$ (Chapter VIII) have been used as photoanodes, while $NdFeO_3$ (Chapters IX and X) was tested as photocathode. All these materials have been prepared by sol-gel-based synthesis methods, which are used for producing solid materials from small molecules [1].

In this chemical procedure, a precursor sol (*i. e*, a colloidal solution) gradually evolves toward the formation of a gel-like diphasic system containing both a liquid phase and solid phase whose morphologies range from discrete particles to continuous polymer networks (Figure 2.1a). Subsequent removal of the remaining liquid (solvent) phase requires a drying process, which is typically accompanied by a significant amount of shrinkage and densification. The rate at which the solvent can be removed ultimately determines the distribution of porosity in the gel. The resulting microstructure will be strongly influenced by changes imposed upon the structural template during this phase of processing. Afterwards, a thermal treatment (annealing process) is often necessary in order to favor further polycondensation and enhance mechanical properties and structural stability *via* final sintering, densification, and grain growth. One of the distinct advantages of using this methodology as opposed to the more traditional processing techniques is that densification is often achieved at a much lower temperature.

The precursor sol can be either deposited on a substrate (such as FTO) by dip-coating, drop casting or spin coating, to form a film, cast into a suitable container with the desired shape, or used to synthesize powders. The sol-gel approach is a cheap and low-temperature technique that allows for a fine control of the chemical composition of the final product. Importantly, even small quantities of dopants, such as rare-earth elements, can be introduced in the sol and end up uniformly dispersed in the final product.

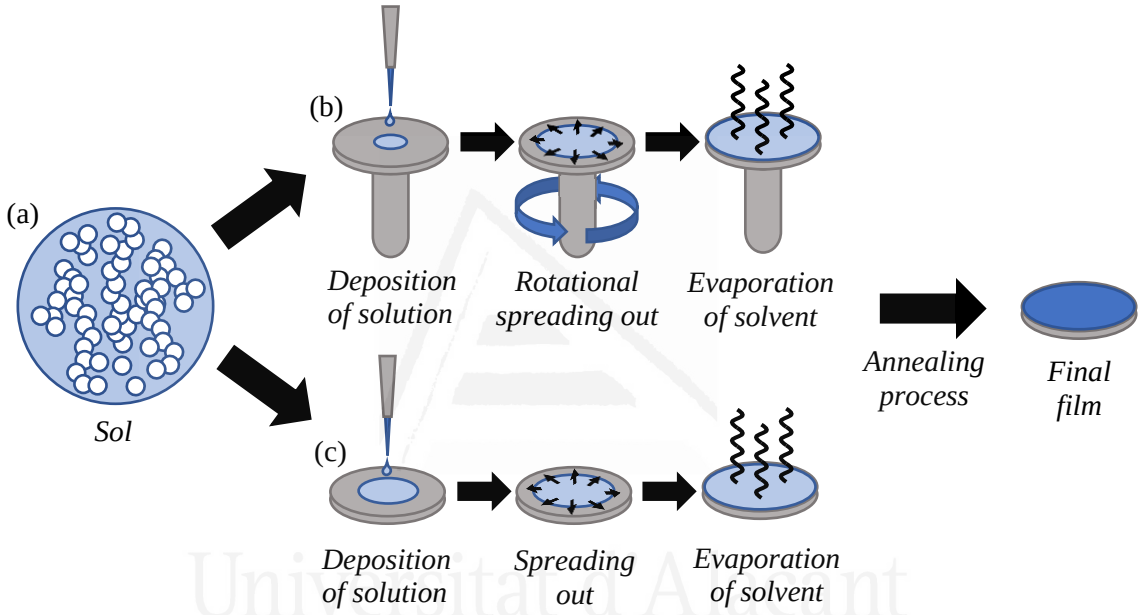

Figure 2.1. (a) Precursor sol, and formation of a thin film through (b) spin coating and (c) drop-casting approaches.

For $BiVO_4$, $FeVO_4$ and $NdFeO_3$ preparation, the deposition of the precursor sol on the FTO substrate was performed by a spin coating approach (Figure 2.1b). Here, a small volume of coating precursor solution is deposited on the center of the substrate, which is then rotated at high speed in order to spread the coating material by centrifugal force. The machine used to this end is called a spinner or spin coater. Rotation is continued while the fluid spins off the edges of the substrate, until the desired thickness of the film is achieved. Since the

employed solvent is usually volatile, it simultaneously evaporates during rotation. The higher the angular speed of spinning, the thinner the film. The thickness of the film also depends on the viscosity and concentration of the solution, and the solvent. On the other hand, the deposition of the sol to obtain $LaFeO_3$ was done by drop-casting it on a previously generated FeOOH deposit (*vide infra*). It simply consists in dropping a certain volume of precursor solution onto a flat surface, followed by evaporation of the solution (Figure 2.1c), to obtain the solid thin film.

$BiVO_4$ films were prepared by layer-by-layer coating through a modified metal-organic decomposition (MOD) method, followed by a thermal treatment (Chapters III, IV and VII) [2,3]. Solutions of 0.2 M $Bi(NO_3)_3 \cdot 5H_2O$ in acetic acid and 0.03 M $VO(C_5H_7O_2)_2$ in acetylacetone, as Bi and V precursors respectively, were mixed, with the help of magnetic stirring, maintaining a Bi:V molar ratio of 1:1. Then, 40 μL of the solution was spread on a FTO substrate and spin-coated at a spin rate of 1500 rpm for 10 s. After drying in air, the coated $BiVO_4$ electrodes were annealed at 500ºC for 30 min. This procedure was repeated six times.

La- and Ce-doped $BiVO_4$ films (Chapters III and IV) were deposited and annealed following the method described above, but modifying the composition of the precursor solution with the desired concentration (in at% with respect to either Bi or V content) of the doping element (here, La and Ce) [2,3]. Concretely, $La(NO_3)_3 \cdot 6H_2O$ and $Ce(NO_3)_3 \cdot 6H_2O$ were used as La and Ce precursors, respectively.

$FeVO_4$ thin film photoanodes were also synthesized by layer-by-layer coating over conducting FTO glass substrates through a modified MOD method followed by a thermal treatment (Chapter IV) [3]. The $FeVO_4$ precursor solution was prepared by mixing $Fe(NO_3)_3 \cdot 9H_2O$ and $VO(C_5H_7O_2)_2$ in equimolar 0.2 M concentration, in a 10-mL solution of

acetic acid and acetylacetone (1:8.25 by v/v) that was magnetically stirred for 24 h. The resulting solution was then spun on FTO glass substrates at 1000 rpm for 30 s and subsequently annealed at 250ºC for 10 min. This process was repeated five times, and then, the films were annealed in two stages: a first annealing at 500ºC for 30 min was applied, and then a second annealing at 550ºC for 1 h to obtain the final films.

$LaFeO_3$ photoelectrodes (Chapter VIII) were prepared by a two-step solution-based route according to a previously reported procedure [4]. First, a nanorod-based layer of β-FeOOH was grown on a FTO substrate from a 0.15 M $FeCl_3 \cdot 6H_2O$ and 1 M $NaNO_3$ aqueous solution contained in a tightly capped glass bottle. The solution was heated up to 100ºC in a stove for 3 hours. After deposition, the samples were rinsed with abundant water and dried with compressed air. In a second step, the resulting FTO/FeOOH electrodes were placed in a pre-heated hot-plate at 100ºC and coated (by drop-casting) with an excess of a 0.1 M $La(NO_3)_3 \cdot 6H_2O$ aqueous solution. The electrodes remained on the hot-plate until the $La(NO_3)_3$ solution evaporated completely. Finally, the $LaFeO_3$ formation was carried out by introducing the $La(NO_3)_3$-coated FeOOH samples into a tubular oven pre-heated at desired temperature (550, 650 or 750ºC) for 20 min, followed by a quick-cooling method: right after the annealing, the electrodes were removed from the oven to allow them to cool-down naturally. The resulting samples were immersed in 0.5 M H_2SO_4 aqueous solution overnight to completely remove the La_2O_3 white crust that covers the electrode surface after the annealing. Two different annealing post-treatments were performed: a hydrogenation annealing at 200ºC for 1 hour and an annealing in air at different temperatures (300, 450 and 650ºC) for 5 hours.

Pristine $NdFeO_3$ thin film photocathodes were prepared layer-by-layer on FTO by a previously reported procedure based on a citric sol-gel route (Chapters IX and X) [5]. The

$NdFeO_3$ precursor solution was prepared by dissolving $Nd(NO_3)_3 \cdot 6H_2O$ 0.3 M and $Fe(NO_3)_2 \cdot 9H_2O$ 0.3 M in water. This solution was magnetically stirred for 1 hour and, then, the appropriate amount of citric acid was added to the mentioned solution to reach a concentration of 0.6 M, and it was stirred again for 20 hours. After that, 30 $\mu L \cdot mL^{-1}$ of acetylacetone and 30 $\mu L \cdot mL^{-1}$ of Triton® X-100 were added. Then, 40 µL of the resulting solution was dropped onto and FTO glass plate and spread over it with a spin-coater at a spin rate of 1500 rpm for 20 s. Finally, the electrodes were annealed in air at 500ºC for 1 hour. This process was repeated four times, and a final annealing at 640ºC for 2 hours was applied to obtain the crystalline perovskite films.

Mg- and Zn-doped $NdFeO_3$ thin film photocathodes (Chapters IX and X) were obtained following the same procedure described above, but substituting the corresponding amount of the Fe precursor salt in the $NdFeO_3$ precursor solution by the dopant salt in the desired concentration (in at% with respect to the Fe content) [5]. In this case, $Mg(NO_3)_2 \cdot 6H_2O$ and $Zn(NO_3)_2 \cdot 6H_2O$ were employed as Mg and Zn precursors, respectively.

Finally, the extracting TiO_2 layer (Chapter X) deposited on the surface of pristine and doped $NdFeO_3$ photocathodes was also prepared by a sol-gel route. The deposition solution was prepared by dissolving $Ti(OCH(CH_3)_2)_4$ 36 mM in 2-propanol. This solution was diluted 10 times with the same solvent. Then, 10 µL of the resulting solution was dropped onto a pristine or doped $NdFeO_3$ photocathode. After deposition, the solvent was allowed to dry naturally, and the resulting films were annealed at 330ºC in air for 1 h.

2.1.2. Electrocatalyst and co-catalyst preparation

In the context of these studies, $Ni(OH)_2$, $Fe(OH)_2$ and $Co(OH)_2$ (and different $Fe(OH)_2$-$Ni(OH)_2$ and $Fe(OH)_2$-$Co(OH)_2$ combinations) have been tested as electrocatalysts for the

oxygen evolution reaction in alkaline media (Chapters V and VI) and as co-catalysts on the surface of $BiVO_4$ and $FeVO_4$ photoanodes (Chapters II and VII). In all cases, these metallic hydroxides have been prepared by a chemical bath deposition (CBD) method. On the other hand, Au and Ni particles synthesized by a potentiostatic electrodeposition procedure were studied as co-catalysts on the surface of $BiVO_4$ photoanodes (Chapter I) and $NdFeO_3/TiO_2$ photocathodes (Chapter X), respectively.

2.1.2.1. Chemical bath deposition

Chemical bath deposition (CBD) is a method to deposit thin films and nanomaterials which can be employed for large-area continuous deposition [6]. It involves two steps (nucleation and particle growth) and is based on the formation of a solid phase on a substrate from a solution containing the corresponding precursors (Figure 2.2). Growth of thin films strongly depends on parameters like topographical and chemical nature of the substrate, bath temperature, pH and concentration of the solution, and deposition time. CBD yields stable, adherent, uniform and hard films with good reproducibility by a relatively simple process.

$Ni(OH)_2$, $Fe(OH)_2$ and $Co(OH)_2$ (and different $Fe(OH)_2$-$Ni(OH)_2$ and $Fe(OH)_2$-$Co(OH)_2$ combinations) were deposited on FTO substrates or on $BiVO_4$ and $FeVO_4$ photoanodes by a CBD procedure [3,7,8]. The deposition solution contained 25 mL of 0.5 M $NiSO_4 \cdot 6\text{-}7H_2O$, $FeSO_4 \cdot 7H_2O$ or $CoSO_4 \cdot 7H_2O$, for the deposition of $Ni(OH)_2$, $Fe(OH)_2$ or $Co(OH)_2$, respectively, 12.5 mL of 1 M urea and 12.5 mL of H_2O. FTO glass plates were vertically supported (either bare or covered with $BiVO_4$ or $FeVO_4$) faced against the wall of the beaker containing the CBD solution. The solution was heated up to 100ºC in a stove (Memmert,100-800). Different deposition times were assayed as to control the amount of

deposited metal hydroxide. After deposition, the samples were rinsed with distilled water, air dried and, in the case of $Ni(OH)_2$ and $Fe(OH)_2$ deposits, annealed at 200ºC in air for 1 h.

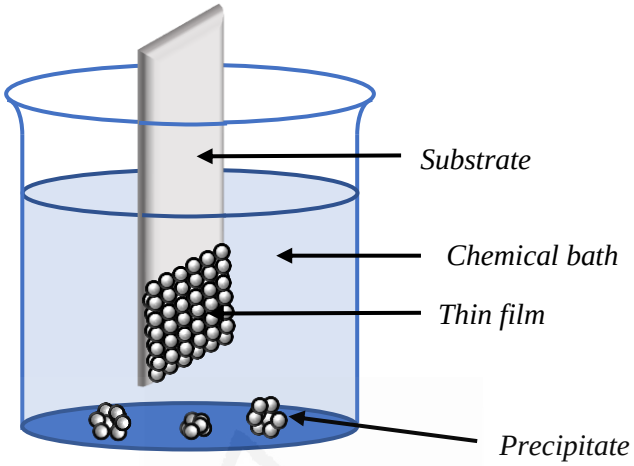

Figure 2.2. Scheme of a chemical bath deposition (CBD) procedure.

2.1.2.2. Electrodeposition

Electrodeposition (or electroplating) is a well-known process that uses an electric current to reduce dissolved metal cations so that they form a thin coherent metal coating on an electrode. A potentiostatic electrodeposition process usually involves submerging the piece to be coated (in this case, the photoelectrode) into a vessel which holds the coating solution and applying a constant potential value for a certain period of time. In the context of these studies, the experimental setup to perform the electrodeposition of Au and Ni nanoparticles was a three-electrode cell (*vide infra*), using the photoelectrode to be coated ($BiVO_4$ or $NdFeO_3/TiO_2$, respectively) as working electrode, and a Pt wire and a Ag/AgCl/KCl(3 M) as counter and reference electrodes, respectively.

Au nanoparticles were deposited on the surface of pristine and doped $BiVO_4$ electrodes by a potentiostatic electrodeposition method at -0.5 V (*vs*. Ag/AgCl). This was performed

for 30 s in a 0.5 M H_2SO_4 aqueous solution containing 2 mM $NaAuCl_4$ and 0.125 mM L-cysteine [2]. On the other hand, Ni was deposited on both pristine and doped $NdFeO_3/TiO_2$ photocathodes following a potentiostatic electrodeposition procedure performed at -1.0 V (*vs*. Ag/AgCl) in an acetate buffer solution 0.1 M (pH = 4.0) containing 1 mM $Ni(NO_3)_2 \cdot 6H_2O$. This procedure was performed for different deposition times (from 5 to 30 s).

2.2. (PHOTO)ELECTROCHEMICAL CELLS AND ILLUMINATION SOURCES

In this section, a brief summary of the equipment used to perform the (photo)electrochemical characterization of the prepared electrodes, along with the illumination sources, is presented.

In all chapters, a standard three-electrode cell (Figure 2.3) able to work both under illumination and in the dark conditions was employed. The main components of a usual three-electrode cell are the working electrode, the reference electrode and the counter electrode, which are immersed in the working electrolyte solution. A reference electrode with a defined and stable potential value is required to properly measure the working electrode potential. A potential bias is then applied between the working and reference electrodes, which allows for the control of the possible processes occurring at the working electrode. The role of the counter electrode is to close the electric circuit and to sustain the electrochemical process (oxidation or reduction) associated to the one taking place on the working electrolyte (reduction or oxidation, respectively) [9,10].

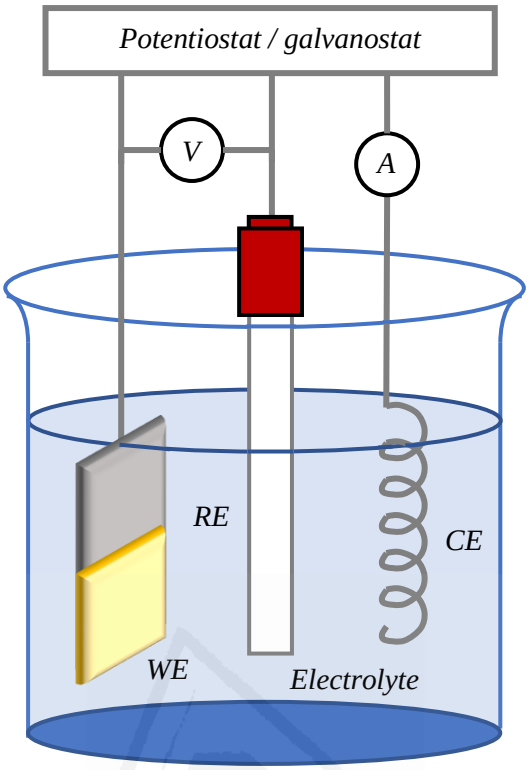

Figure 2.3. Scheme of a three-electrode cell (*WE*: working electrode; *RE*: reference electrode; *CE*: counter-electrode).

A photography of the (photo)electrochemical cell employed in all chapters (except in Chapter VIII) is shown in Figure 2.4. It is a home-made Pyrex glass cell consisting of two compartments, both filled with the same working electrolyte solution and connected by a porous glass plate: one contains the working and counter electrodes, while the other is for the reference electrode. The system allows the purge of the electrolyte solution by an accessory gas inlet piece. When it is considered that the working electrolyte solution is conveniently purged (a gas flow through it of at least 30 min of duration is necessary), the gas flow is redirected toward the head space of the cell throughout the course of the (photo)electrochemical measurements. This avoids the undesired entry of air in the cell. It is

also equipped with a fused silica window, which allows radiation from the light source to illuminate the electrode.

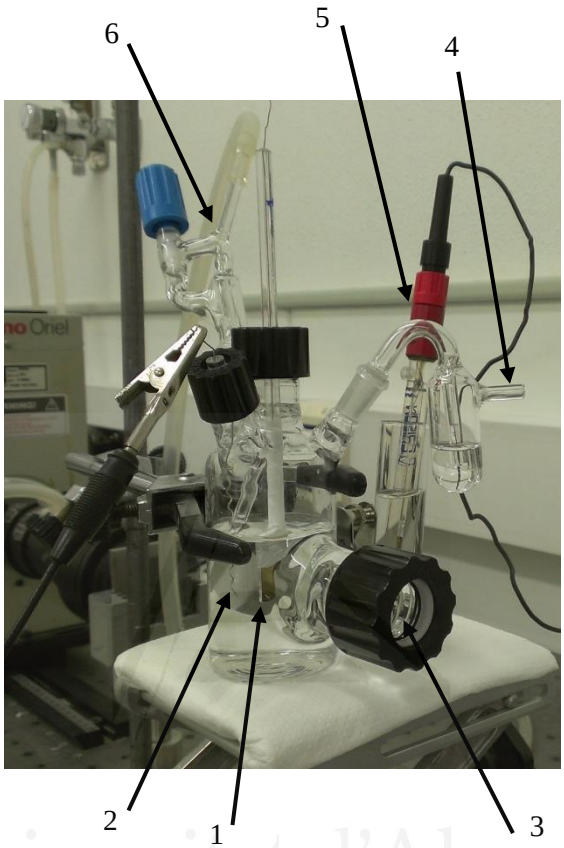

Figure 2.4. Three-electrode (photo)electrochemical cell employed: (1) working electrode, (2) counter-electrode (Pt wire), (3) fused silica window, (4) gas outlet, (5) reference electrode (Ag/AgCl/KCl(sat.)), and (6) gas inlet.

In Chapter VIII, the (photo)electrochemical characterization was performed using a three-electrode electrochemical cell in a Cappuccino configuration (Figure 2.5). This cell is characterized by requiring a smaller electrolyte volume. It is fabricated from PEEK (polyether ether ketone), a chemically resistant polymer that is easier to machine and has improved mechanical properties than PTFE or glass. It allows two methods of sample (*i.e.*, photoelectrode) mounting. One is by pressing the sample against an O-ring, while in the other

method, the top of the sample is clamped in a miniature steel vise. The vise is mounted at the top of the cell, so that the bottom part of the sample is fully immersed in the electrolyte. The top part of the sample should not be coated, so that the vise connects with the conducting back-contact and thereby serves as an electrical contact. The illuminated area is defined by a circular hole at the front of the cell. This cell is easier to handle than the design of Figure 2.4, but with the limitations of not being gas tight and having a wetted area that is around 2–3 times larger than the illuminated

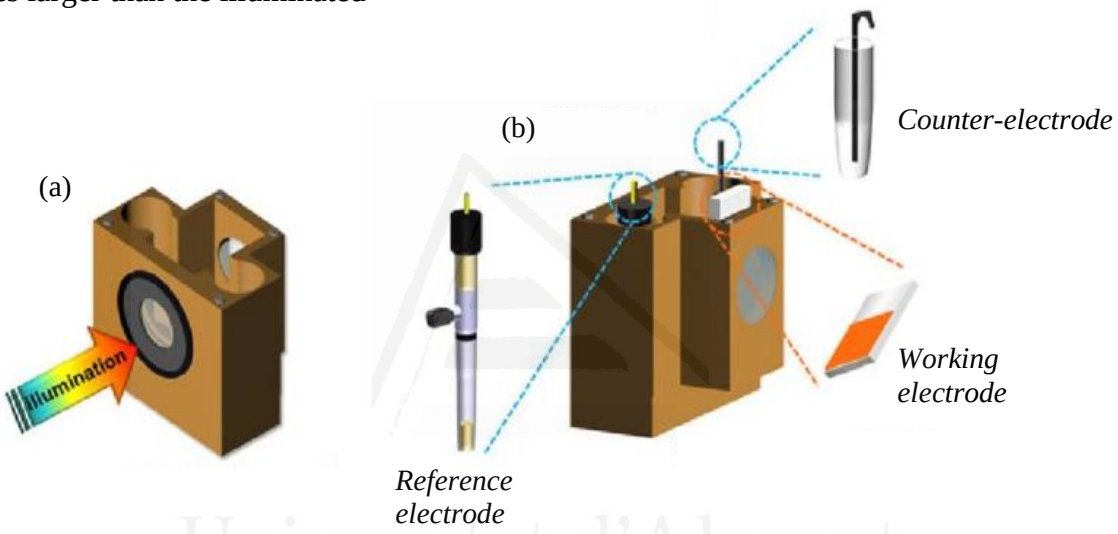

Figure 2.5. Schematic illustration of a Cappuccino cell: (a) front view, and (b) back view [11].

The counter and reference electrodes employed in all measurements presented in this study were a platinum wire and an Ag/Ag/KCl(3M) electrode (Ag/AgCl/KCl(sat.), in Chapter VIII), respectively. Considering that the reversible potential of Ag/AgCl/KCl(3 M) is 0.210 V (0.197 V for the Ag/AgCl/KCl(sat.) electrode) *versus* the standard hydrogen electrode (SHE), the potentials measured with these reference electrodes can be converted into the reversible hydrogen electrode (RHE) scale according to Eq. 2.1 and 2.2, respectively:

$$E_{RHE} = E_{Ag/AgCl/KCl(3M)} + 0.210 + 0.059 \cdot pH \quad \text{Eq. } \mathbf{2.1}$$

$$E_{RHE} = E_{Ag/AgCl/KCl(sat)} + 0.197 + 0.059 \cdot pH \quad \text{Eq. } \mathbf{2.2}$$

The light source for the photoelectrochemical measurements (except in Chapter VIII) was an ozone-free 1000 W Xe(Hg) arc lamp (Newport Instruments, 66921) equipped with a water filter to minimize the infrared contribution of the beam. The photon flux intensity was measured by means of a photodiode power meter (Thorlabs, PM100D), and the typical value obtained in all cases was approximately 100 $mW \cdot cm^{-2}$. Figure 2.6 shows the corresponding irradiance spectrum. In Chapter VIII, the light source was a 450 W Müller Elektronic Xenon-arc lamp coupled with a KG-1 filter (Schott) calibrated to provide 1 sun (AM 1.5G, 100 $mW \cdot cm^{-2}$). With this source, light intensities over 1 sun were achieved by including a calibrated Si diode to determine the irradiance.

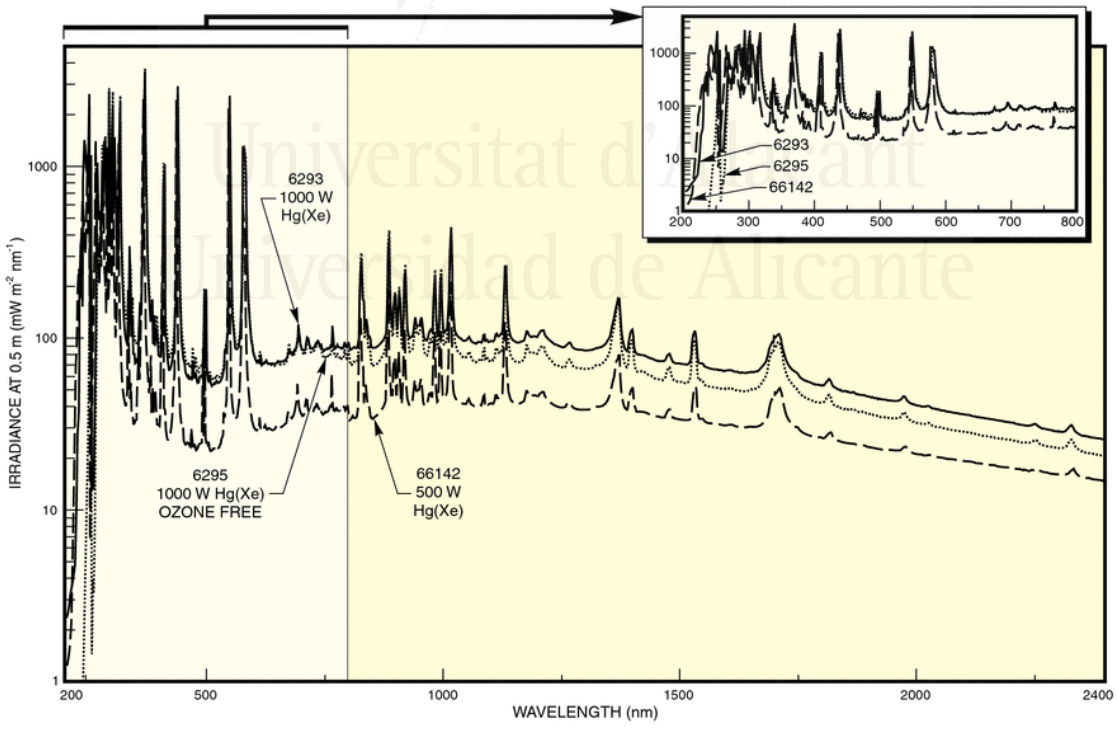

Figure 2.6. Irradiance spectrum of the ozone-free 1000 W Xe(Hg) arc lamp (Newport Instruments, 66921) [12].

Finally, it is important to highlight that all the (photo)electrochemical measurements were conducted with a computer-controlled Autolab (PGSTAT30) potentiostat-galvanostat. In Chapter VIII, a BioLogic (SP-300) potentiostat was employed.

2.3. (PHOTO)ELECTROCHEMICAL METHODS

In this section, the set of (photo)electrochemical techniques employed to measure the (photo)electrochemical performance of the prepared electrodes are briefly described.

2.3.1. Cyclic and linear voltammetry

In the field of Electrochemistry, potential sweep techniques constitute the basis of any preliminary characterization of the electrochemical processes that take place on the surface of an electrode [11,13]. Among them, cyclic voltammetry (CV) is the most common technique. It consists in measuring the electric current (i) flowing between the working and the counter electrode when the working electrode potential is linearly scanned between two potential limits (E_1 and E_2). In a first swept, the applied potential is varied from the initial (E_1) to the final potential (E_2) at a constant scan rate and, once the E_2 potential is reached, the potential is swept in the opposite direction until E_1 is reached again (see Figure 2.7a). Normally, this procedure is subsequently repeated for a certain number of times. The resulting current *versus* potential plot (Figure 2.7b) is known as cyclic voltammogram. It is usual to normalize i values to the geometric area of the electrode and express them in current density (j) terms.

The linear scan voltammetry (LSV) is essentially a CV but without performing the reverse potential scan (the potential value is only varied from E_1 to E_2, Figure 2.7c and d).

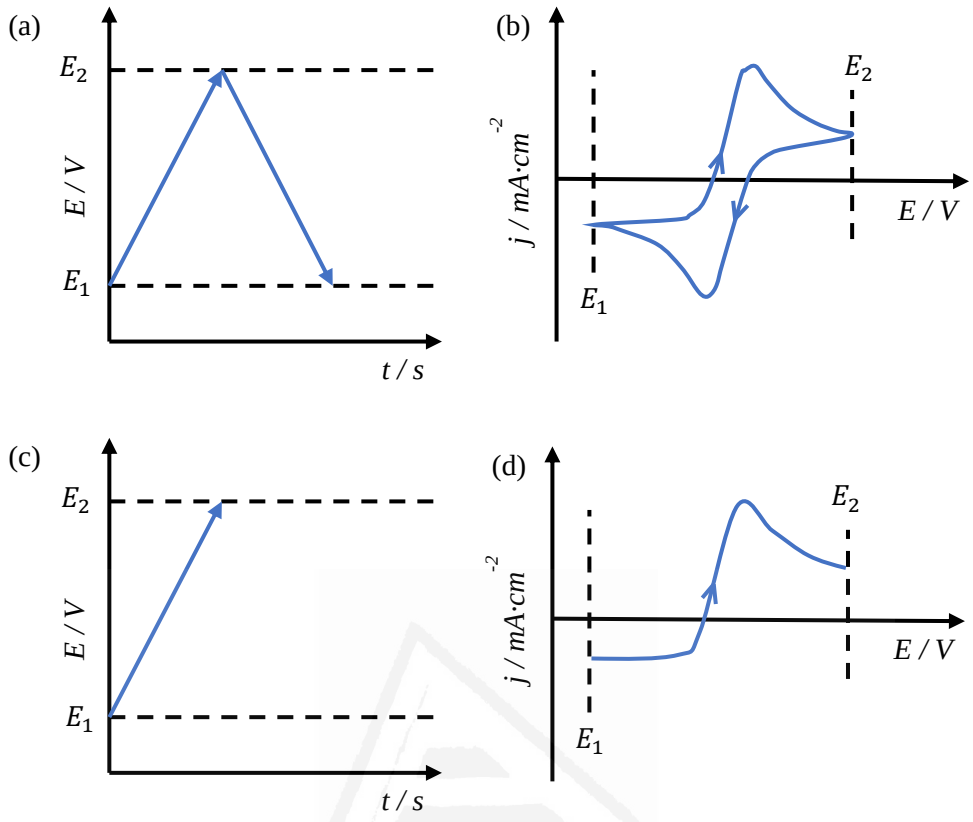

Figure 2.7. Time variation of the applied potential (left) and voltammetric response (right) in a (a,b) cyclic and (c,d) linear voltammetry.

CV is a very useful tool for distinguishing the type of electrochemical process (Faradaic or non-Faradaic processes) that takes place on the electrode surface. On the one hand, a Faradaic process is that implying a redox reaction at the electrode surface, resulting in a net electric charge transfer across the electrode-electrolyte interface. A redox reaction can be generically expressed as $\mathrm{Ox} + n_e \cdot \mathrm{e}^- \leftrightarrows \mathrm{Red}$, where Ox and Red are the oxidized and reduced forms of the corresponding redox couple, respectively, and n indicates the number of electrons transferred in the reaction. These processes are governed by the Faraday's law (Eq. 2.3):

$$|j_F| = \left|\frac{dQ}{dt}\right| = n_e F \left|\frac{dn}{dt}\right| = n_e F A|v| \qquad \text{Eq. } \mathbf{2.3}$$

where j_F is the Faradaic current density, Q is the charge involved in this Faradaic process, n_e is the number of electrons exchanged, n is the number of moles that have reacted in the process, A is the surface area and v is the reaction rate per unit area. As deduced, the current density can be directly related to the reaction rate for a purely Faradaic process.

On the other hand, non-Faradaic processes are those that do not involve an electric charge transfer along the electrode-electrolyte interface. In these cases, the observed current is due to charge/discharge phenomena of the electric double layer, which is accompanied by the adsoption/desorption of ions on/from the electrode surface. Those processes induce a linear dependency between of the electric current with the scan rate at which the CV experiment is performed, according to Eq. 2.4:

$$j_C = C\frac{dE}{dt} = C v_{sr} \qquad \text{Eq. } \mathbf{2.4}$$

where j_C is the capacitive current density, C is the capacitance per geometric unit area, and v_{sr} is the scan rate.

At this point, it is important to distinguish between pure capacitive processes, exclusively related to the charge or discharge of the double layer, and the so-called *pseudo*-capacitive processes. In the case of semiconductor electrodes, the latter ones may also imply a change in the degree of occupancy of either intrinsic or extrinsic surface states.

In the context of the present work, CV has been used in the dark to characterize the electrochemical response of the prepared electrodes. When the corresponding cyclic voltammogram offers information about the charge accumulation region of the electrode, it can be used to get an approximate idea of the conduction and valence band edges location

for *n*- and *p*-type semiconductor electrodes, respectively. In some cases, CV might also provide information regarding the density of states existing within the band gap. Finally, and since *pseudo*-capacitive processes (such as electrosorption and intercalation of ions) can take place in the charge accumulation region, this voltammetric technique can be a proper choice to get insights into double layer electrostatic charge and discharge phenomena. On the contrary, LSV has been performed only under transient illumination conditions. This allows to evaluate the photocurrent as a function of potential by a single measure and to locate the onset of photocurrent, that is, the potential value at which the photocurrent first appears. In this sense, both techniques have been extensively used from Chapter III to Chapter X to obtain basic (photo)electrochemical information of the prepared photoelectrodes.

2.3.2. Chronoamperometry

In the field of (photo)electrochemistry, chronoamperometry is a widely used technique which consists in measuring the electric current between counter and working electrodes as a function of time when a constant potential is applied to the working electrode.

In these studies, chronoamperometry has been used under both transient and continuous illumination conditions. The procedure is done by applying a constant potential more positive or more negative than the photo-onset potential for an *n*- and *p*-type electrode, respectively (Figure 2.8). Initially, the electric current is recorded in the dark (j_{dark}) for a relatively short period of time and, then, the light is turned on. This illumination of the electrode induces an increase in the measured current that, initially, is not stationary. After a reasonable period of time of continuous illumination, the current under illumination tends to stabilize, reaching finally a stationary value (j_{light}). At this point, light is interrupted and the

response in the dark is recorded again. The photocurrent (j_{ph}) is thus calculated as the difference between the stationary current under illumination and the current in the dark (Eq. 2.5):

$$j_{ph} = j_{light} - j_{dark} \qquad \text{Eq. } \mathbf{2.5}$$

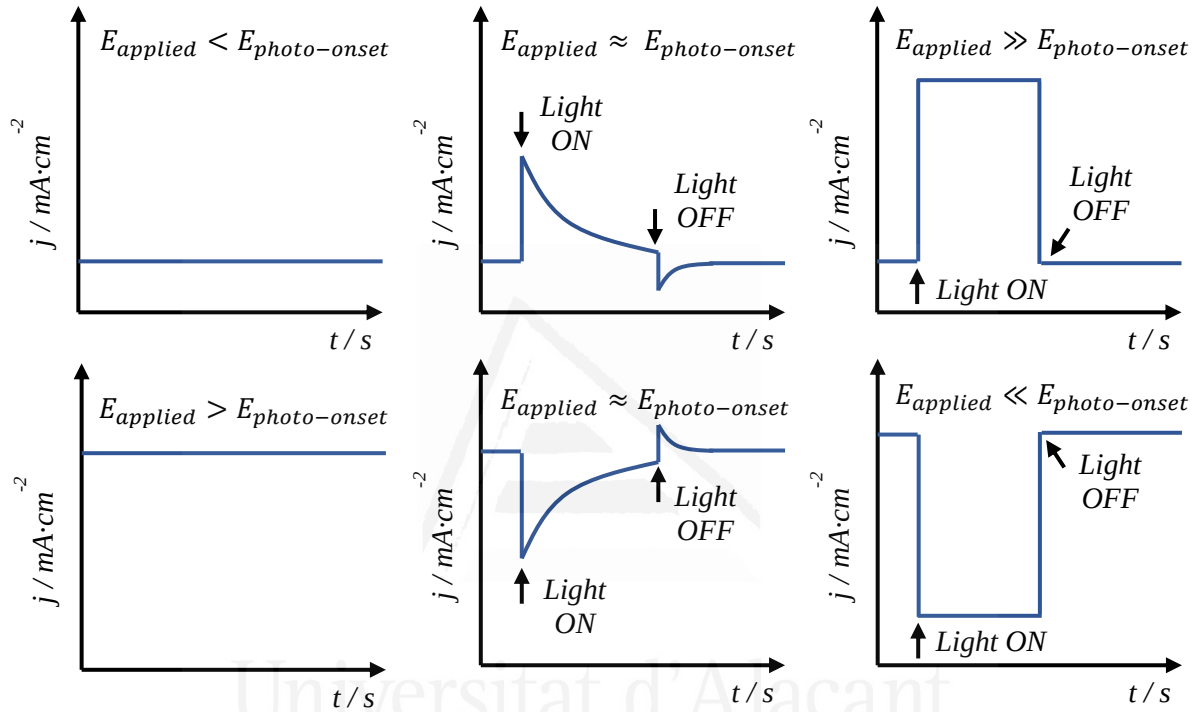

Figure 2.8. Photocurrent transients at three different constant applied potentials for an *n*-type (top) and *p*-type semiconductor.

O many occasions, anodic and cathodic current spikes are observed upon illumination and light interruption. The intensity of these spikes (which depends on the potential value at which the chronoamperometry is performed) provides information about surface recombination processes. In fact, the spike at the beginning of the transient has been traditionally associated with a fast trapping of minority charge carriers at surface states and their subsequent recombination with majority carriers. This effect induces a constant

decrease of the current under illumination until a steady-state value is finally reached. Only when the applied potential is significantly more positive (negative) than that corresponding to the photo-onset of a photoanode (photocathode), the spike virtually disappears since surface recombination diminishes as a consequence of a higher applied driving force.

Here, chronoamperometries have been extensively used to obtain information about the stationary photocurrent magnitude at a certain potential value for the as-prepared photoelectrodes, but they are explicitly shown in Chapter IV.

2.3.3. (Photo)electrochemical impedance spectroscopy

In the context of the techniques employed in the frequency domain to gain additional information on electrode processes, electrochemical impedance spectroscopy (EIS) stands out as one of the most powerful. Apart from information regarding the structure of the interphase and the kinetics of the charge carrier transfer processes, it offers insights into charge carrier density and band edges location [14–16].

In the present study, the EIS technique used is based on the application of a small potential perturbation of sinusoidal type (Figure 2.9) as a function of time (Eq. 2.6):

$$\Delta E(t) = E_0 \cdot \sin(\omega t) \qquad \text{Eq. } \mathbf{2.6}$$

where $\Delta E(t)$ is the applied potential perturbation as a function of time, E_0 is the potential perturbation amplitude, and ω is the angular frequency, which is related to the frequency (f) by $\omega = 2\pi f$.

Consequently, the resulting generated current has the same frequency, but shifted in phase (ϕ) with respect to the potential (Eq. 2.7):

$$\Delta I(t) = I_0 \cdot \sin(\omega t + \phi) \qquad \text{Eq. } \mathbf{2.7}$$

where $\Delta I(t)$ is the resulting current perturbation as a function of time and I_0 is the current perturbation amplitude.

The impedance (Z) is thus defined as (Eq. 2.8):

$$Z(t) = \frac{E_0 \cdot \sin(\omega t)}{I_0 \cdot \sin(\omega t + \phi)} = Z_0 \cdot \frac{\sin(\omega t)}{\sin(\omega t + \phi)} \qquad \text{Eq. } \mathbf{2.8}$$

A very common way to express impedance is using complex notation as in Eq. 2.9:

$$Z(t) = Z_0 \cdot (cos\phi + i \cdot sin\phi) = Z' + i \cdot Z'' \qquad \text{Eq. } \mathbf{2.9}$$

where i is the imaginary unit ($i = \sqrt{-1}$), while Z' and Z'' is the real and the imaginary part of the impedance, respectively.

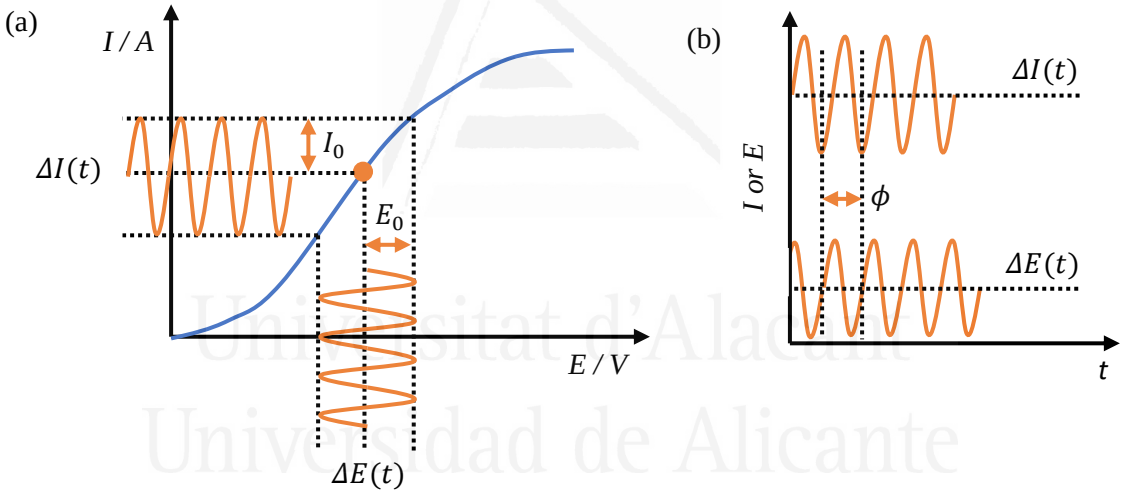

Figure 2.9. (a) Current *vs.* potential curve for a certain electrochemical system together with a scheme showing the superimposed sinusoidal potential perturbation signal ($\Delta E(t)$) with an amplitude of E_0 producing a sinusoidal current response ($\Delta I(t)$) with its corresponding amplitude (I_0). (b) Sinusoidal waves for both $\Delta I(t)$ and $\Delta E(t)$ illustrating the difference in phase (ϕ).

As already stated, a conventional experimental EIS procedure consists in applying to the working electrode a small sinusoidal potential perturbation for a wide range of

frequencies and with a constant amplitude of between 5 and 15 mV, which is over-imposed to a constant bias potential. If these measurements are performed under constant illumination (as done in the context of these studies) the technique is called photoelectrochemical impedance spectroscopy (PEIS). Then, the resulting sinusoidal perturbed current is analyzed. To do so, the so-called Nyquist plot is the most common representation, allowing for an analysis of both the nature of the double-layer phenomena and the kinetic characteristics of the photoelectrochemical reactions.

Another important parameter that can be obtained from impedance data is the capacitance of the space charge region. In this case, the applied frequency is kept constant and the potential value is changed. The results from these measurements, performed in both in the dark and under illumination in this thesis, are plotted according to the so-called Mott-Schottky representation, and allow to obtain essential information about the charge carrier density and the location of the flat-band potential.

2.3.3.1. Constant frequency: Mott-Schottky representation

For an *n*-type semiconductor, the Mott-Schottky equation is defined as (Eq. 2.10):

$$\frac{1}{C_{SCR}^2} = \frac{2}{\varepsilon\varepsilon_0 N_d e}\left(\Delta\phi_{SCR} - \frac{kT}{e}\right) \qquad \text{Eq. } \mathbf{2.10}$$

where C_{SCR} is the capacitance of the space charge region, ε is the dielectric constant, ε_0 is the vacuum electric permittivity, N_d is the density of impurities in the semiconductor, e is the elementary charge, $\Delta\phi_{SCR}$ is the inner potential difference between the semiconductor bulk and the semiconductor surface (band bending), k is the Boltzmann constant, and T is the temperature.

Importantly, this equation can only be applied when the capacitance of the Helmholtz layer (C_H) is significantly greater than that corresponding to the space charge region (C_{SCR}). This restriction implies that the electrode capacitance should be equal to C_{SCR}. For this reason, any change in the applied potential value is exclusively translated to the space charge layer, while the potential drop across the Helmholtz layer remains constant. In other words, Mott-Schottky analysis can only be performed under band edge pinning conditions. Subsequently, it can be admitted that $\Delta\phi_{SCR}$ is equivalent to $E - E_{fb}$, being E and E_{fb} the applied potential and the flat-band potential, respectively, thus obtaining Eq. 2.11:

$$\frac{1}{C_{SCR}^2} = \frac{2}{\varepsilon\varepsilon_0 N_d e}\left(E - E_{fb} - \frac{kT}{e}\right) \qquad \text{Eq. } \mathbf{2.11}$$

As observed, the representation of C_{SCR}^{-2} with respect to E defines a linear region with a positive or a negative slope (for an *n*-type and *p*-type semiconductor, respectively) whose intercept with the *x*-axis would correspond to E_{fb} (Figure 2.10). In this way, the equation (and corresponding representation) provides a straightforward way to determine the flat band potential and the majority charge carrier density that can be calculated from the slope.

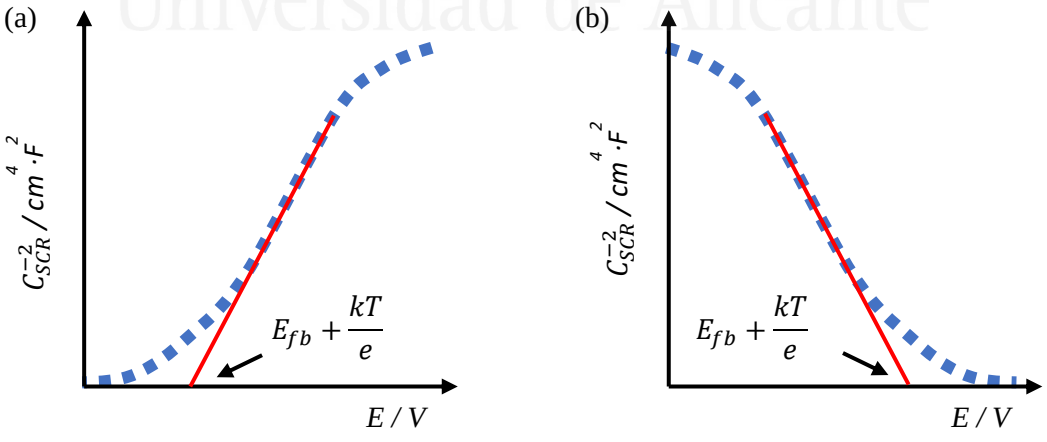

Figure 2.10. Ideal Mott-Schottky plot for an (a) *n*-type and (b) *p*-type semiconductor electrode.

For a correct application of the Mott-Schottky equations, further assumptions must be considered [17–20]: (i) only one type of impurities, fully ionized and homogeneously distributed along the space charge region, is present in the sample; (ii) the electric resistance of both substrate and electrolyte is extremely low, and the measured capacitance is not influenced by a possible loss of current across the interface and does not include contributions from surface states, adsoption processes or the Helmholtz layer; (iii) the dielectric constant of the semiconductor material is frequency-independent; and (iv) the interface is completely planar and two-dimensionally infinite.

The application of this type of analysis to our thin film electrodes is fully consistent since they have a negligible curvature and do not present a tridimensional morphology (as it is the case of nanostructured electrodes) [17,21]. In this thesis, Mott-Schottky analysis have been performed in Chapters III and IX with the aim of determining flat-band potential values and dopant densities for pristine and doped $BiVO_4$ and $NdFeO_3$ photoelectrodes, respectively.

2.3.3.2. Constant potential: Nyquist representation

Nyquist plots are one of the most common outputs of impedance data. They consist of representing minus the imaginary component of the impedance ($-Z''$) with respect to its real part (Z'), with each point representing the impedance value at one frequency. Low and high frequency data are represented on the right and left side of the plot, respectively. Plots with different features appear depending on the nature of the system. One of the typical plots is characterized by its semicircular shape or by a sequence of semicircles, as exemplified in Figure 2.11. Nevertheless, the appearance of linear regions (normally linked to diffusion-controlled processes) cannot be ruled out [10,15,16,22].

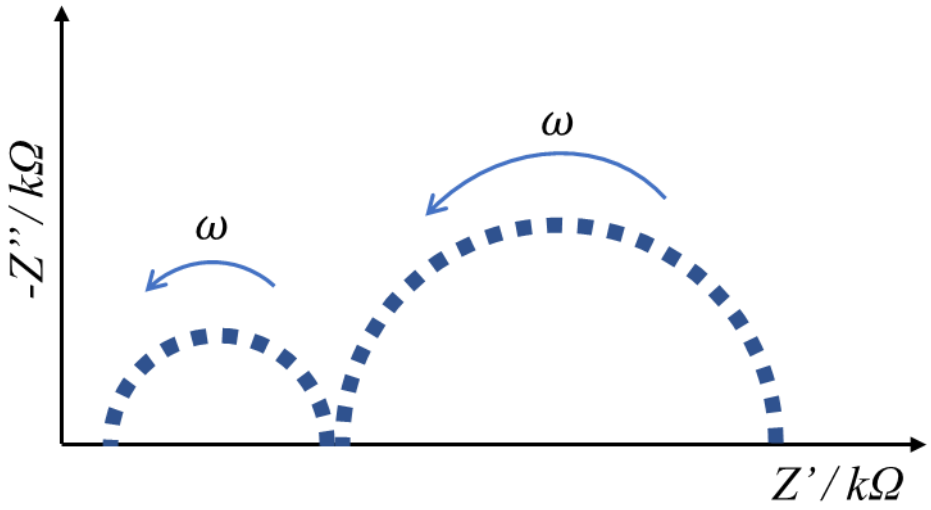

Figure 2.11. Ideal Nyquist plot showing two semicircles (each point corresponds to a different value of frequency).

From this type of plot, important quantitative information regarding the electrochemical processes happening in the system can be obtained but, first, the impedance data is commonly fitted to an equivalent circuit model [23]. These models are based on a network of electrical circuit elements, such as resistors, inductors and capacitors (among others), with an analogous behavior to that shown by the system being studied. In this way, different system parameters as the charge transfer resistance (R_{ct}), the electrolytic solution resistance (R_s) or the capacitance of the space charge region (C_{SCR}) can be determined. It is important that all possible elements in the equivalent model have a real meaning related to some electrochemical process or physical aspect of the system.

However, it is also possible to perform a simply qualitative analysis from the shape of the graph: a semicircular shape in a certain frequency range indicates that the process is kinetically controlled, while a straight line is indicative that it is controlled by diffusion aspects.

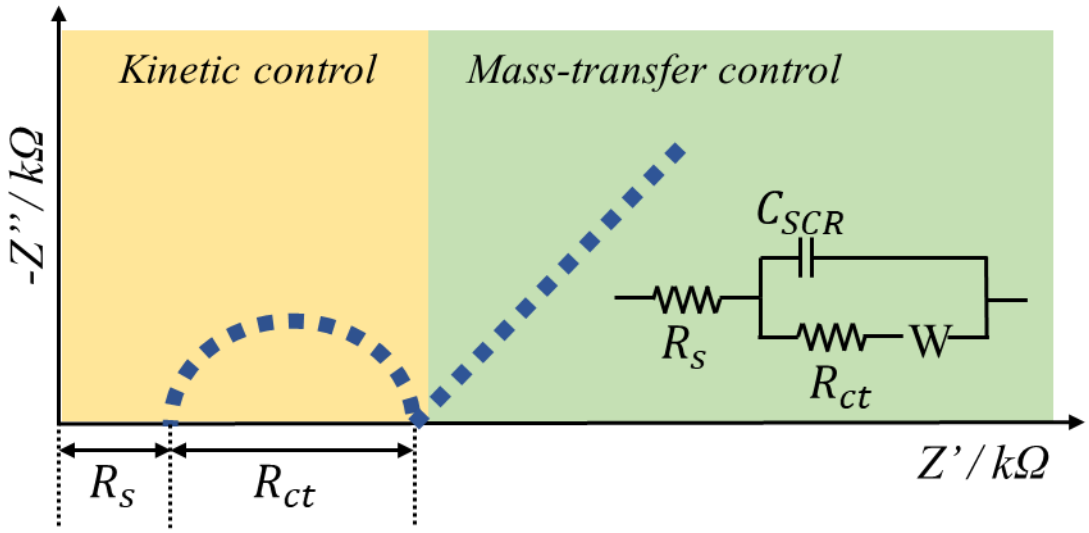

Figure 2.12. Nyquist plot highlighting different control zones. The inset shows the corresponding circuit.

Figure 2.12 shows the scheme of a possible Nyquist plot. According to the literature, if it is fitted to the simple model electric circuit shown in the inset (valid for a one-electron redox process), the diameter of the semicircle appearing at low frequencies would correspond to R_{ct} and the high-frequency intercept on the real axis, to R_s. From a pure quantitative point of view, and from the shape of the plot, it can be said that the process is kinetically and mass-transfer controlled at high and low frequencies, respectively.

In the context of these thesis, PEIS impedance measurements with Nyquist plots are shown in Chapter X to study, from a simply qualitative point of view, the surface modification of $NdFeO_3$ photocathodes with an extracting TiO_2 layer and with a Ni deposit acting as a co-catalyst.

2.3.4. Intensity-modulated photocurrent spectroscopy (IMPS) and intensity-modulated photovoltage spectroscopy (IMVS)

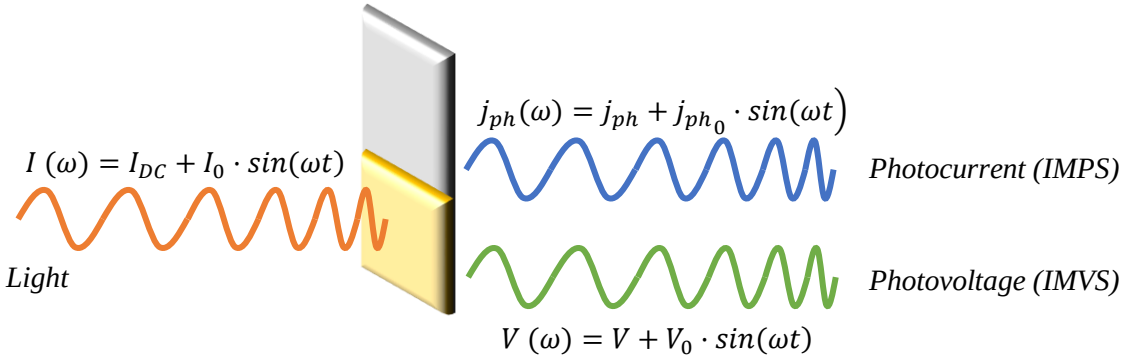

Figure 2.13. Scheme of intensity-modulated photocurrent spectroscopy (IMPS) and intensity-modulated photovoltage spectroscopy (IMVS).

Intensity-modulated photocurrent spectroscopy (IMPS) and intensity-modulated photovoltage spectroscopy (IMVS) are closely related to electrochemical impedance spectroscopy (EIS). In fact, instead of modulating the amplitude of a current or potential signal, both IMPS and IMVS techniques are based on the application of a small-signal harmonic perturbation of the irradiation intensity and the resulting photocurrent (IMPS) or photovoltage (IMVS) is then measured (Figure 2.13). By changing the frequency of the light signal during an experiment, time-dependent information about various processes such as diffusion coefficients or reaction rates can be obtained [24].

In IMPS and IMVS experiments, two electrical contacts are applied: the injecting contact, which is optically transparent and where the irradiation is applied, and the collecting contact. The irradiation consists of a base intensity (I_{DC}) with a superimposed sinusoidal waveform with a certain amplitude (I_0) (Eq. 2.12):

$$I\ (\omega) = I_{DC} + I_0 \cdot sin(\omega t) \qquad \text{Eq. } \mathbf{2.12}$$

When this modulated irradiation is applied through the injecting contact of the photoelectrode, charge carriers are generated in the vicinity of this contact. Since the light intensity is harmonically modulated (by changing the frequency of the sine wave during the experiment), the generation rate of the electron-hole pairs is also a sinusoidal function of time. The generated charge carriers migrate to the collecting contact and the resulting photocurrent (IMPS) or photovoltage (IMVS) is then measured (Eq. 2.13 and 2.14, respectively):

$$j_{ph}(\omega) = j_{ph} + j_{ph_0} \cdot sin(\omega t + \phi) \quad \text{Eq. } \mathbf{2.13}$$

$$V(\omega) = V + V_0 \cdot sin(\omega t + \phi) \quad \text{Eq. } \mathbf{2.14}$$

where j_{ph_0} and V_0 are the amplitude of the modulated photocurrent density and voltage, respectively, and ϕ is the corresponding phase.

Similar to EIS –but in this case with light instead of voltage– the resultant signal has the same frequency as the applied signal, but its phase is shifted with respect to the phase of the incident irradiation.

IMPS and IMVS experiments are shown in Chapter VIII to further characterize the photoelectrochemical characteristics of $LaFeO_3$ photoanodes.

2.4. X-RAY DIFFRACTION (XRD)

X-ray diffraction (XRD) is currently the standard characterization technique for the analysis and identification of crystal structures, including lattice parameters and spacing between lattice planes (Miller indices), of crystalline or partially crystalline materials. However, it can also be applied to the study of non-crystalline phases [25–28].

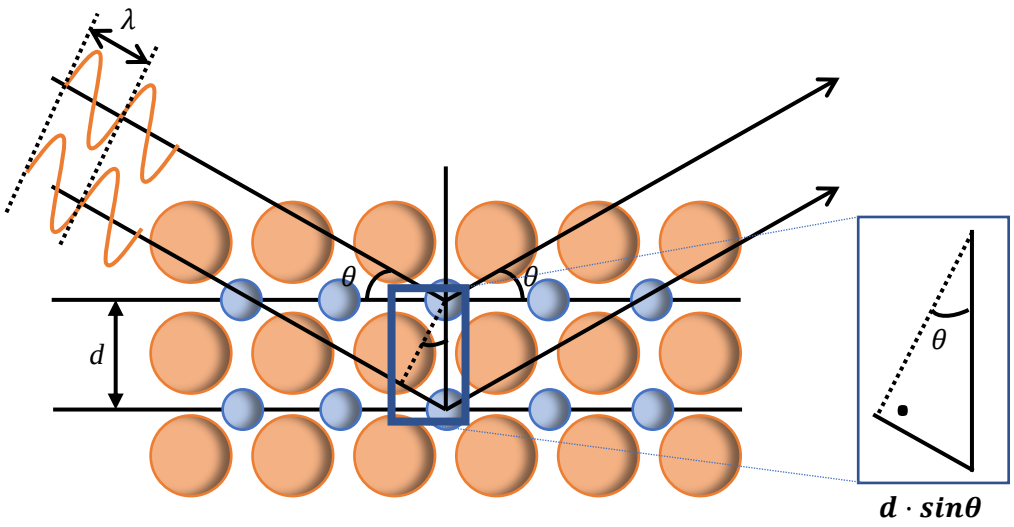

Figure 2.14. Sketch for the X-ray diffraction phenomenon in a crystalline arrangement with interplanar spacing *d*.

The basis of this technique lays on the phenomenon of X-ray diffraction (Figure 2.14): when a beam of this type of radiation interacts with an ordered crystal structure, constructive and non-constructive interferences between the scattered rays are generated because the spacing between planes is in the same order of magnitude that the incident radiation wavelength. Thus, in this technique, an X-ray radiation is directed toward a crystalline sample and the scattered intensity is measured as a function of the outgoing direction (defined from the scattering angle, 2θ). A diffraction pattern is thus obtained, and it is characteristic of the crystalline compound being analyzed.

Constructive interferences obey Bragg's Law (Eq. 2.15):

$$n \cdot \lambda = 2 \cdot d \cdot sin\theta \qquad \text{Eq. } \mathbf{2.15}$$

where n is a positive integer number ($n > 0$) indicating the order of reflection, λ is the wavelength of the X-ray beam, d is the interplanar space of the crystal, and θ is the angle of incidence of the X-rays. According to this equation, when an X-ray with a wavelength λ hits

the sample with an angle θ, a constructive interference is produced when d in the sample allows the wave to cross the $2 \cdot d \cdot sin\theta$ distance n times.

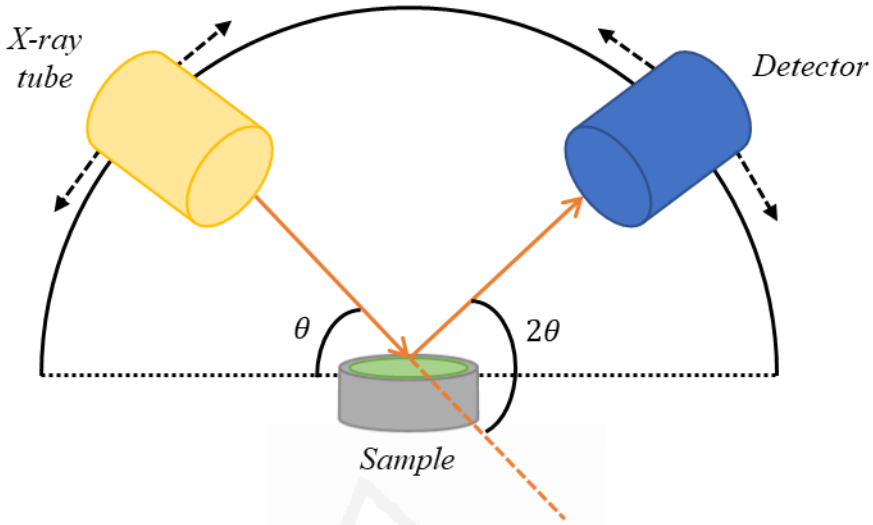

Figure 2.15. Schematic of the basic experimental arrangement to carry out an X-ray diffraction analysis.

The instrument necessary to carry out these experiments is called diffractometer, which is equipped with an X-ray source, a sample holder and an X-ray detector (Figure 2.15). Normally, the relative position of both X-ray source and detector can be adjusted, keeping the angle between the sample and the direction of the X-ray beam (θ) equal to that between the sample and the diffracted beam. The latter arrives finally to the detector and it is analyzed by scanning the diffraction angle between two limit values. The resulting plot (the so-called diffraction pattern) shows the constructive interferences of the X-ray beam with the sample as different peaks at certain 2θ angle values. The characteristic space between diffracting planes of atoms (d) is the magnitude that determine peak positions, and each peak represents a given set of planes of the crystalline sample. The reference diffraction patterns for the

different crystalline materials are gathered in databases, such as the Crystallography Open Database (COD) and the International Center of Diffraction Data (ICDD).

XRD also allows for a determination of the preferential orientation of the material, which is a crucial aspect in the case of synthesis procedures based on direct growth on the substrate. In fact, the orientation of the crystal in the film is able to determine the physical properties, and more importantly in the context of this study, the (photo)electrochemical activity of the electrode. When the material has a clear preferential orientation, only peaks ascribed to these orientations appear in the diffraction pattern.

XRD analysis are presented in Chapters III, IV, V, VIII and IX, and they have been carried out to identify the structure and crystalline phase of the synthesized materials.

2.5. SPECTROSCOPIC METHODS

In this section, the set of spectroscopic techniques employed in this thesis are briefly described. Spectroscopic methods stand out as useful tools for evaluating the electronic structure, composition and light harvesting capability of the sample, among others.

2.5.1. Ultraviolet-visible absorption spectroscopy (UV-vis)

Ultraviolet-visible absorption spectroscopy (UV-vis) is a technique that allows to evaluate the light absorption capability of a material by quantifying the amount of absorbed, transmitted or reflected light by a sample as a function of the incident wavelength [29].

The equipment required for these experiments is called spectrophotometer (Figure 2.16). In it, a collimated light beam coming from a source lamp passes through a monochromator placed between the lamp and the sample, which separates the incoming white light into its different wavelengths. When light with a certain intensity (I_0) interacts

with the sample, the beam can be split in different components. This can be expressed as in Eq. 2.16:

$$I_0 = I_A + R_{sp} + R_d + S + I_T \qquad \text{Eq. } \mathbf{2.16}$$

where I_A is the fraction of light absorbed by the sample, R_{sp} is the specularly reflected light, R_d is the diffuse reflected light, S is the refracted light (which will be considered negligible), and I_T corresponds to the fraction of transmitted light.

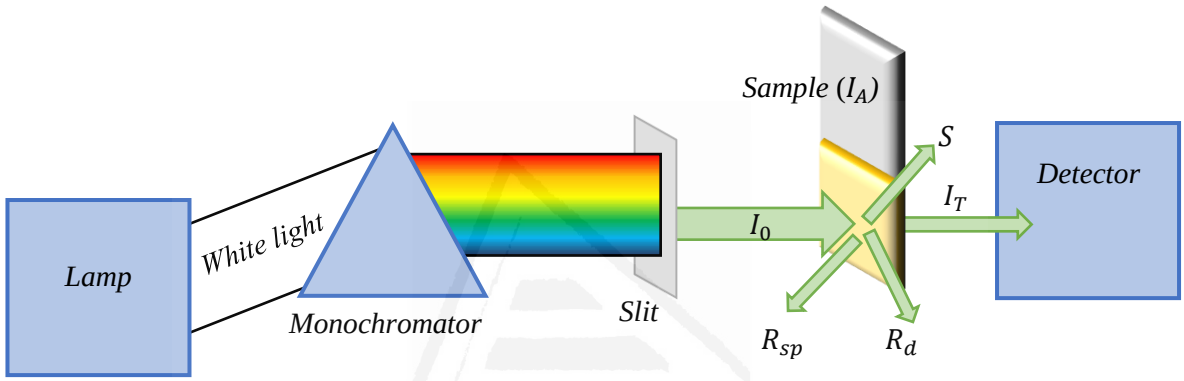

Figure 2.16. Illustration of a spectrophotometer working in transmission mode.

Since measurements consider the light absorption by the semiconductor material and the substrate (in this case, FTO glass), a baseline corresponding to total transmission for the substrate (blank value) is required. The absorbed light is measured as the absorbance (A), related with the transmittance by Eq. 2.17:

$$A = -log\frac{I_T}{I_0} = -\log(T) \qquad \text{Eq. } \mathbf{2.17}$$

The resulting plot of the absorbance *versus* the wavelength is called the absorption spectrum, and it constitutes the first step to obtain information about the electronic structure of the semiconductor and its ability for absorbing light, primarily defined by its band gap value (E_g). It is usually calculated by applying the Tauc equation (Eq. 2.18):

$$\alpha = \frac{B \cdot (h\nu - E_g)^m}{h\nu}$$ Eq. **2.18**

where α is the absorption coefficient, B is a constant, and m is an exponent whose value depends on the nature of the considered optical transition, being 0.5 and 2 for direct and indirect transitions, respectively. In this way, by plotting $(\alpha h\nu)^{1/2}$ or $(\alpha h\nu)^2$ *versus* $h\nu$ (in case of direct or indirect transition, respectively), the value of E_g can be obtained from the interception of the linear region in the resulting plot with the *x* axis. The determination of the variation of the absorption coefficient with the wavelength is obtained from the corresponding absorbance spectrum.

UV-vis absorption spectroscopy measurements have been used in Chapters III, VIII and IX to obtain information about the optical properties of $BiVO_4$, $LaFeO_3$ and $NdFeO_3$, respectively.

2.5.2. X-ray photoelectron spectroscopy (XPS)

X-ray photoelectron spectroscopy (XPS) is a technique suitable to gain insight into the chemical composition, chemical environment and oxidation states of the different elements (especially, those located on the surface) that constitute the sample [28,30].

An XPS instrument is basically a spectrometer provided with an X-ray source (those with magnesium or aluminum blanks are the most commonly used), a sample holder, an analyzer, a detector and a signal processor. This technique is based on the irradiation of the sample with a monochromatic beam of X-rays with photons of a certain energy value ($h\nu$), which induces the emission of electrons from the core of the atoms constituting the sample (Figure 2.17). These electrons are known as photoelectrons, and their kinetic energy (E_{kin})

is measured by the spectrophotometer. In this way, it is defined the binding energy (BE) as the energy required to remove an electron from a certain atomic level as (Eq. 2.19):

$$BE = h\nu - (E_{kin} + \phi)$$ Eq. **2.19**

where ϕ is the characteristic work function of the spectrophotometer. An XPS spectrum is thus obtained by representing the intensity of the flux of photoelectrons emitted as a function of the binding energy, and it exhibits different peaks corresponding to photoelectrons coming from different atoms (or levels). The position of the peaks in the spectrum depends on the number of valence electrons (related to the oxidation state) in the atom and the type of bonds with neighboring atoms (that is, the chemical environment). Importantly, the emitted photoelectrons cannot escape beyond a few nanometers of sample (from 1 to 5 nm), which explains that XPS is an especially indicated technique to obtain information about the surface of a sample without significant contributions from the bulk.

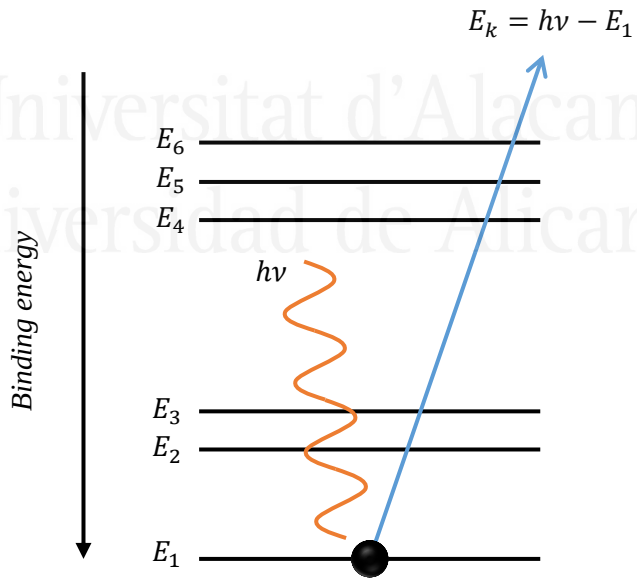

Figure 2.17. Emission of an electron as a result of the interaction of the atom with an X-ray photon.

Given that XPS is a semi-quantitative technique, approximate atomic percentages of the elements present in the sample can also be determined. The equipment usually incorporates a sputtering system (for example, of Ar^+ cations) able to perform in-depth analysis by a progressive elimination (pickling process) of surface material.

In this thesis, XPS measurements are presented in all chapters, and they have been used to obtain information about the surface chemical composition and oxidation states of the prepared photoelectrodes, electrocatalysts and co-catalysts, prior and after the (photo)electrochemical characterization.

2.5.3. Photoluminescence spectroscopy

Photoluminescence spectroscopy is a type of electromagnetic spectroscopy that analyzes photoluminescence from a sample. Photoluminescence is light emission from any form of matter after the absorption of photons. It is one of many forms of luminescence (*i.e.*, light emission) and is initiated by photoexcitation (*i.e.*, photons that excite electrons to a higher energy level in an atom. Following excitation various relaxation processes typically occur in which other photons are re-radiated. Time periods between absorption and emission may vary: ranging from short femtosecond-regime for emission involving free-carrier plasma in inorganic semiconductors up to milliseconds for phosphorescence processes in molecular systems; and under special circumstances delay of emission may even span to minutes or hours. This spectroscopic technique involves using a beam of light, usually ultraviolet light, that excites the electrons in molecules of certain compounds and causes them to emit light; typically, but not necessarily, visible light.

The basis of this technique is related to the fact that molecules have various states referred to as energy levels. Generally, the species being examined has a ground electronic

state (a low energy state) of interest, and an excited electronic state of higher energy. Within each of these electronic states there are various vibrational states. At this point, it is important to highlight that there are two types of photoluminescence that differ in the nature of the ground and excited states: fluorescence and phosphorescence. In both cases, a molecule is excited from a singlet ground state to a singlet excited state by the absorption of radiation in the UV or visible region of the spectrum. This electronic excitation is accompanied by excitation to a higher vibrational energy level. The excited molecules may rapidly lose vibrational energy by collisions with neighboring molecules. In this context, fluorescence is the emission of light at a longer wavelength than the incident radiation as the molecule returns from a singlet excited state to a singlet ground state after the loss of vibrational energy, while phosphorescence is the emission of light at a longer wavelength than the incident radiation as a molecule returns from an excited electronic state to a ground electronic state of different spin multiplicity, generally a triplet excited state returning to a singlet ground state (Figure 2.18). As a result of this electronic relaxation, the molecule then drops down to one of the various vibrational levels of the ground electronic state again, emitting a photon in the process. As molecules may drop down into any of several vibrational levels in the ground state, the emitted photons will have different energies, and thus frequencies. Therefore, by analyzing the different frequencies of light emitted in fluorescence spectroscopy, along with their relative intensities, the structure of the different vibrational levels can be determined.

In a conventional photoluminescence spectrophotometer, the light from an excitation source passes through a filter or monochromator, and strikes the sample. A proportion of the incident light is absorbed by the sample, and some of the molecules in the sample fluoresce. The fluorescent light is emitted in all directions. Some of this fluorescent light passes through a second filter or monochromator and reaches a detector, which is usually placed at 90° to

the incident light beam to minimize the risk of transmitted or reflected incident light reaching the detector.

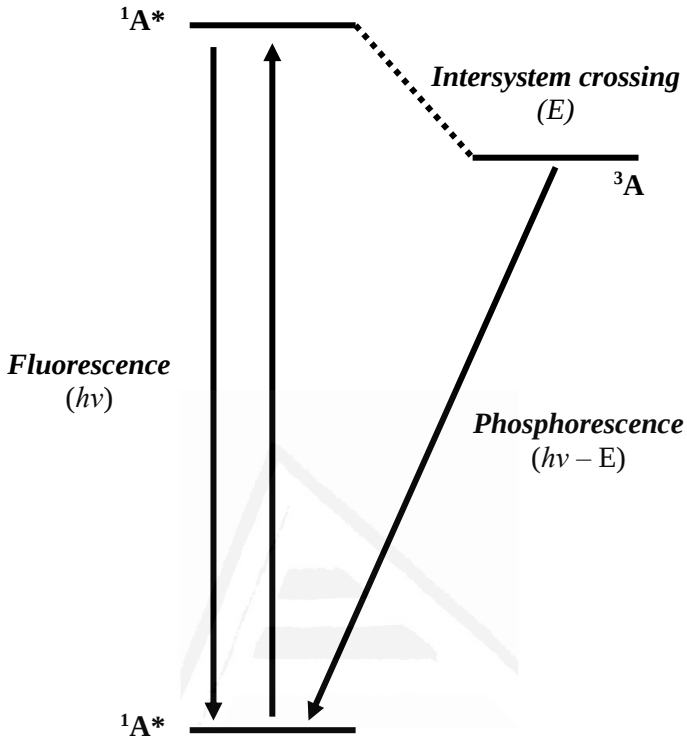

Figure 2.18. Jablonski diagram of an energy scheme showing the difference between fluorescence and phosphoresce.

Steady-state and time-resolved photoluminescence spectrometry has been used in Chapter VIII to elucidate the carrier recombination dynamics without the interference of the electrocatalytic reaction in $LaFeO_3$ photoanodes.

2.5.4. Raman spectroscopy

Raman spectroscopy is a technique that provides information regarding the chemical and physical state of a sample from characteristic vibrational, rotational and other low-frequency modes data obtained by the analysis of scattered photons. This technique, which

stands out for its high spectral resolution, can be used for both qualitative and quantitative purposes by measuring the frequency or the intensity of the scattered radiation, respectively [31,32].

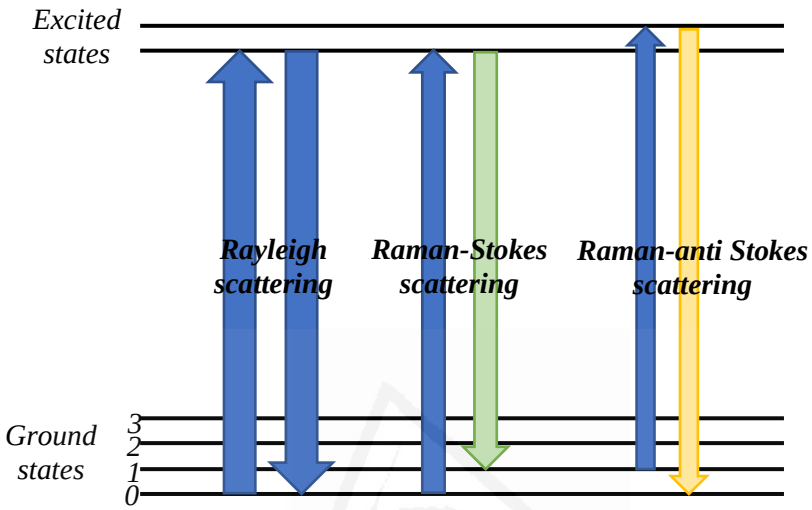

Figure 2.19. Energy level transitions involved in Raman scattering (the width of the arrows is proportional to the strength of the corresponding signal).

To carry out a Raman analysis, the sample is irradiated with an excitation wavelength coming from a laser beam (emitting in the visible, near infrared or near ultraviolet range) and with a certain wavenumber (υ_0). As a result, the sample is excited to a short-lived state, which rapidly decays due to its low stability, delivering scattered radiation. Most of this scattered radiation has the same frequency than that corresponding to the incident radiation due to elastic scattering phenomena (excited species return to their original energy state) and constituting the so-called Rayleigh scattering. However, inelastic scattering processes (when the excited sample returns to a different rotational or vibrational state upon relaxation) imply an energy exchange between incident photons and the sample. As consequence, a small portion of the scattered radiation has a different frequency, phenomenon known as Raman

effect (Figure 2.19). In these circumstances, the Raman shift ($\Delta\nu$), which denotes the energy levels spacing, can be defined as (Eq. 2.20):

$$\Delta\nu = \nu_0 - \nu_{scattered} \quad \text{Eq. } \mathbf{2.20}$$

where $\nu_{scattered}$ is the wavenumber of the scattered radiation. In this way, we refer to Stokes lines, when the frequency of the scattered radiation is lower than that corresponding to the incident radiation, and anti-Stokes lines, when the outcoming frequency is higher [28,33].

Raman measurements are included in Chapters V, VI and VIII to shed more light on the structural characteristics of synthesized materials. This was of special utility in regard to the diverse architectures of different Fe-Ni and Fe-Co electrocatalysts (Chapter VI).

2.6. ELECTRON MICROSCOPIC METHODS

Electron microscopic techniques provide important information about the morphology, topography, size of nanoparticles composition of the studied systems, which are factors that can determine in an important way the final properties of the semiconductors employed as photoelectrodes.

The basis of these microscopic techniques is to irradiate a solid sample with a highly focused beam of electrons. As a result of the interaction between the sample and the electronic beam, different signals can be emitted, including backscattered, secondary, transmitted and Auger electrons, and X-ray and visible photons (Figure 2.20) [34]. Giving this fact, electron microscopy techniques can be divided into two main categories: scanning electron microscopy (SEM), which detects backscattered and secondary electrons, and transmission electron microscopy (TEM), analyzing transmitted electrons [35–37].

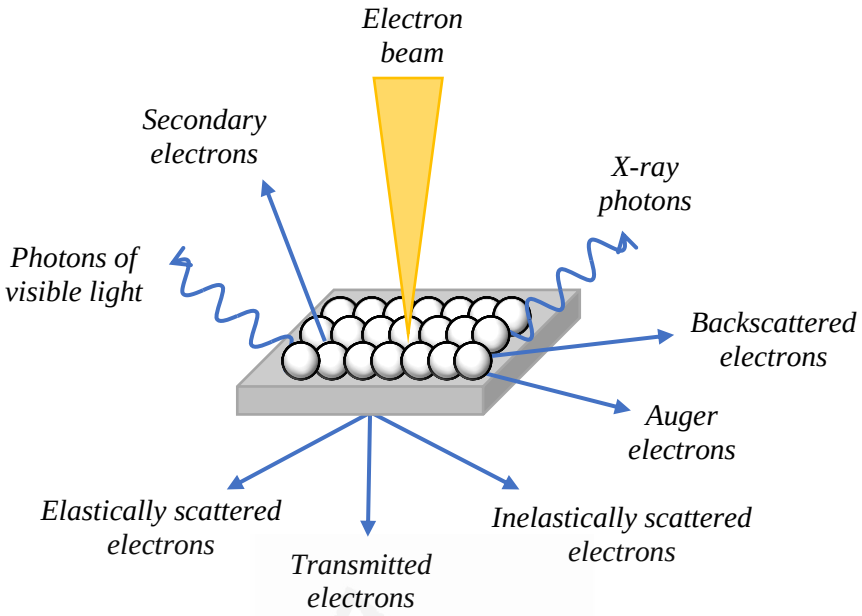

Figure 2.20. Signals generated in electron microscopes when a beam of electrons interacts with a solid sample.

2.6.1. Scanning electron microscopy (SEM)

Scanning electron microscopy (SEM) is a technique able to offer images from the analysis of secondary and backscattered electrons coming from the sample [28,35,37]. Secondary electrons are the result of the interactions between the incident electron beam and weakly bound electrons located near the surface of the sample and not associated with any specific atom. As a consequence, the analysis of these electrons (which present energies lower than 50 eV) do not provide specific elemental information, only offering information on morphology. On the contrary, backscattered electrons are electrons coming from the incident beam scattered by the sample after having interacted with it. Consequently, they are more energetic (with energy levels from 50 eV to that corresponding to the incident beam, usually between 5 and 30 keV) allowing for a compositional analysis of the sample surface. The relation of the intensity of the backscattered signal with the atomic number of the atom

from which it comes enables obtaining a map of the different elements existing in the sample [26,28].

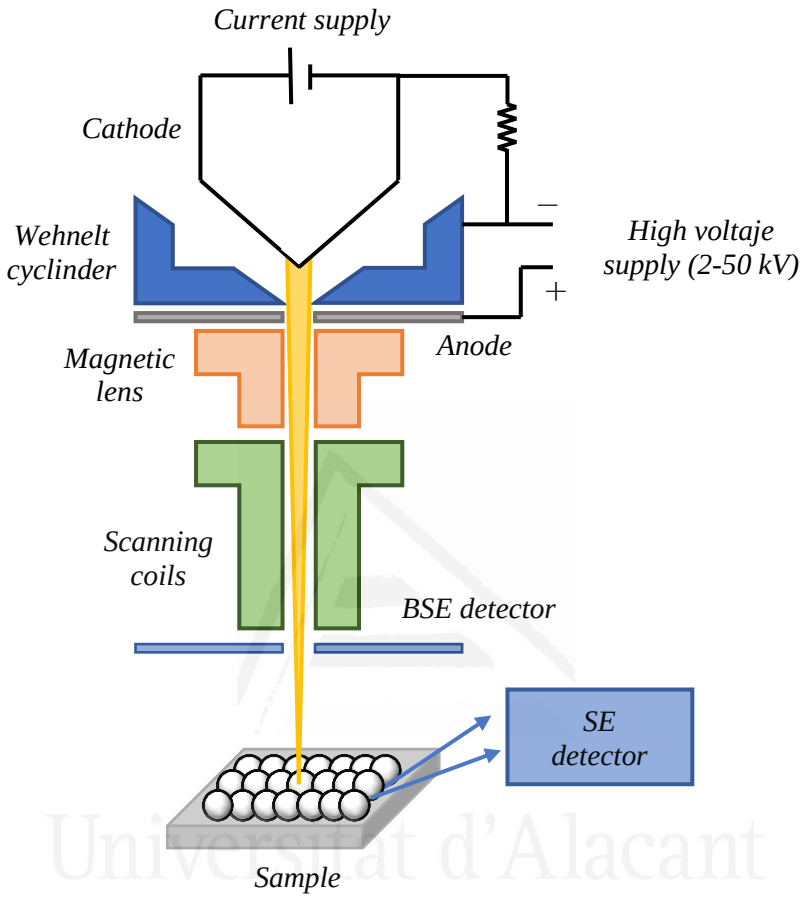

Figure 2.21. Different components of a scanning electron microscope (SEM).

In a conventional SEM equipment (Figure 2.21), the electron beam is generated by an electron gun located at the upper part of the instrument, that usually has a column shape. A Wehnelt cylinder acts as a convergent electrostatic lens that focuses and controls the direction of the generated electron beam. This is accelerated by an anode and focused on an extremely fine region of the sample with a combination of a magnetic condenser and an objective lens. The scanning of the surface of the sample is thus performed in the XY plane directing the electron beam with a combination of electromagnetic coils located in the objective lenses.

The interaction of the beam with the sample originates backscattered and secondary electrons that are collected using an electron detector. It is important to mention that the whole beam path occurs under vacuum conditions to minimize the density of interfering gas molecules.

Modern SEM equipment based on electron field-emission (FE-SEM) can generate images with higher magnifications and more importantly, higher resolutions. In this case, the electron gun is a field emission source able to provide a narrower electron beam at both low and high energy. This improves the spatial resolution at lower acceleration voltages and also minimizes the charging effects on the samples, which avoids their possible damage and enhances the image quality.

FE-SEM images are included in all chapters of this thesis in order to morphologically characterize the prepared materials.

2.6.2. Transmission electron microscopy (TEM)

Contrary to what happens in a SEM analysis, transmission electron microscopy (TEM) is a technique in which transmitted/dispersed electrons are used for imaging ultrathin samples with high resolution in the micro- and nanoscale [28,34,36].

Since a TEM microscope collects the electrons transmitted by the sample, a beam (between 50 and 200 keV) more energetic than in SEM is required. It is important to remark that only the electrons passing through the sample are used to create the image on a screen (Figure 2.22), without considering possible scattered electrons. As a result of the electron beam passing through the sample, its intensity diminishes. This intensity/energy loss is greater in thicker regions of the sample or with presence of elements with high atomic number. The greater the loss of beam intensity in a given area of the sample, the darker the resulting image on the fluorescent screen. In this way, the resulting image consists of a wide

range of grey tonalities given the different interactions and scattering processes experienced by the electron beam passing through the different regions of the sample.

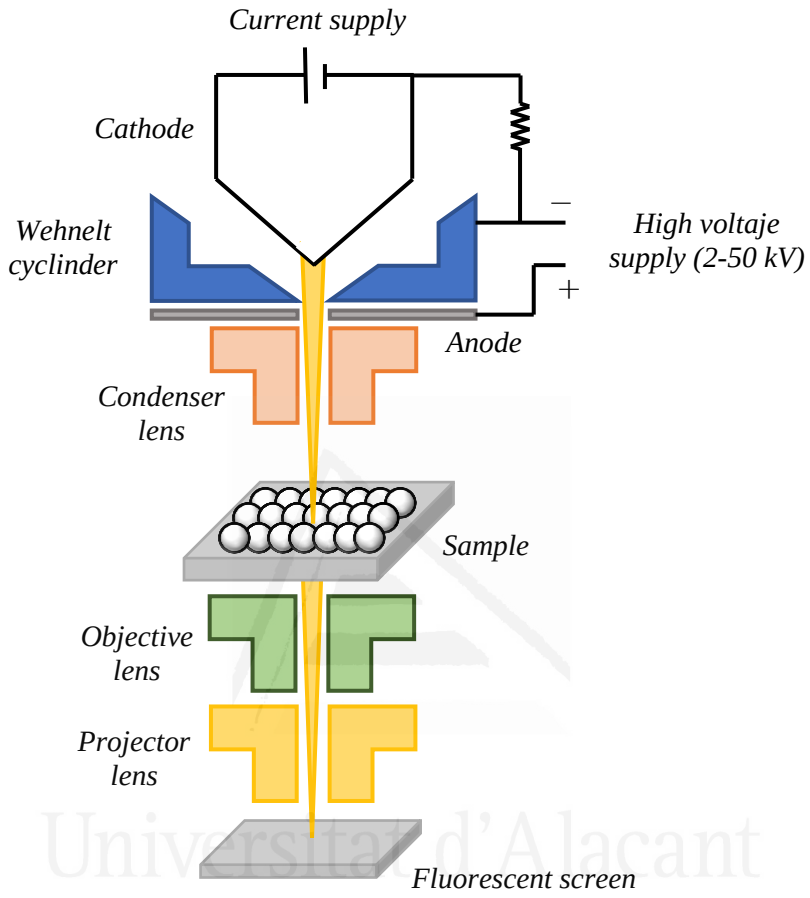

Figure 2.22. Different components of a transmission electron microscope (TEM).

In TEM, the electron beam is also generated in the upper part of the microscope and it is focused and controlled with a Wehnelt cylinder. The generated beam travels along the column through condenser lenses that it is focused on the sample, which transmits it. Finally, and with the transmitted electrons, the objective lens builds the corresponding image, which is magnified by the projector lens on a fluorescent screen or in a digital device. The resolution increases for sample thicknesses lower than 100 nm.

TEM results are shown in Chapter IV to characterize the $Ni(OH)_2$ deposits acting as co-catalysts on the $BiVO_4$ photoanodes.

2.7. OTHER EXPERIMENTAL METHODS

2.7.1. Gas chromatography

Gas chromatography is a common type of chromatography used in analytical chemistry for separating and analyzing compounds that can be vaporized without decomposition. Typical uses of GC include testing the purity of a substance, or separating the different components of a mixture (the relative amounts of such components can also be determined) and the identification of a certain compound.

In gas chromatography, the mobile phase is a carrier gas, usually an inert gas such as helium or an unreactive gas such as nitrogen, while the stationary phase is a microscopic layer of liquid or polymer on an inert solid support, inside a piece of glass or metal tubing called a column. The instrument used to perform gas chromatography is called a gas chromatograph (Figure 2.23). A known volume of gaseous or liquid analyte is injected into the "entrance" (head) of the column, usually using a microsyringe. As the carrier gas sweeps the analyte molecules through the column, this motion is inhibited by the adsorption of the analyte molecules either onto the column walls or onto packing materials in the column. The rate at which the molecules progress along the column depends on the strength of adsorption, which in turn depends on the type of molecule and the stationary phase materials implied. Since each type of molecule has a different rate of progression, the various components of the analyte mixture are separated as they progress along the column, reaching the end of the column at different times (retention time). A detector is used to monitor the outlet stream from the column; thus, the time at which each component reaches the outlet and the amount

of that component can be determined. Generally, substances are identified (qualitatively) by the order in which they emerge (elute) from the column and by the retention time of the analyte in the column.

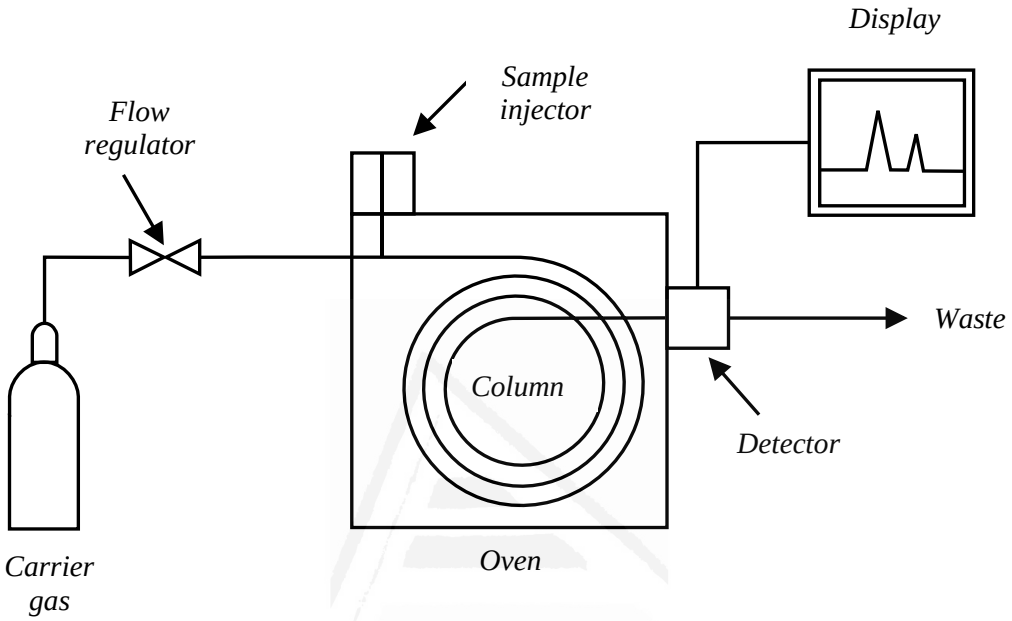

Figure 2.23. Diagram of a typical gas chromatograph.

Gas chromatography is in principle similar to column chromatography (as well as other forms of chromatography, such as HPLC), but has several notable differences. First, the process of separating the compounds in a mixture is carried out between a liquid stationary phase and a gas mobile phase, whereas in column chromatography the stationary phase is a solid and the mobile phase is a liquid. Second, the column through which the gas phase passes is located in an oven where the temperature of the gas can be controlled, whereas column chromatography (typically) has no such temperature control. Finally, the concentration of a compound in the gas phase is solely a function of its vapor pressure.

Gas chromatography using a plasma emission detector has been used in Chapter VIII as an evidence for the oxygen production associated to the photo-assisted water oxidation on $LaFeO_3$ photoanodes.

2.8. COMPUTATIONAL METHODS

In the context of this thesis, computational methods based on density-functional theory (DFT) have been performed in Chapter IX. DFT is a computational quantum mechanical modelling method used in Physics, Chemistry and Materials Science to investigate the electronic (or nuclear) structure (principally that related to the ground state) of many-body systems, in particular, atoms, molecules, and the condensed phases [38]. Using this theory, the properties of a many-electron system can be determined by using functionals (*i.e.*, functions of another function), which in this case is the spatially dependent electron density. So, the name 'density functional theory' comes from the use of functionals of the electron density.

DFT is among the most popular and versatile methods available in computational chemistry since the 1970s. However, DFT was not considered accurate enough for calculations in quantum chemistry until the 1990s, when the approximations used in the theory were greatly refined to better model the exchange and correlation interactions. Computational costs are relatively low when compared to traditional methods, such as exchange only Hartree-Fock theory (and its derivatives) that include electron correlation.

Despite recent improvements, there are still difficulties in using density functional theory to properly describe (i) intermolecular interactions (of critical importance to understanding chemical reactions), (ii) charge transfer excitations, (iii) transition states, (iv) dopant interactions, (v) some strongly correlated systems, and (vi) the band gap and

ferromagnetism in semiconductors. The development of new DFT methods designed to overcome these problems, by alterations to the functional or by the inclusion of additive correction terms is a current research topic.

In Chapter IX, different functionals of electron density (PBE+U and HSE03) are used to obtain electronic information (conduction and valence bands orbital contributions, band gap value and effective masses of charge carriers) in the $NdFeO_3$ perovskite. These DFT calculations have been performed with the Vienna *ab initio* simulation package (VASP, version 5.4.4) software, under the projector augmented wave (PAW) method. VESTA, P4VASP and VASPKIT have been used as visualization programs for 3D structural models, volumetric data such as electron/nuclear densities, density of states, band structure, and crystal morphologies. Regarding the hardware, it is important to mention that all these programs have been executed in a cluster consisting of three nodes (computers) with the following specifications:

- Node01: 8 AMD Opteron(tm) Processor 6380 (64 cores), 251 GB of RAM, 1 NVIDIA Tesla K40c GPU with 12 GB of RAM and 1 NVIDIA GPU Geforce GTX TITAN Black with 6 GB of RAM.

- Node02: 8 ADM Opteron(tm) Processor 6168 (48 cores) with 125 GB of RAM.

- Node03: 2 Intel (R) Xeon (R) 2.20 GHz, 125 GB of RAM and 4 GPU NVIDIA Tesla P100 with 16GB of RAM each.

2.9. REFERENCES

[1] C.J. Brinker, G.W. Scherer, Sol-gel science: the physics and chemistry of sol-gel processing, Academic Press, Inc., San Diego, 1990.
[2] J. Quiñonero, T. Lana-Villarreal, R. Gómez, Appl. Catal. B Environ. 194 (2016) 141.
[3] J. Quiñonero, R. Gómez, Appl. Catal. B Environ. 217 (2017) 437.
[4] J.H. Kim, J.H. Kim, J.-W. Jang, J.Y. Kim, S.H. Choi, G. Magesh, J. Lee, J.S. Lee,

Adv. Energy Mater. 5 (2015) 1401933.
[5] M.I. Díez-García, R. Gómez, ChemSusChem. 10 (2017) 2457.
[6] B.A. Ezekoye, P.O. Offor, V.A. Ezekoye, F.I. Ezema, Int. J. Sci. Res. 2 (2013) 452.
[7] J. Quiñonero, R. Gómez, Electrochim. Acta 274 (2018) 224.
[8] D. Cibrev, M. Jankulovska, T. Lana-Villarreal, R. Gómez, Int. J. Hydrogen Energy. 38 (2013) 2746.
[9] J.S. Newman, Electrochemical Systems (Second Edition), Prentice-Hall, Inc., Englewood Cliffs, 1991.
[10] A.J. Bard, L.R. Faulkner, Electrochemical Methods: Fundamentals and Applications, New York, 2001.
[11] K.D. Malviya, H. Dotan, K.R. Yoon, I.D. Kim, A. Rothschild, J. Mater. Res. 31 (2016) 1565.
[12] 'High power mercury-xenon light sources' can be found under https://www.newport.com/f/research-arc-lamp-sources-450-1000-w, 2020.
[13] P.T. Kissinger, W.R. Heineman, J. Chem. Educ. 60 (1983) 702.
[14] E. Barsoukov, J.R. McDonald, Impedance Spectroscopy Theory, Experiment and Applications, Wiley Interscience, New York, 2005.
[15] S.M. Park, J.S. Yoo, Anal. Chem. 75 (2003) 455A.
[16] A. Lasia, Electrochemical Impedance Spectroscopy and Its Applications, Springer Science, New York, 2014.
[17] F. Cardon, W.P. Gomes, J. Phys. D Appl. Phys. 11 (1978) L63.
[18] G. Horowitz, J. Electroanal. Chem. 159 (1983) 421.
[19] K. Gelderman, L. Lee, S.W. Donne, J. Chem. Educ. 84 (2007) 685.
[20] Y.V. Pleskov, Y.Y. Gurevich, Semiconductor Photoelectrochemistry, Consultants Bureau, New York, 1986.
[21] A. Cots, D. Cibrev, P. Bonete, R. Gómez, ChemElectroChem. 4 (2017) 585.
[22] D.D. McDonald, Electrochim. Acta. 51 (2006) 1376.
[23] F. Ciucci, Curr. Opin. Electrochem. 13 (2019) 132.
[24] E. Barsoukov, J.R. Macdonald, Impedance Spectroscopy. Theory, Experiment, and Applications, Wiley-Int, Hoboken, New Jersey, 2005.
[25] Y. Waseda, E. Matsubara, K. Shinoda, X-Ray Diffraction Crystallography. Introduction, Examples and Solved Problems, Springer, New York, 2011.
[26] K. Oura, V.G. Lifshits, A. Sarain, A.V. Zotov, M. Katayama, Surface Science: An Introduction, Springer, Berlin, 2003.
[27] B.D. Cullity, S.R. Stock, Elements of X-Ray Diffraction, Pearson, Harlow, 2001.
[28] D.A. Skoog, F.J. Holler, S.R. Crouch, Principles of Instrumental Analysis, Brooks Cole, Belmont, 2006.
[29] T. Owen, Fundamentals of UV-vis Spectroscopy, Hewlett Packard, Waldbronn, 1996.
[30] J.F. Moulder, W.F. Stickle, P.E. Sobol, K.D. Bomben, Handbook of X-ray Photoelectron Spectroscopy, Perkin-Elmer Corporation, Eden Prairie, 1991.
[31] H.W. Safford, J. Chem. Edu. 43 (1966) 506.
[32] C.V. Raman, K.S. Krishnan, Nature. 121 (1928) 501.
[33] E. Smith, G. Dent, Modern Raman Spectroscopy-A Practical Approach, John Wiley & Sons, Chichester, 2005.
[34] P.J. Goodhew, F.J. Humphreys, R. Beanland, Electron Microscopy and Analysis, Taylor & Francis, London, 2001.
[35] L. Reimer, Scanning Electron Microscopy, Springer, New York, 1985.

[36] R.D. Heidenreich, Fundamentals of Transmission Electron Microscopy, Interscience Publishers, New York, 1964.
[37] W. Zhou, Z.L. Wang, Scanning Microscopy for Nanotechnology, Springer Science, New York, 2007.
[38] R.G. Parr, W. Yang, Density-Functional Theory of Atoms and Molecules, Oxford University Press, New York, 1989.

PUBLISHED WORKS

CHAPTER III

Improving the photoactivity of bismuth vanadate thin film photoanodes through doping and surface modification strategies

Applied Catalysis B: Environmental 194 (2016) 141–149

Contents lists available at ScienceDirect

Applied Catalysis B: Environmental

journal homepage: www.elsevier.com/locate/apcatb

Improving the photoactivity of bismuth vanadate thin film photoanodes through doping and surface modification strategies

Javier Quiñonero, Teresa Lana–Villarreal*, Roberto Gómez*

Departament de Química Física i Institut Universitari d'Electroquímica, Universitat d'Alacant, Apartat 99, E-03080 Alicante, Spain

ARTICLE INFO

Article history:
Received 3 February 2016
Received in revised form 8 April 2016
Accepted 27 April 2016
Available online 29 April 2016

Keywords:
Photoelectro chemistry
Water splitting
La doping
Ce doping
Gold nanoparticles

ABSTRACT

Currently, one of the most attractive and desirable ways to solve the energy challenge is harvesting energy directly from the sunlight through the so-called artificial photosynthesis. Among the ternary oxides based on earth–abundant metals, bismuth vanadate has recently emerged as a promising photoanode. Herein, $BiVO_4$ thin film photoanodes have been successfully synthesized by a modified metal-organic precursor decomposition method, followed by an annealing treatment. In an attempt to improve the photocatalytic properties of this semiconductor material for photoelectrochemical water oxidation, the electrodes have been modified (i) by doping with La and Ce (by modifying the composition of the $BiVO_4$ precursor solution with the desired concentration of the doping element), and (ii) by surface modification with Au nanoparticles potentiostatically electrodeposited. La and Ce doping at concentrations of 1 and 2 at% in the $BiVO_4$ precursor solution, respectively, enhances significantly the photoelectrocatalytic performance of $BiVO_4$ without introducing important changes in either the material structure or the electrode morphology, according to XRD and SEM characterization. In addition, surface modification of the electrodes with Au nanoparticles further enhances the photocurrent as such metallic nanoparticles act as co-catalysts, promoting charge transfer at the semiconductor/solution interface. The combination of these two complementary ways of modifying the electrodes has resulted in a significant increase in the photoresponse, facilitating their potential application in artificial photosynthesis devices.

1. Introduction

The world is facing serious challenges due to the limited supply of energy and to the global climate change caused by burning fossil fuels. It is widely known that the outstanding technical development experienced by humanity through the employment of non-renewable energy sources has induced an undeniable negative impact on the natural environment. In fact, the use of traditional fossil fuels causes the generation of gases (CO_2, CH_4, SO_2, NO_x...) likely to aggravate certain pollution problems, such as the greenhouse effect and the acid rain. This situation could worsen during the next decades by the sharply growing global energy demand: it has been estimated that global energy consumption will reach almost 27 TW by 2050, while nowadays it is close to 15 TW. The combination of these two factors has motivated the search for new energy sources to minimize the emissions of such pollutant gases and/or economical methods for their recycling (mainly in the case of CO_2) [1].

In this context, artificial photosynthesis – the capture, conversion and storage of solar energy in chemical bonds – stands as a central research subject in the field of renewable energy because it is a very attractive approach to solve the current energy challenges. This is due to its great potential to convert photon energy from sunlight into chemical energy with a minimal environmental impact, as in the case of natural photosynthesis [2]. In fact, nowadays one of the most promising technologies for the production of hydrogen from renewable energy sources is photoelectrochemical (PEC) solar water splitting on semiconductor electrodes because it is a sustainable, carbon neutral and cost-effective process to produce solar fuels [3–5]. The concept of water splitting into oxygen and hydrogen was first demonstrated by Fujishima and Honda in 1972 using a TiO_2 photoanode under ultraviolet light irradiation and a dark platinum cathode [6]. Due to the slow kinetics associated with multi-electron and multi-proton transfers (PEC water splitting has approximately three orders of magnitude lower rate than the hydrogen evolution reaction in conventional water electrolysis [7]), water oxidation is particularly demanding and requires high overpotentials. Therefore, many efforts have been made to develop

* Corresponding authors.
E-mail addresses: teresa.lana@ua.es (T. Lana–Villarreal), roberto.gomez@ua.es (R. Gómez).

http://dx.doi.org/10.1016/j.apcatb.2016.04.057
0926-3373/

CHAPTER IV

Controlling the amount of co-catalyst as a critical factor in determining the efficiency of photoelectrodes: The case of nickel (II) hydroxide on vanadate photoanodes

Applied Catalysis B: Environmental 217 (2017) 437–447

Contents lists available at ScienceDirect

Applied Catalysis B: Environmental

journal homepage: www.elsevier.com/locate/apcatb

Controlling the amount of co-catalyst as a critical factor in determining the efficiency of photoelectrodes: The case of nickel (II) hydroxide on vanadate photoanodes

Javier Quiñonero, Roberto Gómez*

Departament de Química Física i Institut Universitari d'Electroquímica, Universitat d'Alacant, Apartat 99, E-03080 Alicante, Spain

ARTICLE INFO

Article history:
Received 16 March 2017
Received in revised form 31 May 2017
Accepted 3 June 2017
Available online 4 June 2017

Keywords:
Nickel hydroxide
Chemical bath deposition
Oxygen evolution reaction
Photoelectrocatalysis
$BiVO_4$ photoanodes
$FeVO_4$ photoanodes

ABSTRACT

A commonly followed strategy to enhance the performance of photoelectrodes for achieving viable water splitting devices consists in the use of co-catalysts. However, fine control of the amount of co-catalyst deposited on the electrode surface usually does not receive much attention, although it is an essential factor that crucially determines the efficiency of photoelectrodes. In this context, this study illustrates how the dark electrochemical characterization of co-catalyst-modified photoanodes may provide valuable information on the precise amount of electroactive co-catalyst present on the surface, facilitating our understanding of the manner in which co-catalysts work and paving the way for their optimization. For this purpose, ultrathin $Ni(OH)_2$ layers were deposited on either doped or pristine $BiVO_4$ and $FeVO_4$ photoanodes by a cost-effective and versatile chemical bath deposition method in which the deposition time allows to control the $Ni(OH)_2$ loading. The deposited $Ni(OH)_2$ is demonstrated to successfully catalyze the photoelectrochemical water oxidation process on both $BiVO_4$ and $FeVO_4$ electrodes, by improving the effective transfer of photogenerated holes from the semiconductor to solution. In fact, the electrocatalytic activity of the $Ni(OH)_2$-modified photoanodes rapidly increases with the amount of deposited $Ni(OH)_2$ until an optimum value is reached equivalent to only 0.46 and 1.68 $Ni(OH)_2$ monolayers for $BiVO_4$ and $FeVO_4$ electrodes, respectively. Under these conditions, $Ni(OH)_2$ enhances the photocurrent generation by a factor of 2 for $BiVO_4$ and of 1.2 for $FeVO_4$ photoanodes in contact with slightly alkaline solutions. The small loadings of $Ni(OH)_2$ leading to an optimum photoanode behavior indicate that hole transfer is favored on vanadate active surface sites, which would also be the preferential sites for $Ni(OH)_2$ deposition. Additional amounts of co-catalyst deposited for longer times induce a drastic decrease in the photoelectrocatalytic activity due to charge recombination at the semiconductor/$Ni(OH)_2$ interface, probably enhanced by the low carrier mobility in $Ni(OH)_2$. On the other hand, this study demonstrates that the preparation of efficient photoanodes for oxygen evolution with an extremely small amount of co-catalyst through a facile and scalable method is possible.

1. Introduction

In order to overcome the current global warming caused by the employment of fossil fuels and the continuously growing energy consumption, the development of green, non-polluting and renewable alternative technologies for energy supply is desirable. In particular, since its discovery by Fujishima and Honda in 1972 [1], producing H_2 as a solar fuel from photoelectrochemical (PEC) water decomposition methodologies on semiconductor electrodes using only sunlight as input energy has been considered as an interesting goal [2–4]. In this context, the search for efficient semiconductor materials with potential application in the development of photoanodes capable of photooxidizing water has mainly focused on binary metal oxides for the last few decades, basically on TiO_2 (E_g = 3.2 eV, for the anatase phase) [5,6], WO_3 (E_g = 2.7 eV) [7,8] and Fe_2O_3 (E_g = 2.2 eV) [9–11]. However, this research has now been directed in part toward several ternary oxides, such as some tantalates [12–14], titanates [15–18] and wolframates [19–21], among others. These also include certain vanadates ($BiVO_4$ [22–25], $FeVO_4$ [26–28] and $InVO_4$ [29,30]), which are characterized by their electrical *n*-type properties, their relatively low cost and toxicity, intrinsic visible light activity, and acceptable chemical and photochemical stability in aqueous electrolytes.

* Corresponding author.
E-mail address: roberto.gomez@ua.es (R. Gómez).

http://dx.doi.org/10.1016/j.apcatb.2017.06.005
0926-3373/

CHAPTER V

Iron and cobalt hydroxides: Describing the oxygen evolution reaction activity trend with the amount of electrocatalyst

Electrochimica Acta 274 (2018) 224–232

Contents lists available at ScienceDirect

Electrochimica Acta

journal homepage: www.elsevier.com/locate/electacta

Iron and cobalt hydroxides: Describing the oxygen evolution reaction activity trend with the amount of electrocatalyst

Javier Quiñonero, Roberto Gómez*

Departament de Química Física i Institut Universitari d'Electroquímica, Universitat d'Alacant, Apartat 99, E-03080 Alicante, Spain

ARTICLE INFO

Article history:
Received 18 January 2018
Received in revised form
22 March 2018
Accepted 10 April 2018
Available online 12 April 2018

Keywords:
Iron hydroxide
Cobalt hydroxide
Chemical bath deposition
Oxygen evolution reaction
Electrocatalysis

ABSTRACT

Although the amount of oxygen evolution electrocatalyst is a factor determining its efficiency, its fundamental correlation with activity remains unclear. To address this issue, we take advantage of a urea-based chemical bath deposition method (CBD) that enables to control the amount of electrocatalyst ($Fe(OH)_2$ and α-$Co(OH)_2$) deposited on conducting glass. The thickness of the resulting films, whose use in electrocatalysis is unprecedented, is tuned by controlling the deposition time. The turnover frequency (TOF) for O_2 generation decreases drastically as the electrocatalyst amount increases from equivalent coverages of 3.5 monolayers (ML) for $Fe(OH)_2$ and of 0.06 ML for α-$Co(OH)_2$ electrodes. The contrasting behavior of both hydroxides comes from the different structure of the incipient deposits, formed by small acicular nanoparticles in the case of $Fe(OH)_2$ and larger flat microparticles in the case of α-$Co(OH)_2$. The former structure allows a large fraction of the Fe sites to be in direct contact with solution, while such a fraction rapidly diminishes with loading for α-$Co(OH)_2$. In addition, the resulting $Co(OH)_2$ electrodes show TOFs similar or higher than those of electrodes prepared by more complex routes. The optimum ultrathin films are remarkably stable in alkaline media, showing that the preparation of efficient electrocatalysts for oxygen evolution with an extremely small amount of metal through a novel, facile and scalable CBD is possible.

1. Introduction

The electrolysis of water to produce oxygen and hydrogen is being considered as an attractive technology for sustainable and highly efficient energy generation [1–5]. The oxygen evolution reaction (OER), which is characterized by a slow kinetics (*i.e.*, large anodic overpotential) remains a critical step in this process and represents a significant efficiency loss in both electricity-driven and photodriven water splitting [6,7]. This fact prevents the straightforward development of certain clean energy technologies, including rechargeable metal-air batteries, water electrolysis systems, and solar-fuel devices.

Since the earliest works on OER electrocatalysis were reviewed by Trasatti [8,9] and Matsumoto [10] over thirty years ago, considerable research effort has been devoted to the design, synthesis, and characterization of efficient oxygen evolution catalysts (OECs). Currently, the optimal OECs in acidic media are noble metal-based catalysts, such as IrO_2 and RuO_2, since they exhibit the lowest overpotentials for the OER at practical current densities [11–14]. However, the scarcity of the corresponding metals, high cost, and poor long-term stability in alkaline media have hindered large-scale applications and highlighted the need for OECs with prospects of being employed at a practical level.

In this context, several studies have revealed that first-row transition metal oxides and (oxy)hydroxides (Mn [15–17], Fe [18–20], Co [21–23], and Ni [24–26]), along with certain spinel [27–29] and perovskite oxides [30–32], could offer a compromise solution: although they possess nonoptimal OER electrocatalytic activity, their environmental friendliness, low cost, and abundance in nature convert them into practical candidates for OECs [33–35]. In addition, they are stable in neutral to alkaline solutions and display moderate to good electrical conductivities. However, due to the existence of polymorphs, incidental impurity incorporation, and complicating effects of electronic conductivity and electrochemically active surface area, the fundamental correlations of activity with structure, composition, and amount of electrocatalyst are not quantitatively described yet.

In any case, iron-group metal hydroxides ($Fe(OH)_2$, $Co(OH)_2$ and $Ni(OH)_2$) with a layered structure have been suggested to be active,

* Corresponding author.
E-mail address: roberto.gomez@ua.es (R. Gómez).

https://doi.org/10.1016/j.electacta.2018.04.074
0013-4686/

CHAPTER VI

Tuning the oxygen evolution reaction activity of Ni- and Co-modified $Fe(OH)_2$ electrodes through structure and composition control

INTERNATIONAL JOURNAL OF HYDROGEN ENERGY 45 (2020) 17076–17087

Available online at www.sciencedirect.com

ScienceDirect

journal homepage: www.elsevier.com/locate/he

Tuning the oxygen evolution reaction activity of Ni- and Co-modified $Fe(OH)_2$ electrodes through structure and composition control

Javier Quiñonero, Teresa Lana-Villarreal, Roberto Gómez *

Departament de Química Física i Institut Universitari d'Electroquímica, Universitat d'Alacant, Apartat 99, E-03080, Alicante, Spain

HIGHLIGHTS

- Urea-based chemical bath deposition enables fine control of the hydroxide loading.
- Ni or Co and Fe hydroxides can be deposited either sequentially or simultaneously.
- O_2 evolution electrocatalysis is optimal for $Fe(OH)_2$ decorated with either Co or Ni.
- Adjacent Ni/Co and Fe sites exposed to solution are critical for electrocatalysis.
- Underlying $Fe(OH)_2$ enhances electrocatalysis at Ni or Co by a factor of 2 or more.

GRAPHICAL ABSTRACT

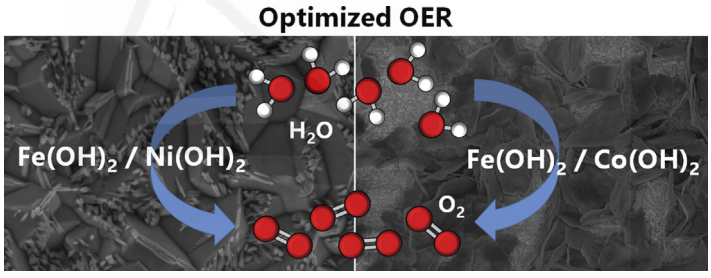

ARTICLE INFO

Article history:
Received 17 February 2020
Received in revised form
28 April 2020
Accepted 30 April 2020
Available online 2 June 2020

Keywords:
Nickel hydroxide
Cobalt hydroxide
Iron hydroxide
Chemical bath deposition
Oxygen evolution reaction
Electrocatalysis

ABSTRACT

NiFe- and CoFe-based (oxy)hydroxides stand out as promising and highly active earth-abundant electrocatalysts for the oxygen evolution reaction (OER) in alkaline media. $Fe(OH)_2$-$Ni(OH)_2$ and $Fe(OH)_2$-$Co(OH)_2$ electrodes have been prepared through a urea-based chemical bath deposition (CBD) method that enables to control and optimize structure and loading. The effect of the spatial arrangement of the metals in the hydroxide deposits on the electrocatalytic activity in alkaline media has been evaluated. Ultrathin films formed by bilayers resulting from the deposition of submonolayer amounts of Ni or Co hydroxides on previously deposited $Fe(OH)_2$ layers were found to exhibit the best electrocatalytic behavior. The turnover frequency for O_2 generation increases drastically as the amount of either Ni or Co decreases, reaching maximum values 2.6 and 1.6 times higher than those for FTO/$Ni(OH)_2$ and FTO/$Co(OH)_2$ electrodes, respectively. This shows that the presence of underlying $Fe(OH)_2$ nanoparticles plays a crucial role in enhancing the electrocatalytic properties of Ni or Co sites. The fact that these ultrathin electrodes, formed by extremely

* *Corresponding author.*
E-mail address: roberto.gomez@ua.es (R. Gómez).
https://doi.org/10.1016/j.ijhydene.2020.04.288

UNPUBLISHED WORKS

CHAPTER VII

Sequentially deposited $Fe(OH)_2/Ni(OH)_2$ oxygen evolution co-catalyst: Boosting the performance of bismuth vanadate photoanodes

7.1. ABSTRACT

To date, the highest-performing water splitting devices to drive the oxygen evolution reaction use semiconducting oxide photoanodes coated with water-oxidation co-catalysts. Given that the quantity of co-catalyst has been identified as a factor crucially determining the photoelectrochemical performance of photoanodes, this study shows a simple strategy to carry out the necessary optimization of the deposited amount of electrocatalyst. In this way, a novel $Fe(OH)_2/Ni(OH)_2$ co-catalyst has been deposited on $BiVO_4$ photoanodes by means of a urea-based chemical bath deposition method that allows for a precise and fine control of the deposited mass loading of the two different hydroxides by only controlling the deposition time. The optimum photoactivity (according to the photocurrent value at 1.23 V *vs*. RHE) for $BiVO_4/Fe(OH)_2/Ni(OH)_2$ photoanodes is obtained for equivalent coverage values of 2.4 and 0.8 monolayers for $Fe(OH)_2$ and $Ni(OH)_2$, respectively, which underlines the relatively small amounts of co-catalyst needed for an optimum photoelectrochemical performance.

7.2. INTRODUCTION

In the context of photoelectrochemical (PEC) water splitting, one of the most common strategies to develop more efficient photoanodes is their coupling with electrocatalytic surface layers or deposits (*i.e.*, co-catalysts) for the oxygen evolution reaction (OER) [1–5]. In fact, introducing co-catalysts has been demonstrated to be the most efficient way to lower the reaction kinetic barrier and promote charge injection to the reactants [6–9], which is manifested through an increase in the photocurrent and/or photopotential [10–12].

Given that heterogeneities at the semiconductor/electrolyte interface can greatly affect the photoelectrocatalysis, a proper optimization of the co-catalyst loading on the

semiconductor surface is critical to design high-performance systems [13]. In fact, a functional coupling of electrocatalysts with photoelectrodes must fulfill certain requirements, as that the co-catalyst does not block sunlight from reaching the light absorber, interfere in the transfer of photogenerated charge carriers or diminish the photoanode surface catalytic efficiency [14]. Although this optimization can only go through a fine control of the amount of electrocatalyst deposited on the electrode surface to prevent the above mentioned deleterious phenomena, there is still a lack of studies dealing with the fundamental correlations between the PEC activity of photoanodes and the co-catalyst loading.

7.3. RESULTS AND DISCUSSION

$Fe(OH)_2$ and $Ni(OH)_2$-based deposits (previously described as an electrocatalyst for the OER in the dark [15–20]) behave as effective co-catalyst on the surface of $BiVO_4$ photoanodes [21–25]. Importantly, the co-catalyst loading is shown to be critical in determining its effect. To this end, we use a urea-based chemical bath deposition (CBD) method which enables us to finely and sequentially deposit variable amounts of the two different metallic hydroxides on the semiconductor surface by only controlling the deposition time to obtain a $Fe(OH)_2/Ni(OH)_2$ architecture (see Supporting Information for full experimental details). The corresponding electrochemical characterization in the dark is used to quantitatively determine the amount of electroactive component (both $Fe(OH)_2$ and $Ni(OH)_2$) and this is correlated with the PEC performance to define an optimum loading of each hydroxide on $BiVO_4$.

The loading of $Fe(OH)_2$ was optimized first by varying the amount (*i.e.*, the deposition time) of deposited $Fe(OH)_2$ on $BiVO_4$ while maintaining constant the amount of deposited $Ni(OH)_2$ (in this case, that corresponding to a $Ni(OH)_2$ deposition time of 20

min, taking previous reports as a reference [26]). Figure 7.1a shows the electrochemical characterization in the dark for $BiVO_4/Fe(OH)_2/Ni(OH)_2$ photoanodes prepared for different $Fe(OH)_2$ deposition times (from 10 to 60 min) and for a constant $Ni(OH)_2$ deposition time of 20 min. As observed, the deposition of $Fe(OH)_2/Ni(OH)_2$ on $BiVO_4$ induces important changes on the characteristic voltammetric profile of this semiconductor material [26,27]. On the one hand, as the deposition of $Fe(OH)_2$ proceeds, a couple of peaks grows between -0.95 and -0.45 V, which according to the literature is associated with the $Fe(OH)_2 + OH^- \leftrightarrows FeOOH + H_2O + e^-$ redox process [28]. On the other, the deposition of $Ni(OH)_2$ leads to a cathodic peak centered at approximately 0.62 V and corresponding to the $NiOOH + H_2O + e^- \rightarrow Ni(OH)_2 + OH^-$ redox transformation [29]. As expected, the charge density corresponding to the oxidation of $Fe(OH)_2$ to FeOOH (q_{Fe}) increases with the $Fe(OH)_2$ deposition time (Figure S7.1a), while that corresponding to the NiOOH reduction peak (q_{Ni}) remains virtually constant at an average value of 0.11 $mC \cdot cm^{-2}$ (Figure S7.1b) (see Supporting Information and Figure S7.2 for full details regarding voltammetric charge estimation).

Linear scan voltammograms recorded under transient illumination for these as-prepared $BiVO_4/Fe(OH)_2/Ni(OH)_2$ electrodes (Figure 7.1b-c) reveal that the photocurrent values clearly depend on the $Fe(OH)_2$ deposition time. In fact, it increases until a maximum value is obtained for a $Fe(OH)_2$ deposition time of 30 min, while for longer times, a progressive decrease in the magnitude of the photocurrents is observed (for a deposition time of 60 min, the evident reduction in photocurrent is accompanied by a significant intensification of the anodic and cathodic spikes upon illumination/light interruption, which are a clear sign of electron-hole recombination). Figure 7.1d displays a plot of the photocurrent at 1.23 V (*vs.* RHE) for the $BiVO_4/Fe(OH)_2/Ni(OH)_2$ photoanodes *vs.* q_{Fe}. As shown, the optimum situation (*i.e.*, highest value of photocurrent)

is reached for a q_{Fe} value of approximately 0.64 mC·cm^{-2}, which corresponds to a $Fe(OH)_2$ deposition time of 30 min.

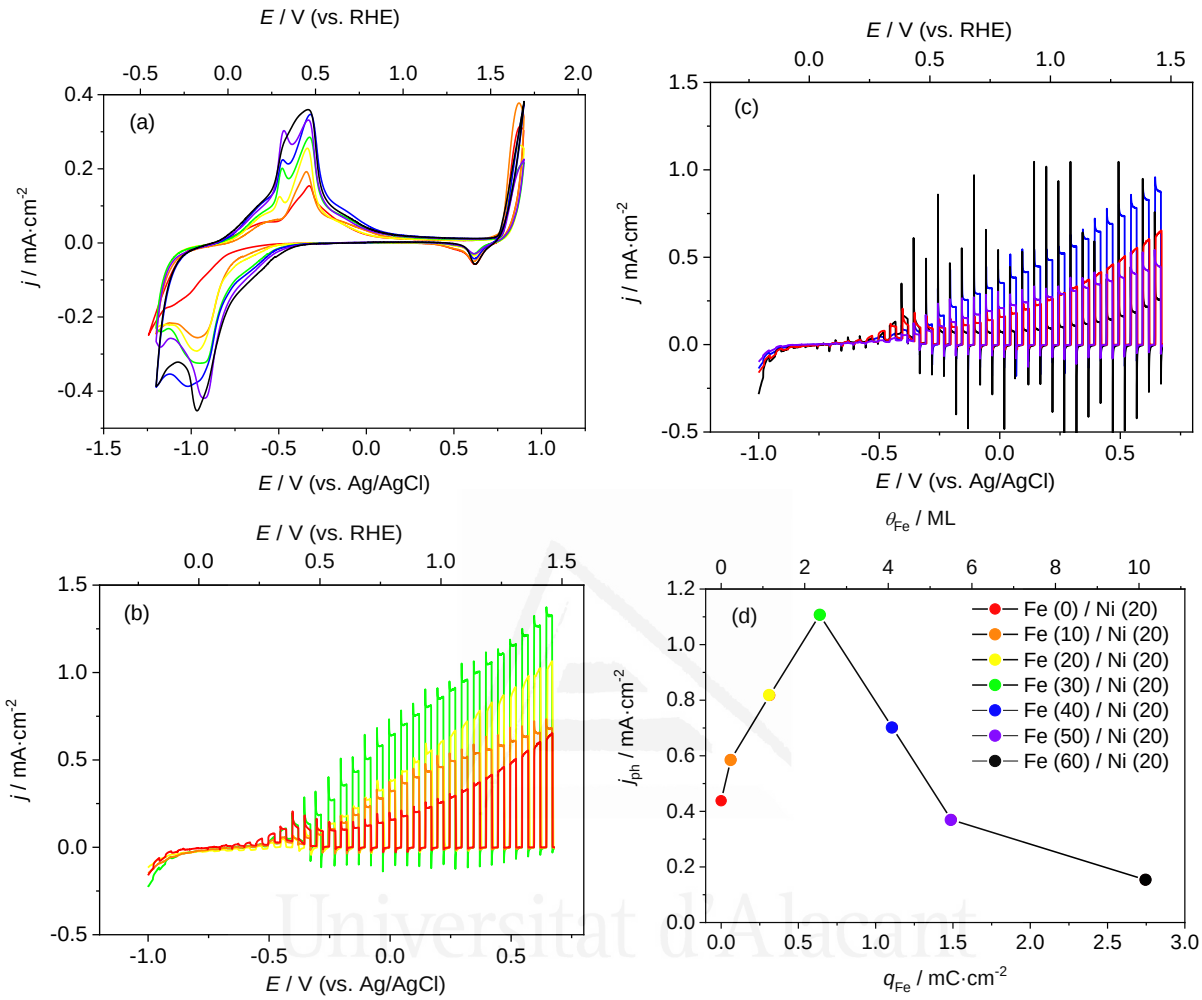

Figure 7.1. (a) Cyclic voltammograms (scan rate: 10 mV·s^{-1}) in the dark and (b, c) linear scan voltammograms (scan rate: 5 mV·s^{-1}) under transient illumination (100 mW·cm^{-2}, approx.) for $BiVO_4/Fe(OH)_2$ (t_d)/$Ni(OH)_2$ (20 min) electrodes, prepared for different $Fe(OH)_2$ deposition times (t_d = 0-60 min). (d) Photocurrent density for the OER at 1.23 V *vs*. RHE for $BiVO_4/Fe(OH)_2$ (t_d)/$Ni(OH)_2$ (20 min) photoanodes, prepared for different $Fe(OH)_2$ deposition times (t_d = 0-60 min), *versus* the charge density corresponding to the oxidation of $Fe(OH)_2$. The color code is common for all panels.

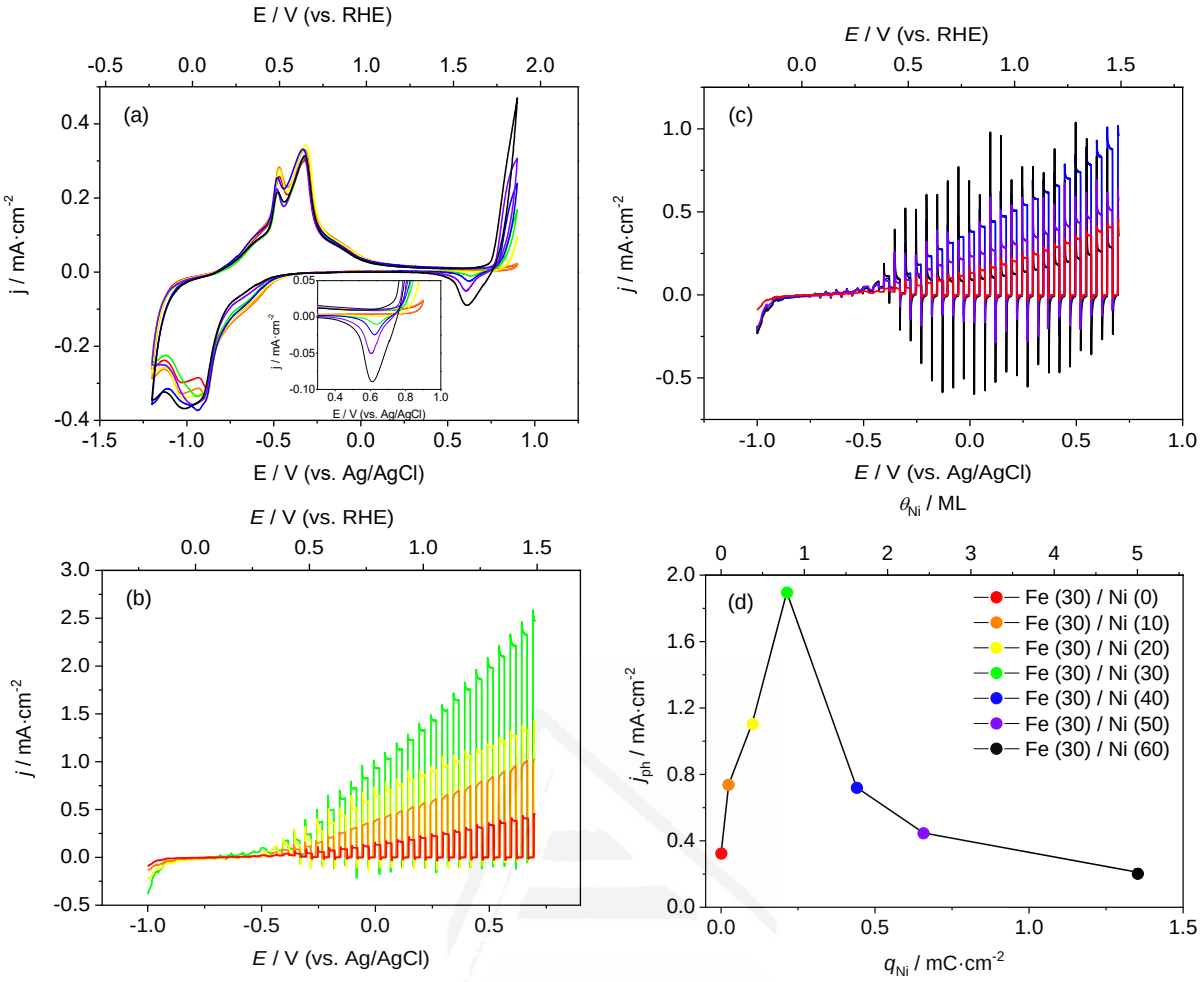

Figure 7.2. (a) Cyclic voltammograms (scan rate: 10 mV·s^{-1}) in the dark and (b, c) linear scan voltammograms (scan rate: 5 mV·s^{-1}) under transient illumination (100 mW·cm^{-2}, approx..) for $BiVO_4/Fe(OH)_2$ (t_d)/$Ni(OH)_2$ (20 min) electrodes, prepared for different $Fe(OH)_2$ deposition times (t_d = 0-60 min). (b) Photocurrent density for the OER at 1.23 V *vs*. RHE for $BiVO_4/Fe(OH)_2$ (30 min)/$Ni(OH)_2$ (t_d) photoanodes, prepared for different $Ni(OH)_2$ deposition times (t_d = 0-60 min), *versus* the charge density corresponding to the oxidation of $Fe(OH)_2$ (and *versus* the $Ni(OH)_2$ coverage on the electrode surface). The color code is common for all panels.

In a second step, the amount of $Ni(OH)_2$ deposited on $BiVO_4/Fe(OH)_2$ was optimized by varying the amount of deposited $Ni(OH)_2$ while keeping constant the optimized amount of $Fe(OH)_2$ on $BiVO_4$ (that corresponding to a deposition time of 30 min). Figure 7.2a shows the electrochemical characterization in the dark for $BiVO_4/Fe(OH)_2/Ni(OH)_2$ photoanodes prepared for different $Ni(OH)_2$ deposition times

(from 10 to 60 min) and for an optimum $Fe(OH)_2$ deposition time of 30 min. As expected, q_{Ni} increases with increasing deposition times (Figure S7.3a), whereas q_{Fe} remains approximately constant at an average value of 0.68 $mC \cdot cm^{-2}$ (Figure S7.3b). Linear scan voltammograms recorded under transient illumination for the $BiVO_4/Fe(OH)_2/Ni(OH)_2$ electrodes (Figure 7.2b-c) reveal once again that the magnitude of the photocurrents strongly depends on the nickel hydroxide loading. It progressively grows until a maximum value is obtained for a $Ni(OH)_2$ deposition time of 30 min and, from this point forward, a drastic decrease in the photocurrent is observed, following a trend similar to that observed in a previous study [26]. As already stated in the $Fe(OH)_2$ optimization step, the appearance of anodic and cathodic spikes indicates electron-hole recombination processes by hole trapping in the increasingly thicker co-catalyst layer. Figure 7.2d shows that the maximum photocurrent value is reached for a $Ni(OH)_2$ deposition time of 30 min (q_{Ni} ~ 0.21 $mC \cdot cm^{-2}$), which is assumed to correspond to the optimum $Ni(OH)_2$ loading on $FTO/BiVO_4/Fe(OH)_2$.

Figure 7.3a displays a representative top FESEM image for a $BiVO_4$ electrode surface-modified with the optimum amounts of $Fe(OH)_2$ and $Ni(OH)_2$ (corresponding to deposition times of 30 min for both hydroxides). This modification induces the appearance of a glomerular overstructure corresponding to the $Fe(OH)_2/Ni(OH)_2$ deposit heterogeneously distributed on the relatively rough surface of the $BiVO_4$ thin film, which remains largely uncoated (*i.e.*, exposed to the solution). Taking into account the loading and the characteristic morphology of each as-synthesized hydroxide (already described in previous reports [28,29]) it can be assumed that the observed overstructure is mainly composed of $Fe(OH)_2$, which on FTO initially grows in the form of fine grains that evolve into more rounded particles (as observed here) as deposition proceeds. As the $Ni(OH)_2$ loading is very low, the optimum $Fe(OH)_2/Ni(OH)_2$ overstructure has the same

morphology as the $Fe(OH)_2$. The presence of $Ni(OH)_2$ is only evident for longer $Ni(OH)_2$ deposition times (Figure S7.4).

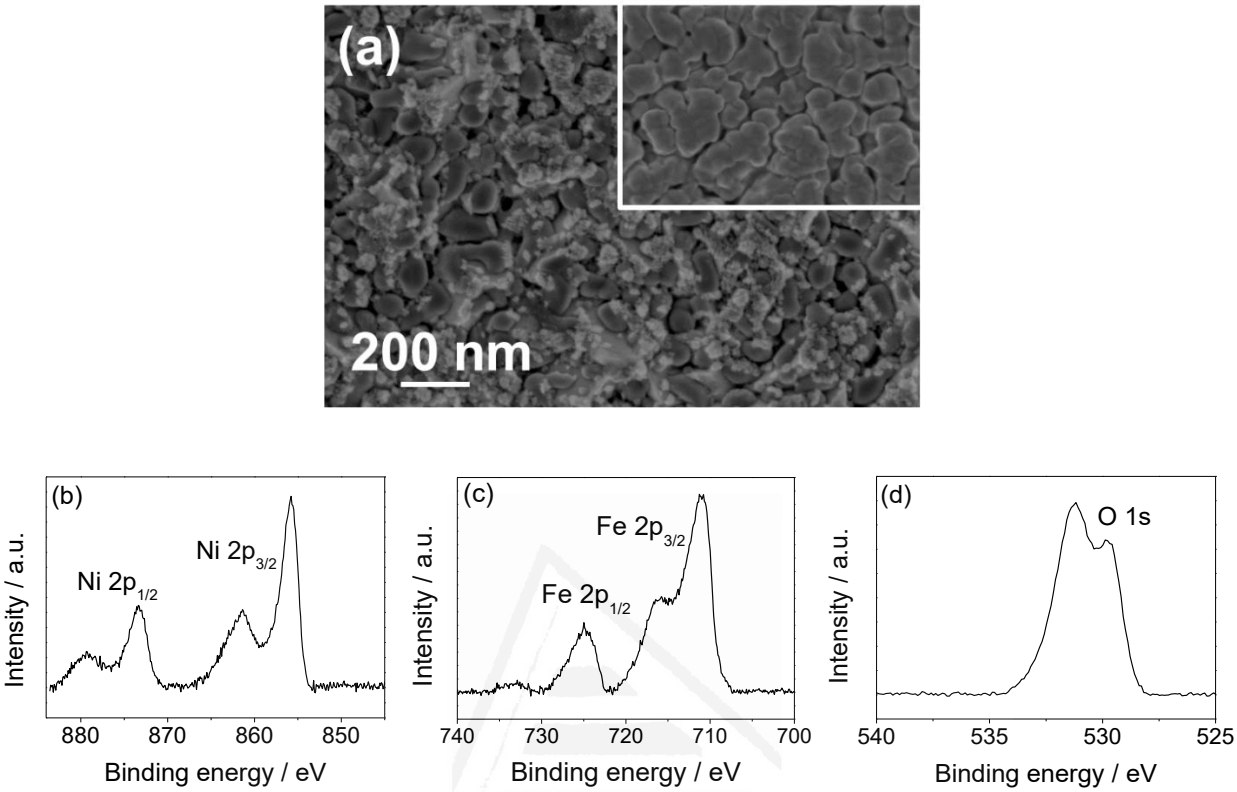

Figure 7.3. (a) FESEM image corresponding to the top view of a $BiVO_4/Fe(OH)_2/Ni(OH)_2$ photoanode prepared for optimum $Fe(OH)_2$ and $Ni(OH)_2$ deposition times of 30 and 30 min, respectively (FESEM image corresponding to a bare $BiVO_4$ photoanode is included as inset). (b) Ni 2*p*, (c) Fe 2*p* and (d) O 1*s* XPS spectra for a $BiVO_4/Fe(OH)_2/Ni(OH)_2$ photoanode prepared for optimum $Fe(OH)_2$ and $Ni(OH)_2$ deposition times of 30 and 30 min, respectively.

The nature of the $Fe(OH)_2/Ni(OH)_2$ deposit on $BiVO_4$ was also studied by XPS (Figure 7.3b-d). The values of binding energies (BE) observed for the main and satellite peaks and the characteristic multiplet splitting of the Fe 2*p* XPS spectrum (Figure 7.3b) clearly indicate the prevalence of Fe^{2+} species, in agreement with previous reports [28,30,31]. On the other hand, the lack of signals associated to NiOOH species and the clear shift of the Ni $2p_{3/2}$ feature to higher BE values in comparison to those usually reported for NiO in the corresponding XPS spectrum for Ni 2*p* (Figure 7.3c) reveals Ni

is present as Ni^{2+} [26,29,32]. Finally, the hydroxide nature of the deposit is supported by the signal at 531.2 eV observed in the O 1*s* XPS spectrum (Figure 7.3d), typically associated with the existence of OH^- groups [28,33] and clearly different from that at 529.6 eV (which indicates the existence of O^{2-} species in the $BiVO_4$ lattice [34]). The XPS spectra for Bi 4*f* and V 2*p* (from the $BiVO_4$ deposit) are given in Figure S7.5.

According to the optimization results, the surface density of metal centers in the optimum $Fe(OH)_2/Ni(OH)_2$ deposit is estimated to be around $2.8 \cdot 10^{15}$ Fe atoms/cm^2 and $9.1 \cdot 10^{14}$ Ni atoms/cm^2, which in terms of equivalent $Fe(OH)_2$ and $Ni(OH)_2$ monolayers (ML, as defined in previous studies [26,28,29]) correspond to 2.4 and 0.8 ML, respectively. To analyze and put in context these values, it is important to consider a previous study on surface modification of $BiVO_4$ photoanodes with $Ni(OH)_2$ following a parallel methodology [26]. In that report, the highest photocurrent value for a $BiVO_4/Ni(OH)_2$ photoanode (0.44 mA·cm^{-2} at 1.23 V *vs*. RHE) was achieved for a q_{Ni} of approximately 0.13 mC·cm^{-2} (corresponding to a deposition time of 20 min), equivalent to a Ni atom surface density of $5.4 \cdot 10^{14}$ cm^{-2} or to an equivalent $Ni(OH)_2$ coverage of around 0.5 ML.

Given that the maximum photocurrent (at 1.23 V *vs*. RHE) achieved with the optimized $BiVO_4/Fe(OH)_2/Ni(OH)_2$ photoanode is of 1.9 mA·cm^{-2}, it is evident that the deposition of $Fe(OH)_2$ between the $BiVO_4$ substrate and the $Ni(OH)_2$ deposit significantly boosts the photoactivity of the system. In fact, it induces an enhancement in photocurrent by a factor of 4.3 compared to optimum $BiVO_4/Ni(OH)_2$ photoanodes [26]. In this $Fe(OH)_2/Ni(OH)_2$ co-catalyst, the optimum $Ni(OH)_2$ loading is slightly higher but in the same order of magnitude to that observed in the previous $Ni(OH)_2$ optimization study. In addition, the photocurrent trend is also similar (progressive grow until optimum q_{Ni} values of around 0.1-0.2 mC·cm^{-2} followed by an important decrease for charge densities

higher than 0.4 $mC \cdot cm^{-2}$). This suggests that the $Ni(OH)_2$ component of the $Fe(OH)_2/Ni(OH)_2$ co-catalyst would be able to play an analogous electrocatalytic role than that previously reported for sub-monolayer $Ni(OH)_2$ deposits on $BiVO_4$ photoanodes, but with enhanced effectiveness.

It is important to highlight the fact that the actual coverage that would be calculated on the basis of the real $BiVO_4$ surface area would be substantially smaller for both hydroxides. This is because this calculation is done by assuming that the photoanode surface is perfectly flat and that the growth of these hydroxides on the $BiVO_4$ surface happens in layer-by-layer regime (which does not happen here, as seen in Figure 7.3a). In any case, the fact that the necessary $Fe(OH)_2$ coverage for an optimum $BiVO_4/Fe(OH)_2/Ni(OH)_2$ PEC performance (estimated to be 2.4 ML) is around 3 times higher than that calculated for $Ni(OH)_2$ suggests that the $Fe(OH)_2$ role in the water splitting mechanism is different from the electrocatalytic one described for $Ni(OH)_2$. In fact, and according to previous studies on the mechanism of water photooxidation on FeOOH-based [35–39] photoanodes, $Fe(OH)_2$ would act as a charge transfer mediator between $BiVO_4$ and $Ni(OH)_2$, significantly decreasing the charge transfer resistance at the semiconductor/$Ni(OH)_2$ interface. In this way, and given that the $Fe(OH)_2$ deposit is in direct contact with the $BiVO_4$ photoanode, the Fe^{2+} centers would be locally oxidized to Fe^{3+} by trapping holes photogenerated in the semiconductor, and, to a minor extent, even to Fe^{4+} by trapping a second hole. The Fe^{4+} species would transfer the photogenerated charge to the adjacent $Ni(OH)_2$ deposit, returning to its reduced form (Fe^{3+}) and initiating a similar process involving Ni species: Ni^{2+} centers are locally oxidized to Ni^{3+} and only a minor fraction of these Ni^{3+} would be further oxidized to Ni^{4+} due to the trapping of a second photogenerated hole. Finally, these Ni^{4+} species would act

as the actual electrocatalytic centers, transferring the hole to the electrolyte with its subsequent reduction to Ni^{3+} and actively participating in water oxidation.

The electrochemical characterization in the dark of FTO/$BiVO_4$/$Fe(OH)_2$/$Ni(OH)_2$ (Figure 7.1a and 7.2a) and also FTO/$Fe(OH)_2$/$Ni(OH)_2$ electrodes (Figure S7.6) discards the possibility of OER electrocatalysis going primarily through the Fe centers, since the current for the oxygen evolution reaction in the dark does not grow with the $Fe(OH)_2$ loading (Figure S7a). This is in contrast with the trend observed in the case of $Ni(OH)_2$ (Figure S7b), which points out its central electrocatalytic role. It is worth noting that the existence of Fe^{4+} species has been detected in NiFe (oxy)hydroxide catalysts during steady-state water oxidation, not being though the active sites in water oxidation [40]. The large loading of $Fe(OH)_2$ compared to $Ni(OH)_2$ and the relatively abundance of Fe^{4+} species able to promote Ni^{2+} oxidation more effectively than photogenerated $BiVO_4$ holes would explain the enhanced photoelectrochemical properties of the $BiVO_4$/$Fe(OH)_2$/$Ni(OH)_2$ system with respect to the $BiVO_4$/$Ni(OH)_2$ one.

The drastic decrease in activity observed for post-optimum deposited amounts of both hydroxides is mainly explained according to the low electrical conductivities of increasingly thicker $Fe(OH)_2$ and $Ni(OH)_2$ deposits. In this situation, the photogenerated holes would accumulate in $Fe(OH)_2$ and $Ni(OH)_2$ islands and would not be transferred to the $Ni(OH)_2$ overlayer and to the electrolyte, respectively. In this regard, it is known that the electrical conductivity of the $Fe(OH)_2$/FeOOH system is significantly lower than that of $Ni(OH)_2$/NiOOH [41]. The fact that the optimum amount of deposited $Fe(OH)_2$ is three times higher than that corresponding to $Ni(OH)_2$ suggests that the morphology described for the $Fe(OH)_2$ deposit favors that most of the iron atoms are in contact with the $BiVO_4$ and in close vicinity with the Ni^{2+} centers, facilitating its role in hole transfer. As the Ni coverage grows, an increasing fraction of deposited Ni atoms would be in second and

successive monolayers, and not in direct contact with the electrolyte, thus being less effective (or even inactive) to promote the OER.

7.4. CONCLUSIONS

In summary, $Fe(OH)_2/Ni(OH)_2$ co-catalyst has been deposited on $BiVO_4$ photoanodes by means of a urea-based chemical bath deposition method that allows for a straightforward and fine control of the deposited quantity of the two different hydroxides by only controlling deposition times. The iron hydroxide underlayer is shown to drastically enhance the efficiency of the $Ni(OH)_2$ co-catalysts. Specifically, the optimum coverages for optimum PEC performance have been determined to be 2.4 and 0.8 ML for $Fe(OH)_2$ and $Ni(OH)_2$, respectively. These amounts of hydroxide induce photocurrent enhancements by a factor of 4.3 and 9.0 compared to optimum $BiVO_4/Ni(OH)_2$ and $BiVO_4$ photoanodes, respectively. The importance of a precise control of the amount of co-catalyst deposited on the photoelectrode surface to obtain an optimized PEC response, as well as the usefulness of electrochemical methods to monitor such an amount are also illustrated.

7.5. ACKNOWLEDGEMENTS

Financial support of the Spanish Ministry of Economy and Competitiveness through project RTI–2018–102061–B–I00 (FONDOS FEDER) is gratefully acknowledged. J. Q. thanks to the Spanish Ministry of Education, Culture and Sport (MECD) for the award of an FPU predoctoral grant (FPU15/02005).

7.6. REFERENCES

[1] C. Ding, J. Shi, Z. Wang, C. Li, ACS Catal. 7 (2017) 675.
[2] E. Fabbri, A. Habereder, K. Waltar, R. Kötz, T.J. Smith, Catal. Sci. Technol. 4 (2014) 3800.

[3] J.R. Galán-Mascarós, ChemElectroChem. 2 (2015) 37.
[4] M.R. Nellist, F.A.L. Laskowski, F. Lin, T.J. Mills, S.W. Boettcher, Acc. Che,. Res 19 (2016) 733.
[5] X. Xu, L. Pan, X. Zhang, L. Wang, J. Zou, Adv. Sci. 6 (2018) 1801505.
[6] C. Ding, J. Shi, Z. Wang, C. Li, ACS Catal. 7 (2017) 675.
[7] C. Jiang, S.J.A. Moniz, A. Wang, T. Zhang, J. Tang, Chem. Soc. Rev. 46 (2017) 4645.
[8] Y. Kuang, T. Yamada, K. Domen, Joule. 1 (2017) 290.
[9] R.L. House, N.Y.M. Iha, R.L. Coppo, L. Alibabaei, B.D. Sherman, P. Kang, M.K. Brennaman, P.G. Hoertz, T.J. Meyer, J. Photochem. Photobiol. C Photochem. Rev. 25 (2015) 32.
[10] C. Du, X.G. Yang, M.T. Mayer, H. Hoyt, J. Xie, G. McMahon, G. Bischoping, D. Wang, Angew. Chemie-Int. Ed. 52 (2013) 12692.
[11] S.D. Tilley, M. Cornuz, K. Sivula, M. Gratzel, Angew. Chemie-Int. Ed. 49 (2010) 6405.
[12] D.K. Zhong, D.R. Gamelin, J. Am. Chem. Soc. 132 (2010) 4202.
[13] S. Luo, T.-D. Nguyen-Phan, A.C. Johnston-Peck, L. Barrio, S. Sallis, D.A. Arena, S. Kundu, W. Xu, L.F.J. Piper, E.A. Stach, D.E. Polyansky, E. Fujita, J.A. Rodriguez, S.D. Senanayake, J. Phys. Chem. C. 119 (2015) 2669.
[14] T.S. Sinclair, H.B. Gray, A.M. Müller, Eur. J. Inor. Chem 4 (2017) 1.
[15] H. Zhang, H. Li, B. Akram, X. Wang, Nano Res. 12 (2019) 1327.
[16] X. Meng, J. Han, L. Lu, G. Qiu, Z.L. Wang, C. Sun, Small. 15 (2019) 1.
[17] J. Zhang, J. Liu, L. Xi, Y. Yu, N. Chen, S. Sun, W. Wang, K.M. Lange, B. Zhang, J. Am. Chem. Soc. 140 (2018) 3876.
[18] S. Jiao, Z. Yao, M. Li, C. Mu, H. Liang, Y.J. Zeng, H. Huang, Nanoscale. 11 (2019) 18894.
[19] T. Tian, M. Zheng, J. Lin, X. Meng, Y. Ding, Chem. Commun. 55 (2019) 1044.
[20] J. Quiñonero, T. Lana-Villarreal, R. Gómez, Int. J. Hydrogen Energy. 45 (2020) 17076.
[21] Y. Tang, R. Wang, Y. Yang, D. Yan, X. Xiang, ACS Appl. Mater. Interfaces. 8 (2016) 19446.
[22] Y. Zhu, J. Ren, X. Yang, G. Chang, Y. Bu, G. Wei, W. Han, D. Yang, J. Mater. Chem. A. 5 (2017) 9952.
[23] Y. He, C. Zhang, J. Hu, M.K.H. Leung, Appl. Energy. 255 (2019) 113770.
[24] X. Lv, X. Xiao, M. Cao, Y. Bu, C. Wang, M. Wang, Y. Shen, Appl. Surf. Sci. 439 (2018) 1065.
[25] Q. Wang, T. Niu, L. Wang, J. Huang, H. She, Cuihua Xuebao/Chinese J. Catal. 39 (2018) 613.
[26] J. Quiñonero, R. Gómez, Appl. Catal. B Environ. 217 (2017) 437.
[27] J. Quiñonero, T. Lana–Villarreal, R. Gómez, Appl. Catal. B Environ. 194 (2016) 141.
[28] J. Quiñonero, R. Gómez, Electrochimica Acta 274 (2018) 224.
[29] D. Cibrev, M. Jankulovska, T. Lana-Villarreal, R. Gómez, Int. J. Hydrogen Energy. 38 (2013) 2746.
[30] M.C. Biesinger, B.P. Payne, A.P. Grosvenor, L.W.M. Lau, A.R. Gerson, R.S.C. Smart, Appl. Surf. Sci. 257 (2011) 2717.
[31] A.P. Grosvenor, B.A. Kobe, M.C. Biesinger, N.S. McIntyre, Surf. Interface Anal. 36 (2004) 1564.
[32] K.S. Kim, Surf. Sci. 43 (1974) 625.
[33] S. Tang, S. Vongehr, Y. Wang, L. Chen, X. Meng, J. Solid State Chem. 183 (2010)

2166.
[34] G.A. Carson, M.H. Nassir, M.A. Langell, J. Vac. Sci. Technol. A. 14 (1996) 1637.
[35] K.J. McDonald, K.S. Choi, Energy Environ. Sci. 5 (2012) 8553.
[36] J.A. Seabold, K. Zhu, N.R. Neale, Phys. Chem. Chem. Phys. 16 (2014) 1121.
[37] J.Y. Kim, D.H. Youn, K. Kang, J.S. Lee, Angew. Chemie-Int. Ed. 55 (2016) 10854.
[38] M.A. de Araújo, D. Coelho, L.H. Mascaro, E.C. Pereira, J. Solid State Electrochem. 22 (2017) 1.
[39] T.W. Kim, K.S. Choi, Science. 343 (2014) 126.
[40] J.Y.C. Chen, L. Dang, H. Liang, W. Bi, J.B. Gerken, S. Jin, E.E. Alp, S.S. Stahl, J. Am. Chem. Soc. 137 (2015) 15090.
[41] J. Qiu, H. Hajibabaei, M.R. Nellist, F.A.L. Laskowski, S.Z. Oener, T.W. Hamann, S.W. Boettcher, ACS Energy Lett. 3 (2018) 961.

7.7. SUPPORTING INFORMATION

7.7.1. Experimental methods

7.7.1.1. Preparation of $BiVO_4$ thin-film electrodes

$BiVO_4$ thin film photoanodes were prepared layer-by-layer on fluorine-doped tin oxide substrates (F:SnO_2, FTO, U-type 12 Ω^2, Asahi Glass Co.) by a previously reported procedure based on a modified metal-organic decomposition method (MOD) followed by a thermal treatment [S1]. Briefly, 0.2 M $Bi(NO_3)_3 \cdot 5H_2O$ (Sigma-Aldrich, 98%) in acetic acid (Scharlau, 99%) and 0.03 M $VO(C_5H_7O_2)_2$ (Fluka Analytical, 97%) in acetylacetone (Fluka Analytical, 99.5%) solutions were prepared and subsequently mixed in a 1:1 mol ratio of Bi and V to obtain the $BiVO_4$ precursor solution. Then, 40 µL of this mixed solution was dropped onto a previously cleaned FTO glass plate (area to be covered: 1 cm^2) and spread over it with a spin-coater (Chemat Technology, KW-4A) at a spin rate of 1500 rpm for 10 s. Finally, the electrodes were annealed at 500ºC for 30 min in air (heating rate: $5ºC \cdot min^{-1}$) using a programmable furnace (Conatec, 7800). This procedure was repeated six times to achieve the optimum $BiVO_4$ film thickness.

7.7.1.2. $Fe(OH)_2/Ni(OH)_2$ surface deposition on $BiVO_4$ photoanodes

$Fe(OH)_2/Ni(OH)_2$ was deposited on FTO conducting glass substrates and on $BiVO_4$ photoanodes by means of a previously reported chemical bath deposition (CBD) procedure [S2]. It is important to highlight that the synthesis of these deposits is performed in two sequential steps: $Fe(OH)_2$ is firstly deposited on the FTO or $BiVO_4$ substrate and then the $Ni(OH)_2$ is deposited after the $Fe(OH)_2$ deposition. To this end, the CBD solution contained 25 mL of 0.5 M $FeSO_4 \cdot 7H_2O$ (Sigma-Aldrich, 99%) or 0.5 M $NiSO_4 \cdot 6\text{-}7H_2O$ (Sigma-Aldrich, for nickel plating), for the deposition of $Fe(OH)_2$ or $Ni(OH)_2$, respectively, 12.5 mL of 1 M urea (Sigma-Aldrich, P.A.) and 12.5 mL of H_2O

(Millipore, Essential Elix 3). The substrates were vertically supported with the conducting side (either bare or covered with $BiVO_4$) faced against the beaker wall, and the solution was heated up to 100ºC in a stove (Memmert, 100-800). Different deposition times for both hydroxides (from 10 to 60 min) were studied as to control the amount of deposited $Fe(OH)_2$ and $Ni(OH)_2$. Finally, the samples were rinsed with abundant distilled water, air dried and annealed at 200ºC in air for 1 h (heating rate: $5ºC \cdot min^{-1}$).

7.7.1.3. (Photo)electrochemical and electrode characterization

All the (photo)electrochemical characterization was carried out at room temperature in a home-made Pyrex glass cell with a fused silica window and a computer-controlled potentiostat-galvanostat (Autolab, PGSTAT30) employing a Ag/AgCl/KCl(3 M) electrode and a Pt wire as reference and counter electrode, respectively. Unless otherwise stated, all the potentials in the text are referred to this Ag/AgCl electrode. An N_2-purged NaB_i (pH = 10.0) buffer solution was used as the working electrolyte for the (photo)electrochemical measurements. The light source was an ozone-free 1000 W Xe(Hg) lamp (Newport Instruments, 66921) equipped with a water filter to minimize the infrared contribution of the beam. In all cases, the electrodes were illuminated from the front-side (electrolyte-electrode illumination). The photon flux intensity was measured by means of a photodiode power meter (Thorlabs, PM100D), and the typical value was approximately 100 $mW \cdot cm^{-2}$.

A SEM study was carried out to characterize the surface morphology of the films using a ZEISS Merlin VP Compact field emission scanning electron microscope (FESEM). For the compositional characterization of the hydroxide deposits, XPS experiments were done with a Thermo-Scientific K-Alpha XPS spectrometer equipped with a monochromatic Al-Kα source (1486.6 eV), operating at 15 kV and 10 mA.

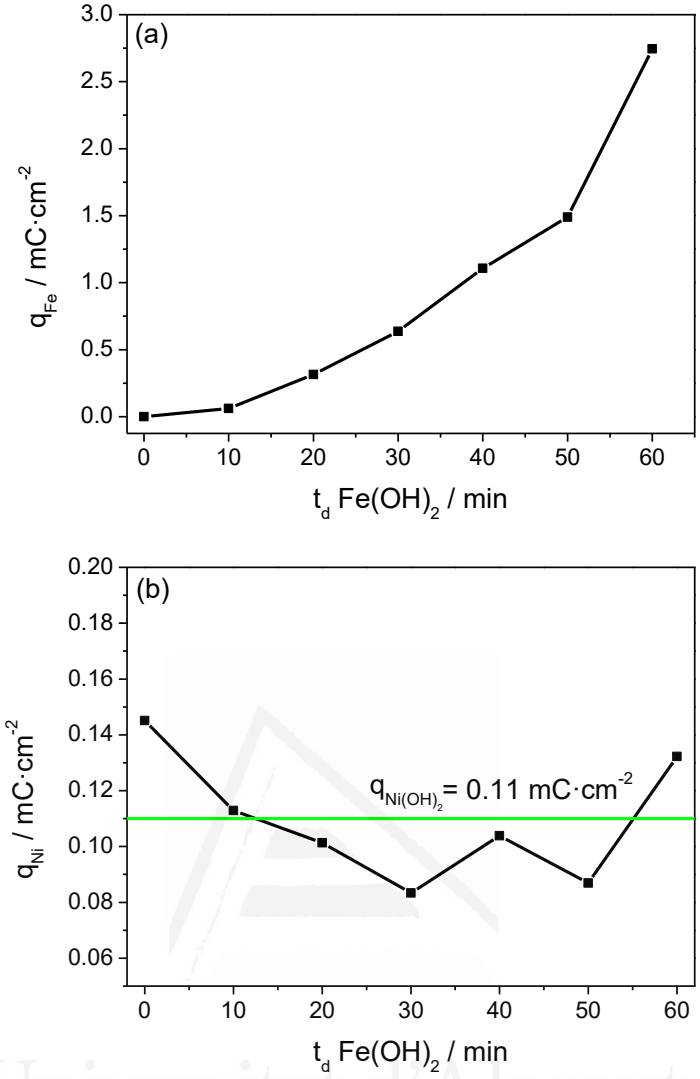

Figure S7.1. (a) Charge density associated with the $Fe(OH)_2$ oxidation peak *vs.* $Fe(OH)_2$ deposition time, for $BiVO_4/Fe(OH)_2$ (t_d)/$Ni(OH)_2$ (20 min) electrodes, prepared for different $Fe(OH)_2$ deposition times (t_d). (b) Charge density associated with the NiOOH reduction peak *vs.* $Ni(OH)_2$ deposition time, for $BiVO_4/Fe(OH)_2$ (t_d)/$Ni(OH)_2$ (20 min) electrodes, prepared for different $Fe(OH)_2$ deposition times (t_d). In green, average q_{Ni} value.

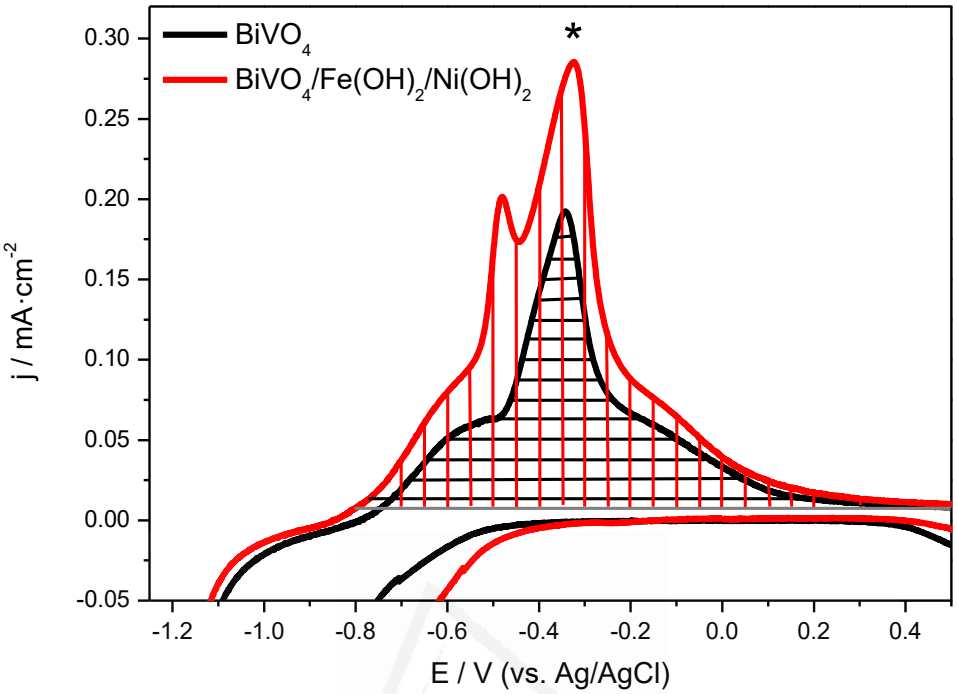

Figure S7.2. Example on how to estimate the charge associated with the $Fe(OH)_2$ oxidation redox process. Vertical red lines indicate the positive charge integrated for the considered $BiVO_4/Fe(OH)_2/Ni(OH)_2$ photoanode, while horizontal black lines indicate that for a representative unmodified $BiVO_4$ electrode. The charge associated with the $Fe(OH)_2$ oxidation redox process can be estimated as the difference between both charge values.

Voltammetric peaks integration. The number of Fe and Ni sites was estimated by integration of the $Fe(OH)_2 \rightarrow FeOOH$ oxidation peak and the $NiOOH \rightarrow Ni(OH)_2$ reduction peak, respectively, in the corresponding cyclic voltammograms in the dark. While the $NiOOH \rightarrow Ni(OH)_2$ reduction peak is free from any interference with other voltammetric features, which allows for straightforward and direct integration, the integration of the $Fe(OH)_2 \rightarrow FeOOH$ oxidation peak is more difficult. In fact, this peak suffers from an interference with the voltammetric wave corresponding to *quasi*-reversible pseudocapacitive processes linked to redox transformations of V surface atoms in $BiVO_4$

(indicated with an asterisk in Figure S7.2) [S3]. As consequence, we estimate the charge associated with the $Fe(OH)_2$ oxidation redox process as the difference between the positive charge integrated in the voltammetry corresponding to the $BiVO_4/Fe(OH)_2/Ni(OH)_2$ photoanode in question and the unmodified $BiVO_4$ electrode (Figure S7.2). This is a valid estimation since the voltammetric scans do not reveal blocking phenomena of the $BiVO_4$ electrochemical active surface after the $Fe(OH)_2/Ni(OH)_2$ deposition.

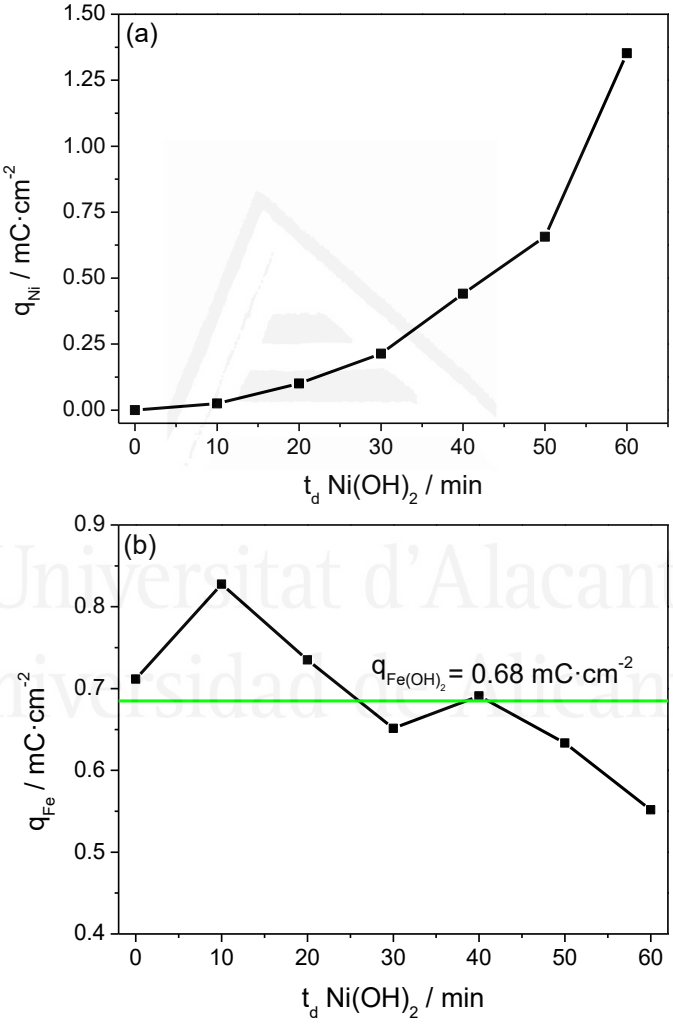

Figure S7.3. (a) Charge density associated with the NiOOH reduction peak *vs*. $Ni(OH)_2$ deposition time, for $BiVO_4/Fe(OH)_2$ (30 min)/$Ni(OH)_2$ (t_d) electrodes, prepared for different $Ni(OH)_2$ deposition times (t_d). (b) Charge density associated with the $Fe(OH)_2$ oxidation peak *vs*. $Ni(OH)_2$ deposition time, for $BiVO_4/Fe(OH)_2$ (30 min)/$Ni(OH)_2$ (t_d) electrodes, prepared for different $Ni(OH)_2$ deposition times (t_d). In green, average q_{Fe} value.

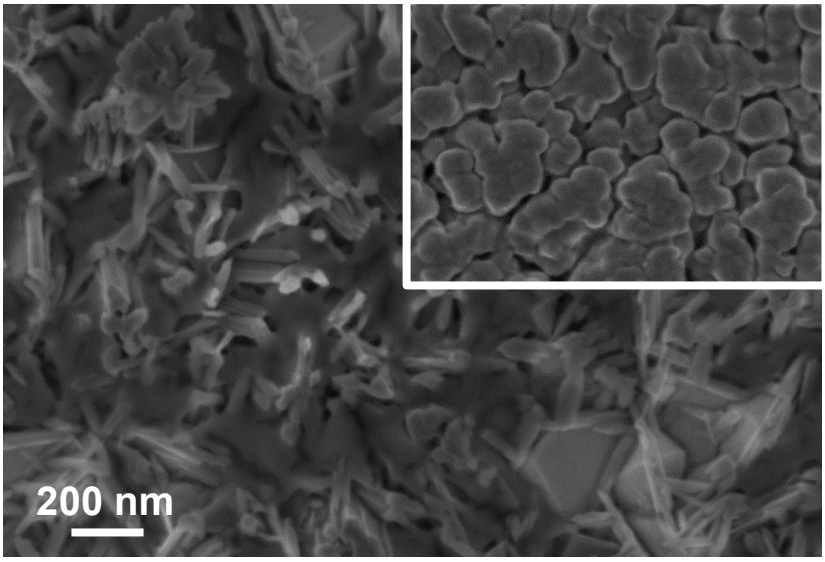

Figure S7.4. FESEM image corresponding to the top view of a $BiVO_4/Fe(OH)_2/Ni(OH)_2$ photoanode prepared for $Fe(OH)_2$ and $Ni(OH)_2$ deposition times of 30 and 50 min, respectively (FESEM image corresponding to a bare $BiVO_4$ photoanode is included as inset).

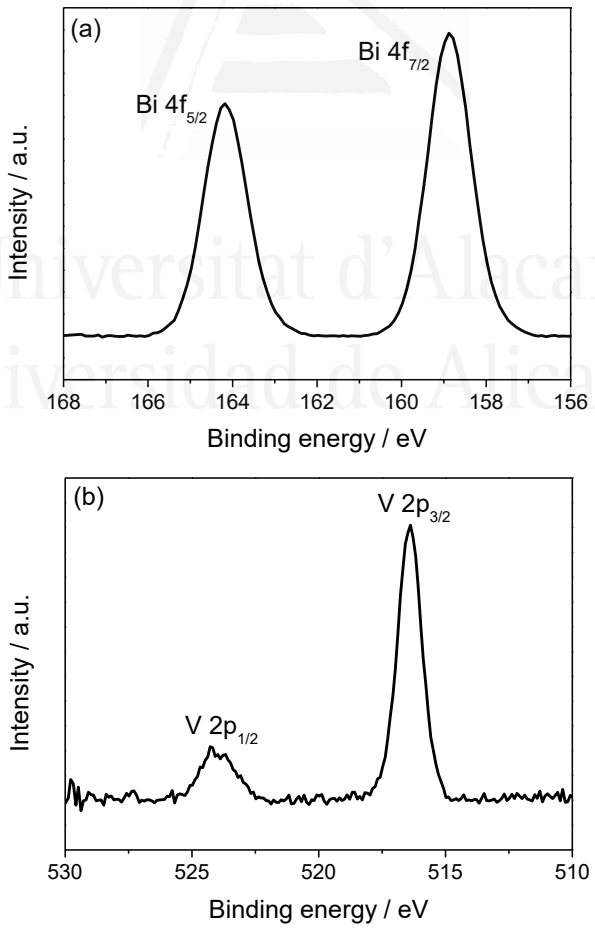

Figure S7.5. (a) Bi 4*f* and (b) V 2*p* XPS spectra for $BiVO_4/Fe(OH)_2$ (30 min)/$Ni(OH)_2$ (30 min) electrodes.

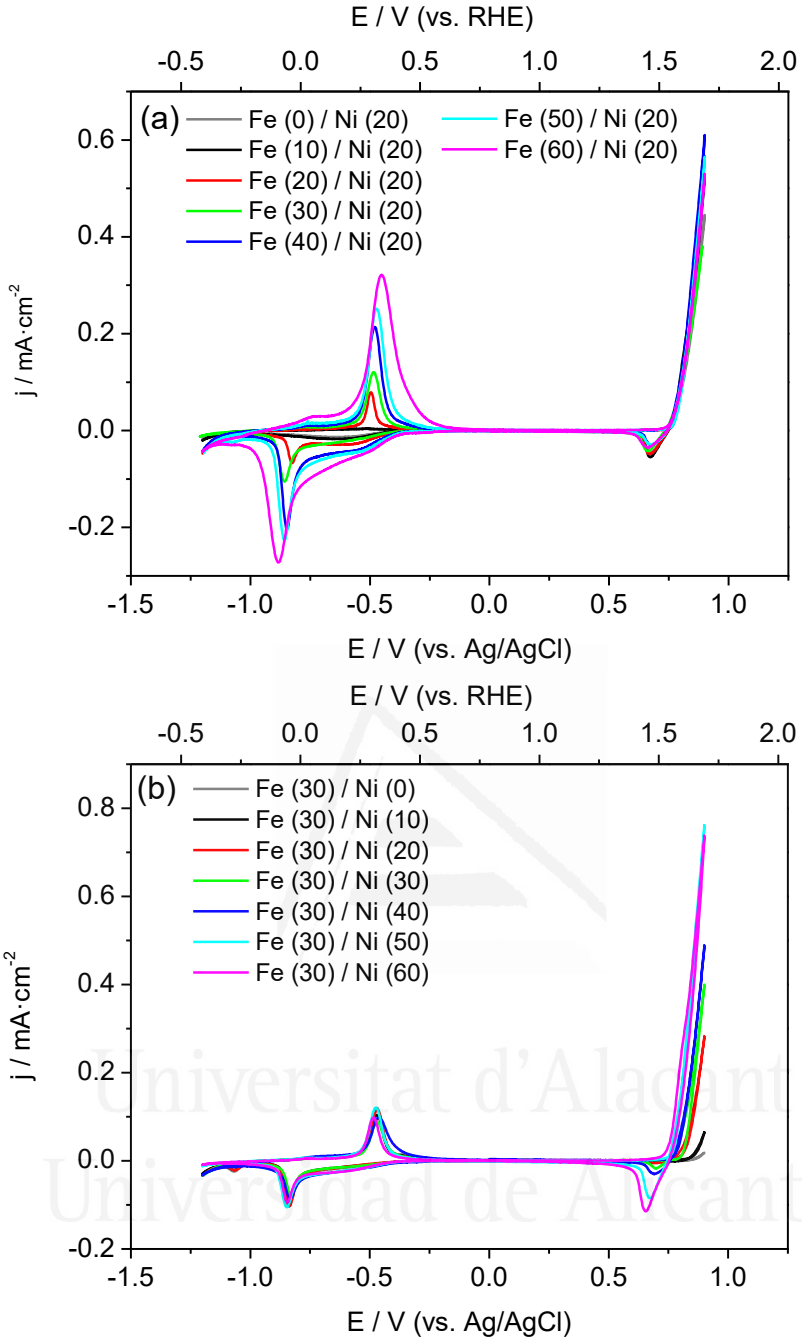

Figure S7.6. (a) Cyclic voltammogram (scan rate: 10 $mV \cdot s^{-1}$) for FTO/$Fe(OH)_2$ (t_d)/$Ni(OH)_2$ (20 min) electrodes, prepared for different $Fe(OH)_2$ deposition times (t_d). (b) Cyclic voltammogram (scan rate: 10 $mV \cdot s^{-1}$) for FTO/$Fe(OH)_2$ (30 min)/$Ni(OH)_2$ (t_d) electrodes, prepared for different $Ni(OH)_2$ deposition times (t_d).

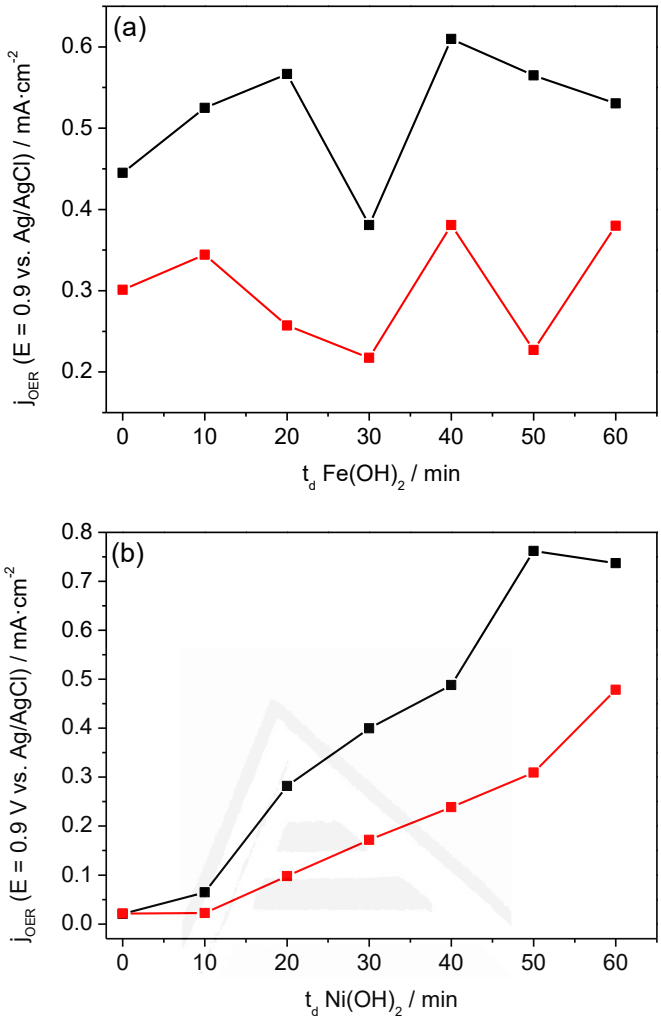

Figure S7.7. (a) Current density attributable to the oxygen evolution reaction in the dark, measured at E = 0.9 V *vs*. Ag/AgCl, *versus* the $Fe(OH)_2$ deposition time for FTO/$Fe(OH)_2$ (t_d)/$Ni(OH)_2$ (20 min) electrodes (black line) and FTO/$BiVO_4$/$Fe(OH)_2$ (t_d)/$Ni(OH)_2$ (20 min) electrodes (red line), prepared for different $Fe(OH)_2$ deposition times (t_d). (b) Current density attributable to the oxygen evolution reaction in the dark, measured at E = 0.9 V vs. Ag/AgCl, *versus* the $Ni(OH)_2$ deposition time for FTO/$Fe(OH)_2$ (20 min)/$Ni(OH)_2$ (t_d) electrodes (black line) and FTO/$BiVO_4$/$Fe(OH)_2$ (30 min)/$Ni(OH)_2$ (t_d) electrodes (red line), prepared for different $Ni(OH)_2$ deposition times (t_d).

7.7.2. References

[S1] J. Quiñonero, T. Lana-Villarreal, R. Gómez, Appl. Catal. B Environ. 194 (2016) 141.
[S2] J. Quiñonero, T. Lana-Villarreal, R. Gómez, Int. J. Hydrogen Energy. 45 (2020) 17076.
[S3] J. Quiñonero, R. Gómez, Appl. Catal. B Environ. 217 (2017) 437.

CHAPTER VIII

Defect engineering nanostructured $LaFeO_3$ photoanodes improves the activity for solar water oxidation

8.1. ABSTRACT

Prospecting low-cost yet highly active materials for solar water oxidation is key to enable a competitive photoelectrochemical (PEC) technology for solar-driven water splitting. The earth abundant composition, renowned catalytic activity towards the oxygen evolution reaction (OER) and visible light absorption has positioned $LaFeO_3$ (LFO) as an emerging candidate for solar water oxidation. Unfortunately, reports on LFO photoanodes still depict a PEC response that lay far behind its ferrite counterparts. With the aim of identifying the key performance bottlenecks in this material and propelling the implementation of LFO as photoanode, here, we combine a new manufacturing route, which produces a nanorod array-type electrode of LFO, with defect and surface engineering protocols, to deliver a benchmarking performance of 0.4 mA cm^{-2} at 1.23 V *vs*. RHE and onset potentials below 0.55 V *vs*. RHE. Firstly, we found that oxygen defects activate the interface towards oxygen evolution reaction (OER), as confirmed by the drop of the Tafel slope from 160 to 110 mV dec^{-1}, while coating with $NiFeO_x$ drastically suppressed the surface recombination. We observed, however, a gradual deterioration of the response resulting from the refilling of oxygen within the structure outcompeting OER reaction. Secondly, we discover a rapid bulk recombination of photogenerated carriers at nanosecond timescales as well as identified weak space-charge field and an ultrashort hole diffusion length (< 5 nm) which ultimately limit the performance. Overall, this work provides guidelines to accelerate the progress on LFO photoanodes as well as new insights into the operational behavior of the emerging family of oxide perovskites for solar fuel production.

8.2. INTRODUCTION

Sourcing commodity chemicals, like hydrogen, from abundant feedstocks and solely using renewable energy is key to decarbonize our economic model and meet the increasingly stringent international policies on carbon emission [1–3]. Photoelectrochemical (PEC) tandem cells for solar water splitting are recognized to be capable of carrying on this energetic transition provided that competitive margins in manufacturing cost, efficiency and durability are achieved [4]. In fact, there have been encouraging advances on the development of low-cost, stable and high-performing photocathodes for solar water reduction, for instance, Sb_2Se_3 [5], $Cu(In,Ga)(S,Se)_2$ [6,7], Cu_2O [8], etc. However, it is the water oxidation half-reaction the one that currently poses serious hurdles for the realization of solar water splitting using tandem cells. Metal oxides such as TiO_2 [9], α-Fe_2O_3 [10], WO_3 [11], $ZnFe_2O_4$ [12] and $BiVO_4$ [13], have been capturing most of the attention in recent years offering not only long-term stability and cheap manufacturing [14], but also complementary light harvesting when integrated in tandem cells [8]. Unfortunately, the photocurrent values delivered by these materials are still below the requirements to realize a competitive tandem cell [4,8,15]. Although research actively continues in further engineering and tweaking these state-of-the-art photoanodes to tap into their theoretical maximum performance [16], growing efforts are turning into exploring new materials whose broader electronic and compositional tunability could disrupt the field of solar water oxidation getting the PEC tandem technology finally off the ground.

Oxide perovskites (ABO_3: A = alkali or rare-earth metals; B = transition metals) have lately come into the spotlight owing to their earth-abundant composition, demonstrated catalytic activity and immense (opto)electronic flexibility [13,17–26]. These features altogether have consolidated them as an excellent platform to enable a new

generation of photoanodes. Perovskite oxides have garnered prominence as light absorbers for photoelectrochemical systems due to their optimum band gaps for sunlight harvesting (1.1–2.4 eV) [17,18,27,28]. Currently, oxynitrides set the benchmark performance amongst perovskite oxide-based perovskites delivering photocurrent values up to 5 mA cm^{-2} at 1.23 V *vs*. RHE [29]. However, the only minutes-long lifespan of most of oxynitrides under operation [30], due to rapid corrosion, and the tedious multistep fabrication of these photoelectrodes has urged to redirect efforts towards the design of highly-active perovskite oxides photoanodes which are more resilient to harsh oxidative conditions and amenable to simple solution processing.

Several non-stoichiometric perovskite oxides have been reported to display an exceptional electrocatalytic activity towards oxygen evolution reaction (OER), even outperforming the state-of-the-art IrO_2. Interestingly, the presence of highly-mobile oxygen vacancy defects in these materials has been ubiquitously acknowledged to be crucial in improving the electrocatalysis, although their specific role still remains controversial. On the one hand, the surface oxygen deficiency in, for instance, $La_{1-x}FeO_{3-\delta}$, $PbBaCo_2O_{6-\delta}$ or $CaMnO_3$, has been argued to favor the to favor the OER by exposing more of the transition-metal B cation, considered to be the redox active centers, and by reducing the adsorption energy of the reaction intermediates [23,25,26].

Among the various oxide perovskites investigated so far as photoanodes, we are particularly interested in prospecting $LaFeO_3$ (LFO) given its suitable band gap of ~2.1 eV for sunlight harvesting [31] and demonstrated catalytic activity towards OER [25]. Admittedly, this dual role as light absorber and electrocatalyst affords the design of single-material photoanodes, circumventing the complexity of multijunction electrodes. Surprisingly, despite this competitive advantage the performance of LFO photoanodes remains far behind its metal oxide counterparts [31]. Several groups have explored the

possibility of activating LFO photoanodes by compositional engineering, *i.e.* replacing partially La^{3+} or Fe^{3+} with low-valent ions such as Mn^{2+}, Cu^{2+}, Sr^{2+}, etc. although in all cases the photocurrent values barely surpassed the few tens of μA cm^{-2} while the late onset potential (> 1.6 V *vs*. RHE) hardly improved with respect the onset recorded in the dark [32–34]. Alternatively, Peng *et al*. demonstrated that the incorporation of a co-catalyst such as Co-P_i enhanced the photocurrent, although to simply reach a very modest 7 μA cm^{-2} at 1.2 V *vs.* RHE [35]. Overall, these early studies hint at the presence of massive carrier losses that prevent the extraction of the vast majority of photogenerated carriers (note that the photocurrent limit for LFO is 12.5 mA cm^{-2}) [36], although no attempts to identify them have been undertaken. Understanding the key parameters that factor-in and limit the response is instrumental in developing a new generation of more efficient LFO photoanodes.

In this work, we introduced for the first time a nanorod array-type LFO electrode, combining oxygen defect engineering and surface passivation with $NiFeO_x$ to set a new benchmark performance among LFO photoanodes for solar water oxidation at photocurrent values of 0.4 mA cm^{-2} (at 1.23 V *vs* RHE) and onset potentials of 0.55 V *vs* RHE. We found that oxygen defects and $NiFeO_x$ act synergistically to activate the reactive interface by reducing the overpotential for OER and the surface recombination. Our investigations evidenced however, the existence of significant photogenerated carrier losses at ultrashort timescales as well as a weak space-charge field and small diffusion length, which altogether limit the PEC response.

8.3. RESULTS AND DISCUSSION

As illustrated in Figure 8.1, LFO photoanodes were prepared by using a modified version of the method previously reported by our group to fabricate spinel ferrite thin film

electrodes [37]. In brief, a nanorod array of β-FeOOH (iron precursor) was directly grown on the transparent conductive substrate (F-doped SnO_2) by using a chemical bath deposition. Subsequently, this film was coated by drop-casting an aqueous solution of $La(NO_3)_3$ (lanthanum precursor) and drying. Subsequent annealing at 650°C in air triggered the formation of LFO coated with a crust of La_2O_3, which originated from the excess of lanthanum precursor. Pristine LFO was obtained by selectively etching away this surface oxide (see Supporting Information for details). Note that although three different temperatures, namely 550, 650 and 750°C, were tested, we will next focus our attention on LFO films prepared at 650°C since they deliver the best performance while not showing any sign of deleterious phase segregation (Figure S8.1).

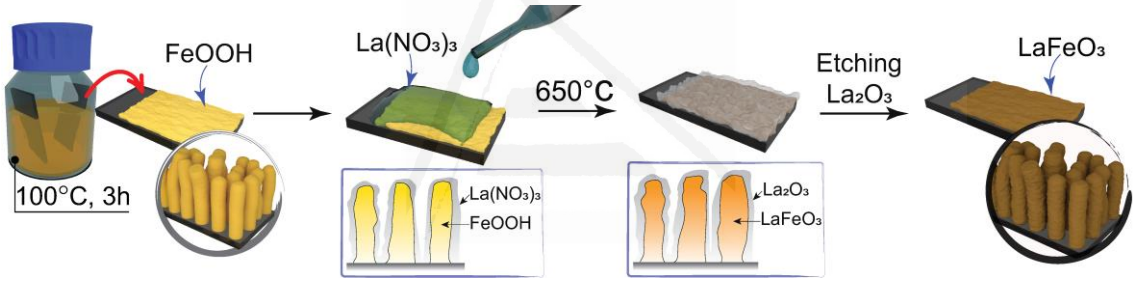

Figure 8.1. Schematics of the fabrication steps to produce nanorod array thin films of LFO. a) The hydrothermal synthesis of a nanorod array of FeOOH (Fe precursor) on the conductive substrate is followed by b) coating with a solution of $La(NO_3)_2$ (La precursor). c,d) Subsequent annealing of the film at 650 °C yields the LFO thin film after etching the resulting surface La_2O_3.

Cross-sectional and top-view scanning electron microscopy (SEM) images (Figure 8.2a,b) evidence that the LFO thin-film consists of randomly oriented nanorods with an average diameter of *ca*. 90 nm that give rise to a 550 nm-thick film. Raman spectroscopy together with X-ray diffractograms (XRD) were utilized to confirm the phase purity and identify the crystal structure of the film. First, Figure 8.2c shows a representative Raman spectrum of an as-prepared LFO thin film, which displays four distinct bands at 270, 410,

660 and 1295 cm^{-1} characteristic for the orthorhombic structure. The weak bands at 270 and 410 cm^{-1} have been assigned to A_g and B_{3g} modes, respectively, whereas the stronger bands at 660 and 1295 cm^{-1} have been reported to be related to two-phonon scattering phenomena [38,39]. Second, the XRD pattern of the as-prepared LFO thin film confirms its single phase orthorhombic perovskite structure (JCPDS #37-1493) [40,41]. It is worth noting that this synthetic route promoted crystal texturing, that is, preferential orientations during the ferrite formation. Indeed, when comparing the relative intensities of the diffractogram peaks with the standard powder diffraction pattern (Table S8.1) it is obvious that the (101) and (202) orientations are favored in these films. Finally, the UV-vis absorption spectrum further verified the formation of LFO, displaying its characteristic features, such as an absorption onset at 600 nm and a direct band gap close to 2.1 eV (inset). All in all, these results confirmed the formation of single-phase LFO and ruled out the presence of other phases such as α-Fe_2O_3 or La_2O_3.

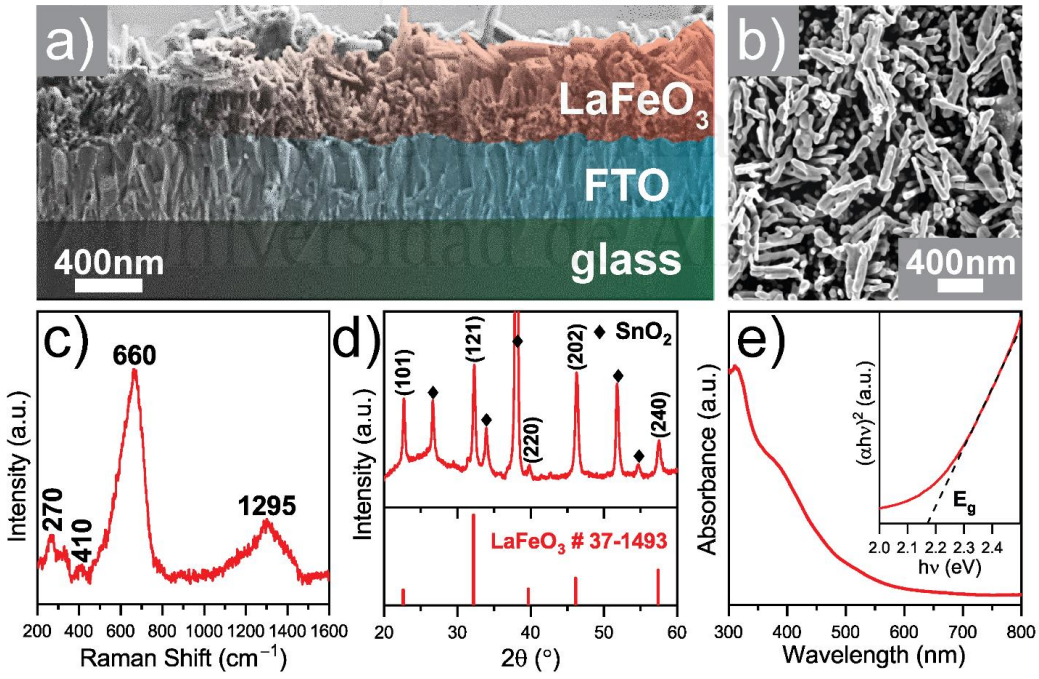

Figure 8.2. a) Cross-sectional and b) top-view SEM image of as-prepared LFO thin films, as well as the c) Raman spectrum and d) XRD, including a reference diffraction pattern. e) Thin film UV-Vis absorption spectrum of LFO and the corresponding Tauc plot analysis for the direct optical band gap energy.

Understanding the catalysis phenomena requires to precisely identify the nature of the semiconductor surface. Therefore, high-resolution X-ray photoelectron spectroscopy (XPS) spectra of La 3*d*, Fe 2*p* and O 1*s* were recorded to define the chemical composition and oxidation state of the LFO surface (see Supporting Information for details). The surface composition extracted from XPS was 15.2 at% La, 8.6 at% Fe and 51.2 at% O revealing a La-rch surface (La/Fe 1.7). We, however, confirmed a bulk La/Fe ratio of 1.1 by ICP-MS that matched well with the fed stoichiometry. It is worth noting that finding La-excess on the surface of LFO is not rare, and indeed previous reports have also displayed surface La/Fe ratios of 1.2 [42]. Note that Stoetzinger *et al.* found by computational simulations that LaO-rich surfaces are more reactive than FeO towards water adsorption [43], which, in turn, favors the OER.

Figure 8.3a shows the linear sweep voltammetry (LSV) under chopped-light illumination (AM 1.5G, 100 mW cm^{-2}) of LFO as a function of different treatments. As-prepared LFO (black line) exhibits both photocathodic and photoanodic response, with the photocurrent switching occurring at around 0.65 V *vs.* RHE. This behavior is commonplace among nanostructured electrodes wherein the charge separation does not occur by a space-charge field but rather by diffusion, and the *p*- or *n*-type character is ultimately determined by the delicate balance between surface charge transfer kinetics, preferential surface trapping and charge collection of one of the carriers [44–47]. Given the low doping density of pristine LFO films and the location (*vide infra*), it would not be unconceivable to suggest that the built-in electric field developed around the *p*-type – *n*-type switching region is barely negligible, allowing diffusion mechanisms to control the PEC response. We hypothesize that at low applied potentials (< 0.65 V) photogenerated electrons are preferentially trapped at the interface, driving, subsequently, the reduction of oxygen dissolve in the electrolyte [44]. At higher applied potentials (>

0.65 V) the drift-like charge separation induced by the increasing band bending starts to take over, resulting in the *n*-type behavior associated to PEC water oxidation. To further strengthen the built-in electric field in the *n*-type region, bare LFO films were intentionally *n*-doped with oxygen vacancies (O_{vac}), by annealing in the presence of H_2, coded as H-LFO. Indeed, comparison of the XPS O 1*s* spectra obtained before and after hydrogen treatment reveals an increase in the ratio between oxygen defects and lattice oxygen (O_{vac}/O_{latt}) from 0.69 to 0.81 (see Figure S8.3 and Supporting information for further details). As a result, the H_2-treatment doubled the photocurrent values in the *n*-type region (red line) reaching values of up to 0.22 mA cm^{-2} at 1.23 V *vs.* RHE, while leaving unchanged the photocurrent switching potential and photocathodic response. In addition, photocurrent transient spikes appeared upon the treatments evidencing surface recombination. Note that the *p*-type photocurrents are much poorer that those observed in the *n*-type regime. This is expected, not only because of the small concentration (traces) of oxygen dissolved in the electrolyte, but also because holes, with lower mobility than electrons in LFO, are more likely to recombine on the way to the substrate.

We next engineered the H-LFO surface by coating with $NiFeO_x$ (NFO). The H-LFO / NFO films delivered a benchmarking photocurrent of 0.4 mA cm^{-2} at 1.23 V *vs.* RHE without noticeable transient photocurrent spikes while the onset potential shifts up to 0.55 V *vs.* RHE. Interestingly, the photocathodic response was completely suppressed, likely because of the passivation of surface electron traps. The incident photon-to-current efficiency (IPCE) spectra recorded for all samples provided evidence that the spectral response matches the LFO absorption spectrum and further corroborated the increased photocurrent upon subsequent treatments (Figure S8.4). In addition, we determined the Faradaic efficiency for solar water oxidation of H-LFO/NFO to be 96 ± 3 % (Figure S8.5).

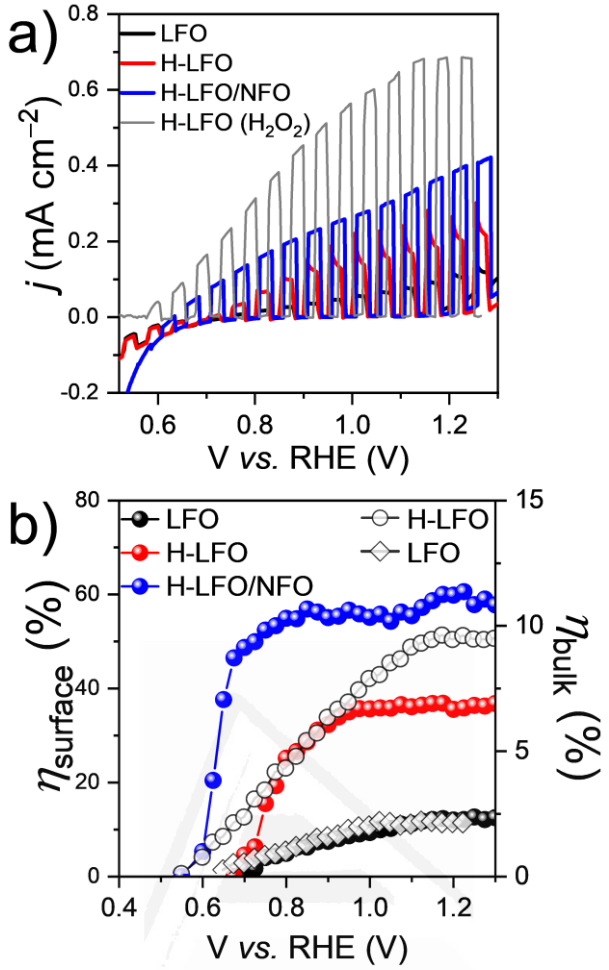

Figure 8.3. a) Linear sweep voltammograms under chopped-light illumination for LFO as a function of the treatment (pristine, annealed, NFO-coated) and electrolyte (baseline corrected for H_2O_2 measurement). b) Charge transfer ($\eta_{surface}$, full markers) and charge separation (η_{bulk}, empty marker) efficiency for LFO as a function of the treatment. The electrolyte employed was 1 M NaOH, except the measurement coded "(H_2O_2)" which was carried out in 1 M NaOH + 0.5 M H_2O_2. All measurements were performed under an irradiance of 1 sun (AM 1.5G) using a scan rate 20 mV s^{-1}.

With the aim of narrowing down the origin of the photogenerated carrier losses, the so-called charge transfer efficiency at the electrode/electrolyte interface ($\eta_{surface}$) and charge separation efficiency in the bulk (η_{bulk}) were calculated (Figure 8.3b) [48]. To do so, H-LFO was first tested in the presence of H_2O_2 (Figure 8.3a, grey line) as sacrificial hole scavenger. Assuming that in the presence of this sacrificial hole scavenger all the

holes arriving to the surface are transferred to the electrolyte, $\eta_{surface}$ is defined as $J_{H_2O}/J_{H_2O_2}$. As observed, although the saturation value of $\eta_{surface}$ is very low (~10 %) for the bare material, it rapidly increased with the H_2-treatment (38%) and further improved with the incorporation of NFO (60%). Admittedly, these treatments demonstrated to improve $\eta_{surface}$ either by activating the catalytic process or mitigating the recombination but were insufficient to completely override the interfacial carrier losses. The photogenerated carrier losses in the bulk can be estimated via η_{bulk}, defined as $J_{H_2O_2}/J_{abs}$, wherein J_{abs} corresponds to the maximum photocurrent density that can be delivered by the photoanode on the basis of its absorption spectra, in this case, J_{abs} was estimated to be 7.5 mA cm^{-2} (Figure S8.6). Pristine LFO depicts a very poor charge separation efficiency, hitting a maximum of 2.5 % at high applied potentials that severely limits the photocurrent recorded. The H_2-treatment, however, caused η_{bulk} to increase 4-fold confirming the impact of the bulk properties as well as on the interface. Admittedly, η_{bulk} remains below the values of other emerging ferrites [12,48] and could be certainly linked to the short minority carrier diffusion length, estimated to be < 5 nm (see Supporting Information) together with bulk transport issues. Overall, these results provide compelling evidence that both surface and bulk recombination are behind the low photocurrent response. Unfortunately, these analyses merely weigh the contribution of surface and bulk losses but cannot pinpoint the underlying limiting electronic/kinetic features of these electrodes. Identifying these parameters is key to rationally engineer the next generation of photoanodes. With this in mind, we will next focus on deciphering the role that oxygen vacancy-implantation and NFO-coating play at enhancing the performance as well as the underlying photogenerated carrier dynamics that govern the PEC response.

The impact of the lattice oxygen vacancies on the bulk transport characteristics was investigated in a solid-state fashion to circumvent any interference from the electrolyte (see Supporting Information for details) [12]. The conductivity in the longitudinal direction (along the nanorod) consistently increased from 9.4 to 23.1 μScm^{-1} upon the H_2-treatment (Figure 8.4a) suggesting that oxygen defects improved bulk charge transport likely by improving the electron density as typically reported in metal oxide photoanodes [49,50].

Several reports dealing with oxide perovskite electrocatalyst have acknowledged the impact of surface oxygen vacancies on the OER catalysis [23,25,26], though this phenomenon has not been brought up yet on perovskite photoanodes. Dark LSVs of LFO and H-LFO photoanodes were recorded to interrogate the impact of oxygen defects on the electrocatalytic performance (Figure 8.4b). Note that we performed an iR-correction that not only compensates for the ohmic resistance but also for the film's resistance, estimated above (Figure 8.4a). As a result, dark LSVs are primarily controlled by the surface catalytic activity. Both electrodes display a steep increase of current at potentials above 1.6 V *vs.* RHE, which corresponds to the OER. This early response, at potentials much more positive than the valence band (see Supporting Information for details on the energy band positions), is not unexpected and, indeed, it has been reported for several oxide photoanodes [48,51]. This phenomenon is commonly accounted for by the presence of a large density of mid-gap states which leads to a significant current leakage at the photoanode/electrolyte interface [52]. Interestingly, the incorporation of surface oxygen vacancies drastically reduced the overpotential to achieve a current density of 10 mA cm^{-2} by 100 mV, *i.e.* from 1.88 V (LFO) to 1.78 V (HLFO), while the Tafel slope decreased from 160 mV dec^{-1} to 110 mV dec^{-1}, respectively. These results lead us to firmly conclude that surface oxygen vacancies activate the catalytic activity of the

perovskite oxide photoanodes' interface. We hypothesize that, the surface oxygen defects favor the OER by exposing more of the iron centers, presumably the redox active centers, and by reducing the adsorption energy of the reaction intermediates, as it has been argued among oxide perovskites electrocatalysts [23,25,26].

Next, a series of spectroelectrochemical techniques were deployed to unravel how NFO activates the H-LFO photoanode towards the solar water oxidation. Photoelectrochemical impedance spectroscopy (PEIS) was utilized first to determine the basic bulk electronic properties of bare H-LFO photoanodes. Assuming, with caution, the validity of the Mott–Schottky (MS) model, we obtained flat band (V_{fb}) potential of around 0.43 V *vs.* RHE (see Supporting information), which matches quite well with that reported by Peng *et al*., although in that case the authors reported a photocurrent onset severely delayed beyond 1.23 V *vs.* RHE [32]. In a broader context, this estimated V_{fb} is very promising, being amongst the lowest when compared with state-of-the-art ferrite photoanodes such as $ZnFe_2O_4$ (0.64 V *vs.* RHE) [37], α-Fe_2O_3 (0.45-0.6 V *vs.* RHE) [53] or $CuFe_2O_4$ (0.7 V *vs.* RHE) [54]. Likewise, MS analysis brought out a relatively low donor concentration (N_D) of 7.32×10^{17} cm^{-3}, when compared with metal oxides such as α-Fe_2O_3 [55] $CuFe_2O_4$ [54] or $BiVO_4$ [13]. This value directly impacts on the depletion width, which is calculated to reach values of ca. 90 nm at 1.2 V *vs*. RHE (see Supporting Information), that is, the diameter of the LFO nanorods. These findings suggest that the nanorods would be near to fully depleted although withstanding a rather weak space-charge field, even upon doping with oxygen vacancies, which will limit the charge separation.

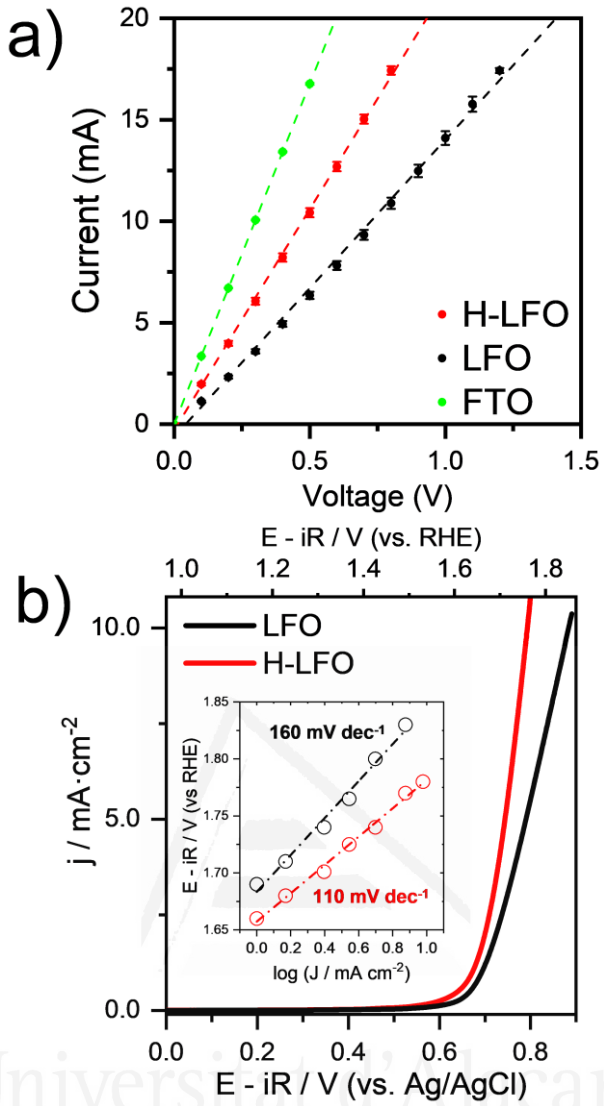

Figure 8.4. a) Current *vs.* voltage characteristics, including FTO as reference. b) *iR*-corrected linear sweep voltammogram of LFO and H-LFO, (inset) corresponding Tafel plot.

To interrogate how the interfacial electronic structure is affected by NFO, the density of surface states (DOS) was plotted as a function of the applied bias (Figure 8.5, see Supporting Information for details). In all cases, the DOS were fitted to a Gaussian function and the corresponding total density of surface states (N_{SS}) was extracted from the integration of the Gaussian function. Surprisingly, the DOS changes drastically with the incorporation of NFO. In fact, whereas H-LFO displays a single broad DOS band ranging from 0.8 V to 1.1 V *vs.* RHE, the deposition of NFO causes the appearance of

two distinct bands extending from 0.65 V to 0.85 V *vs.* RHE and from 0.95 V to 1.05 V *vs.* RHE, respectively. It must be borne in mind that PEIS does not reveal the actual potential of the surface accumulated holes. To determine the actual energy distribution of the DOS, the photovoltage (quasi-Fermi levels splitting) generated by the photoanode must be added to the potential at which DOS are detected by PEIS. It is worth noting that the first band is centered around the photocurrent onset in both photoanodes. This suggests that it corresponds to the build-up of surface holes that precedes the water oxidation reaction, typically in the form of high-valent metal-oxo complexes [53,55,56]. Analysis of these DOS reveals that N_{SS} reaches values of (3.7 ± 0.1) 10^{15} cm^{-2} and (3.7 ± 0.2) 10^{15} cm^{-3} for the bare and coated H-LFO film, respectively. These values are high enough to cause Fermi level pinning (FLP) (> 10^{12} cm^{-3}) [57], which could account for the observed delay in the photocurrent onset with respect to V_{fb}. Aside from the surface recombination involving the reactive intermediate species tracked by PEIS, we cannot rule out the presence of additional surface recombination pathways linked, for instance, to intrinsic surface trap states [58]. The fact that we could not find evidence of them by using rapid-scan cyclic voltammetry, as previously shown for other metal oxides [37,55], points to a very fast trapping-recombination phenomenon, if existing.

Proceeding further on the analysis of Figure 8.5, NFO-coated films display a "late" DOS, with a N_{SS} value of (7.5 ± 0.1) 10^{14} cm^{-3}. The existence of two distinct DOS bands in the presence of NFO bears out the fact that two types of surface reacting holes with different oxidation potential are driving the water oxidation. The fact that the "late" DOS resembles the one observed in the bare films led us to conclude that it corresponds to holes accumulated at bare H-LFO's surface. Note that the porous nature of NFO renders some of the underlying surface of H-LFO virtually unchanged upon the coating. The "earlier" DOS could, however, be associated to holes accumulated either at NFO or at H-

LFO's surface. On the one hand, photogenerated holes could be quickly injected into the NFO and carry out the OER at its surface. The catalytic activity of NFO could account for the shift of the photocurrent onset and DOS [59]. On the other hand, NFO could act as a passivating agent, interacting with interfacial traps and suppressing the surface recombination, while the OER still occurs at the H-LFO's surface. The outcome will be as well a negative shift in the onset potential [60]. Deciphering which one of these scenarios prevails is of utmost importance to understand what limits the performance on LFO photoanodes from either holes accumulated at NFO or at H-LFO's surface.

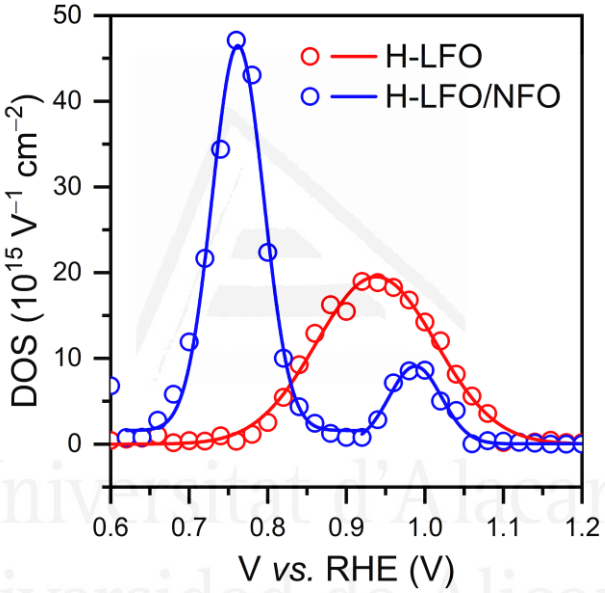

Figure 8.5. Energetic distribution of density of states (DOS) extracted from the impedance response recorded under 1 sun illumination. DOS profiles were fit with Gaussian functions.

To nail down the role of NFO, we next turned to interrogate the interfacial carrier dynamics at the photoanode/electrolyte interface. Figure 8.6a,b shows the intensity-modulated photocurrent spectroscopy (IMPS) Nyquist plots obtained at different applied potentials for bare and NFO-coated H-LFO. Overall, the response features two well-defined semicircles with the characteristic high- (HFI) and low-frequency intercept (LFI) with the real axis. Briefly, HFI is proportional to the flux of holes arriving to the interface,

and thus, it connects directly to the band bending developed within the material, whereas LFI correlates with the amount of holes that are ultimately injected into the electrolyte [53]. In the absence of NFO, HFI barely changes at low applied bias (< 0.8 V) but increases at higher potentials reaching saturation at 1.2 V *vs*. RHE. This sluggish variation of HFI agrees well with the presence of a strong FLP at the nearby of the photocurrent onset, which is mitigated at increasing applied bias. Likewise, LFI rises with potential owing to the increased surface accumulated holes. Strikingly, the incorporation of NFO causes HFI and LFI to increase readily in all the potential range, providing compelling evidence for the suppression of the FLP. By assuming a phenomenological model (see Supporting Information), the rate constant for charge transfer (k_{tran}) and recombination (k_{rec}) at the photoelectrode/electrolyte interface were estimated as a function of the applied potential. At first glance, the incorporation of NFO slightly decreases k_{tran} while causing k_{rec} to plunge. Firstly, in the absence of NFO, k_{tran} gradually increases with the applied potential, from 62 s^{-1} to 135 s^{-1}, which is common sign of FLP [61]. Coating with NFO reprograms k_{tran} to remain virtually unchanged in all the potential range, providing compelling evidence of the suppression, at least partially, of the FLP, and to yield a lower average value (slower reaction). Secondly k_{rec}, decreases with the applied bias in both bare and NFO-coated LFO owing to the strengthening of the space-charge field within the film. It is worth noting that the slope of k_{rec} *vs*. E plot increased from 0.7 to 1.4 s^{-1} V^{-1} supporting the mitigation of the FLP. However, we note that this slope is still far below the value expected for an ideal semiconductor liquid junction (16.5 s^{-1} V^{-1}) [62], likely because of the weak space-charge field in the material. More importantly, k_{rec} drastically drops with NFO from, for instance, 210 s^{-1} to 50 s^{-1} (at 1.2 V *vs*. RHE) indicating the suppression of surface recombination. Overall, the drastic slowdown of the surface recombination and charge transfer, the later expected to radically accelerate in the

presence of an electrocatalyst, confirms NFO's prime role as passivation. We note that recently, Wang and co-workers reported the role of NFO as passivating agent when deposited on hematite photoanodes [60]. It is worth mentioning that the increased k_{tran} in the bare film, with respect the NFO-coated one, could be rationally explained by the higher driving force of the surface holes in the former. The severe FLP present in the film is expected to cause a downward shift of the energy bands, this will result in an increased oxidizing power of the surface (lower quasi-Fermi level of holes) especially at high bias [62].

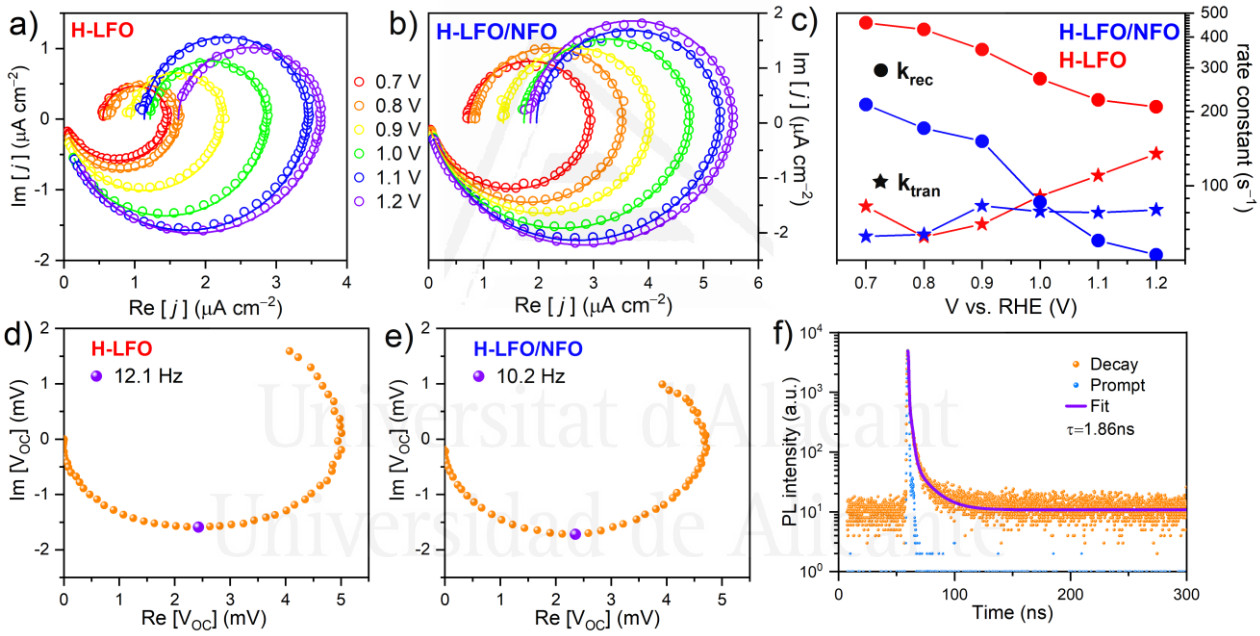

Figure 8.6. IMPS Nyquist plots recorded for a) H-LFO and b) H-LFO/NFO as a function of the applied potential. Corresponding solid lines are the fitting results (see Supporting Information). c) Charge transfer (k_{tran}) and surface recombination (k_{rec}) for bare and NFO-coated H-LFO extracted from IMPS. IMVS Nyquist plots obtained for d) bare and e) NFO-coated H-LFO. All measurements were performed in 1 M NaOH under an irradiance of 1 sun (AM 1.5G). f) Time-resolved photoluminescence (TRPL) decay of an H-LFO thin film electrode. The sample was excited at 340 nm. The fitting was carried out using a double exponential function.

Open circuit measurement such as intensity-modulated photovoltage spectroscopy (IMVS) and time-resolved photoluminescence (TRPL) were performed to elucidate the carrier recombination dynamics without the interference of the electrocatalytic reaction. Figure 8.6d,e show the IMVS Nyquist plots corresponding to bare and NFO-coated H-LFO. Both electrodes display a semicircle in the high-frequency range and an incomplete one in the low frequency. The high-frequency response is often considered to originate from the space charge recombination, whereas the second has been recently linked to the interfacial recombination (involving reactive intermediate species) [53,60]. A first-order electron lifetime can be calculated from the angular frequency at the minimum of the Nyquist plot $\left(\tau_n = 1/2\pi f_{min,IMVS}\right)$, yielding values of 13.2 ms and 15.6 ms, for bare and NFO-coated H-LFO photoanodes. As expected, the surface passivation of NFO would mitigate the FLP and hence afford a stronger space-charge field upon illumination under OCP that could lengthen the lifetime. Admittedly, these extremely long lifetimes are in stark contrast with the low photocurrents recorded. We, therefore, hypothesize that IMVS is accessing the dominant, but slow, recombination process presents within its scope, whereas major carrier losses are missed at earlier stages.

To probe the recombination kinetics at shorter timescales TRPL of H-LFO was recorded at 450 nm (Figure 8.6f). Note that the steady-state PL spectrum of H-LFO exhibits a broad emission band spanning from 400 to 550 nm centered at 450 nm, corresponding to the band-edge emission, as well as a weak band centered at about 750 nm, which has not been reported yet and likely relates to the surface-state emission involving mid-gap trap states (Figure S8.10). TRPL displays an abrupt decay with an average lifetime of only about 1.8 ns. Such a fast decay reflects a rapid annihilation of photogenerated carriers and provide compelling evidence of significant carrier losses early on upon the light absorption. Notably, the TRPL signal barely changed after coating

with NFO (results not shown) reinforcing the notion that the decay is primarily governed by bulk-related recombination pathways. We hypothesize that bulk recombination processes at the nanosecond timescale, and even shorter [63], could reduce severely the amount of free carriers and contribute to the low η_{bulk} described before.

Finally, with a better understanding on the parameters that dictate the PEC response set in place, we evaluated the operational stability of the photoanodes. The photocurrent delivered by both bare and NFO-coated H-LFO at 1.23 V *vs.* RHE decreases steadily over time, losing by about 80% of its value after 1 day. Intriguingly, despite the drop of photocurrent, H-LFO appears to be chemically stable in the electrolyte. For instance, no changes were noticeable neither at first sight nor using XRD, and the absorption spectrum and XPS spectra upon soaking the electrodes in concentrated NaOH solution (10 M) for 3 days remain virtually unchanged (Figure S8.11). Interestingly, we noticed a drop in the surface O_{vac} content upon the stability test. Figure 8.7b displays the XPS O 1*s* spectra of as-prepared LFO and H-LFO before and after the stability test (see Supporting information for further details on the band assignment). It is worth noting that the O_{vac}/O_{latt} ratio decreased from 0.81 to 0.63 after the long-term chronoamperometry, reaching a value similar to the one of pristine LFO (0.69). This provides compelling evidence that the refilling of O_{vac} is occurring in parallel to PEC water oxidation. In fact, the recovery of the photocurrent by repeating the hydrogen treatment (green line) further corroborates that the loss of O_{vac} is the prime culprit of the H-LFO deactivation. We note that Liu *et al*. proposed as well the refilling of the O_{vac} in $La_{0.7}Sr_{0.3}CoO_{3-\delta}$ to account for the deterioration of its dark electrocatalytic response after long periods of operation, although to the best of our knowledge this phenomenon has not been reported yet among photoelectrodes. Indeed, doping with O_{vac} is a common practice among metal oxides such as α-Fe_2O_3 or $ZnFe_2O_4$ to enhance the performance, but the lattice oxygen content

remains unaltered after long operation periods [37,64]. Likely, the characteristic high oxygen diffusivity and structural flexibility of the oxide perovskite to accommodate mobile oxygen ions within the lattice account for this unexpected behavior [65]. We hypothesize that the re-incorporation/intercalation of oxygen in the oxygen-deficient structure starts with the adsorption of OH^- from the electrolyte, as it occurs in OER (Figure 8.7c). Under illumination, OH^- binds to the reactive sites, *i.e.*, iron centers that accumulate photogenerated holes (Fe^{4+}) [66] preferentially via the oxygen vacancies (Figure 8.7c.1). Next, this adsorbed OH species could either undergo a series of oxidative transformations to release O_2 (OER process) or simply deprotonate and incorporate into the lattice (refilling O_{vac}, Figure 8.7c.2). Given the high ionic mobility assisted by the oxygen vacancies, the oxygen ion diffuses rapidly into the lattice allowing for this same mechanism to re-start. As a result, the newly incorporated oxygen fills a vacancy while neighboring Fe^{2+} centers re-oxidize to Fe^{3+} to compensate the negative charge of oxygen consuming holes photogenerated within the material. This phenomenon accounts for the non-ideal faradaic efficiency (< 100 %) since part of the photogenerated holes are used to re-oxidize the lattice rather than the water. It is, thus, not unreasonable to expect the gradual filling of both bulk and surface O_{vac} while the solar water oxidation occurs. The progressive decrease in photocurrent could be thus ascribed to the gradual loss of doping density and preferential adsorption sites (surface oxygen defects). We note that the presence of NFO did not improve the stability of the system, i.e. oxygen still incorporates in the structure under operation. This further supports the notion that the OER takes place preferentially at the oxide perovskite surface.

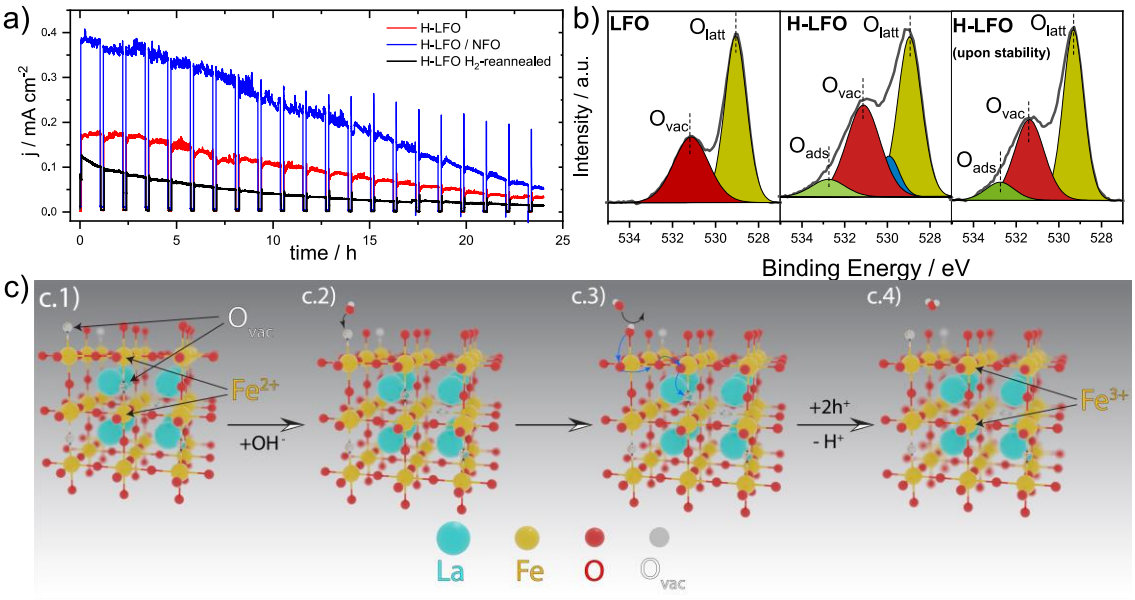

Figure 8.7. a) Extend chronoamperometry of H-LFO (red line) and H-LFO/NFO (blue line) recorded under chopped-light illumination (1 sun) at 1.23 V *vs*. RHE using 1 M NaOH as electrolyte. H-LFO (red line) was annealed again in the presence of H_2 after completing the stability test, and subsequently, it was subjected to the chronoamperometry test, herein coded as "H_2-reannealed". b) XPS O 1*s* spectra of as-prepared LFO and H-LFO, and H-LFO after the stability test, including the assignment of the deconvolved bands. c) Proposed mechanism of oxygen intercalation into H-LFO photoanodes. c.1) As-prepared H-LFO includes O_{vac} (and the corresponding Fe^{2+}) throughout the surface and bulk. c.2) Under illumination, surface O_{vac} on high-valent iron, i.e., accumulating photogenerated holes, will be the preferred site of adsorption of OH^- from the electrolyte. After being deprotonated, the O^{2-} could either undergo oxidation [66] to produce oxygen or c.3,.4) diffuse into the structure (blue arrows) along the octahedral edges filling eventually a bulk O_{vac} and causing the oxidation of the two neighbouring Fe^{2+} centers to Fe^{3+} to compensate the negative charge uptake.

8.4. CONCLUSIONS

In this work, we addressed the current bottleneck in the performance of LFO photoanode by seizing upon a novel electrode nanostructure in combination with post-engineering treatments as well as by parsing the electronic and catalytic characteristics that govern the performance. Our LFO nanorod array-type electrode delivered

photocurrents up to 0.4 mA cm^{-2} at 1.23 V *vs*. RHE with an onset of 0.55 V *vs.* RHE, thus, establishing a new benchmark performance for LFO-based PEC water oxidation. We found that inducing oxygen defects not only improved the carrier transport throughout the film, but specially activated the interface towards the OER leading to a substantial drop of the Tafel slope. Additionally, further engineering the interface by depositing NFO demonstrated to mitigate the deleterious surface recombination as confirmed by IMPS.

Admittedly, given that we determined that a photocurrent onset as low as 0.43 V *vs.* RHE and photocurrent values as high as 7.5 mA cm^{-2} could be achievable given its V_{fb} and light absorption, the benchmark reported herein still remains modest. Our investigations to elucidate the chief performance bottlenecks , revealed the existence of major carrier losses in the bulk (η_{bulk} < 10 %) and, although, in a minor extent at the interface ($\eta_{surface} > 60$ %) in the benchmark films. Firstly, TRPL measurements brought up the fast recombination of photogenerated carriers occurring mainly in the bulk in the nanosecond, or even shorter, timescales. In addition, the weak space-charge field and the short minority carrier diffusion length estimated for this material (< 5 nm) posed severe challenges for an efficient charge separation. Secondly, we found that enhancing the surface catalysis and passivation was key to improve 6-fold $\eta_{surface}$, though not able to fully override the deleterious recombination. In addition, we detected a gradual refilling of $O_{vac}s$ under operation that deteriorated the performance steadily over time. With all this information in hand, we anticipate that further progress on LFO photoanodes depends upon strengthening the space-charge field by, for instance, combining A-site and oxygen doping, as well as on devising a conformal catalytic overlayers that take over the OER to avoid the reinsertion of the oxygen ions in the lattice. Overall, we are convinced that these findings not only represent an encouraging step change in the state-of-the-art performance

for $LaFeO_3$ photoanodes, but more importantly, set forth the key processes that constrain the activity allowing to construct a clear path to further optimize this material.

8.5. ACKNOWLEDGMENTS

J.Q. thanks to the Spanish Ministry of Education, Culture, and Sport (MECD) for the award of an FPU predoctoral grant (FPU15/02005) and a mobility grant (EST17/00429). Y.L. and N.G. thank the Swiss National Science Foundation (SNSF) for funding under the Ambizione Energy Grant (PZENP2_166871). F. Boudoire is gratefully acknowledged for the IMPS data fitting.

8.6. REFERENCES

[1] F. Niu, D. Wang, F. Li, Y. Liu, S. Shen, T. J. Meyer, Adv. Energy Mater. 10 (2020) 1900399.
[2] R. Gao, D. Yan, Adv. Energy Mater. 10 (2020) 1900954.
[3] L. Zheng, F. Teng, X. Ye, H. Zheng, X. Fang, Adv. Energy Mater. 10 (2020) 1902355.
[4] K. Zhang, M. Ma, P. Li, D. H. Wang, J. H. Park, Adv. Energy Mater. 6 (2016) 1600602.
[5] J. Tan, W. Yang, Y. Oh, H. Lee, J. Park, R. Boppella, J. Kim, J. Moon, Adv. Energy Mater. 9 (2019) 1900179.
[6] N. Guijarro, M. S. Prévot, X. Yu, X. A. Jeanbourquin, P. Bornoz, W. Bourée, M. Johnson, F. Le Formal, K. Sivula, Adv. Energy Mater. 6 (2016) 1501949.
[7] N. Guijarro, M. S. Prévot, M. Johnson, X. Yu, W. S. Bourée, X. A. Jeanbourquin, P. Bornoz, F. L. Formal, K. Sivula, J. Phys. D: Appl. Phys. 50 (2017) 044003.
[8] L. Pan, J. H. Kim, M. T. Mayer, M.-K. Son, A. Ummadisingu, J. S. Lee, A. Hagfeldt, J. Luo, M. Grätzel, Nat. Catal. 1 (2018) 412.
[9] M. P. Browne, J. Plutnar, A. M. Pourrahimi, Z. Sofer, M. Pumera, Adv. Energy Mater. 9 (2019) 1900994.
[10] P.-Y. Tang, L.-J. Han, F. S. Hegner, P. Paciok, M. Biset-Peiró, H.-C. Du, X.-K. Wei, L. Jin, H.-B. Xie, Q. Shi, T. Andreu, M. Lira-Cantú, M. Heggen, R. E. Dunin-Borkowski, N. López, J. R. Galán-Mascarós, J. R. Morante, J. Arbiol, Adv. Energy Mater. 9 (2019) 1901836.
[11] M. Jadwiszczak, K. Jakubow-Piotrowska, P. Kedzierzawski, K. Bienkowski, J. Augustynski, Adv. Energy Mater. 10 (2020) 1903213.
[12] X. Zhu, N. Guijarro, Y. Liu, P. Schouwink, R. A. Wells, F. L. Formal, S. Sun, C. Gao, K. Sivula, Adv. Mater. 30 (2018) 1801612.
[13] Z. Tian, P. Zhang, P. Qin, D. Sun, S. Zhang, X. Guo, W. Zhao, D. Zhao, F. Huang, Adv. Energy Mater. 9 (2019) 1901287.
[14] D. K. Lee, K.-S. Choi, Nat. Energy. 3 (2018) 53.
[15] M. S. Prévot, K. Sivula, J. Phys. Chem. C. 117 (2013) 17879.

[16] D. K. Lee, D. Lee, M. A. Lumley, K.-S. Choi, Chem. Soc. Rev. 48 (2019) 2126.
[17] W. Wang, M. Xu, X. Xu, W. Zhou, Z. Shao, Angew. Chem. Int. Ed. 59 (2020) 136.
[18] W.-J. Yin, B. Weng, J. Ge, Q. Sun, Z. Li, Y. Yan, Energy Environ. Sci. 12 (2019) 442.
[19] A. Grimaud, O. Diaz-Morales, B. Han, W. T. Hong, Y.-L. Lee, L. Giordano, K. A. Stoerzinger, M. T. M. Koper, Y. Shao-Horn, Nat. Chem. 9 (2017) 457.
[20] R. P. Forslund, W. G. Hardin, X. Rong, A. M. Abakumov, D. Filimonov, C. T. Alexander, J. T. Mefford, H. Iyer, A. M. Kolpak, K. P. Johnston, K. J. Stevenson, Nat. Commun. 9 (2018) 1.
[21] L. Yang, G. Yu, X. Ai, W. Yan, H. Duan, W. Chen, X. Li, T. Wang, C. Zhang, X. Huang, J.-S. Chen, X. Zou, Nat. Commun. 9 (2018) 1.
[22] J. T. Mefford, X. Rong, A. M. Abakumov, W. G. Hardin, S. Dai, A. M. Kolpak, K. P. Johnston, K. J. Stevenson, Nat. Commun. 7 (2016) 1.
[23] J. Kim, X. Yin, K.-C. Tsao, S. Fang, H. Yang, J. Am. Chem. Soc. 136 (2014) 14646.
[24] X. Liu, L. Zhang, Y. Zheng, Z. Guo, Y. Zhu, H. Chen, F. Li, P. Liu, B. Yu, X. Wang, J. Liu, Y. Chen, M. Liu, Adv. Sci. 6 (2019) 1801898.
[25] Y. Zhu, W. Zhou, J. Yu, Y. Chen, M. Liu, Z. Shao, Chem. Mater. 28 (2016) 1691.
[26] X. Miao, L. Wu, Y. Lin, X. Yuan, J. Zhao, W. Yan, S. Zhou, L. Shi, Chem. Commun. 55 (2019) 1442.
[27] I. Grinberg, D. V. West, M. Torres, G. Gou, D. M. Stein, L. Wu, G. Chen, E. M. Gallo, A. R. Akbashev, P. K. Davies, J. E. Spanier, A. M. Rappe, Nature. 503 (2013) 509.
[28] I. E. Castelli, T. Olsen, S. Datta, D. D. Landis, S. Dahl, K. S. Thygesen, K. W. Jacobsen, Energy Environ. Sci. 5 (2012) 5814.
[29] J. Seo, T. Hisatomi, M. Nakabayashi, N. Shibata, T. Minegishi, M. Katayama, K. Domen, Advanced Energy Materials. 8 (2018) 1800094.
[30] T. Minegishi, N. Nishimura, J. Kubota, K. Domen, Chem. Sci. 4 (2013) 1120.
[31] G. S. Pawar, A. A. Tahir, Sci. Rep. 8 (2018) 3501.
[32] Q. Peng, B. Shan, Y. Wen, R. Chen, Int. J. Hydrog. Energy. 40 (2015) 15423.
[33] I. Natali Sora, F. Fontana, R. Passalacqua, C. Ampelli, S. Perathoner, G. Centi, F. Parrino, L. Palmisano, Electrochim. Acta. 109 (2013) 710.
[34] K. A. Stoerzinger, L. Wang, Y. Ye, M. Bowden, E. J. Crumlin, Y. Du, S. A. Chambers, J. Mater. Chem. A. 6 (2018) 22170.
[35] Q. Peng, J. Wang, Y. W. Wen, B. Shan, R. Chen, RSC Adv. 6 (2016) 26192.
[36] C. Liu, N. P. Dasgupta, P. Yang, Chem. Mater. 26 (2014) 415.
[37] N. Guijarro, P. Bornoz, M. Prévot, X. Yu, X. Zhu, M. Johnson, X. Jeanbourquin, F. L. Formal, K. Sivula, Sustainable Energy Fuels. 2 (2018) 103.
[38] M. Romero, R. W. Gómez, V. Marquina, J. L. Pérez-Mazariego, R. Escamilla, Physica B: Condensed Matter. 443 (2014) 90.
[39] I. Jaouali, H. Hamrouni, N. Moussa, M. F. Nsib, M. A. Centeno, A. Bonavita, G. Neri, S. G. Leonardi, Ceram. Int. 44 (2018) 4183.
[40] G. P. Wheeler, K.-S. Choi, ACS Energy Lett. 2 (2017) 2378.
[41] L. V. Kokhanovskii, Yu. G. Zonov, O. P. Ol'shevskaya, V. V. Pan'kov, Inorg. Mater. 41 (2005) 876.
[42] E. Cao, T. Cui, Y. Yang, Y. Zhang, W. Hao, L. Sun, H. Peng, Mater. Lett. 190 (2017) 143.
[43] K. A. Stoerzinger, R. Comes, S. R. Spurgeon, S. Thevuthasan, K. Ihm, E. J. Crumlin, S. A. Chambers, J. Phys. Chem. Lett. 8 (2017) 1038.
[44] A. Tsujiko, H. Itoh, T. Kisumi, A. Shiga, K. Murakoshi, Y. Nakato, J. Phys. Chem. B. 106 (2002) 5878.

[45] L. Kronik, N. Ashkenasy, M. Leibovitch, E. Fefer, Y. Shapira, S. Gorer, G. Hodes, J. Electrochem. Soc. 145 (1998) 1748.
[46] G. Hodes, I. D. J. Howell, L. M. Peter, J. Electrochem. Soc. 139 (1992) 3136.
[47] N. Guijarro, T. Lana-Villarreal, R. Gómez, Chem. Commun. 48 (2012), 7681.
[48] H. Dotan, K. Sivula, M. Grätzel, A. Rothschild, S. C. Warren, Energy Environ. Sci. 4 (2011) 958.
[49] X. Zhao, J. Feng, S. Chen, Y. Huang, T. C. Sum, Z. Chen, Phys. Chem. Chem. Phys.19 (2017) 1074.
[50] J. H. Kim, Y. J. Jang, J. H. Kim, J.-W. Jang, S. H. Choi, J. S. Lee, Nanoscale. 7 (2015) 19144.
[51] K. Sivula, R. Zboril, F. Le Formal, R. Robert, A. Weidenkaff, J. Tucek, J. Frydrych, M. Grätzel, J. Am. Chem. Soc. 132 (2010) 7436.
[52] X. Ye, J. Yang, M. Boloor, N. A. Melosh, W. C. Chueh, J. Mater. Chem. A. 3 (2015) 10801.
[53] Y. Liu, F. Le Formal, F. Boudoire, N. Guijarro, ACS Appl. Energy Mater. 2 (2019) 6825.
[54] Y. Liu, F. L. Formal, F. Boudoire, L. Yao, K. Sivula, N. Guijarro, J. Mater. Chem. A. 7 (2019) 1669.
[55] B. Klahr, S. Gimenez, F. Fabregat-Santiago, J. Bisquert, T. W. Hamann, Energy Environ. Sci. 5 (2012) 7626.
[56] B. Klahr, T. Hamann, J. Phys. Chem. C. 118 (2014) 10393.
[57] A. J. Bard, A. B. Bocarsly, F. R. F. Fan, E. G. Walton, M. S. Wrighton, J. Am. Chem. Soc. 102 (1980) 3671.
[58] O. Zandi, T. W. Hamann, J. Phys. Chem. Lett. 5 (2014) 1522.
[59] P. Sharma, J.-W. Jang, J. S. Lee, ChemCatChem. 11 (2019) 157.
[60] J. E. Thorne, J.-W. Jang, E. Y. Liu, D. Wang, Chem. Sci. 7 (2016) 3347.
[61] C. Zachäus, F. F. Abdi, L. M. Peter, R. van de Krol, Chem. Sci. 8 (2017) 3712.
[62] L. M. Peter, K. G. U. Wijayantha, A. A. Tahir, Faraday Discuss. 155 (2012) 309.
[63] W. Li, K. Jiang, Z. Li, S. Gong, R. L. Z. Hoye, Z. Hu, Y. Song, C. Tian, J. Kim, K. H. L. Zhang, S. Cho, J. L. MacManus-Driscoll, Adv. Energy Mater. 8 (2018) 1801972.
[64] Z. Wang, X. Mao, P. Chen, M. Xiao, S. A. Monny, S. Wang, M. Konarova, A. Du, L. Wang, Angew. Chem. Int. Ed. 58 (2019) 1030.
[65] J. T. Mefford, W. G. Hardin, S. Dai, K. P. Johnston, K. J. Stevenson, Nat. Mater. 13 (2014) 726.
[66] F. Le Formal, E. Pastor, S. D. Tilley, C. A. Mesa, S. R. Pendlebury, M. Grätzel, J. R. Durrant, J. Am. Chem. Soc. 137 (2015) 6629.

8.7. SUPPORTING INFORMATION

8.7.1. Experimental methods

8.7.1.1. Fabrication of $LaFeO_3$ thin-film electrodes

$LaFeO_3$ photoelectrodes were prepared by a two-step solution-based route according to a previously reported procedure by Kim and co-workers [S1]. First, a nanorod-based layer of β-FeOOH was grown on a fluorine-doped tin oxide (F:SnO_2, FTO) substrate (Solaronix TCO10-10), previously cleaned by sonication in pure acetone and absolute ethanol (for 15 min in each one). Clean FTO substrates were vertically supported with the conductive side facing a 0.15 M $FeCl_3 \cdot 6H_2O$ (99%, Acros Organics) and 1 M $NaNO_3$ (99%, Acros Organics) aqueous solution contained in a tightly capped glass bottle. The area of FTO substrate to be covered with the FeOOH deposit was, approximately, 3.0 cm^2. The solution was heated up to 100ºC in a stove for 3 hours. After deposition, the samples were rinsed with abundant ultrapure water and dried with compressed air. In a second step, the resulting FTO/FeOOH electrodes were placed in a pre-heated hot-plate at 100ºC and coated (by drop-casting) with an excess of a 0.1 M $La(NO_3)_3 \cdot 6H_2O$ (98%, Acros Organics) aqueous solution. The electrodes remained on the hot-plate until the $La(NO_3)_3$ solution evaporated completely. Finally, the $LaFeO_3$ formation was carried out by introducing the $La(NO_3)_3$-coated FeOOH samples into a tubular oven (MTI OTF-1200X) pre-heated at 550, 650 or 750ºC for 20 min, followed by a quick-cooling method: right after the annealing, the electrodes were removed from the oven to allow them to cool-down naturally. The resulting samples were immersed in 0.5 M H_2SO_4 (Sigma Aldrich, 96-98%) aqueous solution overnight to completely remove the La_2O_3 white crust that covers the electrode surface after the annealing.

8.7.1.2. Annealing post-treatments

Two different annealing post-treatments were performed: a hydrogenation annealing at 200ºC for 1 hour (in tubular oven, heating rate: 5ºC·min^{-1}) and an annealing in air at different temperatures (300, 450 and 650ºC) for 5 hours (in programmable oven, heating rate: 5ºC·min^{-1}).

8.7.1.3. $NiFeO_x$ deposition

The post-hydrogenated $LaFeO_3$ samples were coated with $NiFeO_x$ (NFO) based on a previously reported procedure by Smith and co-workers [S2]. Iron (III) 2-ethylhexanoate (50% w/w in mineral spirits, Strem Chemicals) and nickel (II) 2-ethylhexanoate (78% w/w in 2-ethylhecanoic acid, Strem Chemicals) were dissolved in hexane as to achieve a 1:1 Fe:Ni molar ratio and a total concentration of 15% w/w for the metal complexes in solution. This precursor solution was diluted ten times with hexane and around 10 µL·cm^{-2} were drop-casted on the active surface area of the electrode. The electrode was subsequently dried in air and, then, was exposed to UV irradiation (Atlantic Ultraviolet G18T5VH/U lamp) for 15 min. Finally, the electrode was annealed at 100ºC for 1 hour (in programmable oven, heating rate: 5ºC·min^{-1}) [S3].

8.7.1.4. (Photo)electrochemical characterization

All the photoelectrochemical characterization was carried out employing a potentiostat (BioLogic SP-300) and a Capuccino-type PEC cell, where a Ag/AgCl/KCl(sat.) electrode and a Pt wire where used as reference and counter electrode, respectively, and the active geometric area of the working electrode was 0.238 cm^2. Two different electrolytes were employed: 1 M NaOH or 1 M NaOH + 0.5 H_2O_2, purged with O_2 when indicated. Chopped-light linear sweep under illumination were performed using

a 450 W Muller Elektronic Xenon-arc lamp coupled with a KG-1 filter (Schott) calibrated to provide 1 sun (AM 1.5G, 100 mW·cm^{-2}). In all cases, the electrodes were illuminated from the front-side (electrolyte-electrode –EE– illumination). The yield of charge transfer was calculated by using $\eta_{\text{surface}} = j_{H_2O}/j_{H_2O_2}$, whereas the yield of charge separation was determined with $\eta_{\text{bulk}} = j_{H_2O_2}/j_{abs}$, where j_{H_2O} and $j_{H_2O_2}$ correspond to the photocurrent for water and H_2O_2 oxidation, respectively, while j_{abs} is the maximum photocurrent attainable considering that all the light absorbed by the thin film is turned into photogenerated carriers with 100% collection efficiency (see Figure S8.6).

The electrocatalytic activity of the films were evaluated by recording dark linear sweep voltammograms at 20 mV·s^{-1}. Tafel plots were constructed by recording the stable potential (after 5 min) at different fixed currents.

Incident photon-to-current efficiency (IPCE) measurements were performed using a Tunable PowerArc illuminator (Optical Building Block Corporation) as light source coupled to a monochromator and determining the photon flux at each wavelength with a S12VC Photodiode Power sensor (Thorlabs).

Measurement of the oxygen production associated to the photo-assisted water oxidation was performed with a Clarus 480 Gas Chromatograph (Perkin Elmer), equipped with a plasma emission detector (PlasmaDetek), coupled to a three-electrode Cappuccino-type cell. A H-LFO650/NFO electrode was used as a working electrode, while a Pt foil and a Ag/AgCl/KCl(sat.) electrode were used as counter and reference electrodes, respectively. The corresponding calibration line was obtained by using a piece of Pt foil as a working electrode and considering that water oxidation occurs with a 100% Faradaic efficiency (see Figure S8.5).

Chronoamperometry was conducted at 1.23 V (*vs*. RHE) in 1 M NaOH for 24 hours to test the stability.

Hole diffusion length was estimated by a monochromatic illumination (452 nm) experiment under sacrificial agent (0.5 M H_2O_2) oxidation conditions. An array of RGBW Star LEDs (Cree) was used as light source with a calibrated incident photon flux of 1.41 $\times 10^{21}$ m^{-2} s^{-1}. The sample was illuminated from the electrolyte side.

Electrochemical impedance spectroscopy (EIS) was performed on a Bio-Logic SP-300 potentiostat. The voltage perturbation was applied within a frequency range from 100 kHz to 50 mHz with a 25 mV sinusoidal amplitude. An equivalent circuit modelling software ZView (Scribner Associates) was used to fit the EIS data.

For intensity-modulated photocurrent/photovoltage spectroscopy (IMPS/IMVS) measurements, an array of white LED (Cree XLamp MC-E Color) was used as light source. The background illumination was powered by a DC power supply at 600 mA DC current. The additional light perturbation was modulated by an arbitrary function generator (Tektronix AFG3021C) with a 50 mA sinusoidal amplitude (ca. 8% modulation depth) ranging from 10 kHz to 50 mHz. The above-mentioned 3-electrode configuration was used for light modulation measurements. The intensity-modulated photocurrent response was monitored by a digital phosphor oscilloscope (Tektronix DPO7254C) through a 50 Ω series resistor (Velleman E6/E12). The intensity-modulated photovoltage response was recorded by the oscilloscope through a differential probe (Tektronix TDP3500). The entire light modulation setup was covered with blackout materials (Thorlabs) to prevent interference from ambient light. IMPS data was processed and fitted using a custom program written with the Python programming language. The lmfit package for Python was used to perform curve fitting with nonlinear regression.

All experiments were performed at ambient temperature and electrode potentials were converted to the RHE scale using $E\ (vs. RHE) = E\ (vs.\ Ag/AgCl) + 0.197\ V + 0.059pH$, where pH is 13.6 (for 1 M NaOH), and $E\ (vs.\ RHE)$ and $E\ (vs.\ Ag/AgCl)$

are the converted potential versus RHE and the measured potential *versus* Ag/AgCl reference electrode, respectively.

8.7.1.5. Electrode and solution characterization

UV-vis absorption spectra of the thin films were recorded with a UV-vis-NIR UV-3600 (Shimadzu) spectrophotometer equipped with an integrating sphere. SEM imaging was carried out to characterize the surface morphology of the films using a ZEISS Merlin emission electron microscope with an acceleration voltage of 3 keV, 79 pA probe current, and using an in-lens detector with a working distance of 3 mm. XRD patterns were recorded with an Empyrean (PANalytical) diffractometer. Raman spectra were obtained with an Xplora Plus Raman microscope (Horiba Scientific) using an excitation line of 532.19 nm provided by a diode laser. Steady-state photoluminescence (PL) spectra were recorded on a high resolution photoluminescence spectrofluorometer (Horiba Jobin Yvon Fluorolog-3) with an excitation wavelength of 340 nm. In time-resolved photoluminescence spectroscopy (TRPL) measurement, a nanosecond LED with 390 nm peak wavelength (Horiba NanoLED N-390, pulse width < 1.3 ns) was used to excite sample. TRPL decay was tracked at 450 nm. Average lifetime was obtained by fitting the TRPL spectra with DAS6 software (Horiba).

To elucidate the surface chemical composition along with the valence states of the elements present in the films, XPS experiments were performed with a Thermo-Scientific K-Alpha XPS spectrometer equipped with a monochromatic Al-Kα source (1486.6 eV), operating at 15 kV and 10 mA. ICP-MS measurements were performed using a Thermo Elemental (VG PQ-ExCell) analyzer. The LFO thin film was completely dissolved in 1 mL of HCL 37 % after 24 h to carry out the ICP-MS analysis.

8.7.1.6. Determination of the conductivity of the film in solid-state configuration

Current-voltage characteristics were acquired in the direction perpendicular to the substrate, that is, in the axial direction of the nanorods, using a eutectic In-Ga contact as illustrated in Figure S8.1 [S4]. The measurement was carried out using a Keithley 2400 source meter contacting both the In-Ga and FTO contact in a N_2-filled glove box. The data shown in Figure 8.3b (main text) was averaged among 10 measurements performed in each sample in different spots (error bars represent the standard deviation). Linear fits (dotted lines) were performed in all cases in the ohmic regions with $R^2 > 0.99$.

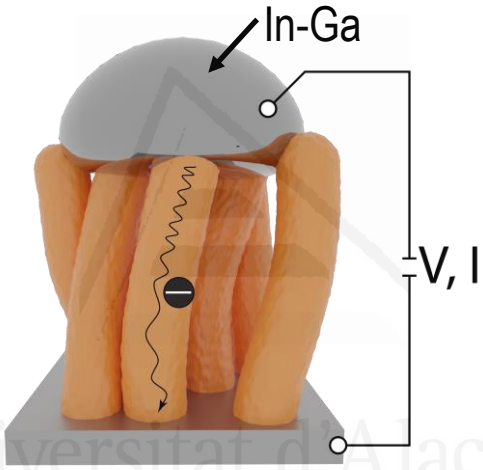

Figure S8.1. Schematics on the solid-state J-V measurement performed to extract the conductivity of the films, with one contact done via the eutectic In-Ga drop deposited on top of the film and the other via the FTO substrate.

To take into account the nanostructured morphology of the LFO when estimating the conductivity of the film from the J-V characteristics we defined the "void percentage" (P_{void}) of the structure [S1]. First, we determined the average number of nanorods (N) in an area of 800 x 800 nm^2 in a top-view SEM image (Figure 8.2b, main text). With this, we could estimate the volume occupied by the nanorods V_N as follows:

$$V_N = N \cdot \pi r^2 h$$

wherein r represents the average radius of the nanorods (45 nm), h is the thickness of the film (550 nm) and N is the averaged number of nanorods (40).

Additionally, the volume for a hypothetical compact structure V_C could be calculates as:

$$V_C = 800 \cdot 800 \cdot h$$

With all this data in hand, we could estimate P_{void} as:

$$P_{void} = 1 - \frac{V_N}{V_C}$$

The film conductivity was estimated by using the following equation:

$$\sigma = \frac{h}{R_{corr} A_{XS} (1 - P_{void})}$$

where R_{corr} is the corrected resistance obtained by subtracting the resistance of the conductive substrate, A_{XS} is the cross-sectional area at the In-Ga / LFO interface (InGa eutectic contact area). The results for both LFO and H-LFO are shown in Table S8.2.

8.7.2. XRD, SEM and Raman analysis for LFO prepared at 550 and 750ºC

The annealing treatment for the synthesis of $LaFeO_3$ was performed at three different temperatures (550, 650 or 750ºC) for 20 min. According to the XRD patterns and SEM images corresponding to the resulting deposits, it is evident that this annealing temperature importantly affects the LFO morphology (Figure S8.1a-b). In fact, it is observed a significant evolution from a clearly nanostructured morphology, consisting of nearly vertically oriented nanorods on the electrode surface (characteristic of LFO550, Figure S8.1a), to a collapsed, much more compact morphology for LFO750 that shows a much lower degree of nanostructuring (Figure S8.1b). More importantly, XRD patterns for these samples indicate that the increase in the temperature of the synthesis also affects the structure and composition of the samples (Figure S8.1c,d): although all films are crystalline and show diffraction peaks whose positions and relative intensities match well with those of orthorhombic $LaFeO_3$, XRD pattern for LFO750 (Figure S8.1d) also contains additional peaks corresponding to α-Fe_2O_3 impurities in the sample. These structural facts are also observed in the corresponding Raman spectra (see Figure S8.1e,f). As an intermediate situation between the two limit temperatures, the LFO synthesized at 650ºC shows a greater degree of crystallinity (sharp and intense crystallographic peaks) than the preparation at 550ºC but does not present the α-Fe_2O_3 impurities observed for the film prepared at 750ºC.

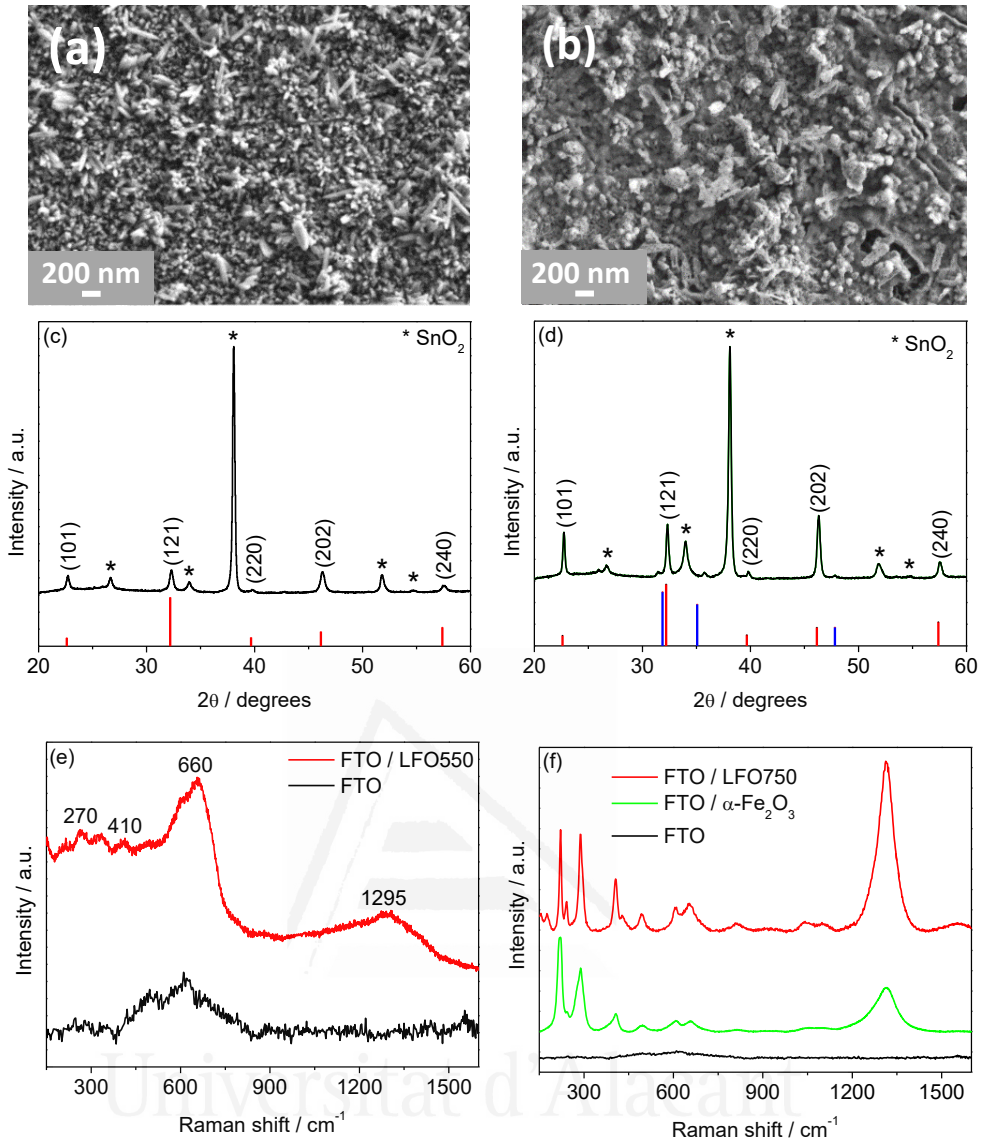

Figure S8.2. Top SEM images for (a) LFO550 and (b) LFO750 films on FTO. XRD patterns for (c) LFO550 and (d) LFO750 films on FTO (in red and blue, representative reference diffraction lines for $LaFeO_3$ and α-Fe_2O_3, respectively). Raman spectra for (e) LFO550 and (f) LFO750 films on FTO.

8.7.3. XPS spectra analysis

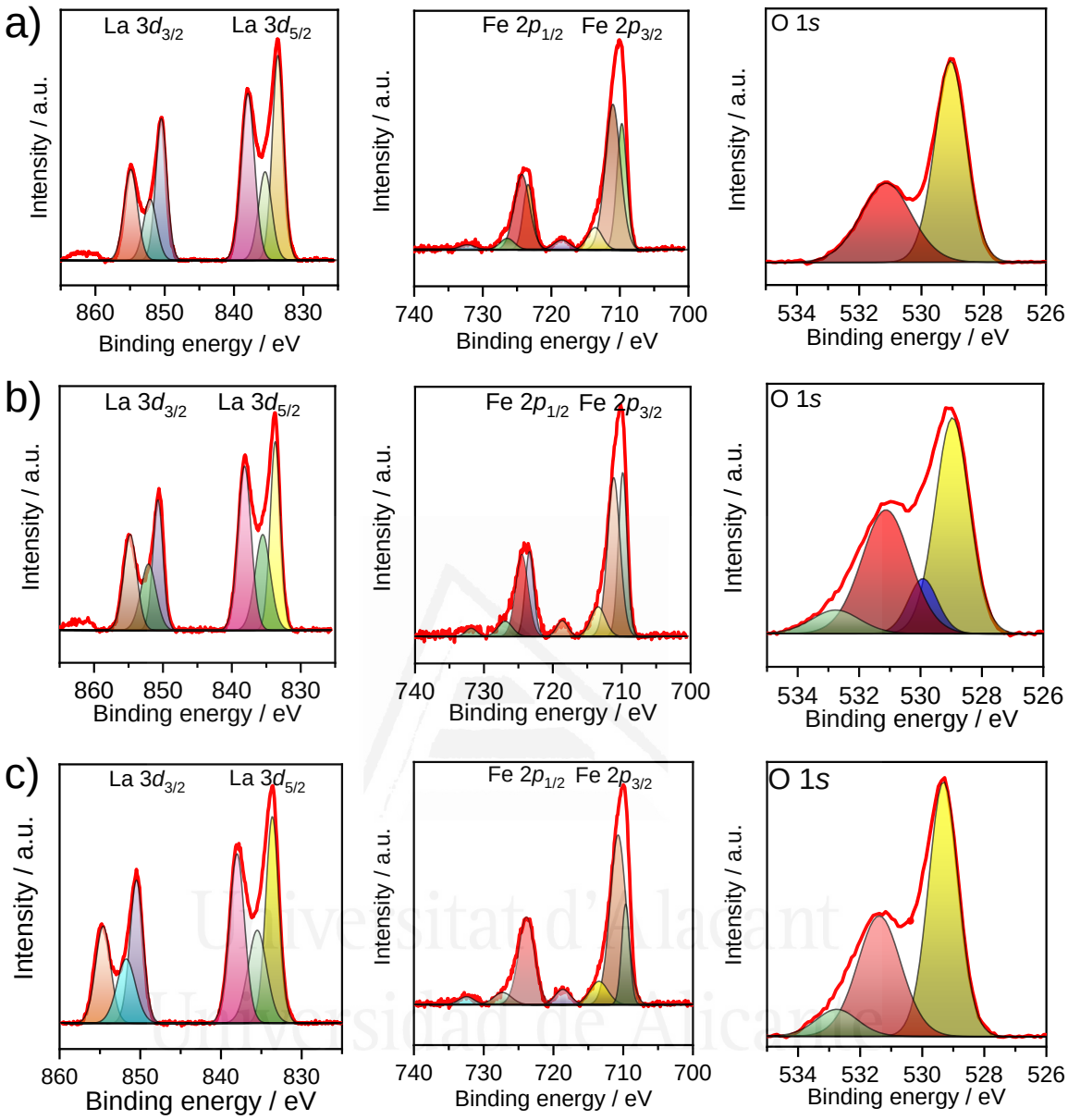

Figure S8.3. Narrow-scan XPS La 3*d*, Fe 2*p* and O 1*s* spectra for a) LFO, b) H-LFO and c) H-LFO after the stability test displayed in Figure 8.7 of the main text. The deconvolution in each case is included.

Figure S8.3 displays the XPS La 3*d*, Fe 2*p* and O 1*s* spectra recorded for the LFO at different stages, that is pristine LFO (a) as well as H-LFO before (b) and after the stability test (c) shown in Figure 8.7 of the main text. At first sight, La 3*d* spectra remain

virtually indistinguishable, whereas subtle changes in the Fe 3*d* signals and a drastic evolution in O 1*s* are noticeable. In all cases the La 3*d* spectra show the two characteristic strong bands associated to La $3d_{5/2}$ and $3d_{3/2}$ with a spin-orbit splitting gap of *ca*. 16.8 eV. We note that each band can be deconvolve into three components that have been ascribed to the presence of La-OH, La-O bonds and a satellite peak [S5,S6]. XPS Fe 3*d* spectra barely changes with the different treatments. The distinct profile with two strong bands centered around 723 and 710 eV assigned to Fe $2p_{1/2}$ and $2p_{3/2}$ and the satellite peak around 718 eV remain regardless of the treatment. However, we noticed slight changes in the deconvolution which are specially more prominent in the $2p_{3/2}$ component, likely because of the stronger signal. We observed that the $2p_{3/2}$ band consist of two contributions, one at higher binding energy linked to the presence of Fe^{3+} and another at lower energy ascribed to Fe^{2+} [S7]. Interestingly, the Fe^{2+} component increases significantly, with respect Fe^{3+} contribution, upon the hydrogen treatment (Figure S8.3b) and decreases after the stability test (Figure S8.3c). The partial reduction of Fe^{3+} into Fe^{2+} under a reducing atmosphere such as hydrogen is not unexpected, and it is linked to the concomitant formation of oxygen vacancies. The oxidation of Fe^{2+} to Fe^{3+} after the stability test is not unreasonable when considering that H-LFO is operating at harsh oxidative conditions. Finally, the changes in the O 1*s* signal appear to suggest that the effect of the hydrogen treatment can be reverted after the stability test. O 1*s* signal of as-prepared LFO contains basically two contributions that correspond to lattice oxygen (O_{latt}) at around 529.10 eV (yellow band) and likely oxygen vacancies (O_{vac}) at 531.10 eV (red band), respectively [S8–S10]. After the hydrogen treatment, H-LFO shows to additional bands at around 529.88 eV (blue band) and 532.78 eV (green band). The latter is likely related to adsorbed oxygen species such as water, whereas the former still remains to be identified, but probably relates to surface oxygen species like OH^-,

superoxide species, etc [S11,S12]. It is worth noting that the relative content O_{vac}/O_{latt} increases from 0.69 (Figure S8.3a) to 0.81 (Figure S8.3b) with the hydrogen treatment demonstrating the incorporation of oxygen vacancies. After the stability test the O_{vac}/O_{latt} ratio decreases up to 0.63 (Figure S8.3c), evidencing the refilling of the oxygen vacancies.

8.7.4. IPCE measurements

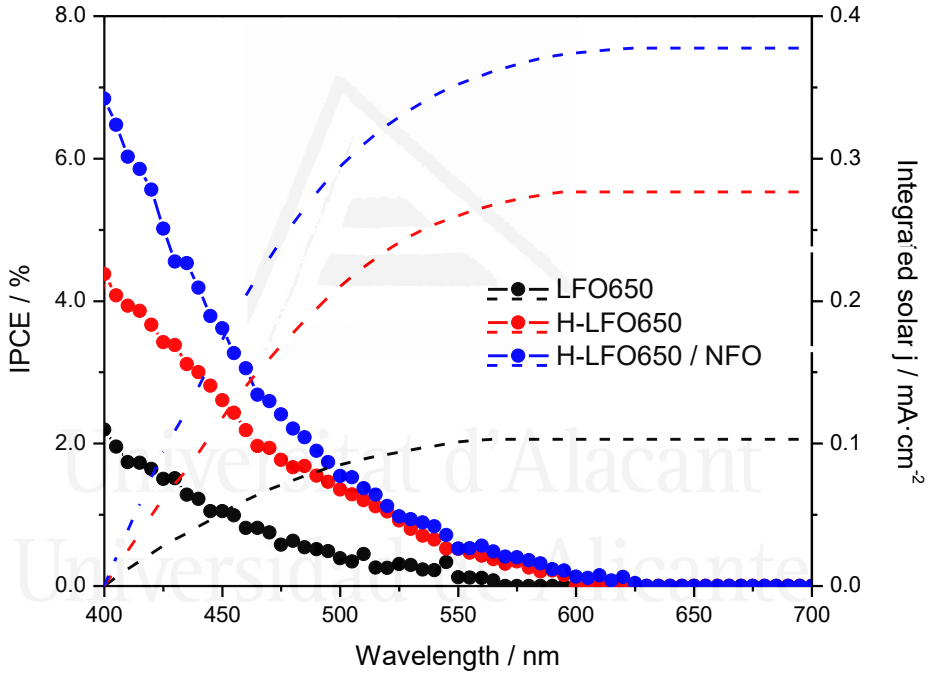

Figure S8.4. Incident photon-to-current spectra of LFO, H-LFO and H-LFO/NFO electrodes recorded at 1.23 V (*vs.* RHE) (dotted line, left axis), including the integrated photocurrent (dashed lines, right axis) considering AM 1.5G irradiance. Measurements were performed using 1 M NaOH as electrolyte.

8.7.5. Calibration line for O_2 detection

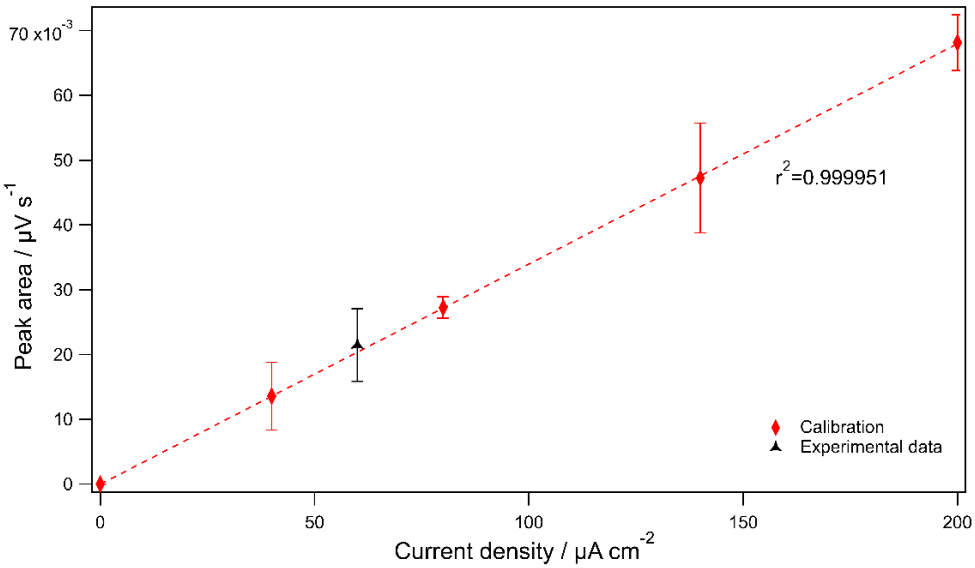

Figure S8.5. Calibration line for the O_2 detection by gas chromatography using a H-LFO/NFO electrode. Measurements were performed using 1 M NaOH as an electrolyte.

8.7.6. Maximum theoretical photocurrent value

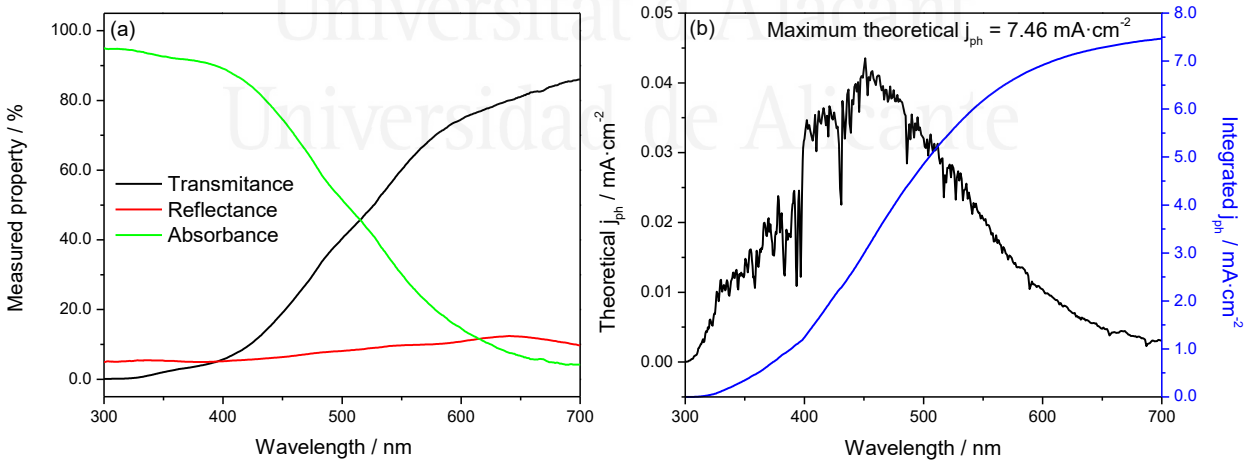

Figure S8.6. (a) Estimated absorbance (as $Absorbed\ light/\% = 100 - Transmitted\ light - Reflected\ light$) for a LFO electrode (calculated from measured transmitance and reflectance). (b) Maximum theoretical photocurrent estimated using the standard solar spectrum and the estimated absorbance of the photoelectrode.

8.7.7. Determination of the minority carrier diffusion length

Minority carrier diffusion length (L_p) was estimated by a monochromatic illumination experiment with a hole scavenger. Based on the Gärtner model, L_p can be estimated by [S13,S14]:

$$\ln(1-\eta) = -\alpha\left(\frac{2\varepsilon\varepsilon_0}{qN_D}\right)^{\frac{1}{2}}(V-V_{fb})^{\frac{1}{2}} - \ln(1+\alpha L_p)$$

where η is external quantum efficiency and α is absorption coefficient (taken to be 53200 cm^{-1} as calculated from UV-Vis spectra at 452 nm). By fitting the linear region at high bias where FLP is in Figure S8.7 where $\ln(1-\eta)$ is plotted against $(V-V_{fb})^{\frac{1}{2}}$, L_p is estimated to be 5 nm. We note that such a short L_p will certainly limit the charge separation, as it has been suggested to occur in other iron-based metal oxide photoanodes [S15].

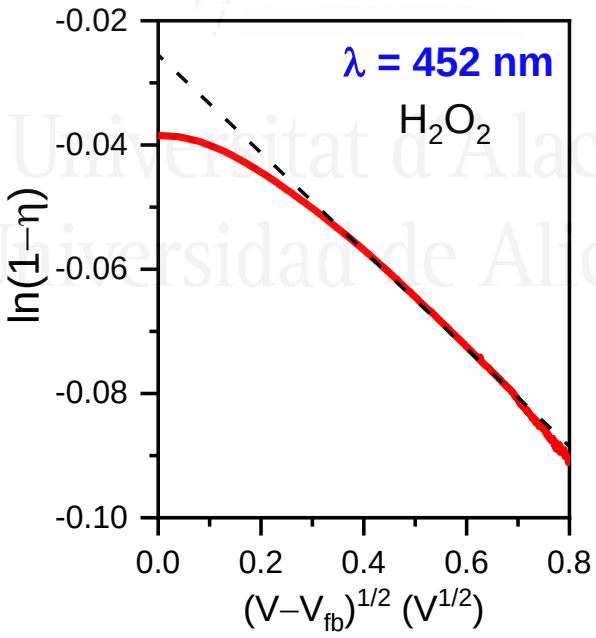

Figure S8.7. Graph of $\ln(1-\eta)$ *vs.* $(V-V_{fb})^{\frac{1}{2}}$ plotted for the H-LFO thin film electrode. Measurement was performed in 1 M NaOH + 0.5 M H_2O_2 using blue LED for monochromatic illumination from electrolyte side.

8.7.8. Photoelectrochemical impedance spectroscopy analysis

8.7.8.1. Mott–Schottky plot

Figure S8.8a shows representative Nyquist plots of H-LFO recorded in the dark (black circles) at 1.2 V *vs.* RHE. Quantitative information on the electronic properties of this film can be extracted by modelling the Nyquist plots with equivalent circuits. In the absence of illumination, the impedance response of H-LFO was fit by the Randles circuit (solid line), which consists of a series resistance (R_s), a bulk capacitance (C_{bulk}) and a charge transfer resistance from the bulk ($R_{ct,bulk}$) components [S16]. Figure S8.8b shows the Mott-Schottky (MS) plot constructed from C_{bulk} measured in the dark at different applied potentials, wherein the positive slope clearly reflects the *n*-type character of the H-LFO. By assuming a dielectric constant of 75 [S17,S18], a donor concentration (N_D) of 7.32×10^{17} cm^{-3} was calculated. From the potential intersection in the MS plot, the flat band potential (V_{fb}) was estimated to be 0.43 V *vs.* RHE.

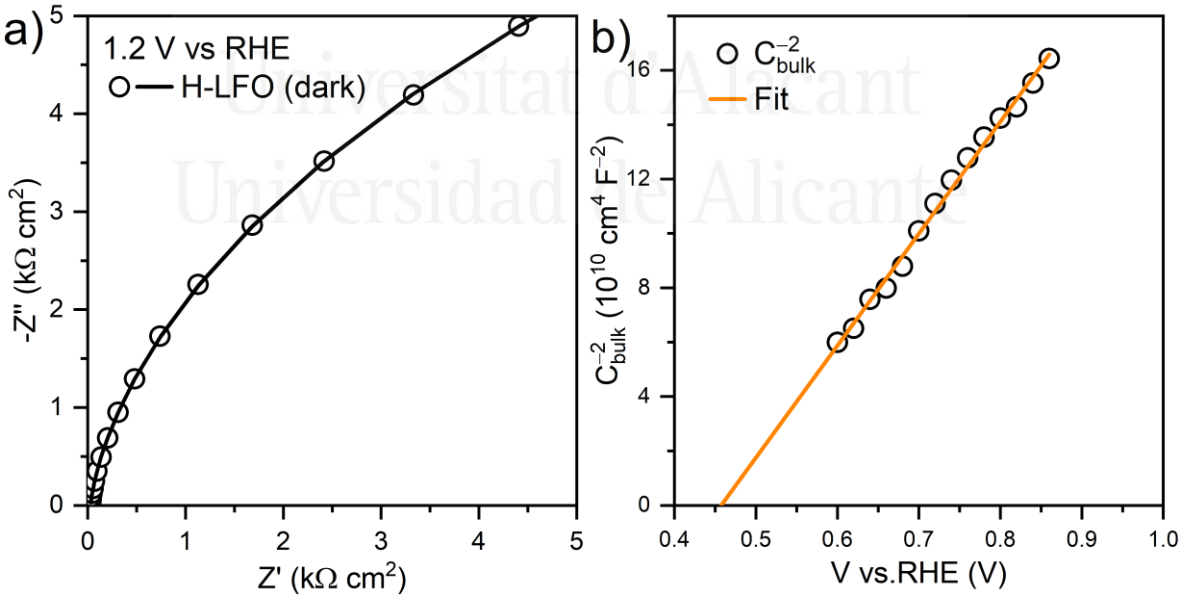

Figure S8.8. a) Representative EIS Nyquist plot for H-LFO recorded in the dark at 1.2 V *vs.* RHE. b) Mott-Schottky plot obtained for H-LFO.

8.7.8.2. Estimation of the depletion width

To provide more information on the electronic features of LFO, the depletion width and Fermi level position were calculated. The depletion width W can be estimated by:

$$W = \sqrt{\frac{2\varepsilon\varepsilon_0}{qN_D}\left|V - V_{fb}\right|}$$

where ε is dielectric constant of $LaFeO_3$, ε_0 is vacuum permittivity and q is elementary charge. At 1.2 V *vs.* RHE, W was estimated to be 93 nm, very close to the actual diameter of LFO nanorods (Figure 8.2b, main text). These results suggest that at relatively high applied potential the band bending would extend throughout almost all the diameter of the nanorod causing it to be nearly fully depleted.

8.7.8.3. Energy bands estimation

The effective density of states in the conduction band N_C is given by [S19]:

$$N_C \equiv 2\left(\frac{2\pi m_{de} kT}{h^2}\right)^{\frac{3}{2}}$$

where k is Boltzmann constant, T is absolute temperature and h is Planck constant. Considering a density-of-state effective mass for electrons m_{de} of 2.6×10^{-30} kg [S20], N_C is estimated to be 1.25×10^{20} cm^{-3}. Since the ratio of N_D to N_C is less than 0.05, H-LFO is a non-degenerate semiconductor. Finally, the Boltzmann statistics can be applied to determine the energy gap between Fermi level E_F and conduction band E_{CB} (Equation 3) [S19], which was calculated to be around 130 mV at flat band conditions.

$$E_{CB} - E_F = kT \ln\left(\frac{N_C}{N_D}\right)$$

8.7.8.4. Determination of the interfacial density of states (DOS)

Figure S8.9 shows representative Nyquist Plots of both H-LFO (red circles) and H-LFO / NFO (blue circles) under illumination recorded at 1.2 V *vs.* RHE. To interrogate the interfacial electronic structure during water photo-oxidation, the impedance response obtained for H-LFO and H-LFO/NFO under illumination was analyzed by using a two time-constant equivalent circuit previously proposed by Bisquert, Hamann and co-workers [S21]. This consists of a series resistance (R_S), bulk capacitance (C_{bulk}), resistance for hole trapping at surface states (R_{trap}), surface state capacitance (C_{SS}) and charge transfer resistance for hole transfer from surface states to the water ($R_{ct,ss}$). By considering that C_{SS} is directly related to the amount of charges accumulated at the electrode/electrolyte interface, a density of surface states (DOS in $V^{-1}cm^{-2}$) could be defined as [S22]:

$$C_{SS} = q \times DOS$$

Figure 8.5 in the main text shows the results obtained from applying Equation 4 to the C_{SS} values extracted from PEIS.

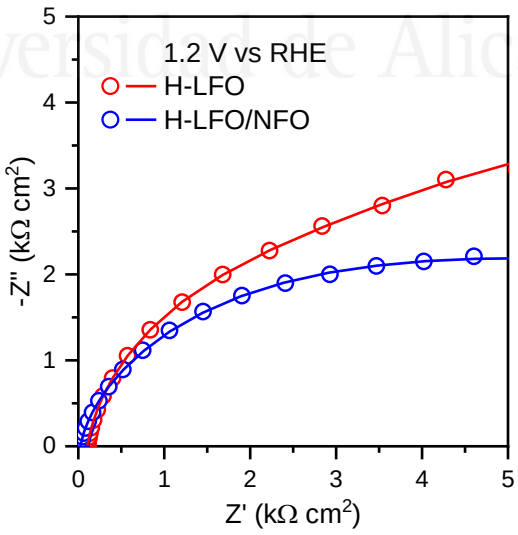

Figure S8.9. Nyquist plot of impedance response measured at 1.2 V *vs.* RHE under illumination.

8.7.9. Intensity-modulated photocurrent spectroscopy (IMPS) analysis

To quantify the kinetics information, intensity-modulated photocurrent response $j(\omega)$ was fitted based on the generalized IMPS theory proposed by Ponomarev and Peter [S23]:

$$j(\omega) = j_h \times \frac{k_{tran} + i\omega\left(\frac{C_H}{1+\frac{C_H}{C_{SC}}}\right)}{k_{tran} + k_{rec} + i\omega} \times \left(\frac{1}{1+(i\omega\tau_d)^{\alpha}}\right)$$

where j_h denotes the hole current towards the interface and α is introduced as a non-ideality factor due to surface inhomogeneity and frequency-dependent dielectric constant [S16]. k_{tran} and k_{rec} are pseudo-first order rate constant for charge transfer and recombination, respectively. C_{SC} and C_H represent capacitance of the space charge layer and the Helmholtz layer. τ_d represents mean transit time for photogenerated electrons and was found to be around 15.6 ms for H-LFO.

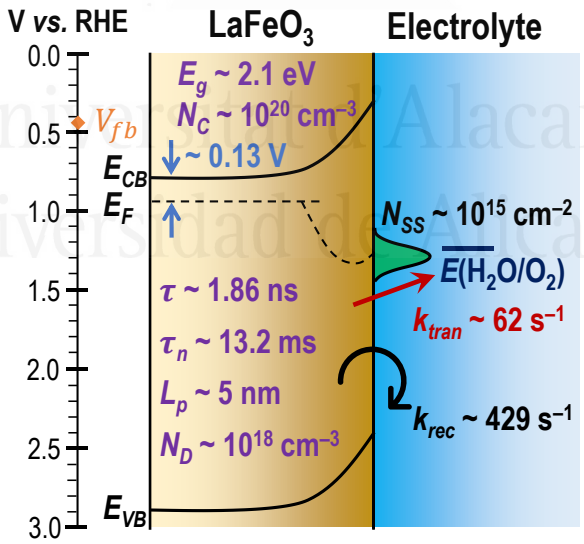

Figure S8.10. Tentative band diagram of a H-LFO photoanode in contact with the electrolyte including some of the most representative parameters extracted from spectroelectrochemical analysis. E_{CB}: conduction band edge, E_{VB}: valence band edge, E_F: Fermi level, E_g: band gap, N_C: effective density of states in the conduction band, N_D: donor density, N_{SS}: total density of surface states, V_{fb}: flat band potential, τ: average

lifetime, τ_n: first-order electron lifetime, L_p: hole diffusion length, k_{tran}: charge transfer rate constant, k_{tran}: surface recombination rate constant.

Figure S8.10 displays the energy bands diagram estimated for LFO, when considering the optical band gap of 2.1 eV of LFO (Figure 8.2e, main text).

8.7.10. Steady-state photoluminescence

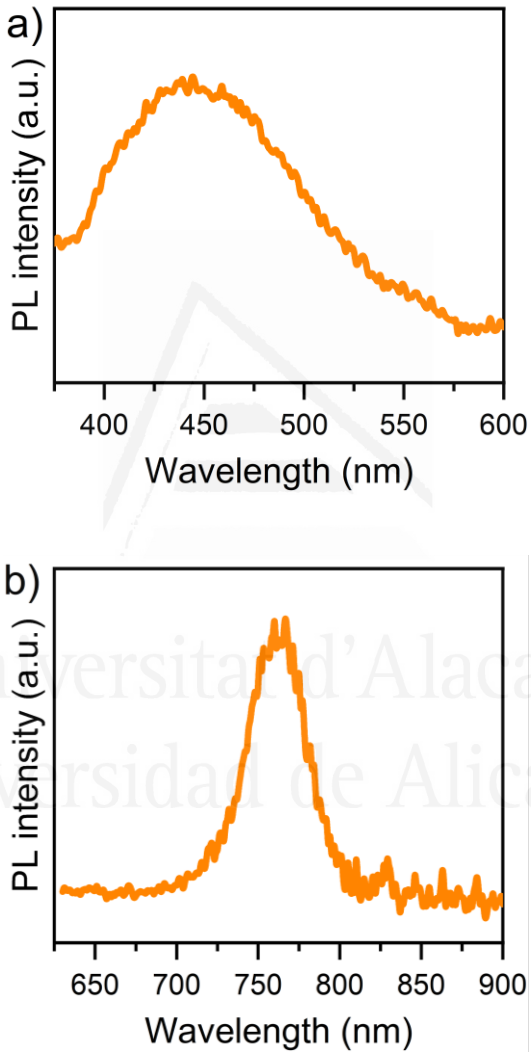

Figure S8.11. Steady-state PL emission spectra of H-LFO thin films recorded after excitation at 340 nm. a) Strong and b) weak emission shown in different plots to facilitate visualization.

8.7.11. Stability under operation conditions

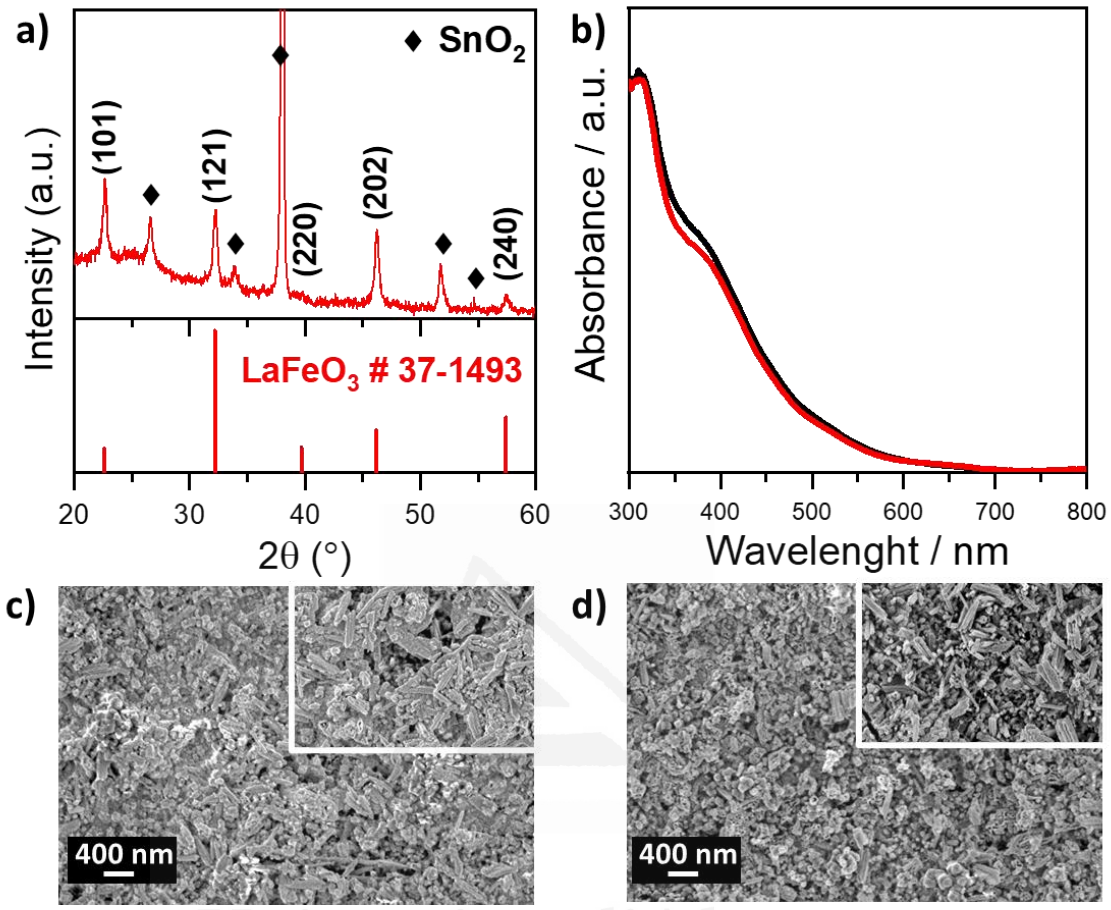

Figure S8.12. a) XRD pattern of H-LFO thin film measured after immersion in a 10 M NaOH solution for 3 days, including the reference pattern b) UV-Vis before (black line) and after (red line) the stability test shown in Figure 8.7. SEM images for a) H-LFO and b) H-LFO/NFO after the stability test, including (inset) representative images of the films before the test.

Table S8.1. Relative XRD peak intensities corresponding to the data base and experimental LFO.

	(121)/(121)	(101)/121)	(220)/(121)	(202)/(121)	(240)/121)
JCPDS #37-1493	1	0.17	0.18	0.30	0.39
LFO (650°C)	1	0.60	0.13	0.98	0.31

Table S8.2. Conductivity measurement.

	R (Ω)	R_{corr} (Ω)	h (nm)	N	P_{void}	A_{XS} (mm)	σ (μS cm^{-1})
LFO	68.3	38.5	550	40	0.61	3.9	9.40
H-LFO	45.9	16.1	550	40	0.61	3.8	23.10

8.7.12. References

[S1] J. H. Kim, J. H. Kim, J.-W. Jang, J. Y. Kim, S. H. Choi, G. Magesh, J. Lee, J. S. Lee, Adv. Energy Mater. 5 (2015) 1401933.

[S2] R. D. L. Smith, M. S. Prévot, R. D. Fagan, Z. Zhang, P. A. Sedach, M. K. J. Siu, S. Trudel, C. P. Berlinguette, Science. 340 (2013) 60.

[S3] J.-W. Jang, C. Du, Y. Ye, Y. Lin, X. Yao, J. Thorne, E. Liu, G. McMahon, J. Zhu, A. Javey, J. Guo, D. Wang, Nature Communications. 6 (2015) 7447.

[S4] E. A. Weiss, V. J. Porter, R. C. Chiechi, S. M. Geyer, D. C. Bell, M. G. Bawendi, G. M. Whitesides, J. Am. Chem. Soc. 130 (2008) 83.

[S5] S. Mickevičius, S. Grebinskij, V. Bondarenka, B. Vengalis, K. Šliužienė, B. A. Orlowski, V. Osinniy, W. Drube, J. Alloy. Compd. 423 (2006) 107.

[S6] E. Cao, T. Cui, Y. Yang, Y. Zhang, W. Hao, L. Sun, H. Peng, Mater. Lett. 190 (2017) 143.

[S7] T. Yamashita, P. Hayes, Appl. Surf. Sci. 254 (2008) 2441.

[S8] N. Guijarro, P. Bornoz, M. Prévot, X. Yu, X. Zhu, M. Johnson, X. Jeanbourquin, F. L. Formal, K. Sivula, Sustainable Energy Fuels. 2 (2018) 103.

[S9] X. Zhu, N. Guijarro, Y. Liu, P. Schouwink, R. A. Wells, F. L. Formal, S. Sun, C. Gao, K. Sivula, Adv. Mater. 30 (2018) 1801612.

[S10] S. Sonsupap, P. Kidkhunthod, N. Chanlek, S. Pinitsoontorn, S. Maensiri, Appl. Surf. Sci. 380 (2016) 16.

[S11] Z. Li, L. Lv, J. Wang, X. Ao, Y. Ruan, D. Zha, G. Hong, Q. Wu, Y. Lan, C. Wang, J. Jiang, M. Liu, Nano Energy. 47 (2018) 199.

[S12] Y. Zhu, W. Zhou, J. Yu, Y. Chen, M. Liu, Z. Shao, Chem. Mater. 2016, 28, 1691.

[S13] J. H. Kennedy, K. W. Frese, J. Electrochem. Soc. 125 (1978) 709.

[S14] A. J. E. Rettie, H. C. Lee, L. G. Marshall, J.-F. Lin, C. Capan, J. Lindemuth, J. S. McCloy, J. Zhou, A. J. Bard, C. B. Mullins, J. Am. Chem. Soc. 135 (2013) 11389.

[S15] C. Lohaus, A. Klein, W. Jaegermann, Nat. Commun. 9 (2018) 4309.

[S16] Y. Liu, F. L. Formal, F. Boudoire, L. Yao, K. Sivula, N. Guijarro, J. Mater. Chem. A. 7 (2019) 1669.

[S17] M. I. Díez-García, R. Gómez, ChemSusChem. 10 (2017) 2457.

[S18] K. J. May, D. P. Fenning, T. Ming, W. T. Hong, D. Lee, K. A. Stoerzinger, M. D. Biegalski, A. M. Kolpak, Y. Shao-Horn, J. Phys. Chem. Lett. 6 (2015) 977.

[S19] S. M. Sze, K. K. Ng, Physics of Semiconductor Devices; John Wiley & Sons, 2006.

[S20] S. Körbel, M. A. L. Marques, S. Botti, J. Mater. Chem. C. 4 (2016) 3157.

[S21] B. Klahr, S. Gimenez, F. Fabregat-Santiago, J. Bisquert, T. W. Hamann, J. Am. Chem. Soc. 134 (2012) 16693.

[S22] B. Klahr, S. Gimenez, F. Fabregat-Santiago, T. Hamann, J. Bisquert, J. Am. Chem. Soc.134 (2012) 4294.

[S23] E. A. Ponomarev, L. M. Peter, J. Electroanal. Chem. 396 (1995) 219.

CHAPTER IX

Photoelectrochemical behavior and computational insights of $NdFeO_3$ thin film photocathodes

9.1. ABSTRACT

Among the different strategies that are being developed to solve the current energy challenge, harvesting energy directly from sunlight through tandem photoelectrochemical (PEC) cell carrying out artificial photosynthesis (water splitting) is one of the most attractive. The implementation of tandem PEC cells requires the development of stable and efficient photocathodes. Among the ternary oxides, $NdFeO_3$ may be considered as a suitable candidate to this end. In this study, transparent $NdFeO_3$ thin film photocathodes have been successfully prepared by a citric-based sol-gel procedure, followed by a thermal treatment. These photocathodes show photocurrents for both the hydrogen evolution and oxygen reduction reactions. DFT calculations have allowed gaining insights into the nature of the *p*-type semiconducting behavior of this material, also pointing to the importance of nanostructuring and passivating Fe surface states to boost the performance of these photocathodes. To improve their photoactivity, Mg^{2+} and Zn^{2+} doping at a concentration of 5 at% has been observed to significantly enhance the photoelectrocatalytic performance of $NdFeO_3$ toward oxygen reduction. Such an improvement, which is primarily attributed to an increase in density and mobility of the majority charge carriers, reveals that $NdFeO_3$ has the potential to be used as photocathode in photoelectrochemical applications.

9.2. INTRODUCTION

In the current context of increasingly growing global energy demand and depletion of fossil fuels, the use of solar energy for photoelectrochemical (PEC) water electrolysis on semiconductor electrodes enables the sustainable generation of H_2 as fuel from water and sunlight [1–5]. In fact, hydrogen is identified as a technically viable and carbon-free

energy vector for applications ranging from the small-scale power supply to large chemical energy exports [6–8].

Since the seminal demonstration of photoelectrocatalytic hydrogen production from water splitting with TiO_2 by Fujishima and Honda [9], revolutionary advances made in the field of PEC water splitting systems have led to H_2 production with solar-to-hydrogen efficiencies higher than 10% [10], but using relatively complex device architectures and/or electrodes made of rare and/or unstable materials. However, the development of viable simple photoelectrochemical tandem cells is hindered by difficulties in the development of efficient, stable and inexpensive photocathodes, which thus stands out as one of the bottlenecks to overcome [10,11].

In this regard, several binary and ternary metal oxides, such as CuO (E_g = 1.0 eV) [12,13], Cu_2O (E_g = 2.1 eV) [14,15], $CaFe_2O_4$ (E_g = 1.9 eV) [16,17], $CuBi_2O_4$ (E_g = 1.8 eV) [18,19], and $CuFeO_2$ (E_g = 1.5 eV) [20,21], can behave as *p*-type semiconductors. However, none of them meets important criteria, such as chemical stability in aqueous environments under irradiation, appropriate optical absorption coefficients and low cost, to be considered as attractive and practical candidates for their use as photocathodes in water splitting devices. These facts, along with the poor charge-carrier mobility and short charge-carrier lifetime that usually characterize photocathode materials, makes critical further research addressing these issues and challenges.

Among ternary oxides, perovskite-type (ABO_3) oxides may constitute suitable candidates since most of them exhibit *p*-type semiconductor behavior and acceptable stability under illumination in aqueous solutions [22]. $LaFeO_3$, the flagship of this family of materials in PEC applications, has been widely identified as a promising electrode material according to several studies on its photoelectrochemical characterization [23–25]. In fact, its bandgap value is reported to be around 2.1 eV, which makes possible the

absorption of a large portion of the visible solar spectrum [26]. In order to intensify its *p*-type character, doping with metals with predominant +2 oxidation state and ionic radii similar to that of Fe^{3+} (such as Mg^{2+} and Zn^{2+}) has been revealed as an effective strategy with applications in both photoelectrochemistry [27] and photocatalysis [28].

On the other hand, in the field of PEC water splitting on semiconductor electrodes, theoretical and computational studies based on DFT calculations have gained great importance [29]. In fact, they provide valuable information regarding key aspects, such as band gap values, band structures, charge transport, charge transfer as well as the kinetics of oxygen and hydrogen evolution reactions at the electrode/electrolyte interface [30]. Thus, DFT has become an essential tool that has substantially contributed to the understanding of the photoactive material response, and it has oriented the optimization of the PEC performance through proper modelling and simulation strategies [31–33].

In the present study, based on the previous work done with the $LaFeO_3$ perovskite, a characterization of $NdFeO_3$ photocathodes is presented, for which a behavior similar to that of $LaFeO_3$ is expected. As far as we know, this is the first photoelectrochemical study of this material, in spite of the fact Nd that is as abundant as La in the Earth's crust. In this way, $NdFeO_3$ prepared on transparent conductive substrates by a straightforward sol-gel procedure is shown to exhibit cathodic photocurrents for H_2O and O_2 reduction over a wide range of potentials. Their magnitude, particularly for oxygen reduction, is significantly intensified by the partial substitution of Fe by either Mg or Zn impurities in the perovskite structure. DFT calculations have also been performed to gain insights into the physics underlying the *p*-type photoelectrochemical behavior of the $NdFeO_3$ electrodes.

9.3. EXPERIMENTAL SECTION AND METHODS

9.3.1. Preparation of pristine $NdFeO_3$ photocathodes

Pristine $NdFeO_3$ thin film photocathodes were prepared on fluorine-doped tin oxide conducting glass (TEC 15, 12-15 Ω/□, Pilkington) following a previously reported procedure based on a citric sol-gel route [27]. The $NdFeO_3$ precursor solution was prepared by dissolving $Nd(NO_3)_3 \cdot 6H_2O$ (Aldrich Chemistry, 99%) 0.3 M and $Fe(NO_3)_2 \cdot 9H_2O$ (Panreac, 98%) 0.3 M in water (Millipore, Elix 3). This solution was magnetically stirred for 1 hour and, then, the appropriate amount of citric acid (Merck, 99.5%) was added to reach a concentration of 0.6 M, and it was stirred again for 20 h. After that, 30 $\mu L \cdot mL^{-1}$ of acetylacetone (Fluka Analytical, 99.5%) and 30 $\mu L \cdot mL^{-1}$ of Triton® X-100 (laboratory grade, Sigma-Aldrich) were added. Then, 40 µL of the resulting solution was dropped onto an FTO glass plate (area to be covered: 1 cm^2), previously cleaned by sonication (Selecta Ultrasonics) for 15 min in acetone (VWR Chemicals, 99%) and ethanol (VWR Chemicals, 96%), and spread over it with a spin-coater (Chemat Technology, KW–4A) at a spin rate of 1500 rpm for 20 s. Finally, the electrodes were annealed in air at 500ºC for 1 hour using a programmable furnace (Conatec, 7800), with a heating rate of $5ºC \cdot min^{-1}$. This process was repeated four times to obtain the optimized film thickness (four layers, see Figure S9.1) and a final annealing at 640ºC for 2 hours was applied to obtain the crystalline perovskite films.

9.3.2. Preparation of doped $NdFeO_3$ photocathodes

Mg (*x* at%)- and Zn (*x* at%)-doped (*x* = 1; 2.5; 5 and 10) $NdFeO_3$ thin film photocathodes were obtained by following the same procedure described above, but substituting the corresponding amount of the Fe precursor salt in the $NdFeO_3$ precursor solution by the dopant salt in the desired concentration (in at% with respect to the Fe

content). In this case, $Mg(NO_3)_2 \cdot 6H_2O$ (VWR Chemicals, 99.4%) and $Zn(NO_3)_2 \cdot 6H_2O$ (Fluka, 99.0%) were employed as Mg and Zn precursors, respectively.

9.3.3. (Photo)electrochemical measurements

(Photo)electrochemical measurements were conducted at room temperature in a home-made Pyrex glass cell with a fused silica window and a computer-controlled potentiostat-galvanostat (Autolab, PGSTAT30). A Pt wire and a Ag/AgCl/KCl(3 M) electrode were used as the counter and reference electrodes, respectively, and a N_2- or O_2-purged 0.1 M NaOH (Panreac, 98.0%) solution was used as working electrolyte. Unless otherwise stated, all potentials are referred to this Ag/AgCl electrode. The light source was an ozone-free 1000 W Xe(Hg) lamp (Newport Instruments, 66921) equipped with a water filter to minimize the infrared contribution of the beam. Unless otherwise stated, the photoelectrochemical measurements were carried out by irradiating the prepared photocathodes through the electrolyte/electrolyte interface (EE illumination). The photoresponse under this type of illumination is higher than that obtained under substrate-electrode (SE) illumination (see Figure S9.2). The photon flux intensity was measured by means of a photodiode power meter (Thorlabs, PM100D), and adjusted to 100 mW cm^{-2}.

Details regarding equipment and measurement conditions for XRD, SEM, XPS and UV-vis spectroscopy are included in the Supporting Information.

9.3.4. Computational methods

DFT calculations have been performed with the Vienna *ab initio* simulation package (VASP) [34], under the projector augmented wave (PAW) [35,36] method with a plane-wave energy cut-off of 520 eV for all the calculations. The number of valence

electrons used has been of eleven for Nd ($5s^2 5p^6 5d^1 6s^2$), eight for Fe ($3d^7 4s^1$) and six for O ($2s^2 2p^4$). The model geometry has been a standard primitive orthorhombic cell (SG number 62), with a total number of atoms of 20, as can be seen in Figure 9.1. The Perdew-Burke-Ernzerhof (PBE) [37] generalized gradient approximation (GGA) functional has been used in conjunction with the single-parameter approach enunciated by Dudarev *et al*. [38] to include the effect of the electronic correlation of the highly localized *d*-electrons in these transition metal oxides, with a U value of 4.0 eV for the Fe *d*-states [39]. In addition, the hybrid Heyd-Scuseria-Ernzerhof (HSE) [40,41] functional (which is known to provide good estimates of electronic properties, in particular, band structure and band gap) has been used to check and complement the results obtained with PBE+U (see details in the Supplementary information). The calculations have been made with a 5x5x3 k-mesh for geometry optimization and with an 11x11x7 *k*-mesh for density of states (DOS) calculations. For the former, the electronic convergence criterion was set at 10^{-6} eV, while forces on atoms were set to be below 0.01 eV $Å^{-1}$. For the latter, the electronic convergence criterion was set at 10^{-8} eV. The Brillouin zone has been integrated with the tetrahedron method with Bloch corrections. All calculations have been made with spin-polarization, adopting a type-G antiferromagnetic arrangement for the Fe atoms [42]. No spin-orbit coupling has been considered. From the calculated band structure, the effective masses of charge carriers have been obtained by means of the Boltztrap2 code [43].

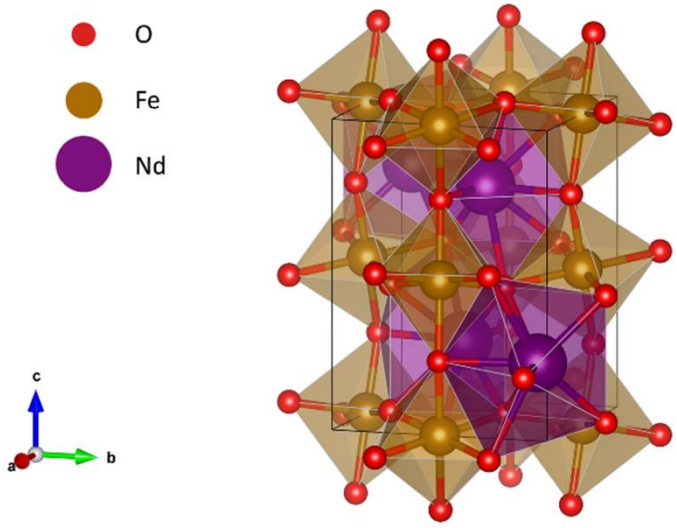

Figure 9.1. Standard primitive orthorhombic $NdFeO_3$ cell used for the calculations.

9.4. RESULTS AND DISCUSSION

9.4.1. Physical and chemical characterization of pristine and doped $NdFeO_3$ photocathodes

Figure 9.2a shows the XRD patterns for pristine, Mg (*x* at%)- and Zn (*x* at%)-doped (*x* = 1 and 10) $NdFeO_3$ thin films deposited on an FTO conductive glass substrate. Apart from FTO, $NdFeO_3$ is the only crystalline phase detected in the film (PDF file: 74–1473). The XRD analysis confirms that the yellowish brown $NdFeO_3$ films are crystalline, presenting an orthorhombic phase with lattice parameters: a = 5.453 Å, b = 5.584 Å, c = 7.768 Å and $\alpha = \beta = \gamma = 90^{o}$. Since there are no significant changes in the XRD patterns upon magnesium and zinc doping compared with that obtained for pristine $NdFeO_3$ films, it can be stated that the orthorhombic phase is maintained after the incorporation of either Mg or Zn in the $NdFeO_3$ crystal structure in the studied density range. This fact is consistent with the relatively small difference in the ionic radii for Fe^{3+} (64.5 pm), Mg^{2+} (72.0 pm) and Zn^{2+} (74.5 pm) and also with reports that confirm the prevalence of the substitution of the Fe atoms in the perovskite structure by Mg or Zn, instead of the formation of new phases, at least for dopant concentrations up to 30% [28,44–46].

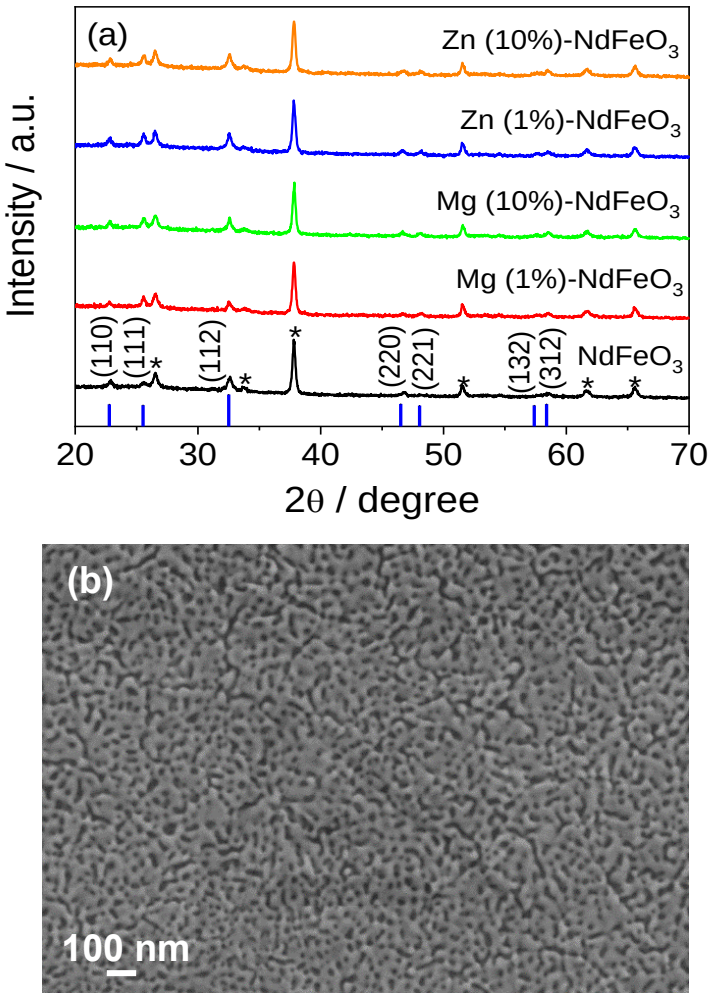

Figure 9.2. (a) XRD patterns for $NdFeO_3$, Mg (1 at%)-$NdFeO_3$, Mg (10 at%)-$NdFeO_3$, Zn (1 at%)-$NdFeO_3$ and Zn (10 at%)-$NdFeO_3$ films on FTO substrates (peaks marked with asterisks correspond to the SnO_2 substrate). (b) FESEM image corresponding to the top view of a $NdFeO_3$ film on FTO.

Figure 9.2b shows a representative FESEM image of a pristine $NdFeO_3$ sample. As observed, it consists of a compact deposit with a low degree of porosity, which corresponds to the typical surface morphology of a thin film. The cross sectional FESEM image (Figure S9.3) reveals that the films have an average thickness of around 150 nm. Representative FESEM images of Mg (x at%)- and Zn (x at%)-doped (x = 5) $NdFeO_3$ deposits are shown in Figure S9.4. From them, it can be deduced that an optimum doping level (in terms of photoelectrochemical performance, *vide infra*) does not induce any

significant alteration in the topographic and surface morphological characteristics of the synthesized thin films. In fact, only an apparently larger grain size can be discerned for cdoped samples.

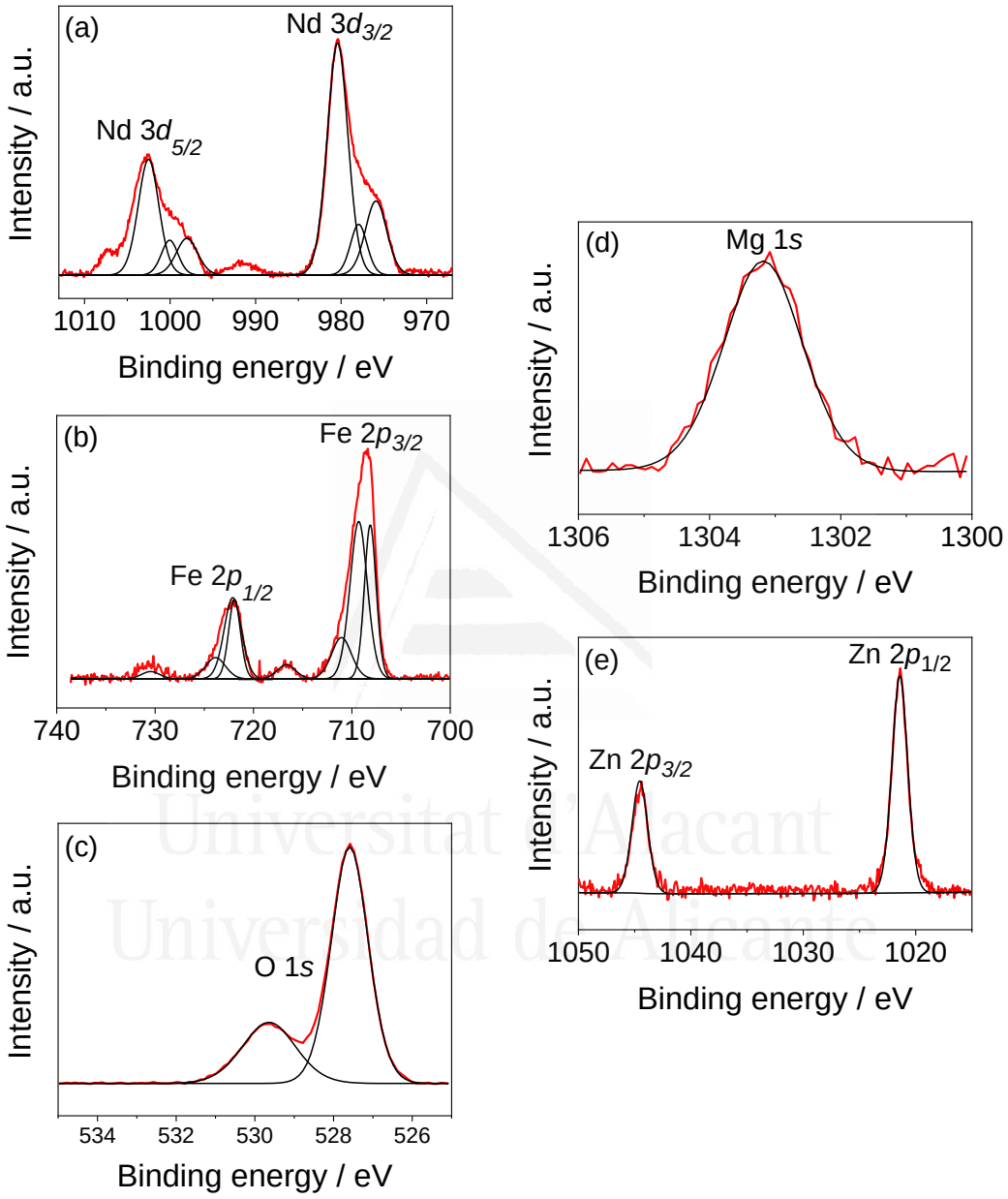

Figure 9.3. (a) Nd 3*d*, (b) Fe 2*p* and (c) O 1*s* XPS spectra (red line) and corresponding deconvolutions (black lines) for an $NdFeO_3$ film on FTO. (d) Mg 1*s* and (e) Zn 2*p* XPS spectra (red lines), and corresponding deconvolutions (black lines) for Mg (5 at%)-$NdFeO_3$ and Zn (5 at%)-$NdFeO_3$ films on FTO, respectively.

Figure 9.3a-c shows XPS spectra for the as-prepared pristine $NdFeO_3$ sample. The Nd 3*d* XPS spectrum for (Figure 9.3a) shows two asymmetric peaks at binding energies (BE) of 1002.5 and 980.4 eV, attributed to the $3d_{5/2}$ and $3d_{3/2}$ transitions, respectively, with shoulders (interpreted as two satellite peaks) separated from their main peak by around 4.5 eV. This complex, characteristic spin-orbit splitting confirms the presence of Nd^{3+} in the sample [47,48]. The Fe 2*p* XPS spectrum (Figure 9.3b) exhibits two main peaks at BEs of 708.5 and 722.0 eV corresponding to the Fe $2p_{3/2}$ and Fe $2p_{1/2}$ transitions, respectively [27]. Although the satellite peak at 716.6 eV is a further indication of the presence of Fe^{3+} in the films [27,49], the existence of minor amounts of Fe^{2+} cannot be ruled out due to the slightly lower BEs for Fe^{3+} than those usually reported [27]. The O 1*s* XPS spectrum (Figure 9.3c) can be deconvoluted into two different components: the first one, at a BE of 528.6 eV, is ascribed to oxide species in the perovskite lattice [50], while the peak at 529.6 eV is assigned to surface hydroxyl groups, which suggests an hydroxylated surface for the $NdFeO_3$ deposit [50,51]. In this regard, it is interesting to point out that certain lanthanide oxides (such as La_2O_3) can adsorb water rapidly with a subsequent conversion of surface anions to yield an hydroxylated surface [50,51].

The XPS analysis of the doped samples confirms the presence of either Mg or Zn at the surface. In the Mg 1*s* spectrum (Figure 9.3d) for the correspondingly doped films, the presence of a peak at a BE of 1303.2 eV indicates the existence of Mg^{2+} species in the studied samples, while the peaks appearing at 1044.6 and 1021.4 eV in the Zn 2*p* spectrum (Figure 9.3e), corresponding to the Zn $2p_{3/2}$ and $2p_{1/2}$ transitions, respectively, confirm the existence of Zn^{2+} cations [27]. The XPS spectra for Nd 3*d*, Fe 2*p* and O 1*s* for Mg (5 at%)- and Zn (5 at%)-doped $NdFeO_3$ deposits (Figure S9.5 and S9.6) are pretty similar to those obtained for the pristine samples. However, it is interesting to note that the surface ratios of Mg/Fe and Zn/Fe in the Mg (5 at%)- and Zn (5 at%)-$NdFeO_3$ deposits

are between 5 and 6 times larger than those expected in the bulk (Table S9.1). This evident segregation could be correlated with the increase in the OH surface concentration in the doped electrodes, as the oxygenated Mg and Zn species are more hygroscopic than those of Fe [27].

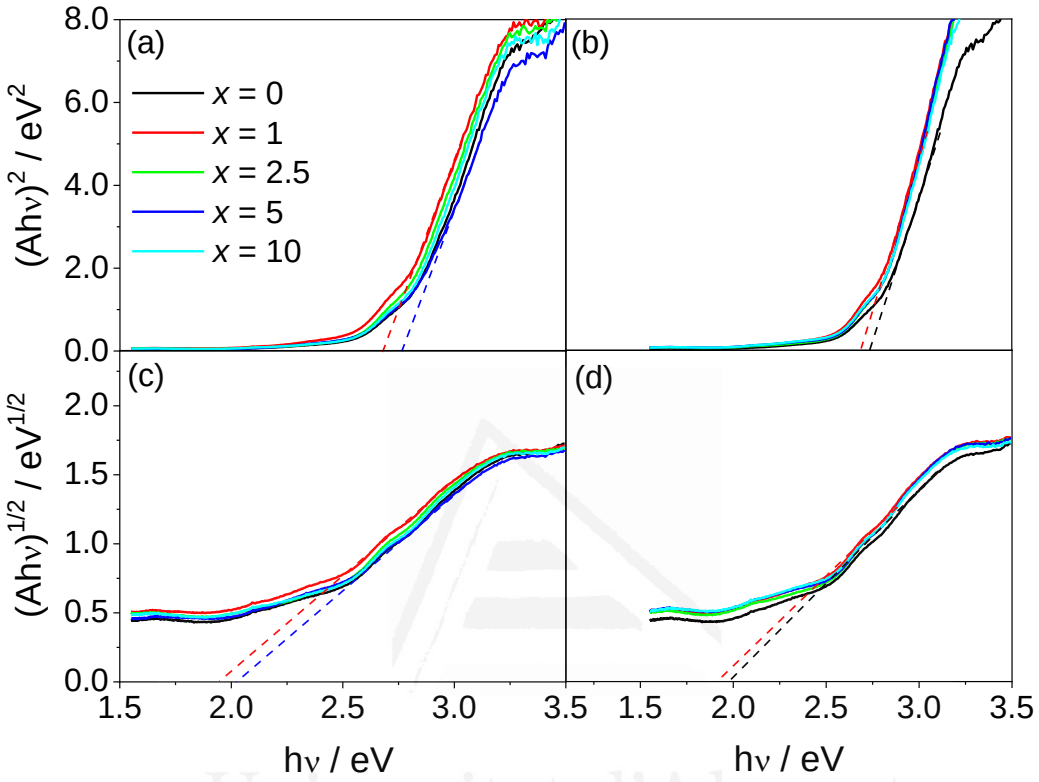

Figure 9.4. (a, b) Direct and (c, d) indirect Tauc plots for (a, c) Mg (*x* at%)-$NdFeO_3$ and (b, d) Zn (*x* at%)-$NdFeO_3$ electrodes.

Figure 9.4 shows direct and indirect Tauc plots for pristine and Mg- and Zn-doped $NdFeO_3$ thin films, obtained from the corresponding UV-visible absorbance spectra (Figure S9.7), characterized by an absorption edge at around 600 nm. The absorbance curves are virtually identical for all the samples, irrespective of the doping level. Direct and indirect experimental optical band gap values of 2.7 eV and 2.0 V, respectively, can be calculated from in Figure 9.4. As observed, doping does not significant alter both direct and indirect band gap values, which are in all cases within a 0.1 eV range.

9.4.2. (Photo)electrochemical characterization of pristine and doped $NdFeO_3$ photocathodes

Cyclic voltammograms in the dark for pristine $NdFeO_3$ photocathodes in either N_2- and O_2-purged 0.1 M NaOH (Figure 9.5a) reveal in both cases the existence of small capacitive currents over a wide potential window and a capacitive region at potentials above 0.2 V, which can be assimilated to the accumulation region for a *p*-type electrode. The small but stable cathodic photocurrents observed in linear voltammetry under transient illumination in an N_2-purged working electrolyte (Figure 9.5b) are indicative of H_2 evolution from water reduction by the photogenerated electrons, further confirming the *p*-type character of the as-prepared semiconductor electrodes. As observed, the photo-onset potential is located at around 0.2 V. Since the potential threshold for the onset of the photocurrent is close to the onset of the capacitive currents in the dark, such accumulation region can be related to the filling/emptying of valence band states [52,53]. Remarkably, the shape of the transients shows clear signs of electron trapping at the electrode surface with the appearance of cathodic spikes upon illumination and anodic ones when light is switched off, which are indicative of electron-hole recombination. In fact, electron trapping at the surface is one of the most important factors limiting the performance of perovskite-based photocathodes [54]. On the contrary, the presence of an electron scavenger such as O_2 in the working electrolyte induces a drastic increase in photocurrent (by around 10 times) and a diminution of the spikes in the illumination transients, which indicates that the surface electron trapping is significantly mitigated in the presence of O_2. No significant changes in the corresponding cyclic voltammetry in the dark when O_2 is present in the working electrolyte are observed.

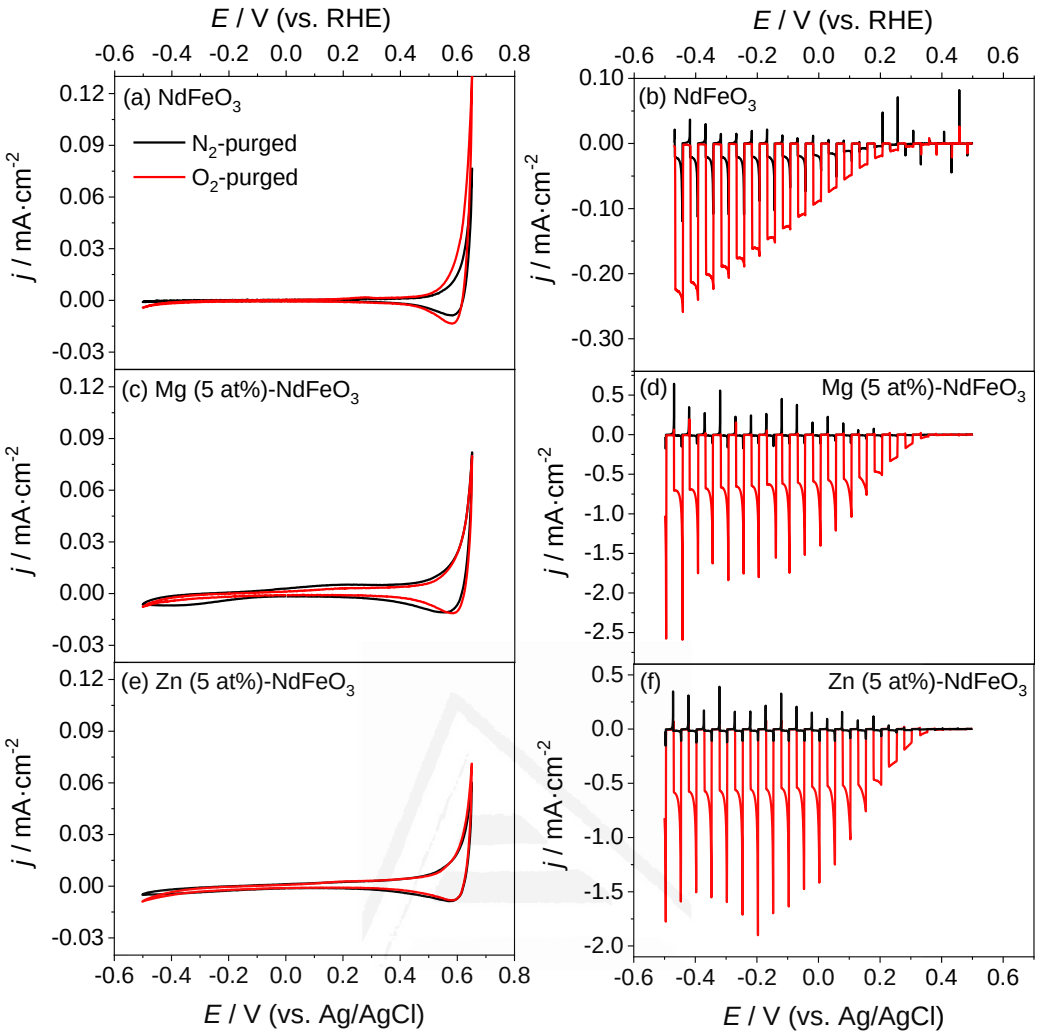

Figure 9.5. Cyclic voltammograms in the dark in N_2- and O_2-purged 0.1 M NaOH for (a) $NdFeO_3$, (b) Mg (5 at%)-$NdFeO_3$ and (c) Zn (5 at%)-$NdFeO_3$ electrodes (scan rate: 20 $mV \cdot s^{-1}$). Linear scan voltammograms under transient illumination in N_2- and O_2-purged 0.1 M NaOH for (d) $NdFeO_3$, (e) Mg (5 at%)-$NdFeO_3$ and (f) Zn (5 at%)-$NdFeO_3$ electrodes (scan rate: 5 $mV \cdot s^{-1}$).

In order to study the doping effects on the (photo)electrochemical properties of $NdFeO_3$ electrodes, cyclic voltammograms in the dark and linear scan voltammograms under transient illumination for Mg- and Zn-doped $NdFeO_3$ photocathodes were recorded. As observed in Figure 9.5c and 9.5e (and also in Figure S9.8a and S9.9a), doping with Mg and Zn does not induce important changes in the voltammetric response of the $NdFeO_3$ electrodes in the dark in either N_2- or O_2-purged working electrolytes.

Only in the presence of O_2, the capacitive region at potentials above 0.2 V seems to present a more defined shape. In the same way, linear scan voltammograms under transient illumination in an N_2-purged electrolyte exhibit the typical response of the pristine $NdFeO_3$ photocathode, with no significant changes in photocurrent magnitude, spike intensity or photocurrent onset location. More importantly, drastic enhancements in the photocurrent values upon Mg and Zn doping (Figure 9.5d and 9.5f, respectively) in the presence of an electron scavenger such as O_2 are observed. This enhancement in the photocurrent is clearly dependent on the $NdFeO_3$ doping level (Figure S9.8b and S9.9b). As observed in Figure S9.10, the stationary photocurrent at 0.1 V increases with the dopant concentration until an optimum value is reached at x = 5 at% for both Mg and Zn. The fact that the photocurrent values and their dependency with the dopant concentration are similar for both Mg and Zn indicates that the role of these cations as dopants in the perovskite structure is analogous.

Mott-Schottky analysis in the dark and under illumination (Figure 9.6) has been performed to further confirm the *p*-type character of the as-prepared pristine and doped $NdFeO_3$ photocathodes and to gain some insights into the mechanism for photocurrent enhancement upon Mg and Zn introduction. In fact, the $1/C^2$ *vs.* E plots show, although only in a limited range of potential, the expected tendency for a *p*-type semiconductor under band edge pinning conditions, linear with a negative slope. From the corresponding intercept with the abscissa axis, the flat band potential (E_{fb}) for the pristine $NdFeO_3$ photocathode can be estimated to be around 0.57 V both in the dark and under illumination. This indicates that the bands are not unpinned under illumination, which suggests that electron trapping at the surface is not substantial. As the slope of the straight line in the Mott-Schottky plot is inversely proportional to the density of the majority charge carriers (N_A), the plots show how the charge-carrier density increases under

illumination. Considering a dielectric constant (ε) of 75 [55], the calculated N_A for the pristine $NdFeO_3$ electrode in the dark and under illumination would be in the order of $6.3 \cdot 10^{18}$ and $7.4 \cdot 10^{18}$ cm^{-3}, respectively.

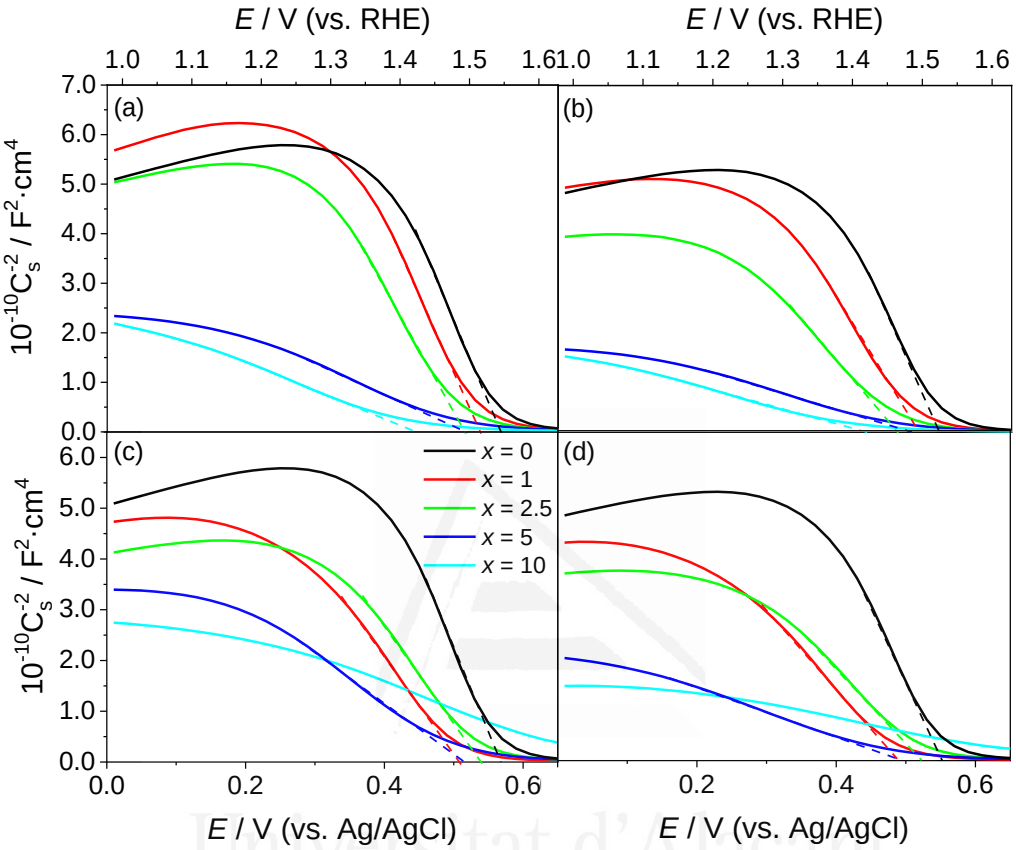

Figure 9.6. Mott-Schottky plots (a, c) in the dark and (b, d) under illumination at a frequency of 1 kHz for (a, b) Mg (*x* at%)-$NdFeO_3$ and (c, d) Zn (*x* at%)-$NdFeO_3$ electrodes in N_2-purged 0.1 M NaOH.

For the Mg- and Zn-doped samples, no significant shifts of the E_{fb} value are observed. In fact, only a minor shift toward less positive potentials (not desirable in the case of photocathodes) can be deduced. It is important to highlight the fact that the obtained flat band potentials are located relatively close to the observed photocurrent onset in either N_2- or O_2-purged electrolytes (around 0.15 V more positive). Thus, the potentials of the conduction band and valence band edges should be very similar for pristine and doped electrodes according to the small variations in E_{fb} and band gap

values. Therefore, the enhancement of the photoresponse cannot be ascribed to an increase in the reducing power of the photogenerated electrons or in the fraction of visible light absorbed by the electrode. The progressive decrease in the slope values as the Mg and Zn dopant density increases (Table S9.2) indicates that such an enhancement can be related to an increase in the density of the majority charge carriers (N_A) in the material. This effect is especially notable for the highest concentrations of Mg and Zn (although they do not exhibit the best photoelectrochemical performance).

9.4.3. Computational results

Figure 9.7 shows the total and partial density of states for $NdFeO_3$ at PBE + U (U (Fe) = 4.0 eV). The distribution of the total DOS is very similar to that obtained with the HSE03 (α = 15%) functional (see Figure S9.11), defining direct bandgap values of 2.4 eV and 3.0 eV with PBE+U and HSE03, respectively. Considering that the experimental direct band gap is around 2.7 eV, a reasonable agreement is obtained with these two theory levels. On the contrary, there is no correspondence with the experimental indirect band gap value, maybe because it originates from transitions implying defect states rather than from interband transitions. Regarding the Nd DOS, it can be seen that, in the energy range close to the Fermi level, there is no significant contribution of this element to the total DOS. In this respect, there is experimental evidence that the main contributions to the valence and conduction bands come from the Fe and the O states [27,56]. Regarding Fe, it can be observed that, according to PBE+U (and HSE03), the occupied states of the Fe are very localized at the Fe atoms and very deep in energy, although there is also a small contribution to the total DOS close to the Fermi level. In the case of the O, computational results show that the O 2*p* states are mainly distributed in the range from -

5 eV up to the Fermi level. It can also be seen that there is an important hybridization between the Fe 3*d* and the O 2*p* states both above and below the Fermi level.

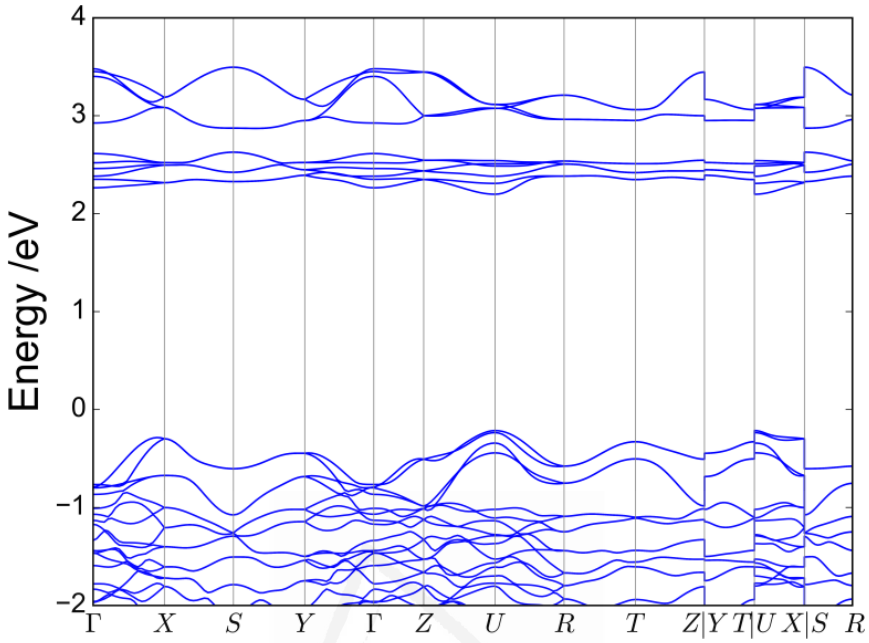

Figure 9.7. Total and partial density of states for $NdFeO_3$ at PBE + U (U (Fe) = 4.0 eV) (the dashed line is the Fermi level, which has been shifted to zero).

Figure 9.8 shows the band structure of $NdFeO_3$ calculated with the PBE+U model. In both cases, a very similar band structure with a direct band gap centered at the high-symmetry U-point (with a value of 2.4 eV with PBE+U and 3.0 eV with HSE03) is obtained. Interestingly, the conduction band seems to be very flat, which underlines the fact that there are highly localized states. This points to the possibility that the photogenerated charge carriers (in this case, electrons) possess very low mobility. In this respect, Table 9.1 shows the effective mass values for electrons and holes along the crystal axis directions, obtained with Boltztrap2 from the PBE + U band structure calculations (see Table S9.3 for results obtained from HSE03 band structure). It is worth noting that, for both charge carriers, the effective masses show anisotropic behavior. This is a crucial factor because the crystal orientation over the substrate is thus relevant as it

influences the photoelectrochemical response. In materials with this anisotropic conductivity, it is highly advantageous to have nanostructures preferentially oriented in the most convenient crystal direction, such as nanosheets or nanorods. However, in this case, the preferential direction is the same for both charge carriers. The fact that, irrespective of the direction, the effective mass of the electron is twice that of the hole can explain in part that (i) the semiconductor exhibits *p*-type behavior and (ii) the higher photocurrent values obtained for EE illumination than for SE illumination (Figure S9.2). In the electrolyte-electrode illumination, photogenerated holes need to travel through the bulk material until they reach the electric contact, while in the SE illumination , it is the electron the charge carrier that should pass through the bulk material before reaching the electrode-electrolyte interface.

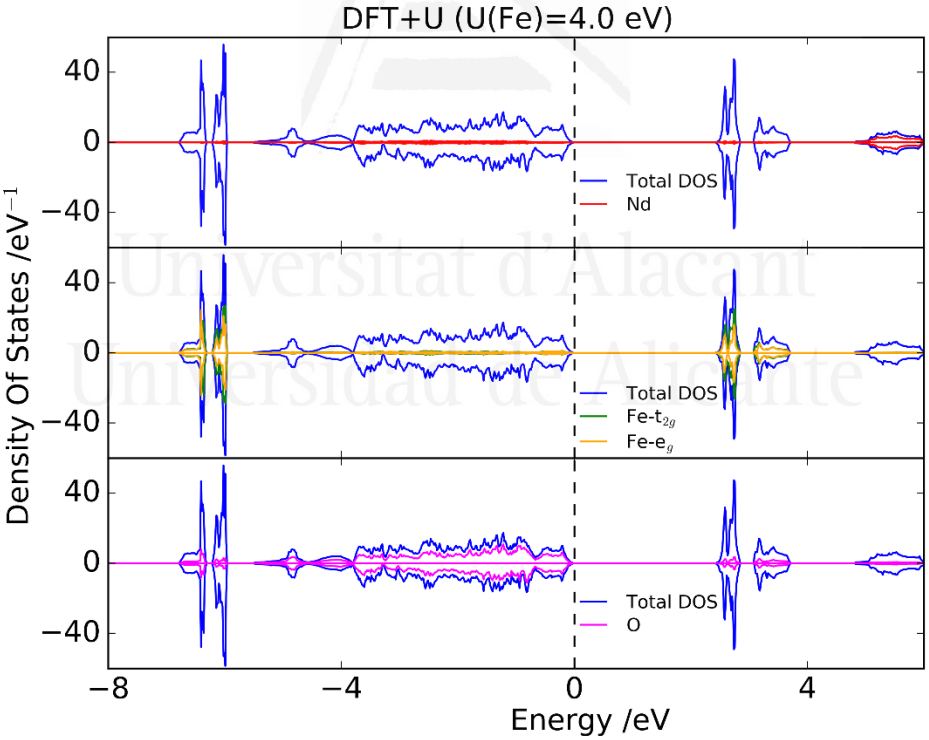

Figure 9.8. Band structure of $NdFeO_3$ calculated with the DFT+U model.

Table 9.1. Calculated band gap and effective masses of carriers in $NdFeO_3$ from band structure (PBE + U).

Calculation	Band gap / eV	Charge carrier	a / m_e	b / m_e	c / m_e
PBE+U	2.4	Electron	11.0	2.8	8.7
		Hole	1.8	1.4	3.0

It is important to highlight the fact that DFT calculations provide evidence that the upper edge of the valence band consists mainly of O 2*p* states, with a minor contribution of the Fe 3*d* e_g states. According to this, photogenerated holes in $NdFeO_3$ can be ascribed to O^- and Fe^{4+} species [27]. In fact, the electric *p*-type nature of certain $AFeO_3$ perovskites is thought to arise from the presence of small amounts of Fe^{4+} in their structure, which is further compensated by the corresponding level of oxygen excess to result in an $AFeO_{3+x}$ stoichiometry [57]. In the case of $LaFeO_3$ obtained by a sol-gel method using the citrate route (similar to that used here for the preparation of $NdFeO_3$), the fraction of Fe^{4+} over total Fe was estimated to be between 2.4 and 3.2% [44]. On the other hand, it is important to highlight that the lower edge of the conduction band consists mainly of Fe 3*d* t_{2g} and e_g states with a minor contribution of O 2*p* states, contrary to what happens with the upper edge of the valence band.

Thus, the increase in $NdFeO_3$ acceptor level density and photoactivity upon Mg and Zn doping can be explained considering a subsequent increase in the concentration of these Fe^{4+} species: the substitution of trivalent iron cations by divalent doping elements (Mg^{2+} and Fe^{2+}, in this case) may induce through a charge compensation mechanism based on either the corresponding oxidation of Fe^{3+} to Fe^{4+} or on a partial loss of oxygen excess (which means decreasing *x* for $NdFeO_{3+x}$). However, the relatively small variation in the majority carrier density calculated on the basis of the Mott-Schottky measurements, could indicate that, in this case, the charge compensation happens through a loss of excess

oxygen rather than by an increase in Fe^{4+} density. The more than likely surface segregation of the dopants (as revealed in previous reports [27] and also in agreement with our XPS analysis) further supports the idea that this modification does not induce major modifications in the material bulk (implying thus a limited increase in bulk Fe^{4+} density).

In this context, the enhancement in the photoelectrochemical response likely relies on other contributions, such as a higher electron mobility. Previous reports have referred to an increase in the mobility of the majority charge carriers with the dopant concentration in certain semiconductors, such as In_2O_3 [58–60] and $SrTiO_3$ [61]. In the case of perovskites, this increase in mobility has usually been justified by considering the lattice distortion induced by doping. Not in vain, important variations of the unit cell parameters have been measured for the $LaFeO_3$ structure upon the incorporation of divalent Zn and Mg ions [28,44,46,62,63]. The slightly different ionic radii of the dopant cations in comparison with Fe^{3+} in the B position of the host structure and its partial oxidation to Fe^{4+} (with a smaller radius of 58.5 pm) would explain this structure distortion.

Finally, an $NdFeO_3$ surface passivation as a consequence of doping cannot be ruled out. This effect would be caused by the Mg and Zn surface segregation and their subsequent hydroxylation, which is confirmed by XPS analysis. Such a passivation should diminish surface recombination thus explaining the higher photoactivity observed in the presence of oxygen.

9.5. CONCLUSIONS

In summary, we have shown that $NdFeO_3$ thin film electrodes prepared by layer-by-layer coating of conducting glass substrates by a citrate-route sol-gel method, followed by a heat treatment, behave as photocathodes for oxygen and water reduction in alkaline

media. Their photoactivity toward the oxygen reduction reaction can be significantly enhanced by doping with either Mg^{2+} or Zn^{2+}. In fact, for the optimum doping level (5 at% for both Mg^{2+} and Zn^{2+}), the photocurrent associated to the oxygen reduction reaction multiplies by factors of 3.4 and 2.8, respectively. This important enhancement of the *p*-type behavior (further confirmed by DFT calculations) of $NdFeO_3$ has been attributed to an increase in the majority charge carrier concentration (as demonstrated by Mott-Schottky measurements). This would result from a dopant-induced increment in the density of Fe^{4+} species in the $NdFeO_3$ lattice caused by charge compensation when Fe^{3+} centers are substituted by divalent Mg and Zn cations. The lattice distortion coming from this substitution effect likely increases in a significant way in the charge carrier mobilities. In addition, Mg^{2+} and Zn^{2+} are thought to segregate at the doped-$NdFeO_3$ film surface, probably contributing to the passivation of deleterious surface states, which as demonstrated through DFT calculations correspond to Fe surface sites.

It has been demonstrated that $NdFeO_3$ can potentially present a very similar photoelectrochemical performance to that of the widely studied $LaFeO_3$ perovskite. This turns $NdFeO_3$ into an attractive candidate material as photocathode in tandem devices due to its environmental friendliness and the relatively high earth abundance of its constituent elements (Nd is even slightly more abundant than La in Earth's crust). As in the case of $LaFeO_3$, $NdFeO_3$ also presents a high photo-onset potential for cathodic currents and a competitive narrow band gap value. Although the doping procedure with Mg and Zn leads to a drastic enhancement of the oxygen reduction photocurrent, it has not lead to an improvement the kinetics of photogenerated electron transfer along the electrode-electrolyte interface to effectively promote the hydrogen evolution reaction from water, which requires the development of different strategies. In this regard, a promising

combination of an extraction layer with a proper metal co-catalyst is currently been tested and optimized in our laboratory.

Finally, DFT calculations at the PBE+U level of the electronic structure of $NdFeO_3$ have provided a band gap value close to that found experimentally and confirmed the *p*-semiconducting character of this material. In addition, the calculated band structure shows a very flat conduction band, indicating a low electron mobility. Importantly, the effective masses of carriers calculated from the band structures indicate a significant anisotropy in the conduction properties, both for electrons and holes, pointing to the importance of nanostructuring. The importance of theoretical calculations in guiding the search for effective enhancement strategies in photoelectrochemistry is thus illustrated.

9.6. ACKNOWLEDGEMENTS

Financial support by the Spanish Ministry of Economy and Competitiveness through project RTI2018–102061–B–I00 (FONDOS FEDER) is gratefully acknowledged. J. Q. and F.J.P. thank to the Spanish Ministry of Education, Culture and Sport (MECD) for the award of FPU predoctoral grants (FPU15/02005 and FPU16/02492, respectively).

9.7. REFERENCES

[1] M. Grätzel, Nature. 414 (2001) 338
[2] H. Tributsch, Int. J. Hydrog. Energy. 33 (2008) 5911.
[3] M.G. Walter, E.L. Warren, H.B. Gray, Chem. Mater. Mater. 26 (2014) 407.
[4] N.S. Lewis, D.G. Nocera, Proc. Natl. Acad. Sci. 2. 103 (2006) 15729.
[5] M.S. Prévot, K. Sivula, J. Phys. Chem. C. 117 (2013) 17879.
[6] A.B. Murphy, P.R.F. Barnes, L.K. Randeniya, I.C. Plumb, I.E. Grey, M.D. Horne, J.A. Glasscock, Int. J. Hydrog. Energy. 31 (2006) 1999.
[7] M.G. Walter, E.L. Warren, J.R. McKone, S.W. Boettcher, Q. Mi, E.A. Santori, N.S. Lewis, Chem. Rev. 110 (2010) 6446.
[8] T. Bak, J. Nowotny, M. Rekas, C. Sorrell, Int. J. Hydrog. Energy. 27 (2002) 991.
[9] A. Fujishima, K. Honda, Nature. 238 (1972) 37.
[10] W. Yang, J. Moon, ChemSusChem. 12 (2018) 1889.
[11] Y.J. Jang, J.S. Lee, ChemSusChem. 12 (2019) 1835.
[12] Y. Li, K. Luo, RSC Adv. 9 (2019) 8350.

[13] S. Masudy-Panah, R.S. Moakhar, C.S. Chua, A. Kushwaha, G.K. Dalapati, ACS Appl. Mater. Interfaces. 9 (2017) 27596.
[14] K. Jung, T. Lim, H. Bae, J. Ha, A.A. Martinez-Morales, ChemCatChem. 11 (2019) 4377.
[15] I.V. Baga, N.R. Chodankar, M.A. Hassan, A. Waseem, M.A. Johar, D.-H. Kim, S.-W. Ryu, Int. J. Hydrog. Energy. 44 (2019) 21351.
[16] K. Kirchberg, R. Marschall, Sustain. Energy Fuels. 3 (2019) 1150.
[17] M.I. Díez-García, R. Gómez, ACS Appl. Mater. Interfaces. 8 (2016) 21387.
[18] Y. Xu, J. Jian, F. Li, W. Liu, L. Jia, H. Wang, J. Mater. Chem. A. 7 (2019) 21997.
[19] W.-H. Lee, J. Kang, H.S. Park, S.K. Cho, J. Electroanal. Chem. 838 (2019) 172.
[20] Y.J. Jang, Y.B. Park, H.E. Kim, Y.H. Choi, S.H. Choi, J.S. Lee, Chem. Mater. 2. 28 (2016) 6054.
[21] T. Jiang, Y. Zhao, H. Xue, J. Mater. Sci. 54 (2019) 11951.
[22] S.H. Porter, S. Hwang, V. Amarasinhge, F. Taghaddos, V. Manichev, M. Li, G. Gardner, A. Safari, E. Garfunkel, M. Greenblatt, G.C. Dismukes, ECS Trans. 72 (2016) 1.
[23] I.N. Sora, F. Fontana, R. Passalacqua, C. Ampelli, S. Perathoner, G. Centi, F. Parrino, L. Palmisano, Electrochim. Acta. 109 (2013) 710.
[24] K.J. May, D.P. Fenning, T. Ming, W.T. Hong, D. Lee, K.A. Stoerzinger, M.D. Biegalski, A.M. Kolpak, Y. Shao-Horn, J. Phys. Chem. Lett. 6 (2015) 977.
[25] Q. Peng, J. Wang, Y.W. Wen, B. Shan, R. Chen, RSC Adv. 6 (2016) 26192.
[26] G.P. Wheeler, K.-S. Choi, ACS Energy Lett. 2 (2017) 2378.
[27] M.I. Díez-García, R. Gómez, ChemSusChem. 10 (2017) 1457.
[28] S. Dong, K. Xu, G. Tian, J. Mater. Sci. 44 (2009) 2548.
[29] X. Zhang, A. Bieberle-Hütter, ChemSusChem. 9 (2016) 1223.
[30] A. V. Akimov, A.J. Neukirch, O. V. Prezhdo, Chem. Rev. 113 (2013) 4496.
[31] P. Liao, E.A. Carter, Chem. Soc. Rev. 42 (2013) 2401.
[32] A. Valdés, J. Brillet, M. Grätzel, H. Gudmundsdóttir, H.A. Hansen, H. Jónsson, P. Klüpfel, G.-J. Kroes, F. Le Formal, I. C. Man, R.S. Martins, J.K Nørskov, J. Rossmeisl, K. Sivula, A. Vojvodic, M. Zäch, Phys. Chem. Chem. Phys. 14 (2012) 49.
[33] Y. Ping, D. Rocca, G. Galli, Chem. Soc. Rev. 42 (2013) 2437.
[34] G. Kresse, J. Furthmüller, Phys. Rev. B - Condens. Matter Mater. Phys. 54 (1996) 11169.
[35] P.E. Blöchl, Phys. Rev. B. 50 (1994) 17953.
[36] G. Kresse, D. Joubert, Phys. Rev. B-Condens. Matter Mater. Phys. 59 (1999) 1758.
[37] J.P. Perdew, K. Burke, M. Ernzerhof, Phys. Rev. Lett. 77 (1996) 3865.
[38] S.L. Dudarev, G.A. Botton, S.Y. Savrasov, C.J. Humphreys, A.P. Sutton, Phys. Rev. B. 57 (1997) 1505.
[39] A. Jain, G. Hautier, C.J. Moore, S. Ping Ong, C.C. Fischer, T. Mueller,K.A. Persson, G. Ceder, Comput. Mater. Sci. 50 (2011) 2295.
[40] J. Heyd, G.E. Scuseria, M. Ernzerhof, J. Chem. Phys. 118 (2003) 8207.
[41] J. He, C. Franchini, Phys. Rev. B-Condens. Matter Mater. Phys. 86 (2012) 235117.
[42] L. Chen, T. Li, S. Cao, S. Yuan, F. Hong, J. Zhang, J. Appl. Phys. 111 (2012) 103905.
[43] G.K.H. Madsen, J. Carrete, M.J. Verstraete, Comput. Phys. Commun. 231 (2018) 140.
[44] P. Porta, S. Cimino, S. De Rossi, M. Faticanti, G. Minelli, I. Pettiti, Mater. Chem. Phys. 71 (2001) 165.
[45] P. Ciambelli, S. Cimino, S. De Rossi, L. Lisi, G. Minelli, P. Porta, G. Russo, Appl.

Catal. B. 29 (2001) 239.
[46] S. Huang, H. Qin, P. Song, X. Liu, L. Li, R. Zhang, J. Hu, H. Yan, M. Jiang, J. Mater. Sci. (2007) 9973.
[47] B.V. Kumar, R. Velchuri, G. Prasad, B. Sreedhar, K. Ravikumar, M. Vithal, Ceram. Int. 36 (2010) 1347.
[48] V. Bilovol, S. Ferrari, D. Derewnicka, F.D. Saccone, Mater. Chem. Phys. 146 (2014) 269.
[49] T. Yamashita, P. Hayes, Appl. Surf. Sci.2. 254 (2008) 2441.
[50] S. Mickevicius, S. Grebinskij, V. Bondarenka, B. Vengalis, K. Sliuziene, B.A. Orlowski, V. Osinniy, W. Drube, J. Alloy. Compd. 423 (2006) 107.
[51] A.M. De Asha, J.T.S. Critchley, R.M. Nix, Surf. Sci. 405 (1998) 201.
[52] A.K. Díaz-García, T. Lana-Villarreal, R. Gómez, J. Mater. Chem. A. 3 (2015) 19683.
[53] M.I. Díez-García, T. Lana-Villarreal, R. Gómez, ChemSusChem. 9 (2016) 1504.
[54] P. Salvador, J. Phys. Chem. 89 (1985) 3863.
[55] J. Shankera, G. Narsinga Rao, K. Venkataramana, D.S. Babu, Phys. Lett. A. 382 (2018) 2974.
[56] E. Niwa, T. Sato, Y. Watanabe, Y. Toyota, Y. Hatakeyama, K. Judai, K. Shozugawa, M. Matsuo, T. Hashimoto, J. Ceram. Soc. Japan. 123 (2015) 501.
[57] M. Idrees, M. Nadeem, M. Atif, M. Siddique, M. Mehmood, M.M. Hassan, Acta Mater. 59 (2011) 1338.
[58] P.F. Newhouse, C.-H. Park, A. Keszler, J. Tate, P.S. Nyholm, Appl. Phys. Lett. 87 (2005) 112108.
[59] N. Yamada, T. Tatejima, H. Ishizaki, T. Nakada, Jpn. J. Appl. Phys. 45 (2006) L1179.
[60] Y. Abe, N. Ishiyama, J. Mater. Sci. 41 (2006) 7580.
[61] T. Okuda, K. Nakanishi, S. Miyasaka, Y. Tokura, Phys. Rev. B. 63 (2001) 113104.
[62] I. Bhat, S. Husain, W. Khan, S.I. Patil, Mater. Res. Bull. 48 (2013) 4506.
[63] X. Liu, B. Cheng, J. Hu, H. Qin, M. Jiang, Sens. Actuators B. 129 (2008) 53.

9.8. SUPPLEMENTARY MATERIALS

9.8.1. XRD, SEM, XPS and UV-vis analysis details

The crystal structure of the $NdFeO_3$ deposits was determined by XRD, using a Bruker, D8-Advance X-ray diffractometer operating at room temperature with Cu-Kα radiation (λ = 1.5416 Å) at 40 kV and 40 mA. The angular velocity was $0.5^{o} \cdot min^{-1}$ within a 2θ range between 20º and 70º.

A SEM study was carried out to characterize the surface morphology of the films using a ZEISS Merlin VP Compact field emission scanning electron microscope (FESEM).

For the film surface composition study, XPS experiments were done with a Thermo-Scientific K-Alpha XPS spectrometer equipped with a monochromatic Al-Kα source (1486.6 eV), operating at 15 kV and 10 mA.

The optical properties of the films were studied by solid-state UV-vis spectroscopy, using a Shimadzu UV-2401 PC spectrophotometer equipped with an integrating sphere and working in the absorbance mode.

9.8.2. Optimization of the $NdFeO_3$ thin film electrode thickness

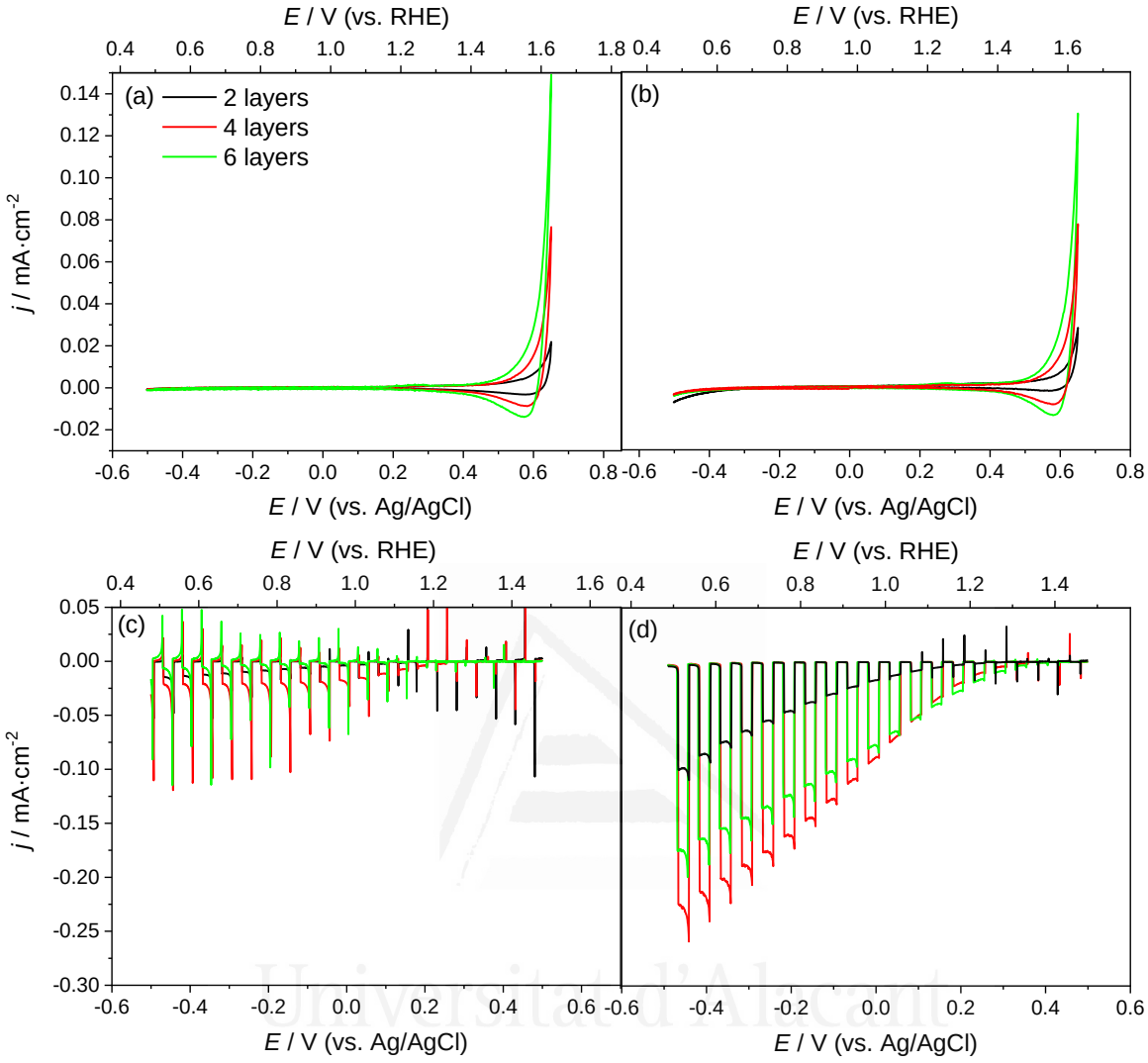

Figure S9.1. Cyclic voltammograms in the dark in (a) N_2- and (b) O_2-purged 0.1 M NaOH for 2–, 4– and 6–layer pristine $NdFeO_3$ electrodes (scan rate: 20 $mV \cdot s^{-1}$). Linear scan voltammograms under transient illumination in (c) N_2- and (d) O_2-purged 0.1 M NaOH for 2–, 4– and 6–layer pristine $NdFeO_3$ electrodes (scan rate: 5 $mV \cdot s^{-1}$).

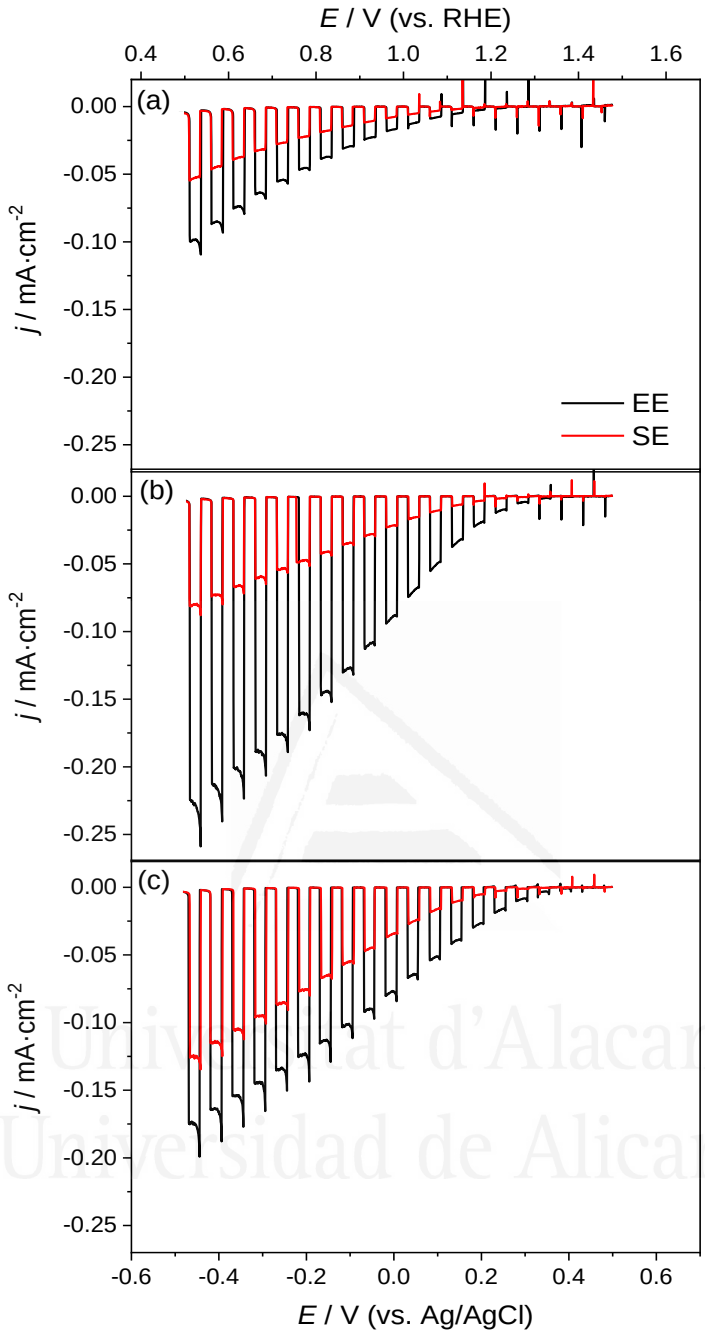

Figure S9.2. Linear scan voltammograms for (a) 2–, (b) 4– and (c) 6–layer pristine $NdFeO_3$ electrodes under transient electrolyte-electrode (EE) and substrate-electrode (SE) illumination (scan rate: 5 $mV \cdot s^{-1}$), in O_2-purged 0.1 M NaOH.

9.8.3. Additional FESEM characterization

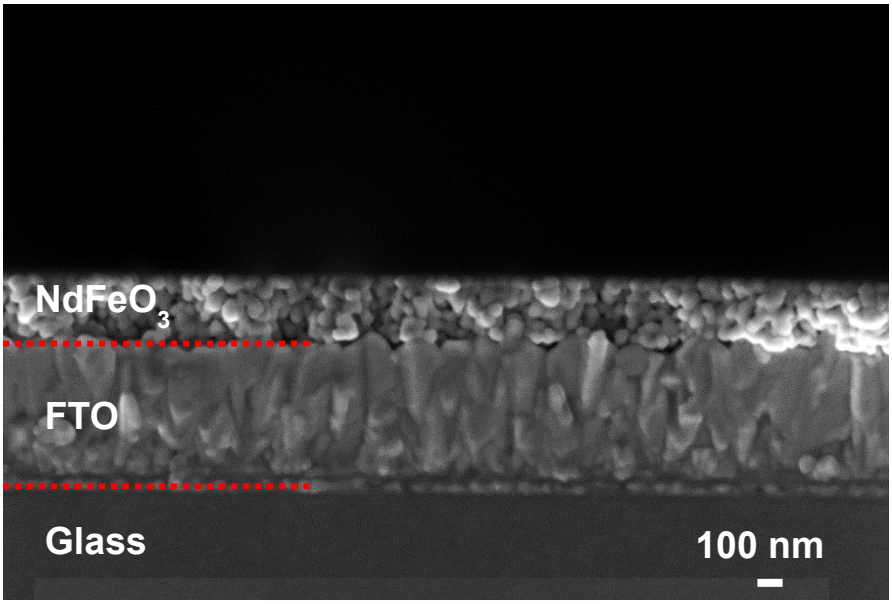

Figure S9.3. Cross-sectional FESEM image for an FTO/$NdFeO_3$ electrode.

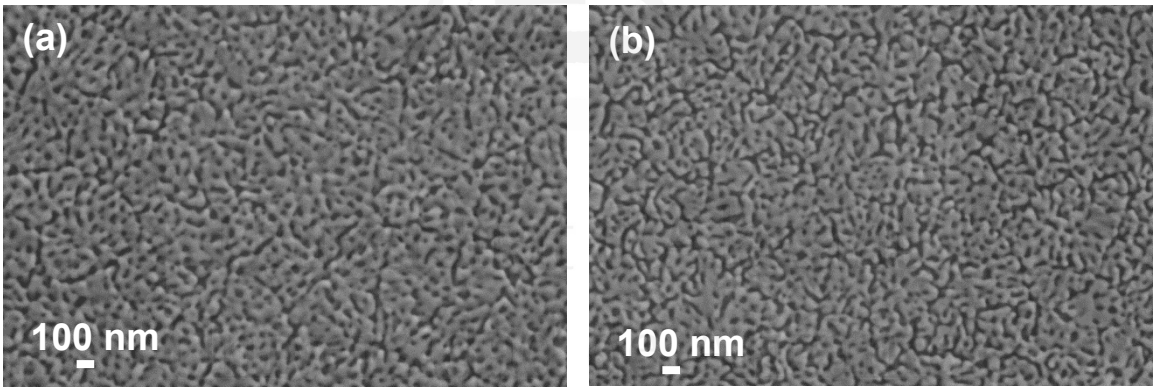

Figure S9.4. FESEM image corresponding to the top view of (a) Mg (5 at%)-$NdFeO_3$ and (b) Zn (5 at%)-$NdFeO_3$ films on FTO.

9.8.4. XPS characterization

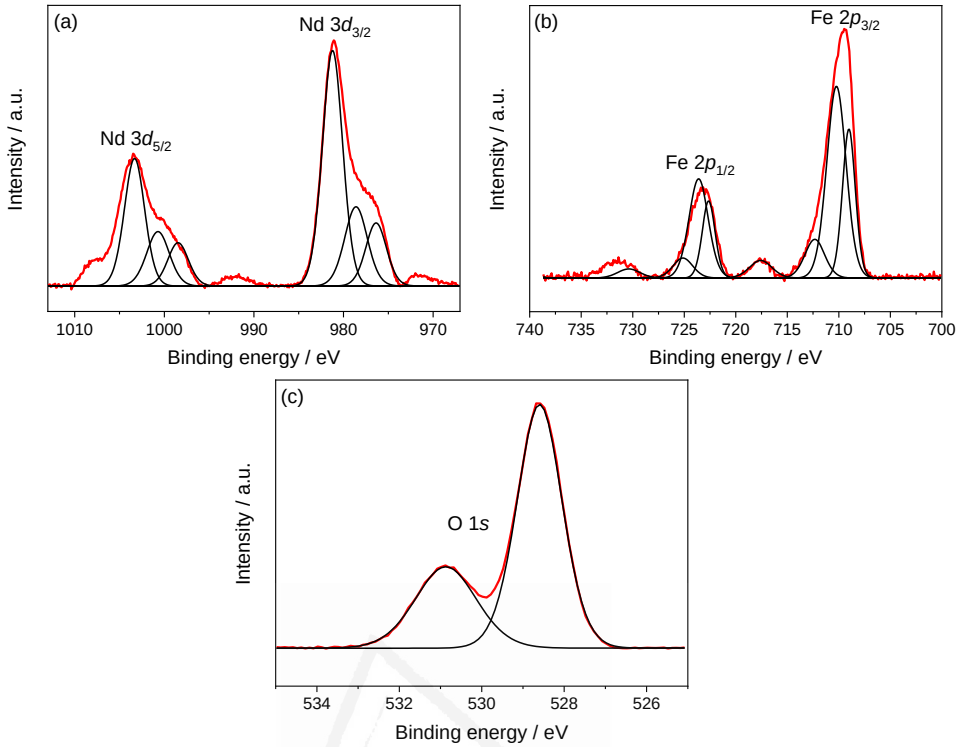

Figure S9.5. (a) Nd 3*d*, (b) Fe 2*p* and (c) O 1*s* XPS spectra (red line), and their corresponding deconvolutions (black lines), for a Mg (5 at%)-$NdFeO_3$ film.

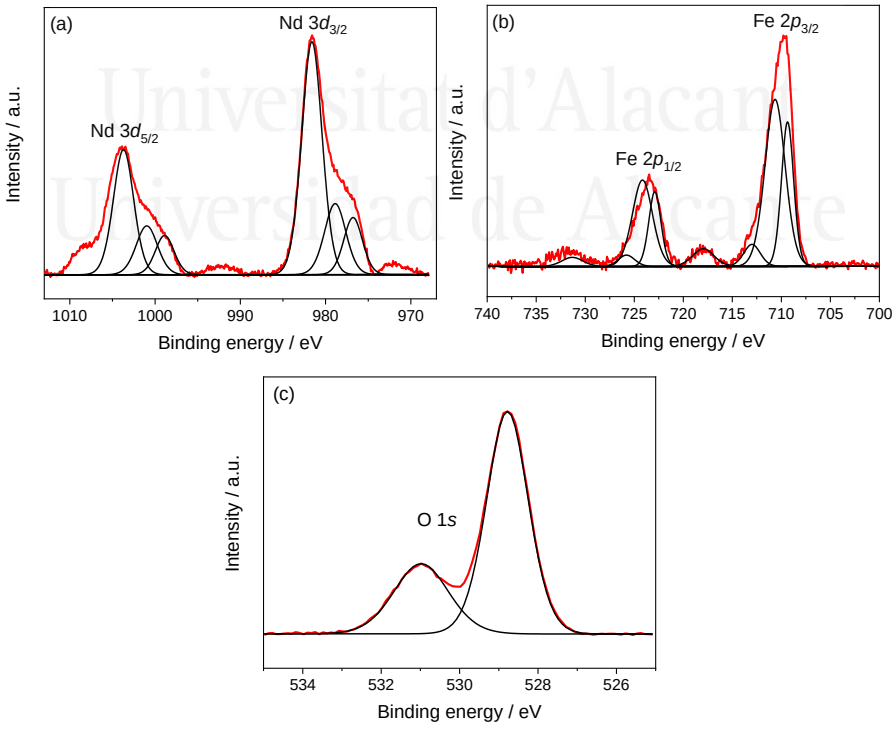

Figure S9.6. (a) Nd 3*d*, (b) Fe 2*p* and (c) O 1*s* XPS spectra (red line), and their corresponding deconvolutions (black lines), for a Zn (5 at%)-$NdFeO_3$ film.

Table S9.1. Atomic ratios obtained by XPS analysis for $NdFeO_3$, Mg (5 at%)-$NdFeO_3$ and Zn (5 at%)-$NdFeO_3$. In parentheses, the corresponding theoretical values in the bulk.

	ATOMIC RATIO (obtained by XPS analysis)			
	Nd / Fe	**Mg / Fe**	**Zn / Fe**	**OH / O_{latt}**
$NdFeO_3$	1.5 (1.0)	-	-	0.37
Mg (5 at%)-$NdFeO_3$	1.4 (1.05)	0.27 (0.05)	-	0.45
Zn (5 at%)-$NdFeO_3$	1.4 (1.05)	-	0.32 (0.05)	0.41

9.8.5. Optical characterization

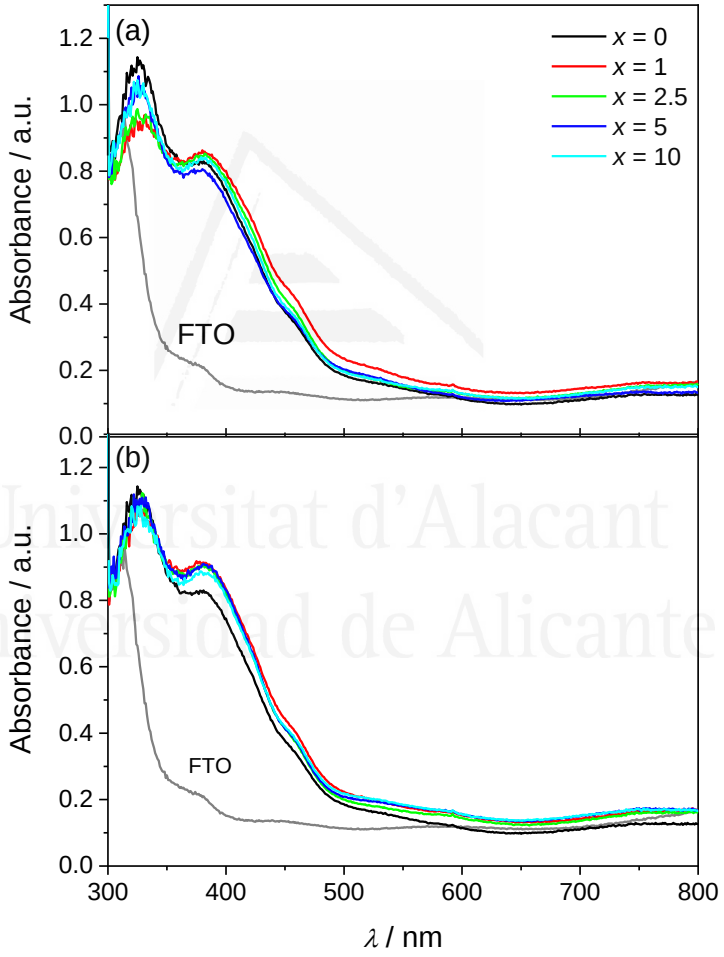

Figure S9.7. UV-visible absorbance spectra for (a) Mg (*x* at%)-$NdFeO_3$ and (b) Zn (*x* at%)-$NdFeO_3$ films.

9.8.6. (Photo)electrochemical characterization

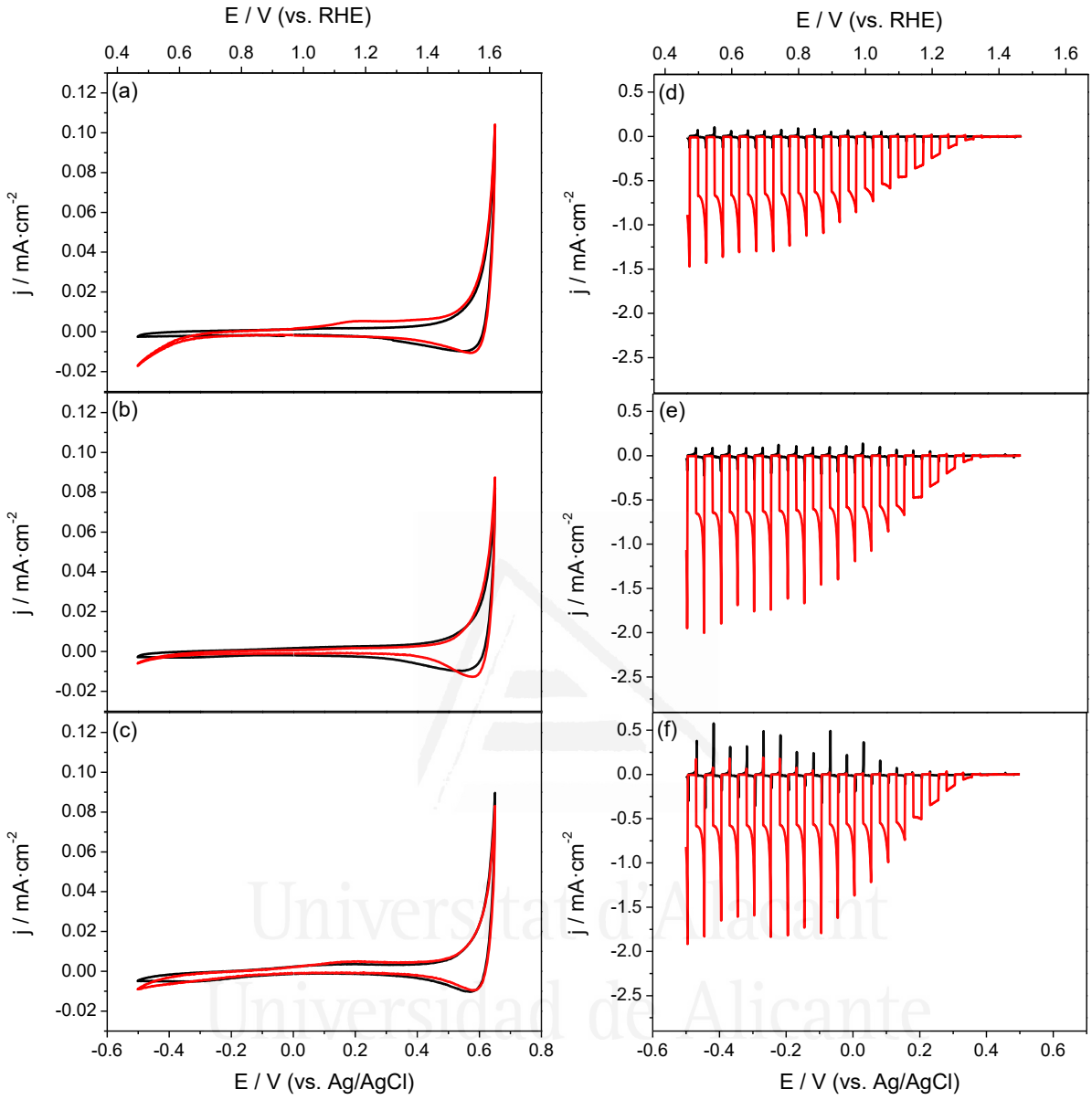

Figure S9.8. Cyclic voltammograms in the dark in N_2- (black line) and O_2-purged (red line) 0.1 M NaOH for (a) Mg (1 at%)-$NdFeO_3$, (b) Mg (2.5 at%)-$NdFeO_3$ and (c) Mg (10 at%)-$NdFeO_3$ electrodes (scan rate: 20 $mV \cdot s^{-1}$). Linear scan voltammograms under transient illumination in N_2- (black line) and O_2-purged (red line) 0.1 M NaOH for (d) Mg (1 at%)-$NdFeO_3$, (e) Mg (2.5 at%)-$NdFeO_3$ and (f) Mg (10 at%)-$NdFeO_3$ electrodes (scan rate: 5 $mV \cdot s^{-1}$).

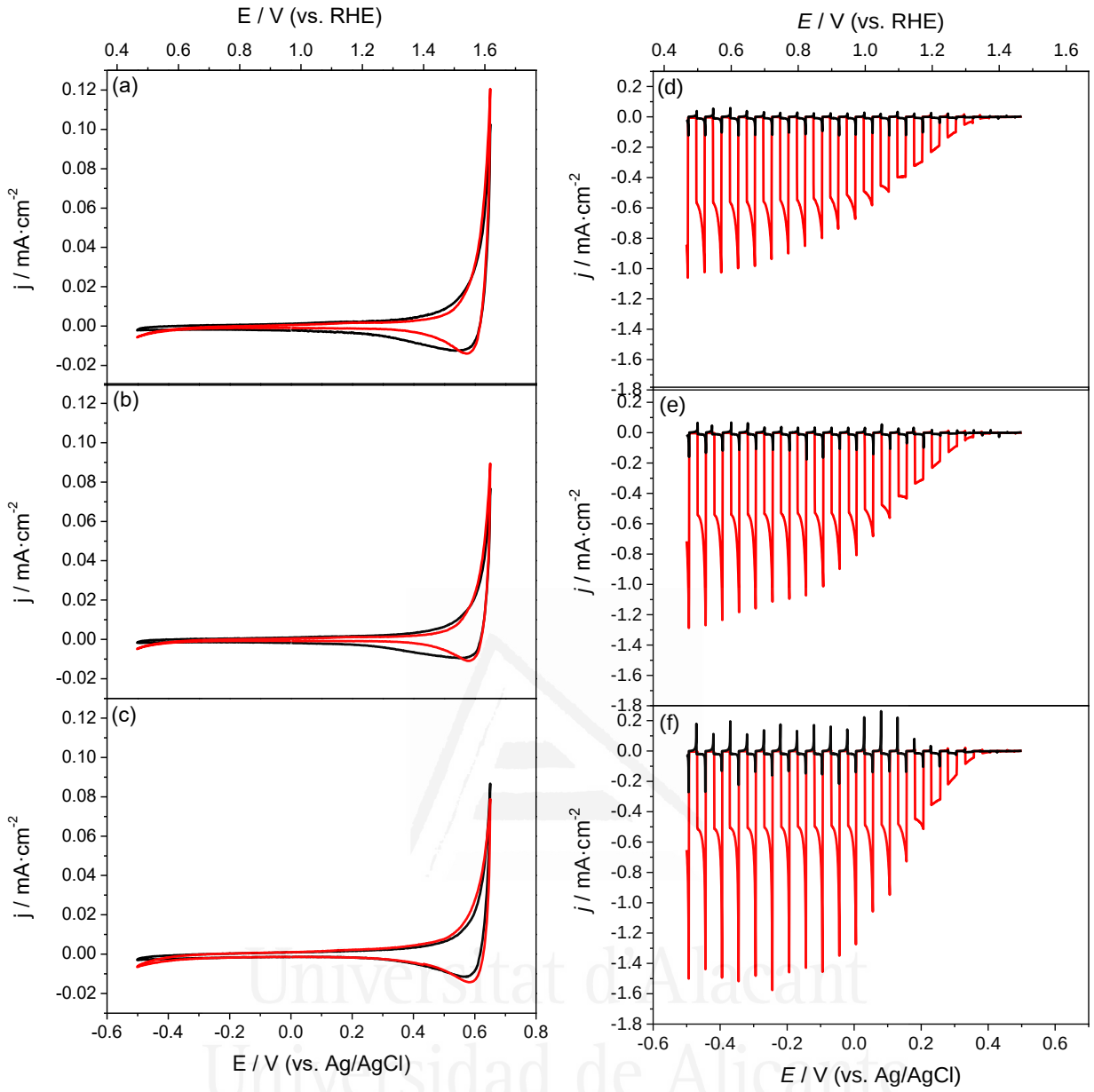

Figure S9.9. Cyclic voltammograms in the dark in N_2- (black line) and O_2-purged (red line) 0.1 M NaOH for (a) Zn (1 at%)-$NdFeO_3$, (b) Zn (2.5 at%)-$NdFeO_3$ and (c) Zn (10 at%)-$NdFeO_3$ electrodes (scan rate: 20 $mV \cdot s^{-1}$). Linear scan voltammograms under transient illumination in N_2- (black line) and O_2-purged (red line) 0.1 M NaOH for (d) Zn (1 at%)-$NdFeO_3$, (e) Zn (2.5 at%)-$NdFeO_3$ and (f) Zn (10 at%)-$NdFeO_3$ electrodes (scan rate: 5 $mV \cdot s^{-1}$).

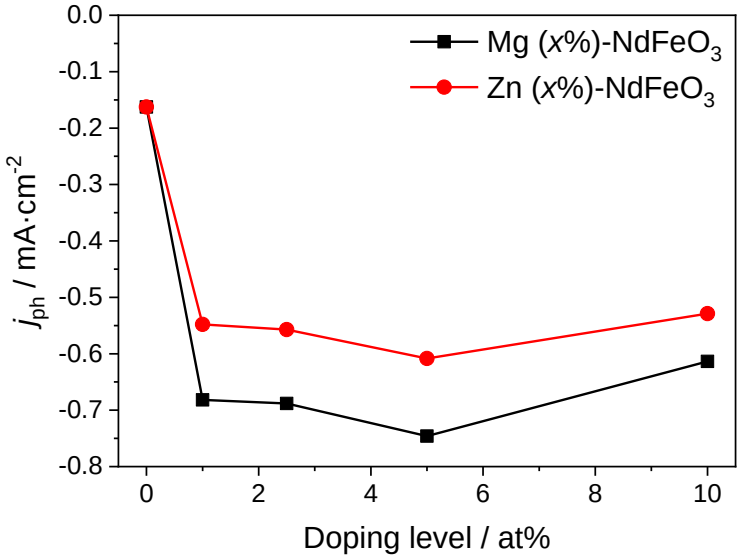

Figure S9.10. Stationary photocurrent at 0.1 V as a function of doping level (*x*) for Mg (*x* at%)- and Zn (*x* at%)-doped $NdFeO_3$ electrodes.

Table S9.2. Absolute values of the slopes of the linear region in the Mott-Schottky plots shown in Figure 9.5 for pristine and doped $NdFeO_3$ electrodes, in the dark and under illumination.

	$\lvert 10^{-10}\cdot\text{slope}\rvert$ / $F^{-2}\cdot cm^{-4}\cdot V^{-1}$	
	Dark	**Illumination**
$NdFeO_3$	30.0	25.9
Mg (1 at%)-$NdFeO_3$	29.3	22.1
Mg (2.5 at%)-$NdFeO_3$	24.4	14.9
Mg (5 at%)-$NdFeO_3$	6.1	4.0
Mg (10 at%)-$NdFeO_3$	5.3	3.8
Zn (1 at%)-$NdFeO_3$	28.2	14.8
Zn (2.5 at%)-$NdFeO_3$	17.5	13.2
Zn (5 at%)-$NdFeO_3$	9.7	4.7
Zn (10 at%)-$NdFeO_3$	5.1	2.7

9.8.7. Additional DFT results

For the HSE functional, the values of the mixing parameter for exact Fock exchange and the screening parameter were 0.15 and 0.3 $Å^{-1}$, respectively. A single-point calculation has been made to obtain the DOS (for the geometry optimized at the PBE+U level) with an energy cut-off of 400 eV, a 5x5x3 k-mesh and an electronic convergence criterion of 10^{-5} eV.

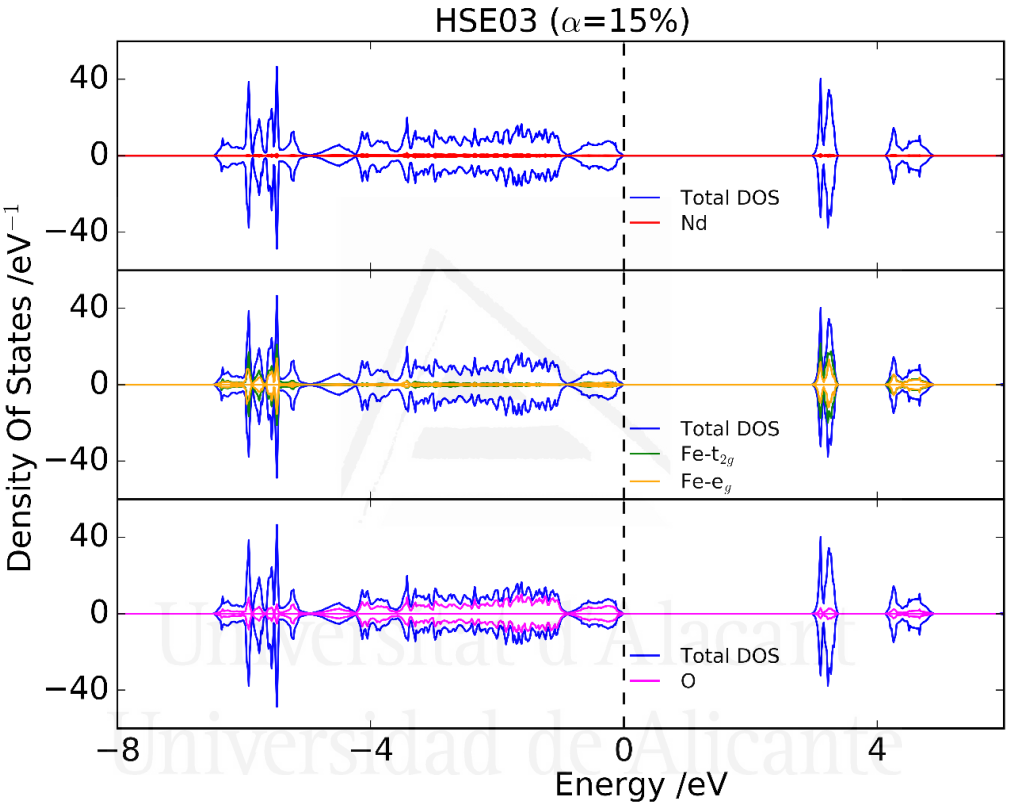

Figure S9.11. Total and partial density of states for $NdFeO_3$ at HSE03 (α = 15%) (the dashed line is the Fermi level, which has been shifted to zero).

Table S9.3. Calculated band gap and effective masses of carriers in $NdFeO_3$ from band structure through HSE03 calculations.

Calculation	**Band gap / eV**	**Charge carrier**	***a* / m_e**	***b* / m_e**	***c* / m_e**
HSE03	3.0	Electron	10.0	2.9	11.4
		Hole	1.4	1.5	10.1

CHAPTER X

Effective interface engineering of $NdFeO_3$ photocathodes for improving photoelectrochemical hydrogen evolution

10.1. ABSTRACT

The coupling of an extraction layer with a metal co-catalyst on the surface of a photocathode is among the most common procedures today to enhance the photoelectrochemical activity for the hydrogen evolution reaction. In this context, we present the deposition of a TiO_2 extracting layer on pristine and doped $NdFeO_3$ photocathodes by means of simple drop-casting procedure, followed by the electrodeposition of controlled amounts of Ni nanoparticles as co-catalysts for the hydrogen evolution reaction. The highest photoactivity (according to the photocurrent value at 0.1 V *vs*. Ag/AgCl) is achieved for optimum coverages of Ni deposit of around 4.7, 4.9 and 3.7 monolayers for $NdFeO_3/TiO_2$/Ni, Mg (5 at%)-$NdFeO_3/TiO_2$/Ni and Zn (5 at%)-$NdFeO_3/TiO_2$/Ni photocathodes, respectively. This implies significant photocurrent enhancements by factors of 5.8, 4.8 and 5.2, respectively, compared to the corresponding pristine or doped $NdFeO_3/TiO_2$ photoelectrode. This study points to the possibility of approaching surface engineering strategies on photocathodes from simple synthesis techniques and without resorting to co-catalysts based on noble metal particles.

10.2. INTRODUCTION

In the context of the development of competent photocathodes for their use in technologies based on photoelectrochemical (PEC) water splitting to obtain H_2 as a fuel from solar energy, engineering the electrode surface is currently a primary focus of research [1–3]. The combination of surface extracting layers and co-catalysts are among the most usual strategies to achieve highly efficient photocathodes [4–7]. In fact, they have been identified as useful procedures for diminishing surface recombination and lowering the kinetic barrier for the transfer of photogenerated electrons from the electrode to the electrolyte, and thus favoring the hydrogen evolution reaction (HER) [8,9].

Extracting layers for *p*-type semiconductors are thin additional layers usually prepared with materials such as Al_2O_3 [10–12] or TiO_2 [13–15] that allow for optimized charge separation at the interface, which finally promote rapid electron transport and transfer to the electrolyte. Sometimes these layers also stabilize the electrode, reducing the phenomena of photocorrosion, and increase the PEC performance with respect to the bare material by suppressing other competitive processes consuming photogenerated electrons. On the other hand, incorporating a co-catalyst (as it is the case of noble metal particles) on the electrode surface is an almost indispensable step to facilitate the transfer of electrons along the photocathode-electrolyte interface as it reduces the energetic requirements for the hydrogen evolution reaction [16–19].

In this study, we present an easy surface modification of pristine and doped $NdFeO_3$ photocathodes based on an optimized combination of these two strategies to improve their PEC activity toward the HER. To this end, a thin TiO_2 extracting layer is firstly deposited on the surface of the $NdFeO_3$ photocathodes through a straightforward sol-gel (drop-casting) route and, then, nickel nanoparticles acting as co-catalysts are further added by means of a potentiostatic electrodeposition procedure. Both synthesis methodologies (drop-casting and electrodeposition) enable us to deposit variable amounts of TiO_2 and Ni in two separate steps on the semiconductor surface by only controlling the volume of TiO_2 precursor solution and Ni electrodeposition time, respectively. The PEC performance under transient illumination of the resulting photocathodes is used to define the optimum loadings of both TiO_2 and Ni on the $NdFeO_3$ surface, that are those which induce the greatest increase in the photoelectrocatalytic activity of our $NdFeO_3/TiO_2$/Ni system.

10.3. RESULTS AND DISCUSSION

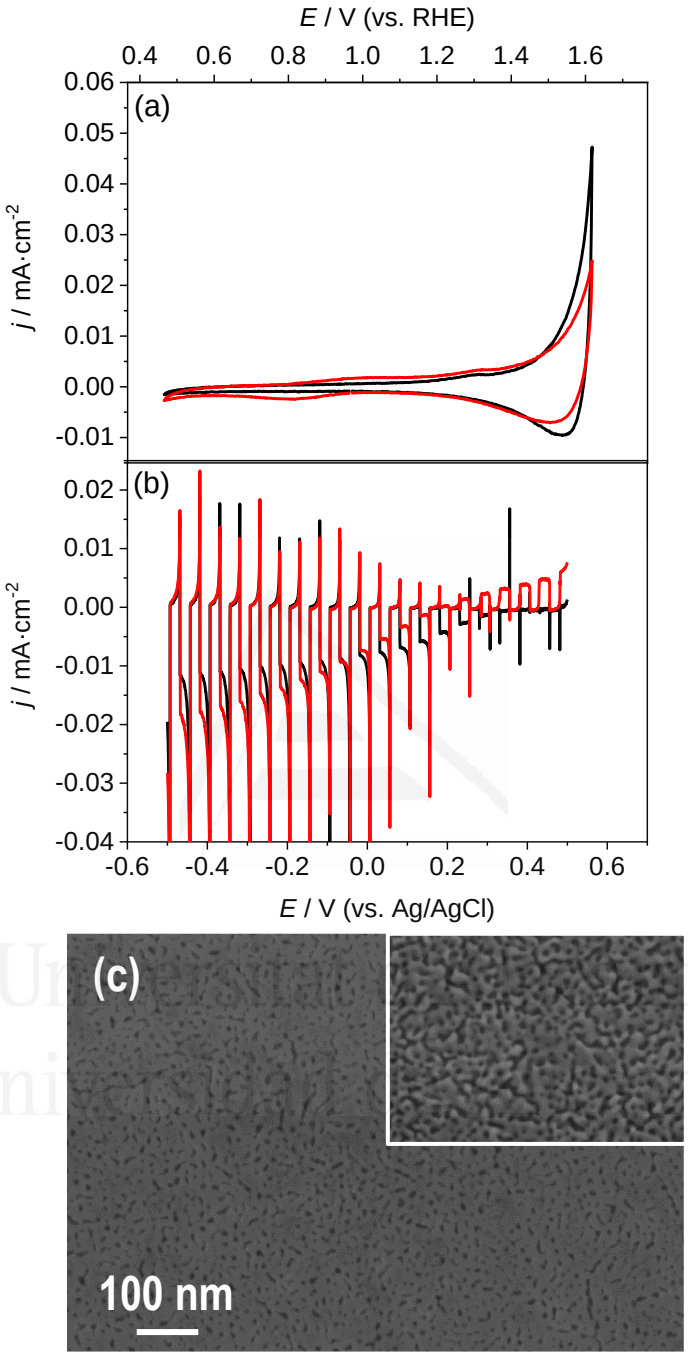

Figure 10.1. (a) Cyclic voltammograms (scan rate: 20 $mV \cdot s^{-1}$) in the dark and (b) linear scan voltammograms (scan rate: 5 $mV \cdot s^{-1}$) under transient illumination for $NdFeO_3$ (black line) and $NdFeO_3/TiO_2$ (red line) photocathodes, prepared for a TiO_2 precursor volume of 10 $\mu L \cdot cm^{-1}$. (c) FESEM image corresponding to a top view of a $NdFeO_3/TiO_2$ photocathode, prepared for an optimum TiO_2 precursor solution volume of 10 $\mu L \cdot cm^{-2}$ (FESEM image corresponding to a bare $NdFeO_3$ film is included as inset).

According to this, the first step is devoted to the optimization of the amount of TiO_2 deposited on the surface of the $NdFeO_3$ photocathode. It was performed by varying the volume of TiO_2 precursor solution (*i.e.*, the TiO_2 deposited amount) deposited by drop-casting onto the photocathode surface and evaluating the corresponding (photo)electrochemical response (Figure S10.1). Figure 10.1a shows the photoelectrochemical characterization under transient illumination for an optimized $NdFeO_3/TiO_2$ photocathode, prepared for a deposited volume of TiO_2 precursor solution of 10 $\mu L \cdot cm^{-2}$. Compared to the unmodified $NdFeO_3$ photocathode, the introduction of the TiO_2 layer induces the development of positive photocurrents at potentials higher than 0.2 V and a subsequent shift of the photo-onset for negative photocurrents of around 0.2 V toward more negative potentials. However, negative photocurrent values remain unaltered below 0.0 V and even increase slightly for increasingly negative potential values. Changes observed in the corresponding voltammetry in the dark (Figure 10.1b) are less significant.

Regarding the optimization of the TiO_2 extracting layer, it is important to consider that both the morphology and thickness of this film play a crucial role in achieving a satisfactory PEC performance. In fact, a clear correlation between the $NdFeO_3$ photocathode PEC activity and the volume of TiO_2 precursor solution deposited on its surface is observed during the optimization process. In this context, we assume that the optimum TiO_2 precursor solution volume (10 $\mu L \cdot cm^{-2}$) induces the growth of a uniform and homogeneous TiO_2 layer that ensures the minor number of defects and maximum contact areas at the $NdFeO_3/TiO_2$ interface, compared to other tested volumes. It thus enhances optimized interfacial charge separation between $NdFeO_3$ and TiO_2, which promotes rapid electron transfer and transport along the TiO_2 extracting layer. On the contrary, for pre-optimum TiO_2 precursor volumes (below 10 $\mu L \cdot cm^{-2}$), the resulting

TiO_2 layer may not be able to completely cover the surface of the photoactive material ($NdFeO_3$), acting mainly as a recombination center since a proper and continuous interface between the two materials is not established. The decrease observed in the *p*-type photoactivity of this $NdFeO_3/TiO_2$ system for post-optimum TiO_2 precursor volumes (12.5 and 15 $\mu L \cdot cm^{-2}$) may be primarily attributed to the fact that an increasingly thicker TiO_2 layer develops an increasingly important characteristic photoelectrochemical response (*n*-type, as observed in this case), which can finally hide and counteract that corresponding to the $NdFeO_3$. Nevertheless, the decrease in conductivity expected for thicker TiO_2 films, able to progressively deteriorate the overall PEC performance due to a sluggish electron transfer, cannot be ruled out.

FESEM characterization of a representative optimized $NdFeO_3/TiO_2$ photocathode (Figure 10.1c) reveals a smoother and much less rough surface compared to the unmodified $NdFeO_3$ film. This observation suggests that the generated TiO_2 layer (whose chemical nature is confirmed by XPS analysis, see Figure S10.2) grows in a conformal manner and homogeneously covering the entire surface of the underlying $NdFeO_3$ film. The same characteristic surface morphology (Figure S10.3) and XPS results (Figure S10.4 and S10.5) are obtained for Mg (5 at%)- and Zn (5 at%)-$NdFeO_3/TiO_2$ photocathodes prepared for the same volume of TiO_2 precursor solution (10 $\mu L \cdot cm^{-2}$, which is assumed as the optimum precursor solution volume), following the same synthesis procedure.

After that, Ni nanoparticles were electrodeposited on the surface of optimum pristine and doped $NdFeO_3/TiO_2$ photocathodes to further improve their photoelectrochemical activity toward the hydrogen evolution reaction. To this end, different Ni electrodeposition times were tested to define an optimum amount of electrodeposited Ni (measured as the charge density associated with the Ni^{2+} reduction

process) on the $NdFeO_3/TiO_2$ photocathodes surface, on the basis of their corresponding photoelectrochemical response. Figure S10.6 shows the electrodeposited charge density as a function of electrodeposition time (between 5 and 30 s) for $NdFeO_3/TiO_2$, Mg (5 at%)-$NdFeO_3/TiO_2$ and Zn (5 at%)-$NdFeO_3/TiO_2$ photocathodes. As expected, the charge associated to the Ni^{2+} reduction process (q_{Ni}) increase for increasing electrodeposition times, and it is equivalent in all cases for equal electrodeposition times. Linear scan voltammograms under transient illumination recorded for these as-prepared photocathodes (Figure S10.7, S10.8 and S10.9) reveal that the magnitude of the photocurrents is clearly Ni electrodeposition time dependent. Interestingly, the effect in photoactivity induced by the presence of Ni does not appear to be homogeneous across the studied potential range. In fact, for short electrodeposition times (up to 10 s), an improvement in the photocurrent values is observed exclusively in the region of the photo-onset of negative currents, almost recovering the photo-onset located around 0.3 V characteristic of the bare $NdFeO_3$, unmodified with TiO_2. For longer times (between 10 and 20 s), this improvement in photo-onset region is maintained and even extended (with greater or lesser intensity) throughout all the range of negative potentials. Finally, for electrodeposition times higher than 20 s, a significant decrease in the magnitude of the photocurrents is observed across all the potential window.

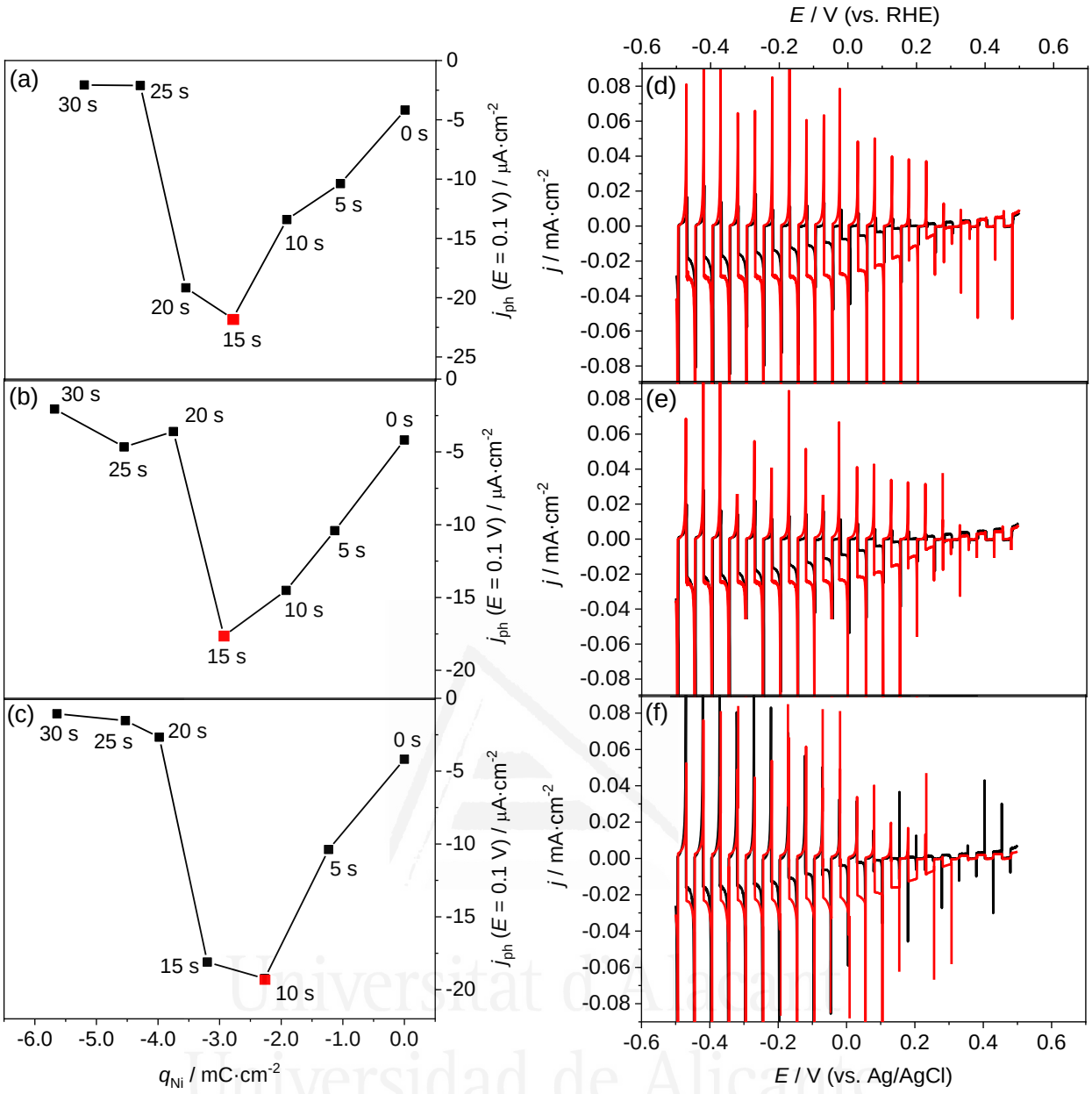

Figure 10.2. Photocurrent density for the hydrogen evolution reaction at 0.1 V for (a) $NdFeO_3/TiO_2/Ni$, (b) Mg (5 at%)-$NdFeO_3/TiO_2/Ni$ and (c) Zn (5 at%)-$NdFeO_3/TiO_2/Ni$ photocathodes, prepared for different Ni electrodeposition times, as a function of the charge density corresponding to the Ni^{2+} reduction process. Linear scan voltammograms (scan rate: 5 mV·s^{-1}) under transient illumination for $NdFeO_3/TiO_2$ (black line) and (d) $NdFeO_3/TiO_2/Ni$, (e) Mg (5 at%)-$NdFeO_3/TiO_2/Ni$ and (f) Zn (5 at%)-$NdFeO_3/TiO_2/Ni$ photocathodes (red line), prepared for the optimum Ni electrodeposition time (red square in panels a, b, and c).

Figure 10.2a-c displays the photocurrent density for the hydrogen evolution reaction at 0.1 V for $NdFeO_3/TiO_2/Ni$, Mg (5 at%)-$NdFeO_3/TiO_2/Ni$ and Zn (5 at%)-

$NdFeO_3/TiO_2$/Ni photocathodes, prepared for different Ni electrodeposition times, as a function of the charge density corresponding to the Ni^{2+} reduction process. As already suggested, photocurrent values progressively increase until a maximum is reached for a Ni electrodeposited charge density of around 3 $mC \cdot cm^{-2}$ (corresponding to electrodeposition times between 10 and 15 s) while, for higher q_{Ni} values, a drastic reduction is observed. Linear scan voltammograms under transient illumination obtained for optimum pristine and doped $NdFeO_3/TiO_2$/Ni photocathodes (those corresponding to the red square in Figure 10.2a-c) are displayed in Figure 10.2d-f. It is important to point out that, in general, the electrodeposition of Ni is accompanied by a significant intensification of the anodic and cathodic spikes upon illumination/light interruption, which is a clear sign of electron-hole recombination. Changes observed in the corresponding voltammetries in the dark (Figure S10.10, S10.11 and S10.12) are less significant, and no voltammetric peaks associated with redox processes undergone by the Ni deposit are observed.

The photoelectrochemical characterization of the as-prepared photocathodes was completed with an impedance study. Figure 10.3 shows Nyquist plots under illumination at 0.1 V for the different photoelectrodes studied. As expected, the introduction of the TiO_2 layer on the surface of the pristine and doped $NdFeO_3$ deposit induces an increase in the impedance values. This is explained on the basis of the shift of the photo-onset towards more positive potentials observed after the introduction of this modification (see above). However, a significant decrease in impedance is observed after the deposition of optimum amounts of Ni on the surface of the $NdFeO_3/TiO_2$ photoelectrodes, which can be associated with the increment in the photocurrent and also with a higher photogenerated electron flow toward the surface to the electrolyte.

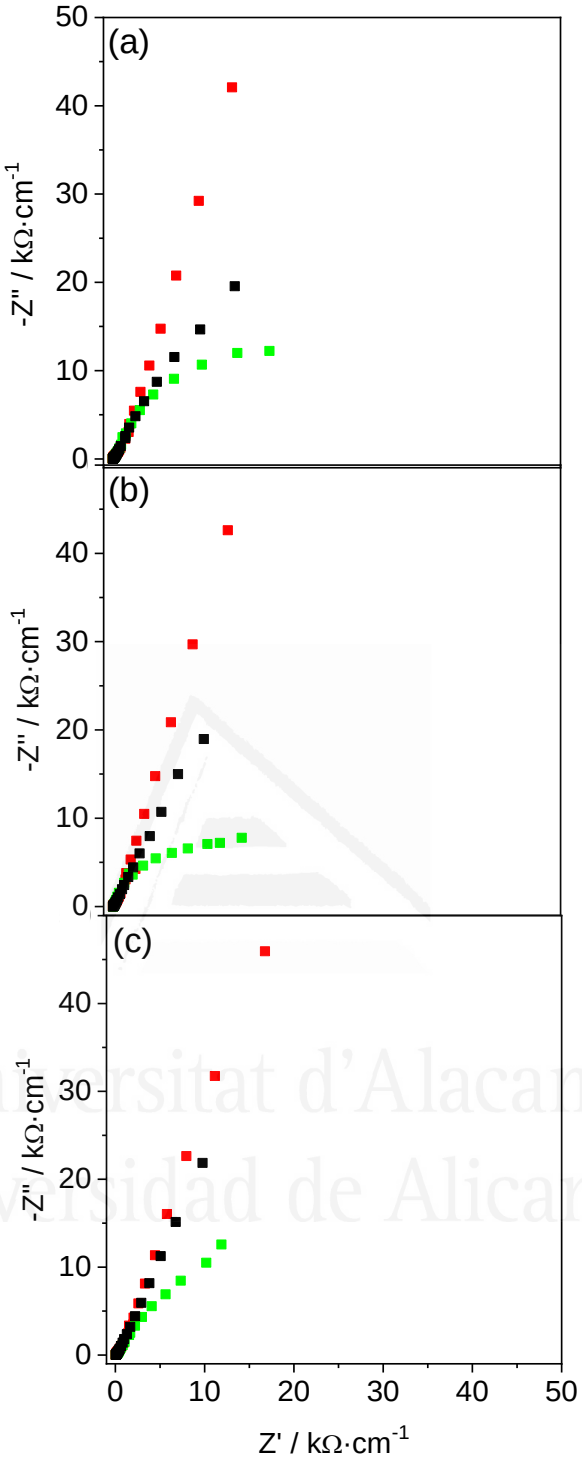

Figure 10.3. Nyquist plots under illumination at 0.1 V for (a) $NdFeO_3$ (b) Mg (5 at%)-$NdFeO_3$ and (c) Zn (5 at%)-$NdFeO_3$ photocathodes (black squares), superficially modified with optimum amounts of TiO_2 ($NdFeO_3/TiO_2$, red squares) and Ni ($NdFeO_3/TiO_2$/Ni, green squares).

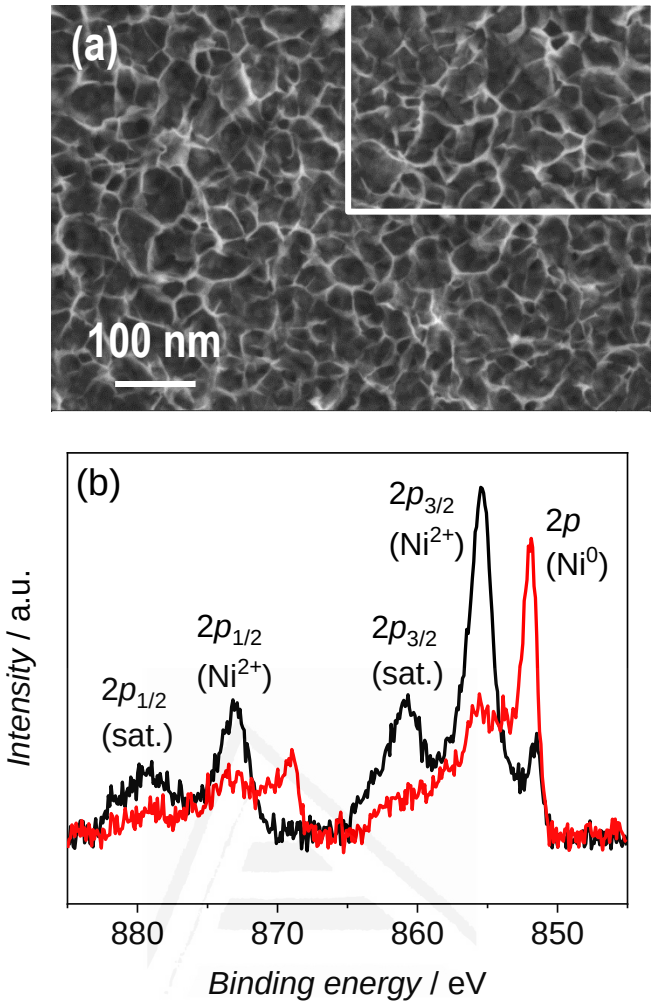

Figure 10.4. (a) FESEM image corresponding to a top view of an optimum $NdFeO_3/TiO_2/Ni$ photocathode prior the photoelectrochemical characterization. Inset: optimum $NdFeO_3/TiO_2/Ni$ photocathode after the photoelectrochemical characterization. (b) Ni 2*p* XPS spectra for an optimum $NdFeO_3/TiO_2/Ni$ photocathode prior (black line) and after (red line) the photoelectrochemical characterization.

Figure 10.4a displays a representative top FESEM image for a $NdFeO_3/TiO_2/Ni$ electrode superficially modified with the optimum amount of Ni (corresponding an electrodeposition time of 15 s) prior and after the (photo)electrochemical characterization. As observed, the electrodeposition procedure induces the appearance of an overstructure homogeneously distributed on the surface of the $NdFeO_3$ film and with an open morphology, corresponding to the Ni deposit. This structure does not undergo significant morphological changes after the (photo)electrochemical characterization. The

corresponding XPS analysis reveals more information about the chemical composition of the Ni electrodeposit prior and after the photoelectrocatalysis (Figure 10.4b). As deposited, the XPS spectrum of Ni 2*p* shows two main peaks with binding energies (BE) of around 855.4 and 873.3 eV, corresponding to the Ni $2p_{3/2}$ and $2p_{1/2}$ transitions, respectively, accompanied by their corresponding satellites at around 860.8 and 879.1 eV. These peaks are attributed to Ni^{2+} in the form of hydroxide ($Ni(OH)_2$) [20,21]. Additionally, a peak located at 851.7 eV indicates the presence of metallic nickel (Ni^0) on the surface of the $NdFeO_3/TiO_2$ electrode [22]. After the photoelectrocatalysis, the XPS results show that the concentration of metallic nickel increases, indicated by an increased metallic Ni peak intensity, and a significant decrease of those corresponding to the Ni $2p_{3/2}$ and $2p_{1/2}$ transitions. This implies that the co-catalyst is deposited mainly in the form of $Ni(OH)_2$ but, as consequence of the application of increasingly negative potentials during the photoelectrochemistry, it is widely reduced to metallic Ni (Ni^0). This is thought to be the actual species responsible for co-catalysis explaining the increase in photocurrent values.

According to the Ni co-catalyst amount optimization results, the surface density of Ni particles for an optimum PEC performance is estimated to be around $8.73 \cdot 10^{15}$, $9.17 \cdot 10^{15}$ and $6.96 \cdot 10^{15}$ Ni atoms/cm^2 for $NdFeO_3/TiO_2$/Ni, Mg (5 at%)-$NdFeO_3/TiO_2$/Ni and Zn (5 at%)-$NdFeO_3/TiO_2$/Ni photocathodes, respectively. In terms of equivalent Ni monolayers (ML, as defined in previous studies [23]) is around 4.7, 4.9 and 3.7 ML, respectively. This estimation is done by considering that the pristine and doped $NdFeO_3/TiO_2$ photocathode surface is perfectly flat and that the deposition of this Ni deposit occurs according to an ordered layer-by-layer regime. However, given FESEM images for the $NdFeO_3/TiO_2$ (Figure 10.1c) and $NdFeO_3/TiO_2$/Ni (Figure 10.4a) deposits, it is evident that both premises are not met in this case, so the actual coverage that would

be calculated on the basis of the real photocathode surface area would be significantly smaller. In any case, the photocurrent values achieved with optimized $NdFeO_3/TiO_2$/Ni, Mg (5 at%)-$NdFeO_3/TiO_2$/Ni and Zn (5 at%)-$NdFeO_3/TiO_2$/Ni photocathodes clearly reveal that the deposition of Ni nanoparticles on the surface of the $NdFeO_3/TiO_2$ structure importantly boosts the photoactivity of the system (especially near the photo-onset region, between 0.3 and 0.0 V), as they act as co-catalysts.

Metallic nickel and Ni-based compounds (such as NiO or $Ni(OH)_2$) have been described as active and low-cost co-catalysts in PEC hydrogen generation applications [[24,25]]. Although to the best of our knowledge there are no precedents in the case of ternary oxide photocathodes, their effectiveness seems to be proved especially in the case of *p*-Cu_2O photocathodes. In this context, Somasundaram *et al.* [26] reported a simple photodeposition method of Ni on Cu_2O that increased the photocurrent for the hydrogen evolution reaction in the presence of a sacrificial hole acceptor, but without the application of a bias potential. Another work, presented by Lin *et al*. [27], showed how the deposition of NiO_x on Cu_2O improves the photoelectrocatalysis and the stability of Cu_2O. More recently, an applied bias photo-to-current efficiency (ABPE) of 2.7% has been reached for a Cu_2O/CuO photocathode surface decorated with Ni [28]. To explain the improvement in the PEC performance due to the loading of such a surface co-catalyst, these studies refer us to the fact that they facilitate the transfer of photogenerated electrons through the semiconductor/electrolyte interface, reducing the energy barrier for the hydrogen evolution reaction. In fact, transition metals (as, in this case, Ni) have been traditionally used as highly active electrocatalysts for the HER in the dark, since they act not only as electron sinks, but also provide effective proton reduction sites [29,30]. In principle, the larger the work function (that is, the lower the Fermi level), the more facile trapping of electrons. In this way, under illumination, the photogenerated electrons can

be transferred to the metal co-catalyst and subsequently to the electrolyte, lowering the kinetic requirements for H_2 production under illumination.

However, the photocurrent evolution observed in the corresponding Ni optimization step for the three different types of studied electrodes is obviously Ni electrodeposition-time dependent: in all cases, a progressive photocurrent grow is observed until optimum q_{Ni} values of around 2.2-2.9 $mC \cdot cm^{-2}$ are achieved, followed by a sudden and significant decrease for higher Ni charge densities. It can then be assumed that for pre-optimum and optimum coverages (submonolayer and a few monolayers coverage situation), the characteristic open morphology of this Ni electrodeposit enables that a high fraction of nickel atoms is directly exposed to solution and also in close contact with the $NdFeO_3/TiO_2$ substrate. This facilitates a quickly and effective exchange of photogenerated electrons with the electrolyte, promoting its role as co-catalyst. The drastic decrease in the activity observed for post-optimum deposited amounts is mainly explained according to the fact that, as a result of the increase in the amount of electrodeposited Ni, an increasing fraction of these Ni atoms would be less effective (or even inactive) for promoting the HER as they are not in direct contact with the electrolyte. In spite of the presumably good electrical conductivity of the nickel deposit (which allows to achieve a situation of optimal photocurrent for relatively high coverages of electrodeposited co-catalyst), the metallic deposit finally becomes a recombination center. This is also evidenced by intense cathodic and anodic spikes upon illumination/light interruption in the linear scan voltammograms under transient illumination.

In any case, the photocurrent values achieved at 0.1 V for our optimized $NdFeO_3/TiO_2$/Ni, Mg (5 at%)-$NdFeO_3/TiO_2$/Ni and Zn (5 at%)-$NdFeO_3/TiO_2$/Ni photoelectrodes represent an enhancement in photocurrent by factors of 5.8, 4.8 and 5.2

compared to corresponding $NdFeO_3/TiO_2$ photocathodes. It is interesting to note that, although the introduction of the TiO_2 layer induces an apparent worsening in the photoelectrochemical properties of the $NdFeO_3$ electrode, it is a necessary step before the introduction of the Ni co-catalyst. In fact, the deposition of equivalent Ni deposit amounts directly on the surface of $NdFeO_3$, Mg (5 at%)-$NdFeO_3$ and Zn (5 at%)-$NdFeO_3$ does not result in a photoelectrochemical improvement of the electrode (results not shown). This suggests that the role played by the TiO_2 layer as an electron extractor and charge transferor between the $NdFeO_3$ film and the nickel deposit is essential for a successful coupling of a photocathode and a co-catalyst. Finally, it is interesting to highlight the unexpected fact that similar results in terms of photocurrent magnitude are obtained for all $NdFeO_3$ electrodes, whether or not doped with Mg or Zn. A previous study on pristine and Mg- and Zn-doped $NdFeO_3$ photocathodes reveals that this doping procedure induces a significant improvement in the $NdFeO_3$ PEC performance in the presence of an electron scavenger as O_2, which suggests an improvement in the electrical properties at the bulk level [31]. However, this effect does not seem to be relevant when trying to further improve the photoelectrocatalytic activity of the $NdFeO_3$ material through a surface engineering procedure like the one tested in this work.

10.4. CONCLUSIONS

In summary, here we present a straightforward procedure to modify the surface of a photocathode to obtain an optimized PEC response. To this end, a TiO_2 extracting layer has been deposited on pristine and doped $NdFeO_3$ photocathodes by means of simple drop-casting procedure, followed by the electrodeposition of controlled amounts of Ni nanoparticles, acting as co-catalysts for the hydrogen evolution reaction under illumination. Optimum coverages of Ni deposit enabling an optimum PEC performance

have been estimated to be around 4.7, 4.9 and 3.7 ML for $NdFeO_3/TiO_2$/Ni, Mg (5 at%)-$NdFeO_3/TiO_2$/Ni and Zn (5 at%)-$NdFeO_3/TiO_2$/Ni photocathodes, respectively, which represent significant photocurrent enhancements by factors of 5.8, 4.8 and 5.2. Although our optimum results may seem modest in terms of absolute photocurrent values (below 30 $\mu A \cdot cm^{-2}$), they show that the preparation of efficient photocathodes for hydrogen evolution without the use of sophisticated synthesis techniques (as ALD or PLD, normally required for the synthesis of the extraction layers) and co-catalysts based on noble metals (such as Pt), is possible.

10.5. ACKNOWLEDGEMENTS

Financial support of the Spanish Ministry of Economy and Competitiveness through project MAT2015–71727–R (FONDOS FEDER) is gratefully acknowledged. J. Q. thanks to the Spanish Ministry of Education, Culture and Sport (MECD) for the award of an FPU predoctoral grant (FPU15/02005).

10.6. REFERENCES

[1] W. Yang, R.R. Prabhakar, J. Tan, S.D. Tilley, J. Moon, Chem. Soc. Rev. 48 (2019) 4979.
[2] X. Li, X. Hao, A. Abudula, G. Guan, J. Mater. Chem. A. 4 (2016) 11973.
[3] N. Mahmood, Y. Yao, J.W. Zhang, L. Pan, X. Zhang, J.J. Zou, Adv. Sci. 5 (2018) 1700464.
[4] B. Koo, S. Byun, S.W. Nam, S.Y. Moon, S. Kim, J.Y. Park, B.T. Ahn, B. Shin, Adv. Funct. Mater. 28 (2018) 1.
[5] C.G. Morales-Guio, S.D. Tilley, H. Vrubel, M. Graẗzel, X. Hu, Nat. Commun. 5 (2014) 1.
[6] J. Tan, W. Yang, Y. Oh, H. Lee, J. Park, R. Boppella, J. Kim, J. Moon, Adv. Energy Mater. 9 (2019) 1970053.
[7] W. Vijselaar, R.M. Tiggelaar, H. Gardeniers, J. Huskens, ACS Energy Lett. 3 (2018) 1086.
[8] J. Mohammed-Ibrahim, S. Xiaoming, J. Energy Chem. 34 (2019) 111.
[9] Y. Yan, B.Y. Xia, B. Zhao, X. Wang, J. Mater. Chem. A. 4 (2016) 17587.
[10] H. Kim, H. Bae, S.W. Bang, S. Kim, S.H. Lee, S.-W. Ryu, J.-S. Ha, Opt. Express. 27 (2019) A206.
[11] H. Xing, E. Lie, D. Zhao, X. Li, M. Ruan, Z. Liu, Chem. Commun. 55 (2019)

15093.
[12] M.J. Park, J.Y. Jung, Y.H. Nam, J.W. Song, C. Jeong, J.H. Lee, Thin Solid Films. 616 (2016) 550.
[13] S. Li, P. Zhang, X. Song, L. Gao, ACS Appl. Mater. Interfaces. 7 (2015) 18560.
[14] Y. Lin, R. Kapadia, J. Yang, M. Zheng, K. Chen, M. Hettick, X. Yin, C. Battaglia, I.D. Sharp, J.W. Ager, A. Javey, J. Phys. Chem. C. 119 (2015) 2308.
[15] B. Seger, T. Pedersen, A.B. Laursen, P.C.K. Vesborg, O. Hansen, I. Chorkendorff, J. Am. Chem. Soc. 135 (2013) 1057.
[16] H. Qi, J. Wolfe, D. Fichou, Z. Chen, Sci. Rep. 6 (2016) 4.
[17] Y. Hou, B.L. Abrams, P.C.K. Vesborg, M.E. Björketun, K. Herbst, L. Bech, A.M. Setti, C.D. Damsgaard, T. Pedersen, O. Hansen, J. Rossmeisl, S. Dahl, J.K. Nørskov, I. Chorkendorff, Nat. Mater. 10 (2011) 434.
[18] M. Basu, Z.W. Zhang, C.J. Chen, P.T. Chen, K.C. Yang, C.G. Ma, C.C. Lin, S.-F. Hu, R.-S. Liu, Angew. Chemie-Int. Ed. 54 (2015) 6211.
[19] C. Yang, P.D. Tran, P.P. Boix, P.S. Bassi, N. Yantara, L.H. Wong, J. Barber, Nanoscale. 6 (2014) 6506.
[20] J. Quiñonero, R. Gómez, Appl. Catal. B Environ. 217 (2017) 437.
[21] D. Cibrev, M. Jankulovska, T. Lana-Villarreal, R. Gómez, Int. J. Hydrogen Energy. 38 (2013) 2746.
[22] A.M. Hengne, A.K. Samal, L.R. Enakonda, M. Harb, L.E. Gevers, D.H. Anjum, M.N. Hedhili, Y. Saih, K.-W. Huang, J.-M. Basset, ACS Omega. 3 (2018) 3688.
[23] C. Schmidthals, D. Sander, A. Enders, J. Kirschner, Surf. Sci. 417 (1998) 361.
[24] T. Sreethawong, Y. Suzuki, S. Yoshikawa, Int. J. Hydrogen Energy. 30 (2005) 1053.
[25] J.S. Jang, S.H. Choi, D.H. Kim, J.W. Jang, K.S. Lee, J.S. Lee, J. Phys. Chem. C. 113 (2009) 8990.
[26] K.R. Sashikala Somasundaram, C. Raman Nair Chenthamarakshan, Norma R. de Tacconi, Int. J. Hydrogen Energy. 32 (2007) 4661.
[27] C.Y. Lin, Y.H. Lai, D. Mersch, E. Reisner, Chem. Sci. 3 (2012) 3482.
[28] A.A. Dubale, C.J. Pan, A.G. Tamirat, H.M. Chen, W.N. Su, C.H. Chen, J. Rickm D.W. Ayele, B.A. Aragaw, J-F. Lee, Y.-W. Yang, B.-J. Hwang, J. Mater. Chem. A. 3 (2015) 12482.
[29] S. Trasatti, J. Electroanal. Chem. 39 (1972) 163.
[30] A.R. Zeradjanin, J.P. Grote, G. Polymeros, K.J.J. Mayrhofer, Electroanalysis. 28 (2016) 2256.
[31] J. Quiñonero, F.J. Pastor, J.M. Orts, R. Gómez, *Photoelectrochemical behavior and computational inights of $NdFeO_3$ thin film photocathodes*, submitted for its publication to ChemSusChem.

10.7. SUPPORTING INFORMATION

10.7.1. Experimental methods

10.7.1.1. Preparation of $NdFeO_3$ photocathodes

$NdFeO_3$ thin film photocathodes were prepared on fluorine-doped tin oxide (TEC 15, 12-15 Ω/□, Pilkington) by a procedure based on a previously reported citric sol-gel route [S1]. The $NdFeO_3$ precursor solution was prepared by dissolving $Nd(NO_3)_3 \cdot 6H_2O$ (Aldrich Chemistry, 99%) 0.3 M and $Fe(NO_3)_2 \cdot 9H_2O$ (Panreac, 98%) 0.3 M in water (Millipore, Elix 3). This solution was magnetically stirred for 1 hour and, then, the appropriate amount of citric acid (Merck, 99.5%) was added to the mentioned solution until a concentration of 0.6 M was reached, and it was stirred again for 20 hours. After that, 30 $\mu L \cdot mL^{-2}$ of acetylacetone (Fluka Analytical, 99.5%) and 30 $\mu L \cdot mL^{-1}$ of Triton® X-100 (laboratory grade, Sigma-Aldrich) were added. Then, 40 µL of the resulting solution was dropped onto an FTO glass plate (to cover an area of $1cm^2$), previously cleaned by 15-min sonication (Selecta Ultrasonics) in acetone (VWR Chemicals, 99%) and ethanol (VWR Chemicals, 96%), and spread over it at a spin rate of 1500 rpm for 20 s with a spin-coater (Chemat Technology, KW–4A). Finally, the electrodes were annealed in air at 500ºC for 1 hour using a programmable furnace (Conatec, 7800), with a heating rate of $5ºC \cdot min^{-1}$. This process was repeated four times to obtain the optimum film thickness before a final annealing at 640ºC for 2 hours was applied to obtain the crystalline perovskite films.

10.7.1.2. Preparation of doped $NdFeO_3$ photocathodes

Mg (5 at%)- and Zn (5 at%)-doped $NdFeO_3$ thin film photocathodes were synthesized following the same procedure described above, but incorporating the corresponding doping element in the $NdFeO_3$ precursor solution at the desired

concentration (in at% with respect to Fe content). In this case, $Mg(NO_3)_2 \cdot 6H_2O$ (VWR Chemicals, 99.4%) and $Zn(NO_3)_2 \cdot 6H_2O$ (Fluka, 99.0%) were employed as Mg and Zn precursors, respectively.

10.7.1.3. TiO_2 deposition on pristine and doped $NdFeO_3$ photocathodes

TiO_2 was deposited on pristine and doped $NdFeO_3$ photocathodes by means of a drop-casting procedure. The deposition solution was prepared by dissolving $Ti(OCH(CH_3)_2)_4$ (Aldrich Chemistry, 97%) 36 mM in 2-propanol (Sigma-Aldrich, 99.5%). This solution was diluted 10 times with the same solvent. Then, 10 μL of the resulting solution was dropped onto a pristine or doped $NdFeO_3$ photocathode (such a volume is to cover an area of 1 cm^2, see Figure S10.1 for optimization details). After deposition, the solvent was allowed to dry naturally, and the resulting films were annealed at 330ºC in air for 1 h (heating rate: $5ºC \cdot min^{-1}$).

10.7.1.4. Ni surface deposition on pristine and doped $NdFeO_3/TiO_2$ photocathodes

Ni was deposited on pristine and doped $NdFeO_3/TiO_2$ photocathodes following a potentiostatic electrodeposition procedure [S2]. This was performed at -1.0 V (*vs.* Ag/AgCl) in an acetate buffer solution 0.1 M (pH = 4.0) containing $Ni(NO_3)_2 \cdot 6H_2O$ (Fluka, 97%) 1 mM for different deposition times (from 5 to 30 s), using the $NdFeO_3/TiO_2$ photocathode as working electrode. A Ag/AgCl/KCl(3 M) electrode and a Pt wire were used as reference and counter electrode, respectively.

10.7.1.5. Physical and (photo)electrochemical electrode characterization

A SEM study was carried out to characterize the surface morphology of the different prepared films using a ZEISS Merlin VP Compact field emission scanning

electron microscope (FESEM). For the compositional characterization of the TiO_2 and Ni deposits on the $NdFeO_3$ photocathodes, XPS experiments were performed with a Thermo-Scientific K-Alpha XPS spectrometer equipped with a monochromatic Al-Kα source (1486.6 eV), operating at 15 kV and 10 mA.

All the (photo)electrochemical characterization was carried out at room temperature in a home-made Pyrex glass cell with a fused silica window and a computer-controlled potentiostat-galvanostat (Autolab, PGSTAT30) employing a Ag/AgCl/KCl(3 M) electrode and a Pt wire as reference and counter electrode, respectively. All the potentials in the text are referred to this Ag/AgCl electrode unless otherwise stated. An N_2-purged NaOH (Labkem, 98%) 0.1 M solution was used as the working electrolyte for the (photo)electrochemical measurements. The light source was an ozone-free 1000 W Xe(Hg) lamp (Newport Instruments, 66921) equipped with a water filter to minimize the infrared contribution of the beam. Impedance measurements (30 points) were performed using a 10 mV amplitude perturbation at 0.1 V (*vs.* Ag/AgCl). In all cases, the electrodes were illuminated from the front-side (electrolyte-electrode illumination). The photon flux intensity was measured by means of a photodiode power meter (Thorlabs, PM100D), and the typical value was approximately 100 $mW \cdot cm^{-2}$.

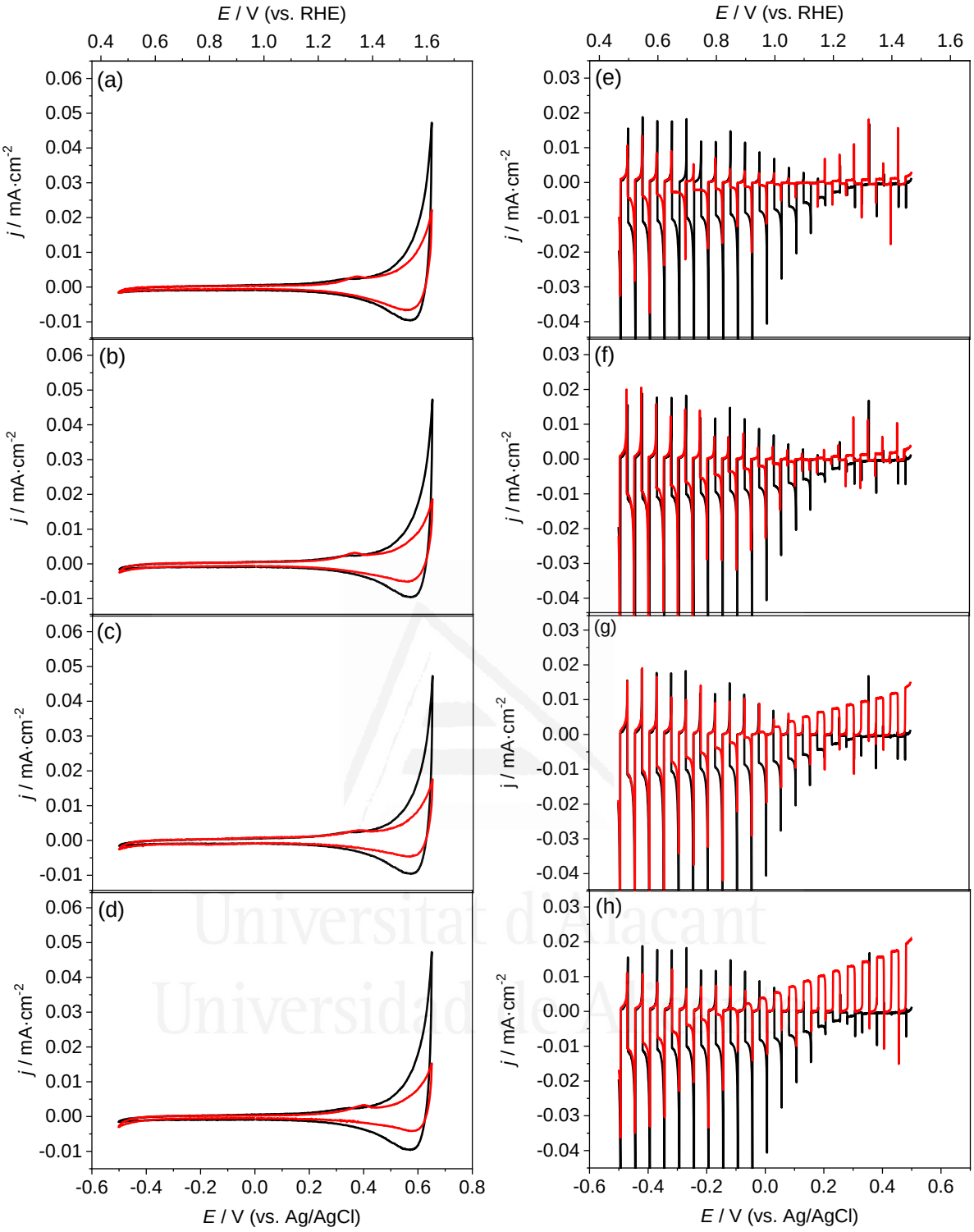

Figure S10.1. (a-d) Cyclic voltammograms (scan rate: 20 $mV \cdot s^{-1}$) in the dark and (e-h) linear scan voltammograms (scan rate: 5 $mV \cdot s^{-1}$) under transient illumination for $NdFeO_3$ (black line) and $NdFeO_3/TiO_2$ (red line) photocathodes, prepared for TiO_2 precursor volumes of (a, e) 5 $\mu L \cdot cm^{-1}$, (b, f) 7.5 $\mu L \cdot cm^{-1}$, (c, g) 12.5 $\mu L \cdot cm^{-1}$, and (d, h) 15 $\mu L \cdot cm^{-1}$.

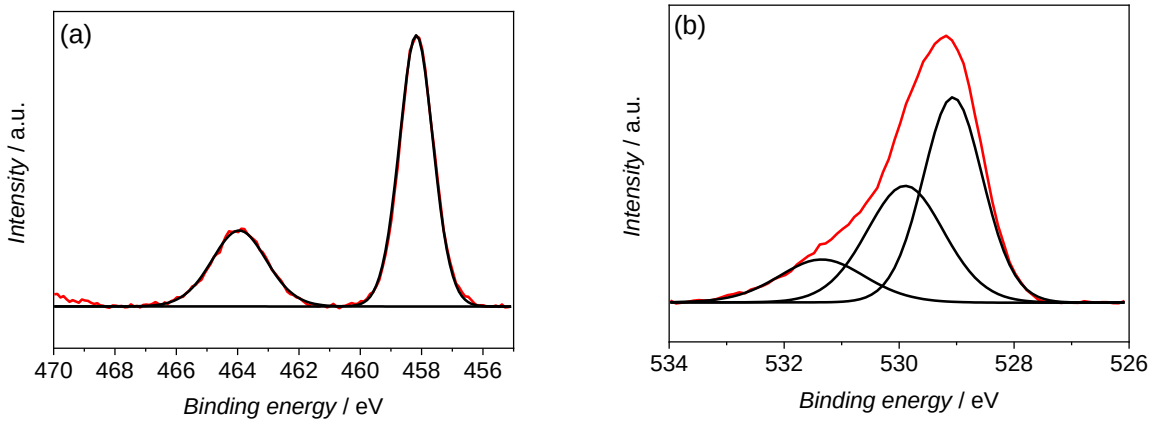

Figure S10.2. (a) Ti 2*p* and (b) O 1*s* XPS spectra (red line) and corresponding deconvolutions (black lines) for a $NdFeO_3/TiO_2$ photocathode, prepared for an optimum TiO_2 precursor solution volume of 10 $\mu L \cdot cm^{-2}$.

The corresponding Ti 2*p* XPS spectrum (Figure S10.2a) shows two main peaks with binding energies (BE) of around 458.2 and 463.9 eV, corresponding to the Ti $2p_{3/2}$ and $2p_{1/2}$ transitions, respectively. These BE values are those typical for the Ti^{2+} in the form of TiO_2 [S3,S4].

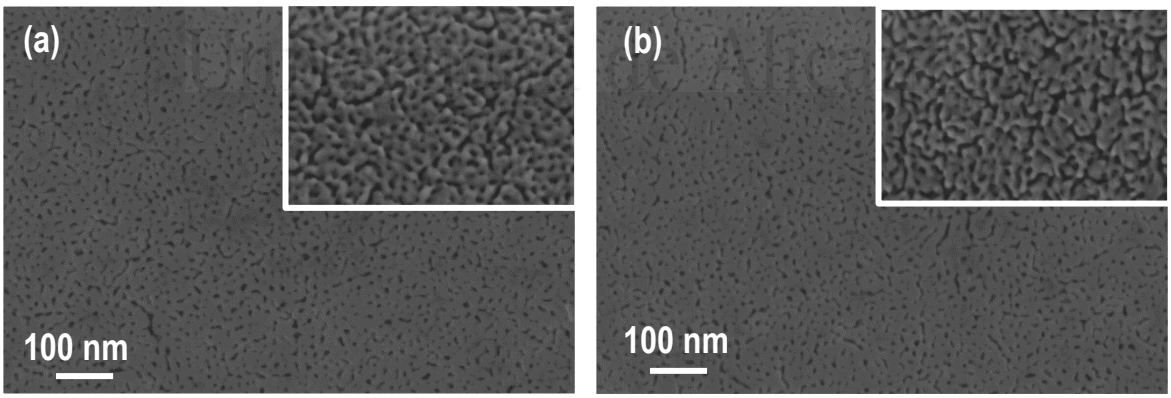

Figure S10.3. FESEM images corresponding to top views of (a) Mg (5 at%)-$NdFeO_3/TiO_2$ and (b) Zn (5 at%)-$NdFeO_3/TiO_2$ photocathodes, prepared for an optimum TiO_2 precursor solution volume of 10 $\mu L \cdot cm^{-2}$ (FESEM image corresponding to bare Mg (5 at%)-$NdFeO_3$ and Zn (5 at%)-$NdFeO_3$ are included as insets).

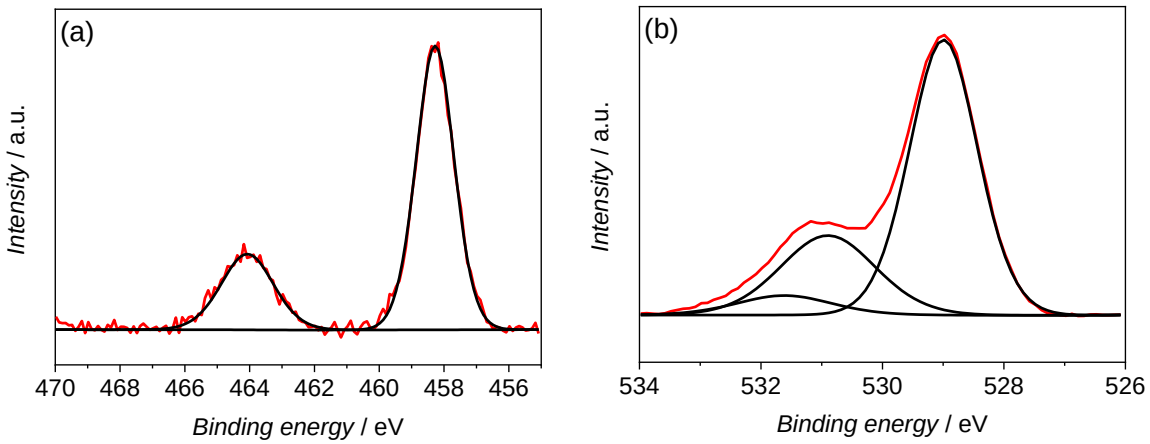

Figure S10.4. (a) Ti 2*p* and (b) O 1*s* XPS spectra (red line) and corresponding deconvolutions (black lines) for a Mg (5 at%).$NdFeO_3/TiO_2$ photocathode, prepared for an optimum TiO_2 precursor solution volume of 10 $\mu L \cdot cm^{-2}$.

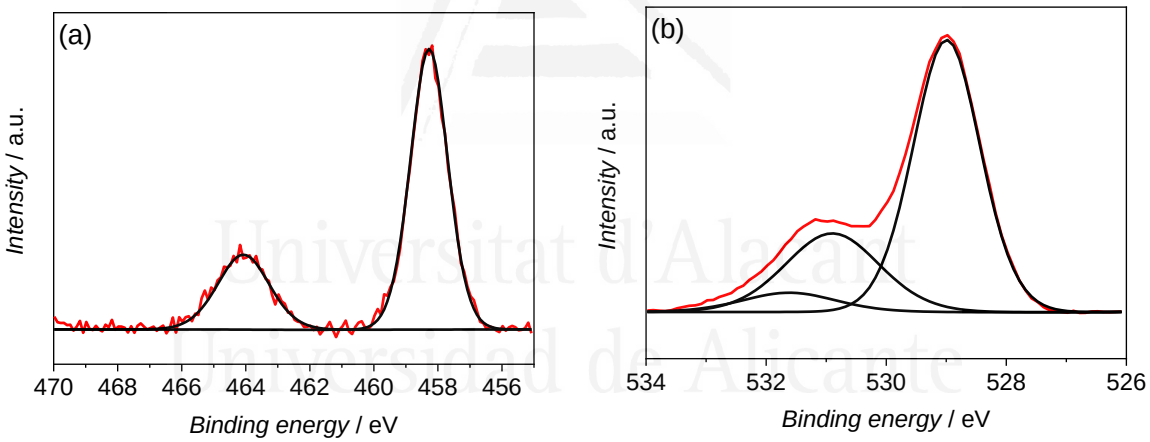

Figure S10.5. (a) Ti 2*p* and (b) O 1*s* XPS spectra (red line) and corresponding deconvolutions (black lines) for a Zn (5 at%).$NdFeO_3/TiO_2$ photocathode, prepared for an optimum TiO_2 precursor solution volume of 10 $\mu L \cdot cm^{-2}$.

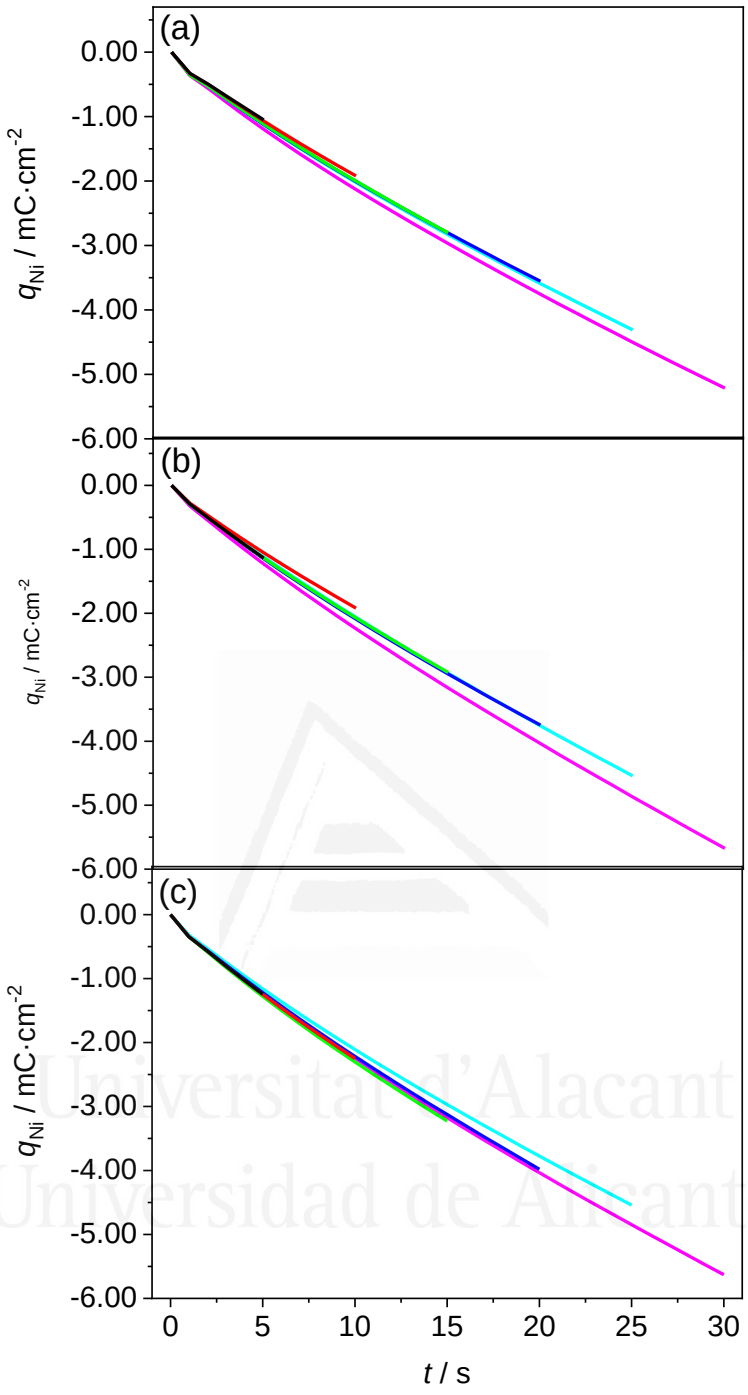

Figure S10.6. Charge density associated to the Ni^{2+} reduction process *vs.* Ni electrodeposition time, for (a) $NdFeO_3/TiO_2$, (b) Mg (5 at%)-$NdFeO_3/TiO_2$ and (c) Zn (5 at%)-$NdFeO_3/TiO_2$ photocathodes.

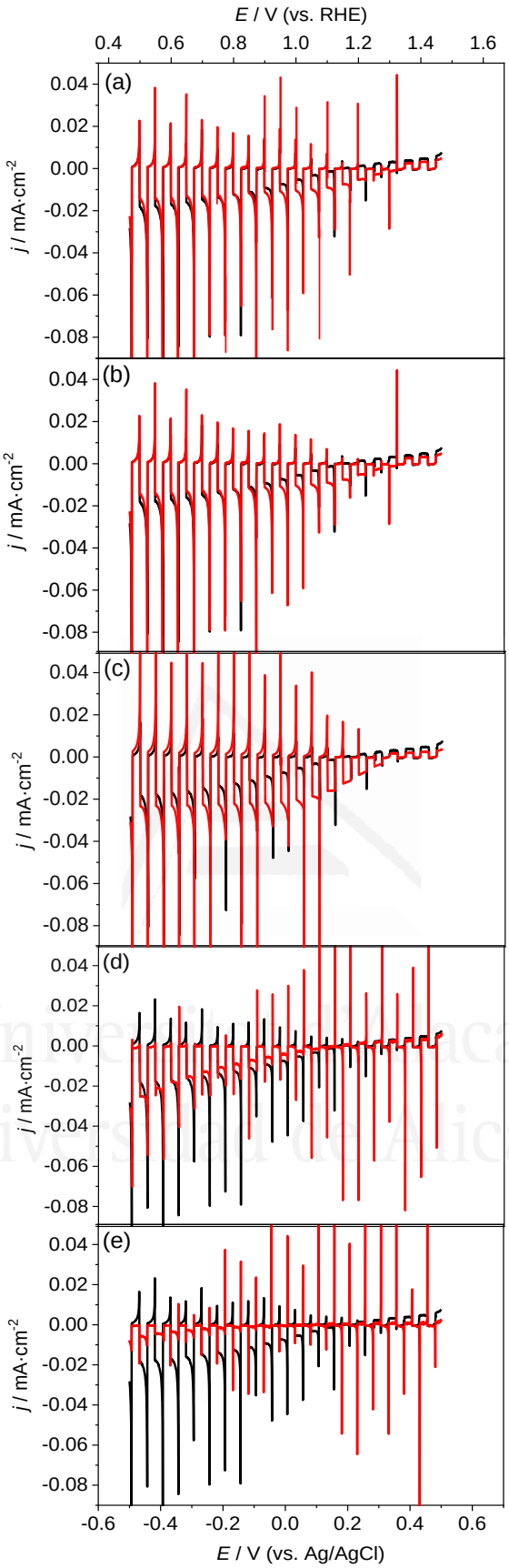

Figure S10.7. Linear scan voltammograms (scan rate: 5 $mV \cdot s^{-1}$) under transient illumination for $NdFeO_3/TiO_2$ (black line) and $NdFeO_3/TiO_2$/Ni (red line) photocathodes, prepared for Ni electrodeposition times of (a) 5 s, (b) 10 s, (c) 20 s, (d) 25 s, and (e) 30 s.

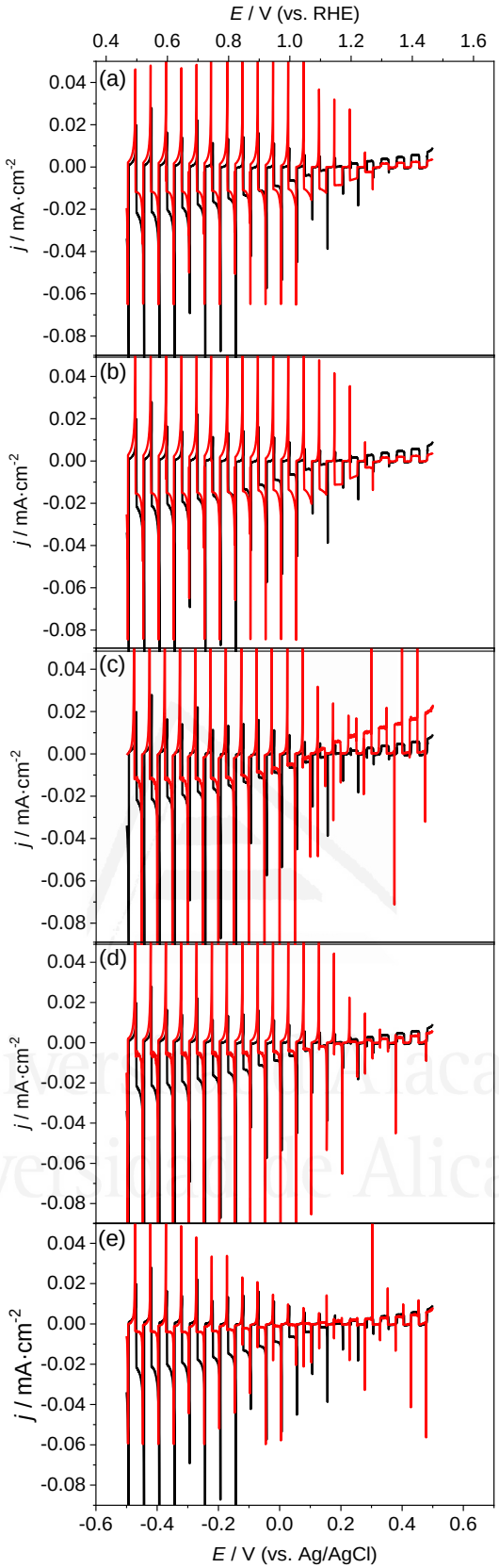

Figure S10.8. Linear scan voltammograms (scan rate: 5 $mV \cdot s^{-1}$) under transient illumination for Mg (5 at%)-$NdFeO_3/TiO_2$ (black line) and Mg (5 at%)-$NdFeO_3/TiO_2$/Ni (red line) photocathodes, prepared for Ni electrodeposition times of (a) 5 s, (b) 10 s, (c) 20 s, (d) 25 s, and (e) 30 s.

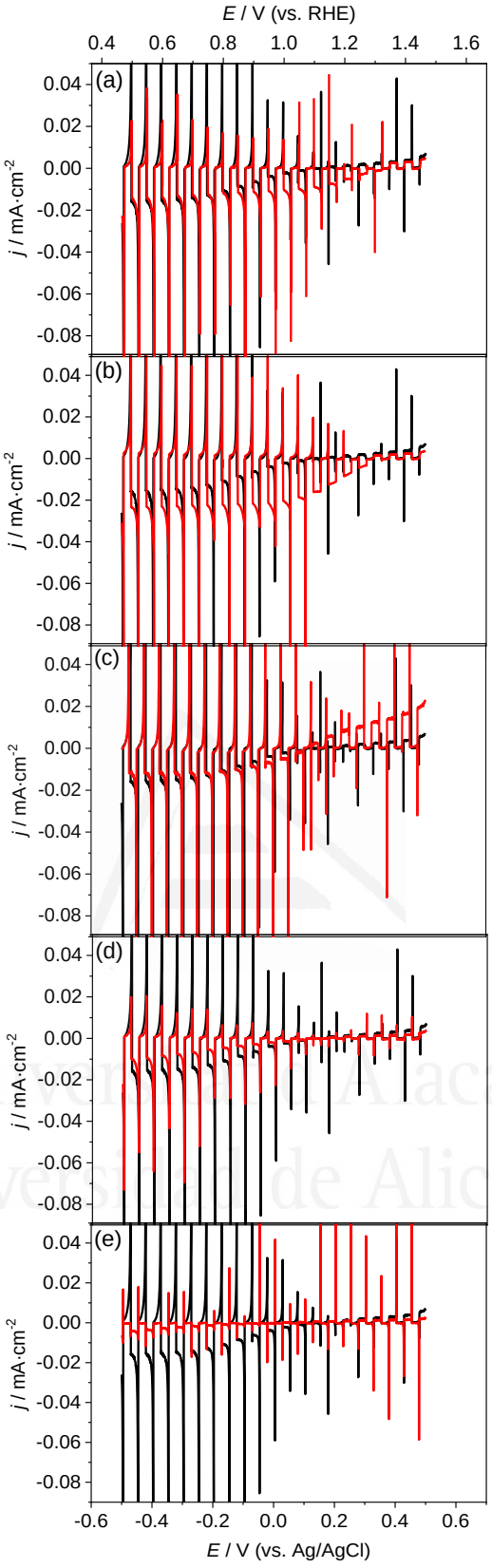

Figure S10.9. Linear scan voltammograms (scan rate: 5 $mV \cdot s^{-1}$) under transient illumination for Zn (5 at%)-$NdFeO_3/TiO_2$ (black line) and Zn (5 at%)-$NdFeO_3/TiO_2$/Ni (red line) photocathodes, prepared for Ni electrodeposition times of (a) 5 s, (b) 15 s, (c) 20 s, (d) 25 s, and (e) 30 s.

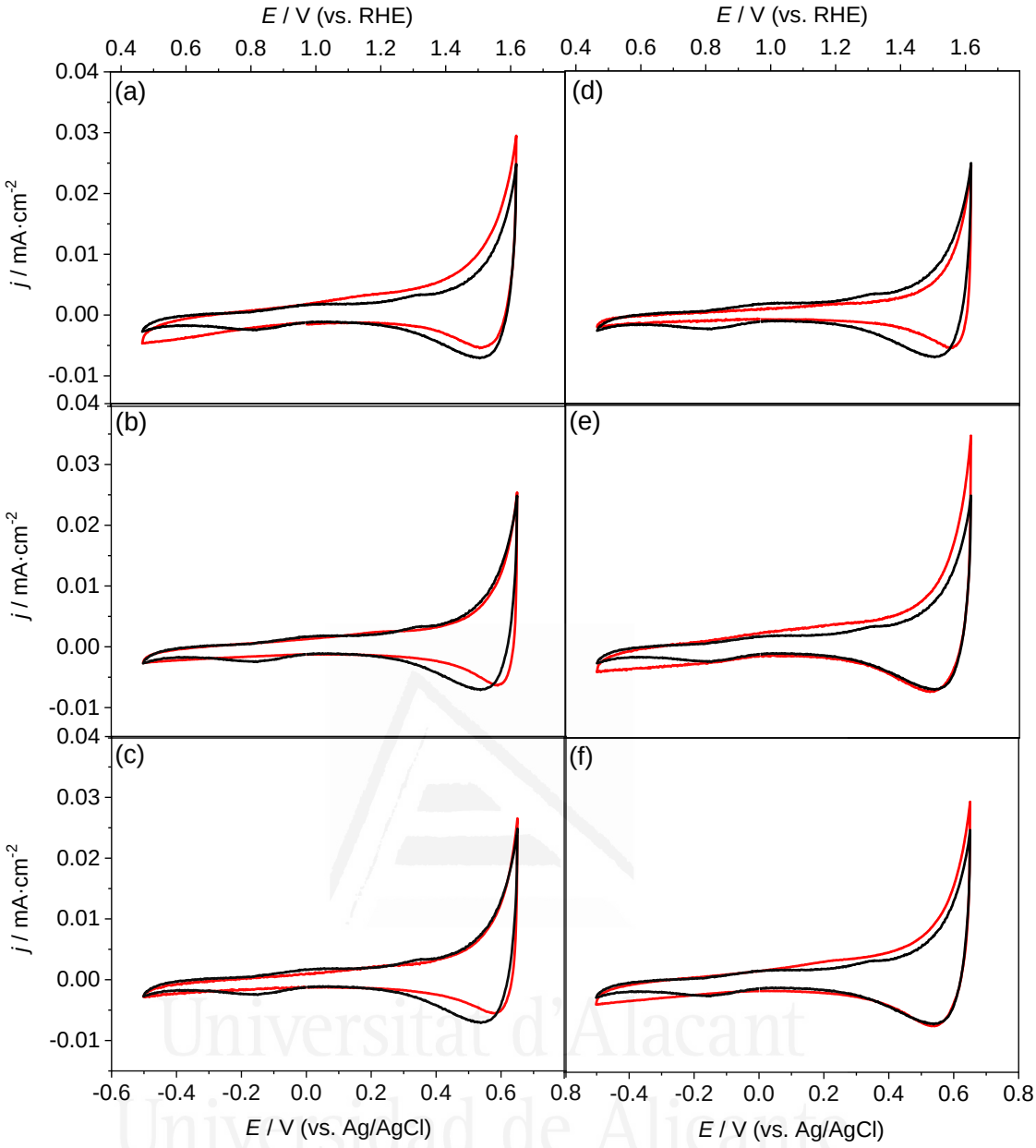

Figure S10.10. Cyclic voltammograms (scan rate: 20 $mV \cdot s^{-1}$) in the dark for $NdFeO_3/TiO_2$ (black line) and $NdFeO_3/TiO_2$/Ni (red line) photocathodes, prepared for Ni electrodeposition times of (a) 5 s, (b) 15 s, (c) 15 s, (d) 20 s, (e) 25 s, and (f) 30 s.

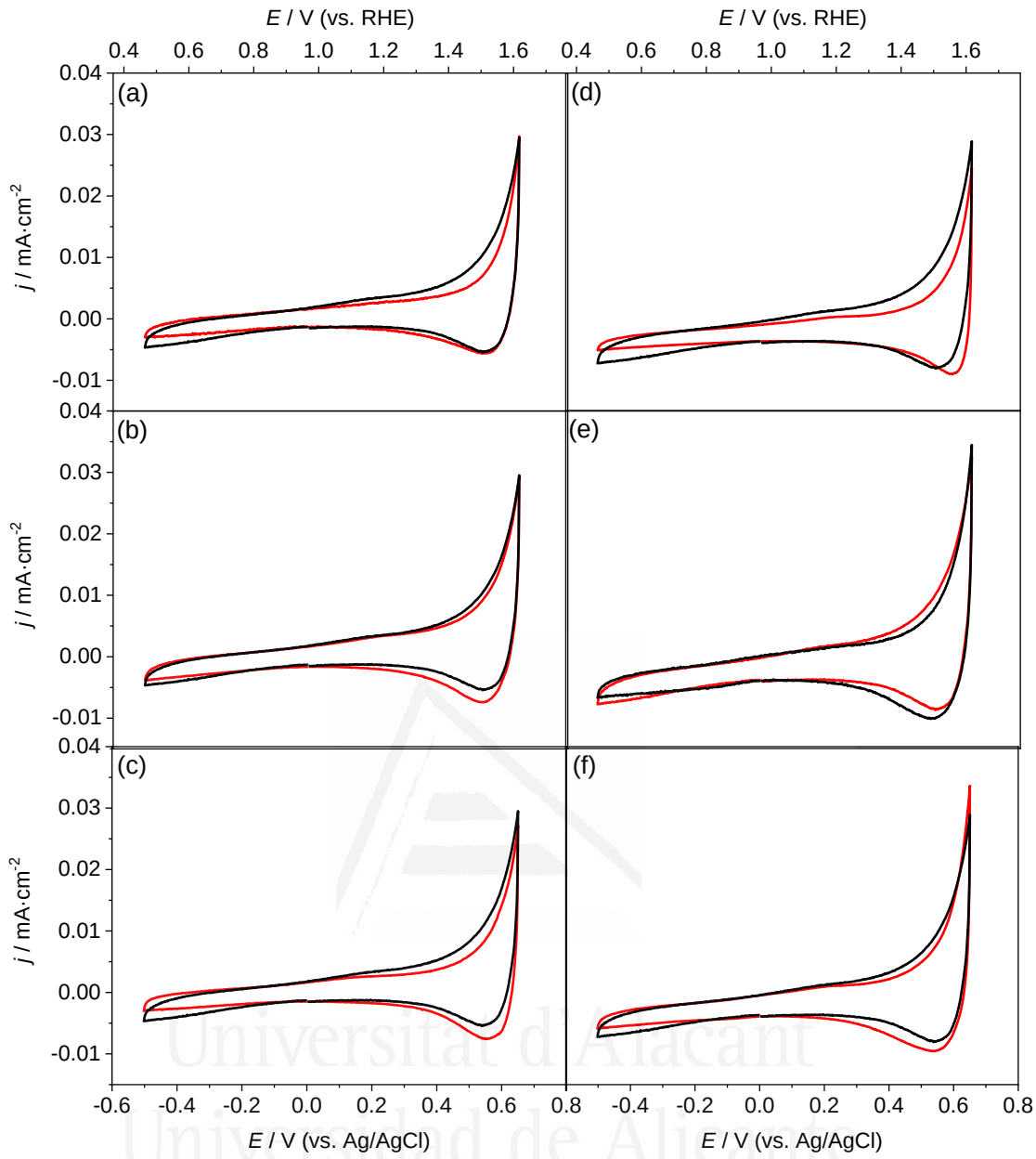

Figure S10.11. Cyclic voltammograms (scan rate: 20 $mV \cdot s^{-1}$) in the dark for Mg (5 at%)-$NdFeO_3/TiO_2$ (black line) and Mg (5 at%)-$NdFeO_3/TiO_2$/Ni (red line) photocathodes, prepared for Ni electrodeposition times of (a) 5 s, (b) 15 s, (c) 15 s, (d) 20 s, (e) 25 s, and (f) 30 s.

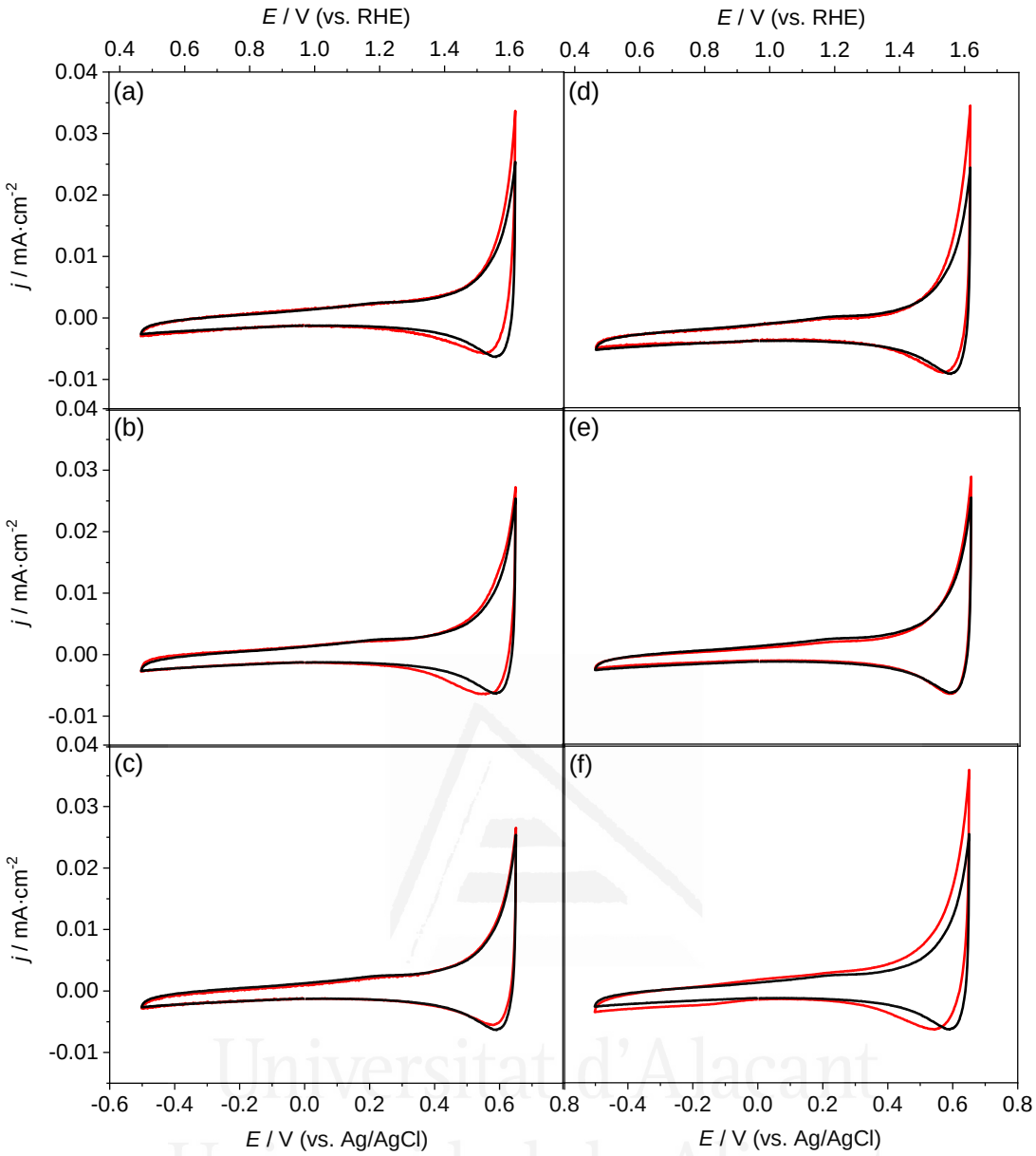

Figure S10.12. Cyclic voltammograms (scan rate: 20 $mV \cdot s^{-1}$) in the dark for Zn (5 at%)-$NdFeO_3/TiO_2$ (black line) and Zn (5 at%)-$NdFeO_3/TiO_2$/Ni (red line) photocathodes, prepared for Ni electrodeposition times of (a) 5 s, (b) 15 s, (c) 15 s, (d) 20 s, (e) 25 s, and (f) 30 s.

10.7.2. References

[S1] J. Quiñonero, F.J. Pastor, J.M. Orts, R. Gómez, *Photoelectrochemical behavior and computational inights of $NdFeO_3$ thin film photocathodes*, submitted for its publication to ChemSusChem.

[S2] A.M. Ghonim, M.M. Saleh, Int. J. Electrochem. Sci. 11 (2016) 621.

[S3] D. Nassoko, Y.F. Li, J.L. Li, X. Li, Y. Yu, Int. J. Photoenergy. 2012 (2012) 716087.

[S4] L. Zhu, Q. Lu, L. Lv, Y. Wang, Y. Hu, Z. Deng, Z. Lou, Y. Hou, F. Teng, RSC Adv. 7 (2017) 20084.

CHAPTER XI

Conclusions

The general conclusions that can be drawn from this doctoral thesis are the following:

i) Doping is an effective strategy to improve the photoelectrochemical properties of both photoanodes and photocathodes. Impurity doping achieved by wet methods induces an increase in the density of one of the electric charge carriers (electrons or holes) as demonstrated by Mott-Schottky plots.

ii) Surface engineering of photoelectrodes –understood as their surface modification with deposits acting as co-catalysts– is a suitable strategy to enhance the photoelectrochemical behavior toward the oxygen and hydrogen evolution reactions.

iii) Iron-group hydroxides ($Ni(OH)_2$, $Fe(OH)_2$, and $Co(OH)_2$), both individually or conveniently combined, act as co-catalysts for the oxygen evolution reaction under illumination on vanadate photoanodes.

iv) The proper combination of a passivating/extracting TiO_2 layer with Ni deposits acting as co-catalysts constitutes a strategy to enhance the photoactivity of $NdFeO_3$ photocathodes toward the hydrogen evolution reaction under illumination.

v) The co-catalyst loading deposited on the photoelectrode surface is a key factor crucially determining its efficiency, which illustrates the need for a careful control of the amount deposited.

vi) Chemical bath deposition and electrodeposition are synthesis methods that allow for a straightforward and fine control of the co-catalyst loading by changing the deposition time.

vii) Electrochemical methods (such as cyclic voltammetry and linear scan voltammetry) stand out as useful techniques for monitoring the co-catalyst loading on the surface of the photoelectrodes, and to characterize their photoelectrochemical activity as a function of such a loading.

The specific conclusions extracted from this doctoral thesis are the following:

i) $BiVO_4$ and $FeVO_4$ thin film electrodes prepared by a layer-by-layer coating on FTO substrates according to a modified metal-organic precursor decomposition method, followed by a heat treatment, behave as efficient photoanodes for water oxidation. Subsequent $BiVO_4$ doping with La (1 at%) and Ce (2 at%) increases the photocurrent associated to water photooxidation and triggers a shift of the $BiVO_4$ flat band potential toward more negative values. This is due to an increase in the majority charge carrier concentration, resulting in enhanced electron conductivity of the $BiVO_4$, and to a passivation of surface states linked to electron–hole recombination. In addition, both pristine and doped $BiVO_4$ photoanodes can be surface modified with gold nanoparticles, which act as co-catalysts, inducing a further enhancement of the electrode photoactivity.

ii) Ultrathin $Ni(OH)_2$ layers have been deposited on pristine and doped $BiVO_4$ as well as on pristine $FeVO_4$ photoanodes by means of a urea-based chemical bath deposition method that allows for a straightforward and fine control of the quantity of deposited co-catalyst. The photoelectrochemical behavior of vanadate photoanodes surface-modified with $Ni(OH)_2$ is dependent on the $Ni(OH)_2$ loading, which, in turn, depends on the $Ni(OH)_2$ deposition time.

iii) When the amount of $Ni(OH)_2$ over the vanadate photoanode surface is low (coverages equivalent to one monolayer and lower), most of the deposited nickel atoms act as active co-catalytic centers for hole transfer to solution as they should be distributed in monolayer islands and directly exposed to the electrolyte. However, thicker $Ni(OH)_2$ layers, obtained for longer deposition times, induce a drastic decrease in the electrocatalytic activity since an increasing number of deposited Ni atoms would not act as active catalytic centers but as recombination centers, as they are not in direct contact with the electrolyte.

iv) Ultrathin $Fe(OH)_2$ and α-$Co(OH)_2$ films have been deposited on FTO substrates by means of a chemical bath deposition method, which constitutes a novel procedure to synthesize $Fe(OH)_2$ and $Co(OH)_2$ electrocatalysts in the form of thin films. The same procedure enables the preparation of electrocatalysts based on $Fe(OH)_2$-$Ni(OH)_2$ and $Fe(OH)_2$-$Co(OH)_2$ mixed deposits. In this regard, a structure based on $Fe(OH)_2$ nanoparticles directly grown on FTO and exposed to solution, surface modified with submonolayers of $Ni(OH)_2$ or $Co(OH)_2$ deposits, exhibits the best electrocatalytic response for the OER (in terms of turnover frequency for O_2 evolution). In fact, for all the electrodes, TOF increases drastically as active hydroxide loading decreases because the amount of hydroxide in direct contact with both substrate and solution is maximum.

v) The $Fe(OH)_2$/$Ni(OH)_2$ co-catalyst has been deposited on $BiVO_4$ photoanodes by means of a urea-based chemical bath deposition method that allows for a straightforward and fine control of the deposited quantity of the two different hydroxides by only controlling deposition times. For optimum $Fe(OH)_2$ and $Ni(OH)_2$ loadings, the iron hydroxide underlayer is shown to drastically enhance the efficiency of the $Ni(OH)_2$ co-catalysts, which illustrates the importance of a precise control of the amount of co-catalyst deposited on the photoelectrode surface to obtain an optimized PEC response.

vi) $LaFeO_3$ nanorod array-type electrodes prepared for the first time by a chemical bath deposition and a sol-gel-based synthesis procedure on FTO substrates, followed by a heat treatment, behave as photoanodes for water oxidation. Further combination of oxygen defect engineering and surface passivation with $NiFeO_x$ sets a new benchmark performance among $LaFeO_3$ photoanodes for solar water oxidation due to a synergistic activation of the reactive interface by reducing the overpotential for the oxygen evolution reaction and surface recombination. However, the existence of significant photogenerated carrier losses at

ultrashort timescales, a weak space-charge field and a small diffusion length limits the photoelectrochemical response.

vii) $NdFeO_3$ thin film electrodes prepared by layer-by-layer coatings on FTO substrates by a citrate-route sol-gel method, followed by a heat treatment, behave as photocathodes for oxygen and water reduction in alkaline media. Subsequent $NdFeO_3$ doping with Mg and Zn (5 at% for both cations) induces an increase in the photocurrent associated to the oxygen reduction reaction mainly attributed to an increase in the majority charge carrier density and, to a lesser extent, to a surface passivation phenomenon. DFT calculations confirm the *p*-semiconducting character of this material and a very flat conduction band, indicating a low electron mobility.

viii) The deposition of a TiO_2 extracting layer on pristine and doped $NdFeO_3$ photocathodes by means of drop-casting, followed by the electrodeposition of controlled amounts of Ni nanoparticles, acting as co-catalysts for the hydrogen evolution reaction under illumination, induces significant photocurrent enhancements for this reaction. The photoelectrochemical behavior of surface modified $NdFeO_3$ is dependent on the amount of deposited TiO_2 and Ni, which, in turn, depends on both the TiO_2 precursor solution volume and Ni deposition time.

Resumen

La presente tesis doctoral ha sido desarrollada en el Departamento de Química Física de la Universidad de Alicante y pretende profundizar en la síntesis de materiales semiconductores y de co-catalizadores, y en el estudio de sus aplicaciones en procedimientos fotoelectroquímicos conducentes a dispositivos que realicen la fotosíntesis artificial. En concreto, se pretende diseñar fotoelectrodos que permitan la fotodisociación del agua prestando una atención particular al uso de determinados co-catalizadores que funcionen sobre la superficie de dichos fotoelectrodos y que incrementen la velocidad de los procesos redox de generación de hidrógeno y de oxígeno.

La radiación solar aporta a nuestro planeta unos 120000 TW de energía cada año, una cantidad que es superior al consumo tecnológico realizado por el hombre en cuatro órdenes de magnitud. Por tanto, y debido a la creciente demanda de energía a nivel mundial, resulta interesante la idea de intentar abordar la problemática energética actual desde el punto de vista de la conversión y acumulación fotoquímicas de energía solar. Esta estrategia permitiría solucionar, además, los graves problemas medioambientales causados por el consumo de combustibles fósiles, que continúan siendo la fuente mayoritaria de energía en la actualidad.

En este contexto, el hidrógeno supone una de las alternativas a los combustibles fósiles más prometedoras y sostenibles. De hecho, como combustible, el hidrógeno destaca por su alta densidad energética y porque su combustión no libera compuestos de carbono perjudiciales para el medio ambiente. En un escenario en el que los métodos tradicionales para obtener hidrógeno puro se enfrentan a grandes desafíos, el agua se presenta como una fuente ideal de dicho gas, abundante y libre de los dañinos gases de efecto invernadero que de otra forma surgen como subproductos. La fotoelectrólisis del agua sobre electrodos semiconductores, que consiste en dividir dicha molécula en sus componentes (oxígeno e

hidrógeno) requiere la aplicación de electricidad desde una fuente externa y el uso de electrocatalizadores adecuados para romper los enlaces químicos. El primer estudio sobre este tema fue publicado por Fujishima y Honda en el año 1972, quienes describieron una célula fotoelectroquímica para la disociación del agua en oxígeno e hidrógeno constituida por un fotoánodo de dióxido de titanio y un contraelectrodo de platino:

$$H_2O_{(l)} \rightarrow H_{2\,(g)} + \tfrac{1}{2}\, O_{2\,(g)} \qquad \Delta G^0_{298\,K} = 237\ \text{kJ} \cdot \text{mol}^{-1}$$

Sin embargo, todavía no se ha conseguido desarrollar un sistema fotoelectroquímico de estas características que ofrezca eficiencias y estabilidad realmente competitivas. La elección y desarrollo de materiales electródicos fotoactivos (fotoánodo y fotocátodo) es una de las variables que condicionan de manera determinante ambos factores. Entre las características principales que deben cumplir los materiales semiconductores para actuar como fotoánodos o fotocátodos destacan las siguientes: (i) transporte eficiente de carga eléctrica, (ii) posición favorable de las bandas de valencia y conducción para inducir las reacciones de reducción y oxidación del agua, (iii) buena absorción de la luz visible (lo que implica un valor de anchura de banda prohibida de entre 1.9 y 3.1 eV), (iv) elevada estabilidad química tanto en medio acuoso como bajo condiciones de iluminación, con el fin de asegurar una larga vida útil de los dispositivos, y (v) bajo coste económico.

Aunque los óxidos semiconductores son los materiales más prometedores dentro de este ámbito, todavía no se ha identificado ningún material semiconductor que cumpla con todos estos requisitos con el que se pueda llevar a cabo la fotodisociación del agua de manera eficiente: muchos tienen una anchura de banda prohibida demasiado grande o muy pequeña o son inestables en medios acuosos. Entre las diferentes estrategias encaminadas a conseguir aumentar la eficiencia de los procesos de generación de oxígeno y de hidrógeno sobre

electrodos semiconductores, destaca su modificación superficial con partículas de electrocatalizador (conocidas como co-catalizadores) que sirvan para mejorar la transferencia de portadores de carga fotogenerados y limitar su recombinación, y disminuir los sobrepotenciales para las reacciones de generación de oxígeno e hidrógeno.

De hecho, para facilitar una reacción eficaz, dichos co-catalizadores deben poseer una alta durabilidad, una elevada actividad catalítica y una gran área superficial. El platino es muy eficiente para la electrocatálisis, pero su elevadísimo precio (superior a los 30.000 dólares por kilogramo) y su poca abundancia hace inviable su uso comercial a gran escala. Por todo ello, surge la necesidad de explorar nuevas vías más factibles que permitan llevar a cabo la electrocatálisis de estos procesos redox y que, en base a las últimas investigaciones realizadas, pueden pasar por ciertos hidróxidos metálicos, nitruros, fosfuros, sulfuros y carburos de determinados elementos de transición.

En este contexto, los principales objetivos de la presente tesis doctoral son los siguientes:

- Sintetizar diferentes electrodos semiconductores nanocristalinos o policristalinos compactos de óxidos ternarios de la familia ABO_4 y de la familia perovskita (ABO_3) mediante técnicas de síntesis por sol-gel, para su uso posterior como fotoánodos o fotocátodos en procesos de disociación fotoelectroquímica del agua.

- Caracterizar desde el punto de vista electroquímico y fotoelectroquímico los diferentes fotoelectrodos sintetizados para evaluar su actividad como fotoánodos o fotocátodos en procesos de disociación fotoelectroquímica del agua.

- Sintetizar diferentes hidróxidos metálicos del grupo del hierro (Fe, Co y Ni) mediante una técnica de síntesis por baño químico, para su uso posterior como electrocatalizadores

para la reacción de generación de oxígeno en medio alcalino y como co-catalizadores de la reacción fotoelectroquímica de generación de oxígeno sobre los fotoánodos obtenidos.

- Caracterizar desde el punto de vista electroquímico y fotoelectroquímico los diferentes hidróxidos metálicos preparados para evaluar su actividad como electrocatalizadores para la reacción de generación de oxígeno en medio alcalino y como co-catalizadores de la reacción fotoelectroquímica de generación de oxígeno sobre los fotoánodos obtenidos con el fin de mejorar las propiedades fotoelectroquímicas de los mismos y potenciar así su aplicabilidad en procesos de disociación fotoelectroquímica del agua.

- Sintetizar partículas metálicas (fundamentalmente, de Ni), mediante una técnica de síntesis por electrodepósito, que puedan ser empleadas como co-catalizadores de la reacción fotoelectroquímica de generación de hidrógeno sobre los fotocátodos obtenidos con el fin de mejorar las propiedades fotoelectroquímicas de los mismos y potenciar así su aplicabilidad en células de fotosíntesis artificial. También se contempla la posibilidad de generar una capa pasivante/extractora de TiO_2 entre la superficie del fotocátodo y el depósito de co-catalizador que favorezca la actividad de este.

- Caracterizar los fotoelectrodos y los electrocatalizadores preparados estructural, composicional y morfológicamente mediante técnicas de difracción de rayos X, técnicas espectroscópicas (espectroscopía de absorción ultravioleta-visible, espectroscopía fotoelectrónica de rayos X y espectroscopía Raman), y técnicas de microscopía (microscopía electrónica de barrido y de transmisión).

El desarrollo de estos objetivos, los resultados correspondientes y las conclusiones obtenidas se exponen en detalle en once capítulos relacionados. El Capítulo I consiste en una introducción donde se presentan los principios físicos y electroquímicos básicos de los

semiconductores y se presenta el estado del arte de los diferentes materiales utilizados a lo largo de esta tesis. En el Capítulo II se revisan las diferentes técnicas de síntesis y caracterización empleadas en esta investigación. Los Capítulos III a X están específicamente dedicados al desarrollo de los objetivos antes mencionados relacionados con la preparación y caracterización de fotoelectrodos, electrocatalizadores y co-catalizadores. Es importante señalar que los Capítulos III a VI se han publicado en revistas indexadas, mientras que los resultados mostrados en los Capítulos VII a X ya se han enviado o se enviarán para su publicación en un futuro próximo. Finalmente, en el Capítulo XI se recogen las conclusiones generales y específicas de esta tesis.

Capítulo I. Introducción.

En el Capítulo I se revisa, en primer lugar, el contexto general con respecto al desafío energético y medioambiental actual donde se puede ubicar esta tesis doctoral. La demanda de energía en continuo crecimiento, junto con los graves problemas ambientales derivados de la emisión excesiva de gases contaminantes procedentes de la combustión de combustibles fósiles, han motivado la búsqueda de fuentes de energía sostenibles y ecológicas.

Dado que el hidrógeno ha sido identificado como uno de los vectores energéticos más prometedores, las nuevas metodologías basadas en la fotosíntesis artificial sobre electrodos semiconductores para generar hidrógeno solar han recibido mucha atención durante las últimas décadas. En tanto que la búsqueda y optimización de materiales semiconductores que actúan como absorbentes de luz es un elemento clave en el desarrollo de dispositivos fotoelectroquímicos eficientes, en este Capítulo I se presenta una revisión de las principales propiedades físicas y electroquímicas de los dichos materiales.

En este sentido, también se describen las principales características, propiedades y avances recientes realizados en el campo de los óxidos semiconductores ternarios utilizados en esta tesis, tanto como fotoánodos ($BiVO_4$, $FeVO_4$ y $LaFeO_3$) y como fotocátodos ($NdFeO_3$). Finalmente, y con respecto al uso de co-catalizadores en fotoelectrodos como una estrategia para mejorar su rendimiento, se exponen los puntos principales del uso de hidróxidos metálicos del grupo hierro ($Fe(OH)_2$, $Co(OH)_2$ y $Ni(OH)_2$) y partículas metálicas (Ni) para tal fin y también como electrocatalizadores.

Capítulo II. Métodos experimentales.

En el Capítulo II se presentan en detalle los principales procedimientos experimentales y las técnicas de caracterización estructural, morfológica, composicional y (foto)electroquímica empleadas en el contexto de estas tesis.

Primero, se describen brevemente los métodos de síntesis para la preparación de los fotoelectrodos semiconductores y los electrocatalizadores y co-catalizadores estudiados en los siguientes capítulos. En este sentido, es importante resaltar que los materiales fotoelectródicos se han preparado mediante un procedimiento de síntesis sol-gel, mientras que los procedimientos de depósito por baño químico y por electrodepósito se han utilizado para la síntesis de electrocatalizadores y co-catalizadores.

Después, se presentan las configuraciones experimentales (principalmente, células (foto)electroquímicas y fuentes de iluminación) utilizadas para la caracterización (foto)electroquímica de los materiales preparados, incluyendo las células de tres electrodos utilizadas en estos estudios. Finalmente, se exponen los fundamentos y características de las técnicas (foto)electroquímicas (voltametría cíclica, voltametría lineal de barrido, cronoamperometría y espectroscopía de impedancia electroquímica), espectroscópicas (UV-

vis, XPS y Raman), técnicas de difracción (XRD) y microscópicas (SEM y TEM) y de los métodos computacionales empleados en estos estudios.

Capítulo III. Mejora de la fotoactividad de fotoánodos de capa fina de vanadato de bismuto a través de estrategias de dopado y modificación de la superficie.

El Capítulo III está referido a la preparación de fotoánodos de vanadato de bismuto (dopado y sin dopar) y a la descripción de su comportamiento fotoelectroquímico para la reacción de fotooxidación del agua.

De hecho, entre los óxidos semiconductores ternarios, el vanadato de bismuto se ha convertido recientemente en un prometedor fotoánodo. Por ello, se han sintetizado fotoánodos de capa fina de $BiVO_4$ mediante un método basado en la descomposición de precursores organometálicos, seguido de un tratamiento térmico. Con el fin de mejorar las propiedades fotocatalíticas de este material semiconductor para la oxidación fotoelectroquímica del agua, los electrodos preparados se han modificado (i) mediante dopado con La y Ce, modificando la composición de la disolución precursora de $BiVO_4$ con la concentración deseada de elemento dopante, y (ii) mediante la modificación de su superficie con nanopartículas de Au sintetizadas mediante electrodepósito potenciostático. El dopado con La y Ce en concentraciones de 1 y 2 at% en la disolución precursora de $BiVO_4$, respectivamente, mejora significativamente el rendimiento fotoelectrocatalítico de $BiVO_4$ sin introducir cambios importantes ni en la estructura ni en la morfología del material, según la caracterización de XRD y SEM. Además, la modificación de la superficie de los fotoelectrodos con nanopartículas de Au produce un aumento todavía mayor de la fotocorriente ya que tales nanopartículas metálicas actúan como co-catalizadores, fomentando la transferencia de carga a lo largo de la interfase semiconductor/electrolito.

Estas dos formas diferentes pero complementarias de modificar los fotoelectrodos de $BiVO_4$ han resultado en un aumento significativo de la fotorrespuesta, facilitando por tanto su potencial aplicación en dispositivos de fotosíntesis artificial.

Capítulo IV. La cantidad de co-catalizador como factor crítico que determina la eficiencia de los fotoelectrodos: el caso del hidróxido de níquel (II) sobre fotoánodos de vanadato.

El Capítulo IV está dedicado a la modificación de la superficie de fotoánodos de vanadato ($BiVO_4$ y $FeVO_4$) con cantidades controladas de $Ni(OH)_2$, que actúa como co-catalizador. De hecho, una estrategia comúnmente seguida para mejorar el rendimiento de los fotoelectrodos con el fin de lograr dispositivos viables para la fotodisociación del agua consiste en el uso de co-catalizadores. Sin embargo, y aunque es un factor esencial que determina de manera crucial la eficiencia de los fotoelectrodos, el control fino de la cantidad de co-catalizador depositada en la superficie del electrodo generalmente no recibe mucha atención.

En este contexto, en el Capítulo IV se ilustra cómo la caracterización electroquímica en oscuridad de fotoánodos modificados con co-catalizador puede proporcionar información valiosa sobre la cantidad precisa de co-catalizador electroactivo presente en su superficie, facilitando nuestra comprensión sobre la forma en que estos funcionan y allanando el camino para su optimización. Para este propósito, se depositaron capas ultrafinas de $Ni(OH)_2$ sobre fotoánodos $BiVO_4$ (dopados y sin dopar) y $FeVO_4$ mediante un método de depósito por baño químico muy versátil que permite modular la cantidad depositada de co-catalizador mediante el control del tiempo de depósito. De esta manera, se demuestra que el $Ni(OH)_2$ depositado cataliza con éxito el proceso de oxidación fotoelectroquímica del agua sobre los electrodos

de $BiVO_4$ y $FeVO_4$, al mejorar la transferencia efectiva de los huecos fotogenerados desde el semiconductor a la disolución. De hecho, la actividad electrocatalítica de los fotoánodos modificados con $Ni(OH)_2$ aumenta rápidamente con la cantidad depositada de $Ni(OH)_2$ hasta que se alcanza un valor óptimo para recubrimientos equivalentes a solo 0.46 y 1.68 monocapas de $Ni(OH)_2$ para $BiVO_4$ y $FeVO_4$, respectivamente.

En estas condiciones, y en medio alcalino, el $Ni(OH)_2$ aumenta la magnitud de la fotocorriente en un factor de 2 para los fotoánodos de $BiVO_4$ y de 1.2 para los de $FeVO_4$. Las pequeñas cantidades de $Ni(OH)_2$ que conducen a un comportamiento óptimo del fotoánodo indican que se favorece la transferencia de huecos a través de los sitios activos de la superficie de vanadato, que también serían los sitios preferenciales para el depósito de $Ni(OH)_2$. Cantidades adicionales de co-catalizador generadas para tiempos depósito más largos inducen una disminución drástica en la actividad fotoelectrocatalítica de $Ni(OH)_2$ debido a la recombinación de cargas en la interfase semiconductor/$Ni(OH)_2$, probablemente intensificada por la baja movilidad de los portadores a lo largo del depósito de $Ni(OH)_2$.

Este estudio demuestra que la preparación de fotoánodos eficientes para la generación de oxígeno con una cantidad extremadamente pequeña de co-catalizador a través de un procedimiento sencillo y escalable es posible.

Capítulo V. Hidróxidos de hierro y cobalto: describiendo la tendencia existente entre la electroactividad con respecto a la reacción de generación de oxígeno y la cantidad de electrocatalizador.

En el Capítulo V se muestra una caracterización detallada de depósitos de hidróxido de hierro y cobalto como electrocatalizadores para la reacción de generación de oxígeno en medio alcalino, a modo de primer paso antes de su uso como co-catalizadores en la superficie

de los fotoánodos de vanadato. Este tipo de estudios preliminares son esenciales en tanto que, aunque la cantidad de electrocatalizador para la generación de oxígeno es un factor que determina su propia eficiencia, la correlación fundamental con su electroactividad sigue sin estar clara.

Para abordar este problema, se hace uso de un método de depósito por baño químico a base de urea que permite controlar la cantidad de electrocatalizador ($Fe(OH)_2$ y α-$Co(OH)_2$) depositado sobre un sustrato de vidrio conductor. El espesor de los depósitos resultantes, cuyo uso en electrocatálisis no tiene precedentes, se modula controlando el tiempo de depósito. La frecuencia de cambio para la generación de O_2 disminuye drásticamente a medida que aumenta la cantidad de electrocatalizador, concretamente para recubrimientos superiores a 3.5 y 0.05 monocapas de $Fe(OH)_2$ y de α-$Co(OH)_2$, respectivamente. El comportamiento tan diferente de ambos hidróxidos se explica a partir de la estructura de los depósitos incipientes, formados por pequeñas nanopartículas aciculares en el caso de $Fe(OH)_2$ y por micropartículas planas más grandes en el caso de α-$Co(OH)_2$. La primera estructura permite que una gran fracción de los sitios de Fe esté en contacto directo con la disolución, mientras que dicha fracción disminuye muy rápidamente al aumentar la cantidad de α-$Co(OH)_2$. Es importante resaltar que los electrodos de $Co(OH)_2$ preparados en este estudio muestran números de cambio muy similares (o incluso superiores) a los de los electrodos también de $Co(OH)_2$ preparados por rutas más complejas. Las películas ultrafinas óptimas de ambos hidróxidos son notablemente estables en medios alcalinos, lo que demuestra que es posible la preparación de electrocatalizadores eficientes para la generación de oxígeno con una cantidad extremadamente pequeña de metal a través de un depósito por baño químico que es novedoso, fácil y escalable.

Capítulo VI. Optimización de la electroactividad con respecto a la reacción de generación de oxígeno de electrodos de $Fe(OH)_2$ modificados con Ni y Co a través del control de su estructura y composición.

El Capítulo VI da un paso adelante con respecto al Capítulo V y presenta (oxi)hidróxidos mixtos de NiFe y CoFe como electrocatalizadores prometedores y altamente activos para la reacción de generación de oxígeno en medios alcalinos. Siguiendo una estrategia similar a la que se presenta en el capítulo anterior, se han preparado diferentes electrodos de $Fe(OH)_2$-$Ni(OH)_2$ y $Fe(OH)_2$-$Co(OH)_2$ a través de un depósito por baño químico a base de urea que permite controlar y optimizar la estructura y la cantidad de hidróxido depositada. De esta manera, se ha evaluado el efecto de la disposición espacial de los metales en los depósitos de hidróxido sobre la actividad electrocatalítica en medios alcalinos, llegándose a la conclusión de que los electrodos formados por una capa de $Fe(OH)_2$ depositada sobre el sustrato de vidrio conductor sobre la que, a su vez, se depositan cantidades variables (pero inferiores a la monocapa) de hidróxidos de Ni o Co son los que exhiben mejor comportamiento electrocatalítico. La frecuencia de cambio para la generación de O_2 aumenta drásticamente a medida que disminuye la cantidad de Ni o Co, alcanzando valores máximos 2.6 y 1.6 veces más altos que los obtenidos para electrodos de FTO/$Ni(OH)_2$ y FTO/$Co(OH)_2$, respectivamente. Esto demuestra que la presencia de nanopartículas de $Fe(OH)_2$ subyacentes juega un papel crucial en la mejora de las propiedades electrocatalíticas de los sitios electrocatalíticamente activos de Ni o Co. El hecho de que estos electrodos ultrafinos, formados por cantidades extremadamente pequeñas de electrocatalizadores, muestren una buena estabilidad en medios alcalinos allana el camino para su uso como electrodos transparentes o co-catalizadores sobre fotoánodos que promuevan la disociación fotoelectrocatalítica del agua.

Capítulo VII. Depósito secuencial de $Fe(OH)_2/Ni(OH)_2$ como co-catalizador para la generación de oxígeno: aumentando el rendimiento de fotoánodos de vanadato de bismuto.

Es conocido que los dispositivos de disociación fotoelectroquímica de agua de mayor rendimiento utilizan fotoánodos de óxidos semiconductores recubiertos con co-catalizadores para la reacción de oxidación de agua. En este sentido, el Capítulo VII constituye la culminación del proceso iniciado en capítulos anteriores referido al desarrollo de fotoánodos optimizados y superficialmente modificados con co-catalizadores a base de hidróxido. Dado que la cantidad de co-catalizador ha sido identificada como un factor que determina de manera crucial el rendimiento fotoelectroquímico de los fotoánodos (tal y como se muestra en el Capítulo II), el Capítulo VII muestra una estrategia simple para llevar a cabo la optimización necesaria de la cantidad depositada de electrocatalizador. Así, el electrocatalizador $Fe(OH)_2/Ni(OH)_2$ previamente desarrollado en el Capítulo VI se ha depositado a modo de co-catalizador sobre fotoánodos de $BiVO_4$ por medio de un método de depósito por baño químico a base de urea que permite un control secuencial, preciso y fino de la cantidad depositada de los dos hidróxidos diferentes controlando solo el tiempo de depósito. La fotoactividad óptima (de acuerdo con el valor de la fotocorriente medida a 1.23 V *vs*. RHE) para fotoánodos de $BiVO_4/Fe(OH)_2/Ni(OH)_2$ se obtiene para valores de recubrimiento equivalentes a 2.4 y 0.8 monocapas de $Fe(OH)_2$ y $Ni(OH)_2$, respectivamente, lo que subraya las cantidades relativamente pequeñas de co-catalizador necesarias para un rendimiento fotoelectroquímico óptimo.

Capítulo VIII. La existencia de vacantes de oxígeno en fotoánodos nanoestructurados de $LaFeO_3$ mejora la actividad para la oxidación del agua solar.

La búsqueda de materiales de bajo coste, pero altamente activos para la oxidación del agua con los que conseguir una tecnología competitiva para la disociación fotoelectroquímica del agua impulsada por el sol, ha posicionado a $LaFeO_3$ como un candidato emergente para su uso como fotoánodo. Desafortunadamente, los estudios realizados en este ámbito revelan que este material exhibe una respuesta fotoelectroquímica muy inferior a la registrada con otros fotoánodos basados en ferritas. Con el objetivo de identificar los principales factores que limitan el rendimiento de este material y propulsar su implementación como fotoánodo, en el Capítulo VIII se presenta una nueva ruta sintética que da lugar a un electrodo de $LaFeO_3$ de tipo *nanorod*, en la que también se contemplan estrategias de mejora del material basadas en la incorporación de vacantes de oxígeno en su estructura y en su modificación superficial. De esta manera, se obtiene un fotoánodo de $LaFeO_3$ que ofrece una densidad de fotocorriente de 0.4 mA cm^{-2} (medida a 1.23 V *vs.* RHE) y un potencial de inicio de la fotocorriente inferior a 0.55 V *vs.* RHE.

El estudio realizado permite determinar que los defectos de oxígeno en la estructura del material aumentan su actividad con respecto a la reacción de generación de oxígeno, tal y como lo confirma la caída de la pendiente de Tafel de 160 a 110 mV dec^{-1}, mientras que su recubrimiento con $NiFeO_x$ suprime drásticamente la recombinación de las cargas fotogeneradas a nivel de la superficie. Sin embargo, se observa un deterioro gradual de la fotorrespuesta como consecuencia de la pérdida de dichas vacantes de oxígeno en la estructura del material. Por otro lado, la existencia de fenómenos de recombinación de portadores fotogenerados a nivel del seno del material y a escala de nanosegundos, junto con la generación de un campo de carga espacial débil identificado y una longitud de difusión

ultracorta de los huecos fotogenerados (< 5 nm) termina por limitar el rendimiento de estos fotoánodos. En general, en el Capítulo VIII se proporcionan pautas para acelerar el desarrollo de fotoánodos de $LaFeO_3$, así como nuevos conocimientos sobre el comportamiento fotoelectroquímico de los materiales pertenecientes a la familia emergente de perovskitas para la producción de combustible solar.

La investigación que condujo a los resultados mostrados en este Capítulo se llevó a cabo en las instalaciones del *Laboratory for Molecular Engineering of Optoelectronic Nanomaterials* (LIMNO) en la École Polytechnique Fédérale de Lausanne (EPFL), en Lausana (Suiza), durante una estancia de investigación de tres meses realizada bajo la supervisión del Dr. Kevin Sivula y del Dr. Néstor Guijarro.

Capítulo IX. Comportamiento fotoelectroquímico e información computacional de fotocátodos de capa fina de $NdFeO_3$.

El Capítulo IX constituye el primer estudio sobre el empleo de ferrita de neodimio ($NdFeO_3$) como fotocátodo hasta la fecha. De hecho, la ferrita $NdFeO_3$ puede considerarse como un candidato adecuado para este fin debido a su similaridad con uno de los óxidos ternarios pertenecientes a la familia de las perovskitas más estudiados: el $LaFeO_3$.

Así, el Capítulo IX se refiere a la preparación de fotocátodos transparentes de capa fina de $NdFeO_3$ mediante un procedimiento de sol-gel mediado por ácido cítrico, seguido de un tratamiento térmico. Los resultados obtenidos revelan que estos fotocátodos son activos tanto para la reacción de generación de hidrógeno como para la reacción de reducción de oxígeno. Los cálculos DFT han permitido obtener información sobre la naturaleza del comportamiento semiconductor tipo *p* de este material, y también han servido para resaltar la importancia de la nanoestructuración y la pasivación de los estados de superficie de Fe para aumentar el

rendimiento de estos fotocátodos. Para mejorar su fotoactividad, se ha observado que el dopado con Mg^{2+} y Zn^{2+} en una concentración igual a 5 at% en la disolución precursora aumenta significativamente el rendimiento fotoelectrocatalítico de $NdFeO_3$ por lo que respecta a la reducción de oxígeno. Tal mejora, que se atribuye principalmente al aumento de la densidad y la movilidad de los portadores de carga mayoritarios, revela que el $NdFeO_3$ tiene el potencial necesario para ser utilizado como fotocátodo en procesos fotoelectroquímicos.

Capítulo X. La ingeniería de superficie como estrategia efectiva para mejorar la fotoactividad de fotocátodos de $NdFeO_3$ con respecto a la reacción de generación de hidrógeno.

El Capítulo X se centra en el desarrollo de una estrategia para mejorar la fotoactividad de los fotocátodos de $NdFeO_3$ previamente desarrollados en el Capítulo IX basada la combinación de una capa extractora con partículas metálicas que actúan como co-catalizadores. De hecho, el acoplamiento de una capa de estas características con un co-catalizador metálico a nivel de la superficie de un fotocátodo es uno de los procedimientos más comunes hoy en día para mejorar su actividad fotoelectroquímica para la reacción de generación de hidrógeno.

Por ello, el Capítulo X presenta un procedimiento basado en el depósito de una capa extractora/pasivante de TiO_2 sobre fotocátodos de NdFeO3 (dopados y sin dopar) mediante un procedimiento de *drop casting*, seguido del electrodepósito de cantidades controladas de nanopartículas de Ni como co-catalizadores para la reacción de generación de hidrógeno. La fotoactividad más alta (de acuerdo con el valor de la fotocorriente a 0.1 V *vs*. Ag/AgCl) se logra para recubrimientos óptimos de Ni de alrededor de 4.7, 4.9 y 3.7 monocapas para

fotocátodos de $NdFeO_3/TiO_2$/Ni, Mg (5 at%)-$NdFeO_3/TiO_2$/Ni y Zn (5 at%)-$NdFeO_3/TiO_2$/Ni, respectivamente. Esto implica mejoras significativas de la fotocorriente en factores de 5.8, 4.8 y 5.2, respectivamente, en comparación con el fotoelectrodo $NdFeO_3/TiO_2$ dopado o sin dopar correspondiente.

Este estudio apunta a la posibilidad de abordar estrategias de ingeniería de superficie en fotocátodos a partir de técnicas de síntesis simples y sin recurrir a co-catalizadores basados en partículas de metales nobles.

Capítulo XI. Conclusiones.

El Capítulo XI recoge las principales conclusiones generales y específicas obtenidas como consecuencia del desarrollo de esta tesis. De esta manera, las conclusiones generales que se pueden extraer de esta tesis doctoral son las siguientes:

i) El dopado constituye una estrategia efectiva para mejorar las propiedades fotoelectroquímicas tanto de fotoánodos como de fotocátodos. El dopado con impurezas logrado por métodos húmedos induce un aumento en la densidad de uno de los portadores de carga eléctrica (electrones o huecos), tal y como lo demuestran las medidas de Mott-Schottky.

ii) La ingeniería de superficie practicada sobre fotoelectrodos, entendida como la modificación de su superficie con depósitos que actúan como co-catalizadores, constituye una estrategia adecuada para mejorar su comportamiento fotoelectroquímico con respecto a las reacciones de generación de oxígeno e hidrógeno.

iii) Los hidróxidos del grupo de hierro ($Ni(OH)_2$, $Fe(OH)_2$ y $Co(OH)_2$), tanto a nive individual como combinados convenientemente, actúan como co-catalizadores para la reacción de generación de oxígeno bajo iluminación sobre fotoánodos de vanadato.

iv) La combinación adecuada de una capa de pasivante/extractora de TiO_2 con depósitos de Ni que actúan como co-catalizador constituye una estrategia efectiva para mejorar la fotoactividad de fotocátodos de $NdFeO_3$ hacia la reacción de generación de hidrógeno bajo iluminación.

v) La cantidad de co-catalizador depositada en la superficie del fotoelectrodo es un factor clave que determina crucialmente su eficiencia, lo que ilustra la necesidad de realizar un control cuidadoso de la cantidad depositada.

vi) El depósito por baño químico y el electrodepósito son métodos de síntesis que permiten un control directo y fino de la cantidad depositada de co-catalizador mediante el control del tiempo de depósito.

vii) Los métodos electroquímicos (como la voltametría cíclica y la voltametría lineal) destacan como técnicas útiles para monitorear la cantidad existente de co-catalizador en la superficie del fotoelectrodo y para caracterizar su actividad fotoelectroquímica en función de dicha cantidad.

Las conclusiones específicas extraídas de esta tesis doctoral son las siguientes:

i) Los electrodos de capa fina de $BiVO_4$ y $FeVO_4$ preparados capa a capa sobre sustratos FTO a partir de un método de descomposición de precursores organometálicos, seguido de un tratamiento térmico, se comportan como fotoánodos eficientes para la reacción de oxidación del agua. El dopado posterior de $BiVO_4$ con La (1 at%) y Ce (2 at%) aumenta la fotocorriente asociada a la fotooxidación del agua y provoca un desplazamiento del potencial de banda plana del $BiVO_4$ hacia valores más negativos. Esto se debe a un aumento en la concentración del portador de carga mayoritario, lo que resulta en una conductividad electrónica mejorada del $BiVO_4$, y a una pasivación de los estados de la superficie vinculados a la recombinación electrón-hueco. Además, tanto los fotoánodos de $BiVO_4$ dopados como

no dopados pueden modificarse superficialmente con nanopartículas de oro, que actúan como co-catalizadores, lo que induce una mejora adicional de la fotoactividad del electrodo.

ii) Se han depositado capas ultrafinas de $Ni(OH)_2$ sobre fotoánodos de $BiVO_4$ (dopado y no dopado) y de $FeVO_4$ mediante un método de depósito por baño químico a base de urea que permite un control directo y fino de la cantidad de co-catalizador depositado. El comportamiento fotoelectroquímico de los fotoánodos de vanadato superficialmente modificados con $Ni(OH)_2$ depende de la cantidad de $Ni(OH)_2$, que, a su vez, depende del tiempo de depósito de $Ni(OH)_2$.

iii) Cuando la cantidad de $Ni(OH)_2$ sobre la superficie del fotoánodo de vanadato es pequeña (recubrimientos equivalentes a una monocapa e inferiores), la mayoría de los átomos de níquel depositados actúan como centros catalíticos activos para la transferencia de huecos a la disolución en tanto que están en islas directamente expuestas al electrolito. Sin embargo, las capas más gruesas de $Ni(OH)_2$, obtenidas para tiempos de depósito más largos, inducen una disminución drástica en la actividad electrocatalítica, ya que un número creciente de átomos de Ni depositados no actuaría como centros catalíticos activos sino como centros de recombinación, ya que no están en directo contacto con el electrolito.

iv) Se han depositado películas ultrafinas de $Fe(OH)_2$ y α-$Co(OH)_2$ sobre sustratos de FTO mediante un método de depósito por baño químico, que constituye un nuevo procedimiento para sintetizar estos electrocatalizadores en forma de películas delgadas. Este mismo procedimiento permite la preparación de electrocatalizadores basados en depósitos mixtos de $Fe(OH)_2$-$Ni(OH)_2$ y $Fe(OH)_2$-$Co(OH)_2$. A este respecto, una estructura basada en una capa de nanopartículas de $Fe(OH)_2$ crecida directamente sobre FTO modificada superficialmente con submonocapas de depósitos de $Ni(OH)_2$ o $Co(OH)_2$, exhibe la mejor respuesta electrocatalítica para la reacción de generación de oxígeno (en términos de

frecuencia de cambio para la generación de O_2). De hecho, para todos los electrodos, la frecuencia de cambio aumenta drásticamente a medida que disminuye la cantidad de hidróxido activo porque la cantidad de hidróxido en contacto directo con el sustrato y la disolución es máxima.

v) Se ha generado un depósito de $Fe(OH)_2/Ni(OH)_2$ sobre la superficie de fotoánodos de $BiVO_4$ mediante un método de depósito por baño químico a base de urea que permite un control directo y fino de la cantidad depositada de los dos diferentes hidróxidos controlando solo los correspondientes tiempos de depósito. Para cantidades óptimas de $Fe(OH)_2$ y $Ni(OH)_2$, se comprueba que la capa inferior de hidróxido de hierro mejora drásticamente la eficiencia del co-catalizador de $Ni(OH)_2$, lo que ilustra la importancia de un control preciso de la cantidad de co-catalizador depositado en la superficie del fotoelectrodo para obtener una respuesta fotoelectroquímica optimizada.

vi) Los electrodos de $LaFeO_3$ de tipo *nanorod* preparados por primera vez mediante un baño químico y un procedimiento de síntesis basado en sol-gel sobre sustratos FTO, seguido de un tratamiento térmico, se comportan como fotoánodos para la oxidación del agua. La combinación adicional de ingeniería de defectos de oxígeno en su estructura y pasivación de superficie con $NiFeO_x$ establece un nuevo rendimiento de referencia para los fotoánodos de $LaFeO_3$ para la oxidación del agua. Esto se debe a una activación sinérgica de la interfase reactiva al reducir el sobrepotencial para la reacción de generación de oxígeno y la recombinación de superficie. Sin embargo, la existencia de fenómenos de recombinación significativa de portadores de carga en escalas de tiempo ultracortas, de un campo de carga espacial débil y la pequeña longitud de difusión de los portadores limitan su respuesta fotoelectroquímica.

vii) Los electrodos de película delgada de $NdFeO_3$ preparados capa por capa sobre sustratos de FTO mediante un método sol-gel mediado por citrato, seguido de un tratamiento térmico, se comportan como fotocátodos para la reducción de oxígeno y de agua en medios alcalinos. El dopado posterior de $NdFeO_3$ con Mg y Zn (5 at% para ambos cationes) induce un aumento en la fotocorriente asociada a la reacción de reducción de oxígeno atribuida principalmente a un aumento en la densidad del portador de carga mayoritario y, en menor medida, a un fenómeno de pasivación superficial. Los cálculos DFT confirman el carácter semiconductor tipo *p* de este material y revelan una banda de conducción muy plana, lo que indica una baja movilidad de electrones.

viii) El depósito de una capa extractora/pasivante de TiO_2 en fotocátodos de $NdFeO_3$ dopados y sin dopar mediante mediante *drop casting*, seguido del electrodepósito de cantidades controladas de nanopartículas de Ni, que actúan como co-catalizadores para la reacción de generación de hidrógeno bajo iluminación, induce una mejora significativa de la fotocorriente. El comportamiento fotoelectroquímico del $NdFeO_3$ modificado en superficie depende de la cantidad de TiO_2 y Ni depositados, lo que, a su vez, depende tanto del volumen de la disolución precursora de TiO_2 como del tiempo de depósito de Ni.

Scientific impact

PEER-REVIEWED PUBLICATIONS

1. J. Quiñonero, T. Lana-Villarreal, R. Gómez, Improving the Photoactivity of Bismuth Vanadate Thin Film Photoanodes through Doping and Surface Modification Strategies, *Applied Catalysis B: Environmental*, **2016**, *194*, 141-149.

2. J. Quiñonero, R. Gómez, Controlling the Amount of Co-catalyst as a Critical Factor in Determining the Efficiency of Photoelectrodes: The Case of Nickel (II) Hydroxide on Vanadate Photoanodes, *Applied Catalysis B: Environmental*, **2017**, *217*, 437-447.

3. J. Quiñonero, R. Gómez, Iron and Cobalt Hydroxides: Describing the Oxygen Evolution Reaction Activity Trend with the Amount of Electrocatalyst, *Electrochimica Acta*, **2018**, *274*, 224-232.

4. J. Quiñonero, T. Lana-Villarreal, R. Gómez, Tuning the Oxygen Evolution Reaction Activity of Ni- and Co-Modified $Fe(OH)_2$ Electrodes through Structure and Composition Control, *International Journal of Hydrogen Energy*, **2020**, *45*, 17076-17087.

CONFERENCE CONTRIBUTIONS

1. J. Quiñonero, T. Lana-Villarreal, R. Gómez, Improving the Photoactivity of $BiVO_4$ Thin Film Photoanodes through Doping and Surface Modification Strategies (Poster Contribution). XII Jornadas Científicas del Instituto Universitario de Materiales (IUMA) de la Universidad de Alicante (UA). Alicante, Spain, January 21st-22nd, 2016.

2. J. Quiñonero, R. Gómez, Nickel (II) Hydroxide as a Co-catalyst for Photoelectrochemical Water Oxidation on Bismuth and Iron Vanadate Electrodes (Poster

Contribution). XIII Jornadas Científicas del Instituto Universitario de Materiales (IUMA) de la Universidad de Alicante (UA). Alicante, Spain, January 19th-20th, 2017.

3. J. Quiñonero, R. Gómez, The Amount of Co-catalyst as a Key Factor Determining the Efficiency of Photoelectrodes: The Case of Iron-Group Metal Hydroxides for Oxygen Evolution Reaction (Oral Contribution). Photoelectrocatalysis at the Atomic Scale (PECAS) Summer School. Universidad del País Vasco- Euskal Herriko Unibertsitatea (UPV-EHU). San Sebastián-Donostia, Spain, June 27th-30th, 2017.

4. J. Quiñonero, R. Gómez, Iron and Cobalt Hydroxides: Describing the Oxygen Evolution Reaction Activity Trend with the Amount of Electrocatalyst (Poster Contribution). XIV Jornadas Científicas del Instituto Universitario de Materiales (IUMA) de la Universidad de Alicante (UA). Alicante, Spain, January 18th-19th, 2018.

5. J. Quiñonero, R. Gómez, Tuning the Oxygen Evolution Reaction Activity of $Fe(OH)_2/Ni(OH)_2$ Electrodes through Structure and Composition Control (Poster Contribution). XV Jornadas Científicas del Instituto Universitario de Materiales (IUMA) de la Universidad de Alicante (UA). Alicante, Spain, January 23rd-25th, 2019.

6. J. Quiñonero, R. Gómez, Metal Doping and Co-catalysis to Enhance the Photoelectrochemical Behavior of $NdFeO_3$ Photocathodes (Poster Contribution). 7th International Conference on Semiconductor Photochemistry (SP7). Società Chimica Italiana – Università degli Studi di Milano (UNIMI). Milan, Italy, September 11th-14th, 2019.

7. J. Quiñonero, T. Lana-Villarreal, R. Gómez, $Fe(OH)_2/Ni(OH)_2$ Deposition on $BiVO_4$ Photoanodes: An Example on How to Address the Optimization of the Amount of Co-catalyst (Oral Contribution). 7th International Conference on Semiconductor Photochemistry (SP7). Società Chimica Italiana – Università degli Studi di Milano (UNIMI). Milan, Italy, September 11th-14th, 2019.

8. J. Quiñonero, R. Gómez, Metal Doping and Co-catalysis to Enhance the Photoelectrochemical Behavior of $NdFeO_3$ Photocathodes (Poster Contribution). XVI Jornadas Científicas del Instituto Universitario de Materiales (IUMA) de la Universidad de Alicante (UA). Alicante, Spain, January 23rd-24th, 2019.

RESEARCH STAYS

1. Entity: École Polytechnique Fédérale de Lausanne (EPFL), Lausanne, Switzerland. Supervisor: Prof. Dr. Kevin Sivula. Duration: 3 months (from April 1st, 2018 to June 30th, 2018). Research tasks: Development and optimization of $LaFeO_3$ photoelectrodes for solar water splitting. This research stay was funded by the Spanish Ministry of Education, Culture, and Sport (MECD) through a mobility grant (EST17/00429).